

**Calculating hydraulic conditions of turbidity currents from
surficial and subsurface deepwater channel architecture**

Adriana Crisóstomo Figueroa

Submitted in accordance with the requirements for the degree of
Doctor of Philosophy

The University of Leeds
School of Earth and Environment
Institute of Applied Geoscience

May 2022

The candidate confirms that the work submitted is her own, except where work which has formed part of jointly-authored publications has been included. The contribution of the candidate and the other authors to this work has been explicitly indicated below. The candidate confirms that appropriate credit has been given within the thesis where reference has been made to the work of others.

The work in Chapter 3 of the thesis has appeared in publication as follows:

Crisóstomo-Figueroa, A., McArthur, A.D., Dorrell, R.M., Amy, L. and McCaffrey, W.D., 2021. A new modelling approach to sediment bypass prediction applied to the East Coast Basin, New Zealand. *Bulletin of the Geological Society of America*, 133, p. 1734-1748.

Submitted: 9th March 2020

Re-submitted: 16 August 2020

Accepted: 20 Oct 2020

As the primary author, I led the research, undertook the modelling work, collected and interpreted data, and prepared the manuscript (figures, plots and writing). The MATLAB script for the turbidity current modelling was developed from scratch by me and RMD. The MATLAB script for the Flow-Power Flux Balance model was written and provided by RMD. All co-authors contributed to the discussion of data results and manuscript review.

In July 2022, the work in Chapter 4 was accepted for publication in *Sedimentology* pending major revisions. The reviewer's suggestions have not been incorporated into the chapter.

Crisóstomo-Figueroa, A., McArthur, A.D., Amy, L., Dorrell, R.M. and McCaffrey, W.D., (in revision). A critical test of calculating deepwater palaeo-hydraulic conduits from subsurface channel architecture: examples from the Hikurangi Margin, New Zealand.

Submitted: 26th April 2022

As the primary author, I led the research, undertook the seismic mapping and modelling work, collected and interpreted data, and prepared the manuscript (figures, plots and writing). The MATLAB script for the turbidity current modelling was developed from scratch by me and RMD. The MATLAB script for the Flow-

Power Flux Balance model was written and provided by RMD. All co-authors contributed to the discussion of data results and manuscript review.

This copy has been supplied on the understanding that it is copyright material and that no quotation from the thesis may be published without proper acknowledgement.

The right of Adriana Crisóstomo Figueroa to be identified as Author of this work has been asserted by her in accordance with the Copyright, Designs and Patents Act 1988.

© 2022 The University of Leeds and Adriana Crisóstomo Figueroa

Acknowledgements

Firstly, I would like to thank Bill McCaffrey and Adam McArthur for taking me as a student in the TRG and giving me the opportunity to pursue a doctoral degree at Leeds. Your support and guidance throughout the PhD have been invaluable. Thank you also for providing me with the opportunity to travel abroad and see beautiful places with amazing geology during the sponsor's meetings. I am also very grateful for the supervision of Lawrence Amy and Rob Dorrell, this work would not have been possible without your support, expertise and discussions. Thank you all for sharing your knowledge and wisdom which I'm sure I'll take on forever in my professional and personal life.

I am grateful for the financial support of CONACyT-SENER throughout this project, as well as the TRG sponsors'. I am also grateful for the financial support provided by the PGR Pandemic Support Fund. I would also like to thank the National Institute of Water and Atmospheric Research (New Zealand) and WestenGeco Multiclient for providing the bathymetry and seismic data sets, respectively, used in chapters 3 and 4.

I want to thank all the friends I made in Leeds who made my student experience unforgettable, particularly Dan, Laura, Danita, Kaixuan and Junia. Thanks for your friendship and support, it was great to have shared many memorable moments during the PhD!

I am deeply grateful for the continuous support that the GeoLatinas community has provided me since the start of my PhD. I cannot thank enough for the mentoring, support and friendship of Rocío Caballero-Gill and Clara Rodriguez. You inspire me every day to be a better leader and geoscientist through your example, I am truly honoured to be learning from you. Thank you for always being there, for helping me beat that impostor syndrome and teaching me to always do things with intention. I also want to deeply thank all my IMPETU friends for being a great company during all our writing sessions, you were an amazing support while writing papers and this thesis.

I cannot forget to thank all my friends in Mexico who have been following my experiences and haven't been rooting for me ever since the day I moved. I am grateful for all your support, love and friendship throughout the years.

I would like to thank the support and love of my partner Sergio. It has been great to share this journey with you and I am excited to see what the future holds for us. I also want to thank my family for always being very supportive and for cheering me up in every step of the way.

Finally, I want to give special thanks to my mother and sister who have been my rock and have encouraged me to follow my interests and goals even if it is thousands of kilometres apart from them. I love you and I dedicate this huge milestone to you. This work is also dedicated to my father who, although could not see me reaching this stage in my career, was a huge support in my early professional education and I would not be here without him.

Abstract

Turbidity currents, a form of particulate gravity current, are an important agent of sediment, nutrient and pollutant transport into deep marine settings. They commonly form submarine channels, whose geometry can be used to condition hydraulic models that reconstruct the dynamics of formative flows. This approach has here been extended to integrate theoretical models of turbidity current dynamics with channel geometry to address three key challenges in deep-water sedimentology.

Firstly, a new modelling approach is applied to two surficial channels of the Hikurangi Margin of New Zealand to predict whether turbidity currents can bypass sediment, depending upon flow height, the sorting of the sediment in suspension and the slope. Thick flows with well-sorted suspensions are shown to be more efficient in bypassing sediment than shallow flows transporting poorly-sorted sediment in suspension; these latter flows need steeper gradients to transport an equivalent median particle size of suspended material. Model results for the spatial distribution of sand from poorly-sorted flows are in good agreement with seismic amplitude maps and drop core data.

Secondly, using high-resolution 3D seismic data, the new modelling approach is applied to mapped subsurface channel-forms within the Omakere Channel Complex of the Hikurangi Margin to determine if they represent palaeohydraulic conduits. The derivation of disequilibrium flow conditions at some channel bends suggests that these channel-forms either represent compound bodies or that they were not in equilibrium with traversing flows, possibly due to the presence of a mass-transport-deposit substrate. These factors constitute important sources of modelling uncertainty in the calculation of palaeo-hydraulic conditions from subsurface channel architecture.

Finally, changes in the tilt of the flow-ambient fluid interface are modelled to assess whether a strong latitudinal control exists in the development of channel sinuosity. The effects of the slope (also proposed as a dominant control), channel size and flow properties are also evaluated. The outcomes suggest that the tendency of channels to become sinuous cannot be predicted by single end-members like latitude or slope. At any latitude, large, low-gradient channels predominantly traversed by dilute, shallow flows may be characterised by low sinuosities, whereas small, high gradient channels traversed by dense, deep flows may be sinuous.

Table of Contents

Acknowledgements	v
Abstract	vi
Table of Contents	vii
List of Tables	xii
List of Figures	xiii
Abbreviations and symbols	xxi
Chapter 1 Introduction	1
1.1 Background and rationale	1
1.2 Aims and objectives	3
1.3 Thesis outline	4
Chapter 2 Literature review	7
2.1 Turbidity currents.....	7
2.1.1 Definition and significance.....	7
2.1.2 Triggers	7
2.1.3 Flow structure and dynamics.....	8
2.1.3.1 Horizontal and vertical structure	8
2.1.3.2 Flow states and evolution	10
2.1.3.3 Sediment bypass.....	11
2.2 Submarine channels.....	14
2.2.1 Overview	14
2.2.2 Morphology and evolution	15
2.2.2.1 Cross-sectional morphology and longitudinal profile	16
2.2.2.2 Planform morphology - sinuosity	18
2.2.3 Subsurface channel-forms	22
2.3 Modelling of channelised turbidity currents from channel architecture	25
2.3.1 The surface-slope equation.....	26
2.3.1.1 Theory	26
2.3.1.2 Application to channel systems	28
Chapter 3 A new modelling approach to sediment bypass prediction applied to the Hikurangi Margin, New Zealand	33
3.1 Abstract.....	33
3.2 Introduction	33

3.2.1 Terminology	34
3.3 Geological setting.....	36
3.4 Methods	38
3.4.1 Datasets and morphological analysis	38
3.4.2 Turbidity current modelling	40
3.4.3 Modelling of the net erosion and net deposition threshold for turbidity currents.....	43
3.5 Results	44
3.5.1 Madden canyon – channel morphology.....	44
3.5.2 Modelled turbidity current conditions in the Madden channel.....	47
3.5.3 Omakere channel morphology	50
3.5.4 Modelled turbidity current conditions in the Omakere channel.....	51
3.5.5 Sediment bypass conditions in the Madden channel	53
3.5.5.1 Well-sorted flows.....	53
3.5.5.2 Poorly-sorted flows.....	54
3.5.6 Sediment bypass conditions in the Omakere channel.....	56
3.5.6.1 Well-sorted flows.....	56
3.5.6.2 Poorly-sorted flows.....	56
3.6 Discussion	58
3.6.1 Controls on sediment bypass and implications for sand distribution.....	58
3.7 Conclusions.....	62
Chapter 4 Calculating deepwater palaeo-hydraulic conditions from subsurface channel architecture: a critical test using examples from the Hikurangi Margin, New Zealand	63
4.1 Abstract.....	63
4.2 Introduction	64
4.3 Geological setting.....	66
4.4 Study area.....	68
4.4.1 The Omakere Trough	68
4.5 Dataset and methodology	68
4.5.1 Seismic dataset and interpretation	68
4.5.2 Morphometric analysis	69
4.5.3 Modelling of palaeo-hydraulic conditions.....	70
4.5.3.1 Sensitivity Analysis.....	72

4.5.4	Estimating the net erosion - net deposition threshold.....	75
4.6	Results	76
4.6.1	Seismic facies and depositional elements in the Omakere Trough.....	76
4.6.2	Seismic stratigraphy and geomorphology of the Omakere Channel Complex.....	78
4.6.2.1	Area 1.....	78
4.6.2.2	Area 2.....	78
4.6.2.3	Area 3.....	80
4.6.3	Channel-form A morphometrics and flow modelling results	82
4.6.3.1	Channel-form morphometrics.....	82
4.6.3.2	Model sensitivity	85
4.6.3.3	Calculated palaeo-hydraulic conditions	85
4.6.3.4	Calculated sediment bypass conditions	87
4.7	Discussion	90
4.7.1	Modelling as a critical test of the interpretation of subsurface channel-forms as palaeo-hydraulic conduits.....	90
4.7.1.1	Disequilibrium palaeo-hydraulic properties due to the presence of compound channel-forms	90
4.7.1.2	Disequilibrium palaeo-hydraulic properties due to disequilibrium channel morphologies controlled by MTDs.....	91
4.7.2	Comparing calculated modern to palaeo-hydraulic conditions in the Omakere Channel	92
4.7.3	Sources of modelling uncertainty and suggested solutions.	96
4.8	Conclusions.....	96
	Chapter 5 Modelling changes in the flow-ambient fluid interface tilt of turbidity currents: implications for the development of sinuous submarine channels.....	98
5.1	Introduction	98
5.2	Methods	102
5.2.1	Estimating the tilting of the flow-ambient fluid interface.....	102
5.2.2	Validating model tilt predictions with observed tilting in the NAMOC.....	104
5.2.3	Calculating changes in the tilting due to hydraulic, morphological and latitudinal changes	105
5.2.4	Calculating the downchannel transition slope	105
5.3	Results	107

5.3.1	NAMOC tilting and morphometric relationships.....	107
5.3.2	Comparing model predictions of the tilt to the NAMOC tilting.....	109
5.3.3	Variations in the tilting of the flow-ambient fluid interface..	111
5.3.4	Variations in the tilting transition slope <i>ST</i>	116
5.3.5	<i>ST</i> and global submarine channel data	119
5.4	Discussion.....	121
5.4.1	Controls on the effect of Coriolis based on changes in the flow-ambient fluid interface tilting	122
5.4.2	Controls on <i>ST</i> and implications for the development of sinuosity in submarine channels	123
5.5	Conclusions.....	125
Chapter 6 Discussion and Conclusions		126
6.1	Implications for the formation of sand-detached systems and bypass-related upslope turbidite pinchouts	126
6.2	Implications for sedimentation and erosion models based on Coriolis force changes.....	130
6.3	Synthesis.....	134
6.3.1	Uncertainty in known and unknown parameters in the modelling of turbidity currents	135
6.3.1.1	Flow height.....	135
6.3.1.2	Turbidity current interface tilting (cross-channel slope)	138
6.3.1.3	Drag coefficient	139
6.3.1.4	Ambient water entrainment	140
6.3.2	General recommendations	141
6.4	Conclusions.....	142
6.4.1	Summary.....	142
6.4.2	Chapter 3	142
6.4.3	Chapter 4	143
6.4.4	Chapter 5	144
6.5	Recommendations for future research	145
References		148
Appendix A Submarine channel data from Chapter 3		174
A.1	Madden Channel morphometrics	174
A.2	Omakere Channel morphometrics.....	175

Appendix B Channel-form data from Chapter 4	175
B.1 Channel-form A morphometrics	175
Appendix C Submarine channel data used in Chapter 5.....	177
C.1 NAMOC morphometrics	177
C.2 Global channel data	178
Appendix D MATLAB code for turbidity current modelling	179
D.1 Script	179
D.2 Function	180

List of Tables

Table 2.1 Summary of studies that used Komar (1969) surface-slope method to calculate bulk turbidity current properties. Columns for water entrainment and mixing list the reference to the equation used to parameterize each flow aspect.....	30
Table 3.1 Slope gradient values required to bypass very fine sand for the flow properties calculated in the Madden and Omakere channels.....	58
Table 4.1 Parameters assessed in the sensitivity analysis of Equations 4.2 and 4.3.....	73
Table 4.2 Deepwater depositional elements identified in the Omakere Trough are based on their seismic cross-section character and geomorphology.	77
Table 5.1 Input parameters used in the modelling of the flow-ambient fluid interface tilting.....	105
Table 5.2 Input parameters in the calculation of ST	106
Table A.1 Channel morphometrics used as input parameters in the turbidity current modelling for the Madden Channel. Values of 99999 correspond to straight channel sections.	174
Table A.2 Channel morphometrics used as input parameters in the turbidity current modelling for the Omakere Channel. Values of 99999 correspond to straight channel sections.	175
Table B.1 Channel morphometrics used as input parameters in the turbidity current modelling for channel-form A. Values of 99999 correspond to straight channel sections.	176
Table C.1 Parameters extracted from Klaucke et al., (1997) that were used in the calculations of the NAMOC tilting.....	177
Table C.2 Summary of data used from nine submarine channel systems. r , θ and Si were obtained from Sylvester and Pirmez (2019).....	178

List of Figures

Figure 2.1 Turbidity current produced in laboratory experiments (adapted from Sequeiros et al., 2009).....	8
Figure 2.2 (A) Sketch of the horizontal structure of a turbidity current divided in the head, body and tail (modified from Hansen et al., 2015). (B) Typical velocity and density/concentration profiles in turbidity currents.	9
Figure 2.3 Schematic diagram illustrating how bypass and erosion by sediment gravity flows might form upslope turbidite pinchout traps in proximal upslope areas (adapted from Amy, 2019).....	13
Figure 2.4 Submarine channel classification from Peakall and Sumner (2015) according to their morphology and occurrence in the continental slope and basin plain.	16
Figure 2.5 Compressed high-intensity radar pulse subbottom profile from the Lucia Chica channel system and schematic turbidity current (adapted from Maier et al. (2011).	16
Figure 2.6 (A) Schematic diagram of a channel slope profile (solid line) and the theoretical equilibrium slope profile (dashed line) that is achieved over time through erosion (1) or deposition (2) (from Amy and Dorrell, 2021); (B) schematic illustration of an aggradational channel and its sinuous planform; (C) schematic illustration of an erosional channel and its straight planform (B and C adapted from Kneller, 2003).	17
Figure 2.7 Block diagrams showing (A) overbanking or overspilling and (B) flow stripping by turbidity currents. Arrows indicate the flow direction (from Mulder, 2011).....	18
Figure 2.8 Examples of sinuous submarine channels. (A) Bathymetry image of a highly sinuous planform from Cap Timiris Canyon, offshore Mauritania, (B) root-mean-square seismic horizon slice from a sinuous subsurface channel, offshore West Africa; high amplitudes shown in red and low amplitudes in blue (adapted from Wynn et al., 2007).	19
Figure 2.9 Conceptual diagram showing the three-stage model from Peakall et al. (2000) for the development of high sinuosity, aggradational submarine channels.	20
Figure 2.10 Diagrams illustrating the four end-member submarine channel-structure interactions (A) confinement by pre-existing structures, (B) diversion by inactive structural high, (C) deflection by and (D) blocking by an actively growing structure (from Clark and Cartwright, 2009).....	22

Figure 2.11 Uninterpreted and interpreted seismic profiles across a channel-levee system on the Indus Fan, Arabian Sea, with well-defined external (outer) and internal levees confining channel-forms that show discontinuous-chaotic high-amplitude reflectors (D-C HARs) or continuous-parallel high-amplitude reflectors (C-P HARs) (from Deptuck et al., 2003).	23
Figure 2.12 (A) Seismic cross-section showing shingled reflections product of lateral channel migration with a sketch of their geometry below; (B) Cut and fill patterns in seismic profile and sketch characteristic of channel avulsion (A and B are adapted from Abreu et al., 2003) (C) Stacking patterns of submarine channels (adapted from Pickering et al., 1995).	24
Figure 2.13 The Coriolis effect causes turbidity current deflection to the right under strong northern hemisphere rotation (A) and to the left under strong southern hemisphere rotation (B) looking downstream (adapted from Wells and Dorrell, 2021).	26
Figure 2.14 Parameters obtained from the channel morphology are used as inputs into the surface-slope equation (from Komar, 1969).	27
Figure 3.1 Process terminology used in this study for a channelized turbidity current.	36
Figure 3.2 Study area. (A) The Hikurangi Margin is located on and offshore of the North Island, New Zealand and is limited to the east by the Hikurangi Trough and to the west by the axial ranges. (B) Offshore bathymetry map and bathymetric contours (500 m) of the study area (courtesy of the National Institute of Water and Atmospheric Research, New Zealand). (C) Regional cross-section across the Hikurangi subduction complex (after Nicol et al., 2007).	38
Figure 3.3 Sketch showing the morphometric parameters measured at channel bends, levee-bound channel cross-sections and erosional channel cross-sections of the Madden and Omakere channels.	39
Figure 3.4 (A) The bathymetry map and bathymetric contours (500 m) courtesy of NIWA, show the Madden Channel and Omakere Channel systems. The channel thalweg line styles differentiate the sub-channel sections described in this study. (B) Selected cross-sectional profiles (with orientation looking downstream) of the Madden Channel highlighting the down-channel evolution from the canyon-confined portion (transect A1) to the Akitio Trough (transect A6). Transect location shown in A. (C) Selected cross-sectional profiles of the Omakere Channel from the channel upper reaches (transect B1) to the northern Akitio Trough (transect B7).	46

Figure 3.5 (A) Seafloor dip map of the Madden and Omakere channels derived from 3D seismic data provided by WesternGeco Multiclient. (B) Interpreted seafloor dip map showing morphological features of the channels resulted from tectonic and sedimentary processes. The interpretation of the crests of thrust-faulted bathymetric ridges is derived from Barnes et al. (2010)..... 47

Figure 3.6 Calculated dimensions and turbidity current conditions in the Madden Channel from the upper reaches through the lower reaches section (sub-sections of the channel are shown at the top of the plots and differentiated with grey shading). (A) Channel thalweg depth profile (black solid line) and slope gradient profile (red dotted line) with values presented in degrees. (B) Average channel height profile (solid line) and cross-channel slope values (triangles). (C) Average channel width (solid line) and channel area (crosses). (D) Downstream turbidity current velocity profile. (E) Froude number profile, dashed line at 1 indicates the threshold between subcritical and supercritical flow. Downstream (F) shear velocity, (G) bulk sediment concentration, (H) flow discharge and sediment discharge profiles. 49

Figure 3.7 Calculated dimensions and turbidity current conditions in the Omakere Channel from the upper reaches through the Akitio Trough section (sub-sections of the channel are shown at the top of the plots and differentiated with blue shading). (A) Channel thalweg depth profile (black solid line) and slope gradient profile (white dotted line) with values presented in degrees. (B) Average channel height profile (solid line) and cross-channel slope values (triangles). (C) Average channel width (solid line) and channel area (crosses). (D) Downstream turbidity current velocity profile. (E) Froude number profile, dashed line at 1 indicates the threshold between subcritical and supercritical flow. Downstream (F) shear velocity, (G) bulk sediment concentration, (H) flow discharge and sediment discharge profiles. 52

Figure 3.8 Plots showing the thresholds of equilibrium flow for the modelled turbidity current traversing each section of the Madden Channel. The thresholds vary from well-sorted ($\sigma = 0.5$) to poorly-sorted ($\sigma = 2$) sediment in suspension. For a given slope value (S), the grain sizes (ϕ) above a given threshold represent sediment bypass under erosional flow conditions and grain sizes below a given threshold represent deposition. The average flow height, H , and average bulk sediment concentration, C , used for the calculation of the thresholds are shown in each plot for the (A) channel upper reaches (B) Porangahau Trough, (C) channel lower reaches and (D) channel lower reaches and Akitio Trough. (E) Channel thalweg depth profile. The numbers in black squares show the positions of the slope gradient values plotted in A-D. 55

Figure 3.9 Plots showing the thresholds of equilibrium flow for the modelled turbidity current traversing the Omakere Channel. The thresholds vary from well-sorted ($\sigma = 0.5$) to poorly-sorted ($\sigma = 2$) sediment in suspension. For a given slope value (S), the grain sizes (ϕ) above a given threshold represent sediment bypass under erosional flow conditions and grain sizes below a given threshold represent deposition. The average flow height, H , and average bulk sediment concentration, C , used for the calculation of the thresholds are shown in each plot for the (A) channel upper reaches (B) upper reaches sub-basin, (C) Paoanui Trough and (D) channel lower reaches and Akitio Trough. (E) Channel thalweg depth profile. The numbers in black squares show the positions of the slope gradient values plotted in A-D. 57

Figure 3.10 (A-D) Potential sand distribution maps of the Madden and Omakere Channel systems. The maps show the deposition from (A) a well-sorted turbidity current transporting very fine sand; (B) a poorly-sorted turbidity current transporting very fine sand and very fine sand to medium silt; (C) a well-sorted turbidity current transporting very fine sand and coarse silt, assuming downstream erosion of sand; (D) a poorly-sorted turbidity current transporting very fine sand and very fine sand to medium silt assuming downstream erosion of sand. (E) Root Mean Square (RMS) amplitude map of the seafloor with drop core locations M1-M3. High RMS amplitude values are interpreted to represent deposits with higher sand content. Low RMS amplitude responses are interpreted to represent soft homogeneous finer-grained deposits. Enlarged areas showing the RMS amplitude distribution of the (F) Madden Channel upper reaches and Porangahau sections, (G) Madden Channel lower reaches, (H) Omakere upper reaches and (I) Omakere Channel Paoanui and lower reaches sections. 62

Figure 4.1 Study area. (A) The Hikurangi Margin is located on and offshore of the North Island, New Zealand. (B) Offshore bathymetry map and bathymetric contours (500 m) of the Hikurangi Margin (courtesy of the National Institute of Water and Atmospheric Research, New Zealand). The dashed black outline indicates the 3D seismic survey area. (C) Regional cross-section across the Hikurangi subduction complex (adapted from McArthur et al., 2022).	66
Figure 4.2 3D perspective view of the seafloor with corresponding seismic cross-section showing the structural style of the subduction wedge where the Omakeke Trough is located. The studied interval of the Omakeke Channel complex is found at depths of up to ~ 300 mbsf.	68
Figure 4.3 Plots showing the sensitivity of calculated values sediment concentration and Froude number to the input parameters to Equations (4.2) and (4.3). In each case, the parameter shown on the x axis was varied whilst the others remained fixed. Variations in sediment concentration are shown for varying (A) cross-channel slope, (B) radius of curvature, (C) down-channel slope, (D) latitude, and (E) flow height. Variations in Froude number are shown for varying (F) down-channel slope and (G) cross-channel slope.	74
Figure 4.4 (A) Uninterpreted and (B) interpreted spectral decomposition maps and (C) interpretation of the Omakeke Trough where the Omakeke Channel Complex is located. See Figure 4.1 for map location.	79
Figure 4.5 (A-E) Uninterpreted and corresponding interpreted cross-sections of the Omakeke Channel Complex through Areas 1 to 3 based on the identified seismic facies and depositional elements.	81
Figure 4.6 (A) MTD A located in Area 1 of the Omakeke Channel Complex, (B) RMS amplitude map of channel-form A (C) MTD B, extending from Area 2 to Area 3.	82

- Figure 4.7 Morphology (A-D) and turbidity current modelling results (E-I) of channel-form A. (A) Palaeobathymetry and corresponding cross-sections (looking down-channel). (B) Channel-form thalweg depth profile and down-channel slope values shown in decimal degrees. (C) Mean channel-form height and cross-channel slope. (D) Channel-form width and area. (E) Downstream flow velocity. (F) Shear velocity. (G) Froude number; the dashed line at 1 indicates the threshold between sub-critical and super-critical flow. The labels B1-B6 and grey bars highlight the data points and results for channel-form bends. (H) Channel-form flow and sediment discharge; reference lines correspond to the average discharge calculated in the modern Omakere Channel from Crisóstomo-Figueroa et al. (2021). (I) Sediment concentration showing original estimations for channel-form A and estimations obtained from increasing γ one order of magnitude in B1 and B3.; the dashed line at 1% and 9% (0.09 v/v) indicates the theoretical limit for concentration values of turbidity currents (Bagnold, 1956; Talling et al., 2012). 85**
- Figure 4.8 Equilibrium threshold plots calculated for channel-form A. The thresholds vary from well-sorted ($\sigma = 0.5$) to poorly-sorted ($\sigma = 2$) sediment in suspension. For a given slope value (S), the grain sizes (ϕ) above a given threshold represent sediment bypass under erosional flow conditions, and grain sizes below a given threshold represent deposition. The average flow height, H , and average bulk sediment concentration, C , used for the calculation of the thresholds are shown in each plot for (A) Area 1, (B) Area 2 and (C) Area 3. (D) Channel-form A thalweg depth profile. The numbers in black squares show the positions of the slope gradient values plotted in A–C. 89**
- Figure 4.9 Subsurface vs surface modelling results and uncertainties. (A) Seafloor map of the Omakere Channel. (B) Calculated turbidity current conditions in the surficial channel (Crisóstomo-Figueroa et al., 2021). (C) Spectral decomposition map of the Omakere Channel Complex (see Figure 4.4 for the interpretation) showing the sources of modelling uncertainties in the subsurface. (D) Calculated turbidity current conditions in subsurface channel-form A. 95**
- Figure 5.1 Schematic diagram of submarine channels on the slope and basin plain (adapted from Wells and Cossu, 2013) and proposed controls on the development of sinuosity in submarine channels (see text). 99**
- Figure 5.2 Changes in cross-channel forces due to Coriolis. Force balance and tilting under (A) weak northern hemisphere rotation and (B) strong northern hemisphere rotation; cross-sections looking in the downstream direction. (C) and (D) indicate the coordinate normal system used in the calculation of the tilt γ_c . 101**

- Figure 5.3 NAMOC morphometrics extracted from Klaucke et al., (1997). (A) Downchannel changes in the measured tilt and sinuosity. Zone 1 corresponds to the ‘equilibrium channel’ whereas zone 2 to the ‘modified equilibrium channel’. Red arrows indicate locations of levee collapse. (B) Morphometric relationships for each channel zone with calculated R^2 values. Blue circles correspond to data points from zone 1 and black asterisks to zone 2. 108**
- Figure 5.4 Changes in calculated turbidity current tilt for the NAMOC. (A) Calculated tilting from three different sediment concentrations. (B) Absolute values of the calculated tilting compared to the measured tilting. (C) Absolute calculated tilting against measured tilting. Data broken down into the sediment concentration and NAMOC zones defined in Methods. 110**
- Figure 5.5 Calculated tilting γ_c and ratio γ_r at $C=0.02\%$. The latitude increases in each panel horizontally as 5° , 35° and 55° . (A-C) $r=500$ (D-F) $r=3$ km. (G-I) $r=30$ km. Vertical blue arrows indicate the tilting transition slope ST . Horizontal bars indicate zones of tilting instability..... 113**
- Figure 5.6 Calculated tilting γ_c and ratio γ_r at $C=0.2\%$. The latitude increases in each panel horizontally as 5° , 35° and 55° . (A-C) $r = 500$ (D-F) $r = 3$ km. (G-I) $r = 30$ km. Vertical blue arrows indicate the tilting transition slope ST . Horizontal bars indicate zones of tilting instability..... 114**
- Figure 5.7 Calculated tilting γ_c and ratio γ_r at $C=2\%$. The latitude increases in each panel horizontally as 5° , 35° and 55° . (A-C) $r = 500$ (D-F) $r = 3$ km. (G-I) $r = 30$ km. Vertical blue arrows indicate the tilting transition slope ST . Horizontal bars indicate zones of tilting instability..... 115**
- Figure 5.8 Calculated absolute Rossby number as a function latitude, sediment concentration and radius of curvature for (A) small, $r = 500$ m, (B) intermediate, $r = 3,000$ m and (C) large, $r = 30,000$ m, bends. Symbols show transition slopes. (D) Transition slopes observed for all modelling results of γ_c (see Figures 5.5 to 5.7).116**
- Figure 5.9 Changes in the calculated tilting transition slope ST with (A) sediment concentration, (B) flow height and (C) latitude. 118**
- Figure 5.10 Global channel data extracted from Sylvester and Pirmez (2019). (A) Latitude versus sinuosity and (B) radius of curvature versus sinuosity..... 120**
- Figure 5.11 Contours of the tilting transition slope ST co-plotted with seafloor channel data as a function of latitude and radius of curvature for (A) deep and dilute currents, (B) deep and dense currents, (C) shallow and dense currents and (D) shallow and dilute currents. Channel data from Sylvester and Pirmez (2019). Symbol colours correspond to the magnitude of the downchannel slope in each system. 121**

Figure 6.1 Schematic diagram showing the effect of changes in the upper slope gradient, flow thickness and grain size distribution in the formation of upslope pinchouts (A to F adapted from original sketches in Pohl et al., 2020a; G and H adapted from Amy, 2019).	129
Figure 6.2 Block diagrams illustrating the changes in intrachannel sedimentation patterns due to Coriolis for (A-C) traction-dominated flows and (D-F) suspension fallout (Davaranah Jazi et al., 2020).	131
Figure 6.3 Schematic 3-dimensional diagram illustrating the expected sedimentation patterns at channel bends due to changes in the balance between Coriolis and centrifugal forces as a function of latitude, downchannel slope gradient and channel size (individual block diagrams are from Davaranah Jazi et al., 2020).	134
Figure 6.4 (A) Changes in flow velocity and (B) sediment concentration with variations in the height of the velocity maximum.	138
Figure 6.5 Changes in (A) flow velocity and (B) sediment concentration with variations in the drag coefficient.	140

Abbreviations and symbols

3D	Three-dimensional
AR	Akitio Ridge
km	Kilometres
MRS	Motuokura Ridge south
MTD	Mass-transport deposit
m	Metres
mbsf	Metres below the seafloor
NAMOC	Northwest Atlantic Mid-Ocean Channel
NE	Northeast
ORN	Omakere Ridge North
ORS	Omakere Ridge South
PR	Porangahau Ridge
RMS	Root-mean-square
SW	Southwest
β	Rouse number
γ	Cross-channel slope
γ_c	Calculated current tilting
γ_{ca}	Absolute value of the calculated current tilting
γ_m	Measured channel tilting / cross-channel slope
γ_r	Tilting ratio
ε	Entrainment efficiency parameter
θ	Channel latitude
ρ_f	Ambient water density
ρ_t	Turbidity current density
ρ_s	Particle density
$\Delta\rho$	Excess density of the flow with respect to ambient water ($\rho_t - \rho_f$)
ΔH	Channel levee height difference
σ	Particle size distribution standard deviation

\emptyset	Particle size in phi units
Ω	Earth's rotation rate
\forall	Assertions hold for all instances
∞	Infinity
$^{\circ}$	Degrees
\rightarrow	tends to
\cong	Approximately equal to
A	Channel area
C	Depth-averaged sediment concentration
C_d	Drag coefficient
c^-	Concentration in the active layer
c_m	Packing concentration of the bed
d	Particle diameter
d_{50}	Median particle diameter
E	Entrainment function
e_w	Ambient water entrainment
$F(Z)$	Eddy diffusivity function
f	Coriolis acceleration
Fr	Densimetric Froude number
g	Gravitational acceleration
H	Maximum channel height
\bar{H}	Average flow height
h	Minimum channel height
h_{max}	Flow height at the velocity maximum
k	von Kármán constant
k_s	Eddy diffusivity
L	Characteristic length scale
N	Number of particle classes
Q	Flow discharge

Q_s	Sediment discharge
R	Particle submerged specific gravity
Ri	Bulk Richardson number
Ro_R	Rossby number
$ Ro_R $	Absolute Rossby number
r	Channel thalweg radius of curvature
S	Down-channel slope
S_T	Tilting transition slope
Si	Channel sinuosity
U	Depth-averaged flow velocity
U_{max}	Velocity maximum
u^*	Shear velocity
W	Channel width
W_b	Channel floor width
w_s	Particle settling velocity
Z	Dimensionless height above the bed
Subscripts	
$.i$	Index parameter indicating the i th particle class

Chapter 1 Introduction

1.1 Background and rationale

Turbidity currents are sediment-laden submarine flows driven by their excess density compared to the ambient fluid (Kuenen, 1938; Kneller and Buckee, 2000; Wells and Dorrell, 2021). They often run out over long distances, travelling thousands of kilometres from shallow-to-deepwater, and transporting sediment (Khripounoff et al., 2003; Stevenson et al., 2013; Talling et al., 2013), organic carbon (Rabouille et al., 2019; Hage et al., 2020) and pollutants (Kane and Clare, 2019; Pohl et al., 2020b; Zhong and Peng, 2021). Individual turbidity currents can transport more than 100 km³ of sediment (Piper and Aksu, 1987; Talling et al., 2012) and collectively they form some of the largest sedimentary deposits on Earth (Piper and Normark, 2001; Curray et al., 2003). Their ability to suspend sediment and travel for great distances is highly dependent on their hydraulic properties together with the type of sediment in suspension and the sediment on the bed, which they can either erode, deposit or bypass (Parker, 1982; Garcia, 1991; Stevenson et al., 2014; Heerema et al., 2020; Heijnen et al., 2022). A better understanding of turbidity current processes can aid assessments of the distribution of sedimentary deposits, which might be exploited for hydrocarbon exploration (Pettingill and Weimer, 2002; Pettingill, 2004) or CO₂ storage (Marshall et al., 2016) and may also aid geohazard assessments as they may cause damage to seafloor infrastructure (Carter et al., 2014).

During their passage through submarine slopes and across basin floors, turbidity currents commonly construct channels, which therefore constitute important conduits for sediment transport to the deep sea (Hesse et al., 1987; Pirmez and Flood, 1995; Babonneau et al., 2002). Submarine channels display a concave up form with erosional or aggradational (levee-bound) architectures in cross-sectional view (Nakajima and Kneller, 2013; Hansen et al., 2015). Although channels may develop a sinuous planform morphology similar to rivers (Abreu et al., 2003; Wynn et al., 2007) fundamental differences exist between submarine and subaerial processes and deposits (Peakall et al., 2000; Kolla et al., 2007).

Channelised turbidity currents have been widely studied through laboratory experiments (e.g., Keevil et al., 2007; Peakall et al., 2007; Islam and Imran, 2008; Straub et al., 2008), theoretical and numerical modelling (e.g., Komar, 1969; Imran et al., 1999; Das et al., 2004; Abd El-Gawad et al., 2012; Konsoer et al.,

2013; Dorrell et al., 2014) and by direct monitoring in natural environments (e.g., Xu et al., 2014; Azpiroz-Zabala et al., 2017; Symons et al., 2017; Paull et al., 2018; Simmons et al., 2020; Pope et al., 2022); which have led to significant advances in the understanding of their internal structure and evolution. A key approach to estimating the properties of channelised turbidity currents is that of Komar (1969), who used the channel geometry to describe the momentum balance of cross-channel forces, i.e., the centrifugal force, the Coriolis force and the pressure gradient (Komar, 1969). This force balance has been used to estimate turbidity current velocity in the Amazon Channel (Pirmez and Imran, 2003), the Northwest Atlantic Mid-Ocean Channel (Klaucke et al., 1997), among others (Bowen et al., 1984; Ren et al., 1996); and it has helped to estimate sediment concentrations of the Grand Banks flow event (Stevenson et al., 2018).

Despite important advances in the study of channelised turbidity currents and submarine channels, there are still mechanisms governing their development that are not well constrained. Of particular interest here are:

1. Determining whether a current will be erosional, depositional, or fully bypassing. This determination remains a challenge, yet it is critical to understanding the extent and thickness of turbidity current deposits (Stevenson et al., 2015). Theoretical models have been used to approximate the state of suspended-load dominated flows (e.g., Bagnold, 1966; Leeder et al., 2005; Cantero et al., 2012; Halsey et al., 2017; Dorrell et al., 2018); a review of these models demonstrates that a Flow-Power Flux-Balance type model (Dorrell et al., 2018) outperforms other equilibrium criteria for turbidity currents (Amy and Dorrell, 2021). However, critical parameters such as flow height and sediment concentration need to be approximated in order to apply this model to natural settings.

2. The controls on submarine channel sinuosity are contested: slope gradient has been invoked to control sinuosity via an inverse relationship (low sinuosity at high slope and vice versa; Clark et al., 1992); Coriolis forcing has also been invoked as the principal control, with changing sedimentation patterns reducing lateral bend migration, and hence sinuosity development at high latitudes (Peakall et al., 2012; Wells and Cossu, 2013; Cossu et al., 2015); other workers have argued that Coriolis forcing is only dominant within large-scale channels (Sylvester and Pirmez, 2019). Hence, it remains to be established whether a latitudinal control dominates over factors such as slope gradient and channel scale, hampering understanding of the development of sinuosity, changes in intrachannel sedimentation patterns and channel architecture (Peakall and Sumner, 2015);

these factors are of economic significance as they control reservoir distribution and heterogeneity (Mayall et al., 2006).

3. Channel-forms in the subsurface are often confined within wider concave-up surfaces (e.g., Deptuck et al., 2003; Janocko et al., 2013b). Hence, hierarchical schemes have been developed to characterize them according to their geometry, scale and organization (Cullis et al., 2018). Although it might be clear that compound surfaces of higher hierarchical level such as channel complexes do not constitute palaeo-hydraulic conduits, it remains challenging to define whether smaller channel-forms constitute palaeo-hydraulic conduits or compound elements formed by channel amalgamation (Hodgson et al., 2016; Hubbard et al., 2020). To distinguish palaeo-hydraulic conduits is particularly challenging in seismic reflection data due to limitations in both vertical and horizontal resolution. To date, a technique that helps to distinguish a compound channel-form from a true palaeo-conduit has not been developed. Identifying the likelihood of channel-forms representing palaeo-hydraulic conduits is a critical consideration for the analysis of subsurface deepwater systems in terms of flow dynamics (Li et al., 2018; Gong et al., 2020).

Further understanding of each of the challenges outlined above is necessary to enable better analysis of channel evolution and estimation of turbidite deposit character. Hence, the focus of this work is to use theoretical turbidity current modelling techniques (i.e., the model of Komar (1969) and the Flow-Power Flux Balance model) to address them. Furthermore, this work also seeks to incorporate the effect of downchannel forces in combination with the model of Komar (1969) and use an optimization method to solve the governing equations, which would constitute a significant improvement in the application of this technique.

1.2 Aims and objectives

This research project aims to use theoretical models to calculate the bulk properties of channelized turbidity currents using submarine channel geometries to investigate three key aspects of deepwater sedimentology: i) the control exerted by factors such as variations in bulk flow properties and slope in determining whether turbidity currents bypass or deposit sediment in a channel, and the implications for the distribution of sand in a system ii) whether or not subsurface channel-forms observed in 3D seismic data constitute palaeo-hydraulic conduits and the factors that may pose challenges in the calculation of palaeo-hydraulic conditions that are not encountered in modelling of surficial

channels, and iii) the role of the Coriolis force in the development of submarine channel sinuosity and the influence of other parameters such as channel size, downchannel slope and bulk turbidity current conditions. Hence, the research is divided into three principal components which are outlined in section 1.3.

To achieve the aims of this thesis, the objectives are as follows:

1. To develop a turbidity current modelling methodology that yields more robust solutions of bulk turbidity current properties than have been achieved hitherto, based on the channel geometry following the theory of Komar (1969)
2. To combine the newly developed turbidity current modelling methodology with an established Flow-Power Flux-Balance type sediment transport model to investigate sediment bypass conditions, evaluating the combined approach on a case study of surficial channels from the Hikurangi Margin, New Zealand.
3. To conduct seismic mapping, seismic facies analysis and attribute extraction using high resolution 3D seismic from the Hikurangi Margin, New Zealand to map and measure the geometries of subsurface channel-forms.
4. To apply the combined modelling technique to mapped subsurface channel-forms of the Omakere Channel Complex of the Hikurangi Margin, New Zealand to investigate whether the observed channel forms might constitute palaeo-hydraulic conduits.
5. To adapt the turbidity current modelling methodology to calculate the changes in the flow-ambient fluid interface tilt due to Coriolis forces and conduct a parametric analysis to investigate whether latitude is a dominant control in the development of channel sinuosity.

1.3 Thesis outline

The thesis includes material that has been published or is under review in two manuscripts: Chapter 3 is based upon a paper published in the Bulletin of the Geological Society of America; Chapter 4 is under review in *Sedimentology*.

Chapter 2: *Literature review.* This chapter presents a review of the literature relevant to this thesis including turbidity current structure and dynamics, the morphology and description of submarine channels and subsurface channel forms, and modelling examples that have used channel geometries to calculate bulk turbidity current properties.

Chapter 3: *A new modelling approach to sediment bypass prediction applied to the Hikurangi Margin, New Zealand.* This data chapter contains a version of the manuscript published in the Bulletin of the Geological Society of America. A novel

methodology is presented to calculate bulk turbidity current properties from the geometry of the Madden and Omakere modern channels of the Hikurangi Margin, New Zealand, based on the theory of Komar (1969) that is combined with a flow-power flux-balance type sediment transport model to investigate sediment bypass conditions in the system. The morphology of the channels (extracted from bathymetry data) and calculated flow properties are described in detail. The equilibrium thresholds derived from the sediment transport model are used to interpret the grain sizes that could be bypassed through the studied channel reaches with a key focus on sand bypass. The results in this chapter demonstrate the effect that the flow height, slope gradient and grain size distribution have on sediment bypass; the implications for sand distribution in the system are discussed.

Chapter 4: *Calculating deepwater palaeo-hydraulic conditions from subsurface channel architecture: a critical test using examples from the Hikurangi Margin, New Zealand.* This data chapter contains a version of a manuscript submitted to *Sedimentology*. A 3D seismic dataset from the Hikurangi Margin, New Zealand is used to map the subsurface Omakere Channel Complex. Seismic cross-sections and attribute maps are used to describe the seismic facies and geomorphology of the channel complex. The flow modelling technique presented in chapter 3 is applied to channel-forms within the complex to estimate palaeo-hydraulic properties and test whether the observed channel-forms might represent a palaeo-hydraulic conduit. The morphology of the channel-forms and palaeo-hydraulic modelling results are described in detail. The obtained disequilibrium palaeo-hydraulic properties are discussed in relation to the presence of compound channel-forms and complex MTD substrates. This work highlights the challenges related to the application of turbidity current modelling techniques that rely on the extraction of channel morphometrics for model inputs.

Chapter 5: *Modelling changes in the flow-ambient fluid interface tilt of turbidity currents: implications for the development of sinuous submarine channels.* The methodology used in Chapters 3 and 4 to solve for bulk turbidity current properties using the model of Komar (1969) is adapted in this chapter to estimate the conditions under which Coriolis forces deflect the upper interface tilt of turbidity currents. The interface deflection is linked to a modification of the 3D structure of the currents in a way that diminishes sinuosity development in submarine channels. Model validation is undertaken through the comparison of the calculated turbidity current tilting against the measured tilting of channel levees in the Northwest Atlantic Mid-Ocean Channel using the data from Klaucke et al. (1997). Additionally, the channel sinuosities, radii of curvature and latitudes

from nine channel systems are obtained from Sylvester and Pirmez (2019) to evaluate whether changes in channel sinuosity are controlled by latitude. Changes in the tilting and the threshold downchannel slope needed for the development of sinuosity are then evaluated as a function of latitude, radius of curvature, slope gradient, flow height and sediment concentration. The effect of these parameters on the influence of Coriolis forces are discussed within the context of the current debated controls on the development of channel sinuosity.

Chapter 6: *Discussion and Conclusions*. This chapter discusses additional implications following from the results presented in Chapters 3 and 5. Additionally, it presents the conclusions of this thesis and makes suggestions for future research; recommendations for future application of the methodologies used in this work are also made.

Chapter 2 Literature review

2.1 Turbidity currents

2.1.1 Definition and significance

Turbidity currents are sediment-laden, gravity-driven underflows (also referred to as density-driven flows) (Daly, 1936; Kuenen, 1938; Meiburg and Kneller, 2010) that transport sediment from shallow to deep-marine environments and together with other types of underwater sediment gravity flows (e.g., hybrid and debris flows, Haughton et al., 2009) shape submarine slopes and form some of the largest sedimentary environments on Earth (Piper and Normark, 2001; Covault and Graham, 2010). They also play an important role in the distribution of organic carbon (Hage et al., 2020), pollutants (Zhong and Peng, 2021) and microplastics (Kane and Clare, 2019; Pohl et al., 2020b) into the deep sea.

As powerful agents of sediment transport, turbidity currents may damage seafloor equipment (Khripounoff et al., 2003) and infrastructure such as pipelines, and communication cables (Heezen and Ewing, 1952; Carter et al., 2014). Therefore, advances in the understanding of turbidity current dynamics have an important impact on the identification of geohazards in submarine slopes. Also, the deposits associated with turbidity current processes, turbidites (Lowe, 1982; Mutti and Normark, 1987), are of economic significance due to their potential to act as hydrocarbon reservoirs (Pettingill, 2004) or for carbon capture storage (Marshall et al., 2016). Hence, the study of turbidity currents has spanned a broad range of techniques including: i) experimental modelling (e.g., Mohrig and Buttles, 2007; Sequeiros et al., 2009), ii) numerical and theoretical modelling (Kneller, 2003; Abd El-Gawad et al., 2012; Amy and Dorrell, 2021), iii) observations from natural systems, albeit limited due to their naturally challenging environmental setting (e.g., Azpiroz-Zabala et al., 2017; Paull et al., 2018) and iv) reconstruction of their properties from their depositional record (e.g., Hubbard et al., 2014; McArthur et al., 2020b); all of which have provided deep insights into the structure and dynamics of turbidity currents and their deposits.

2.1.2 Triggers

Understanding the triggering mechanism of turbidity currents is important as it influence the dynamics of the current and the character of the turbidity current deposit. Piper and Normark (2009) defined three major mechanisms for turbidity current initiation: i) Sediment failure which may be related to earthquakes (e.g.,

1929 Grand Banks event (Piper and Aksu, 1987)) or slope failures unrelated to earthquakes that lead to flow transformation; ii) Hyperpycnal flows associated to river discharge of high-sediment loads often linked to flood events, or through subglacial meltwater discharge; and iii) Oceanographic processes that resuspend coastal, shelf or upper-slope sediment during major storms, waves or tides. After being triggered, turbidity currents may travel downslope 100's of kilometres for several days (Talling et al., 2013). Their flow power and run-out is often linked to the strength of the triggering mechanism (e.g., Zhang et al., 2018) among other factors such as the slope gradient (Normark and Piper, 1991) and flow stratification (Dorrell et al., 2014); however, flow monitoring in the Monterey Canyon has shown that fast-moving long-runout currents with speeds of up to 5 ms^{-1} may be formed by small perturbations during normal wave heights in the upper canyon instead of known major triggers (Paull et al., 2018).

2.1.3 Flow structure and dynamics

Turbidity currents are driven by their excess density (due to their sediment load) relative to the ambient water (Figure 2.1) where the grains in suspension are mainly supported by the the downslope gravitational force accelerating the flow and by turbulent mixing (Menard and Ludwick, 1951; Meiburg and Kneller, 2010; Wells and Dorrell, 2021).

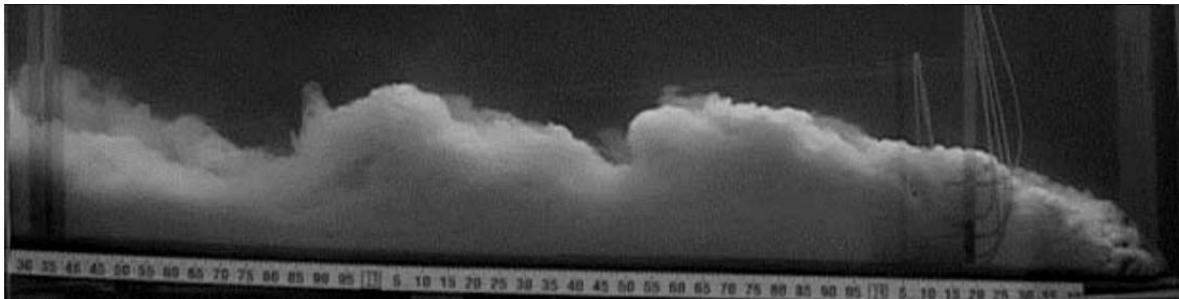


Figure 2.1 Turbidity current produced in laboratory experiments (adapted from Sequeiros et al., 2009).

2.1.3.1 Horizontal and vertical structure

Turbidity currents generated under experimental conditions have shown a well-defined three-part horizontal structure as the head, the body and the tail (Middleton, 1993; Kneller and Buckee, 2000) (Figure 2.2A) where the thickness of the current decreases from head to tail and each part has distinct hydraulics. The head represents an erosional, highly turbulent portion of the flow driven by the pressure gradient downslope due to the density contrast between the head and the ambient fluid in front of it (Middleton, 1966a; Stacey and Bowen, 1988a). The acceleration of the frontal ambient fluid produces higher resistance than the

friction at the bed or at the flow-ambient fluid interface, which may make this flow region thicker (Middleton, 1993). Due to intense ambient fluid mixing and shear at the head, flow instabilities in the form of billows, named Kelvin-Helmholtz instabilities may occur (Figure 2.2A) (Middleton, 1993; Kneller and Buckee, 2000). The body has been described as a steady-state portion characterized by a decrease in current height and more uniform thickness but faster than the head as it experiences frictional resistance at the interface and bed only (Middleton, 1993). It is driven by the downslope component of the gravitational force. Therefore, it has been approximated by a gravity reduced Chezy type equation dependent on the slope (Stacey and Bowen, 1988b; Meiburg and Kneller, 2010). The tail follows the body and comprises the thinnest and most diluted flow region due to flow dissipation.

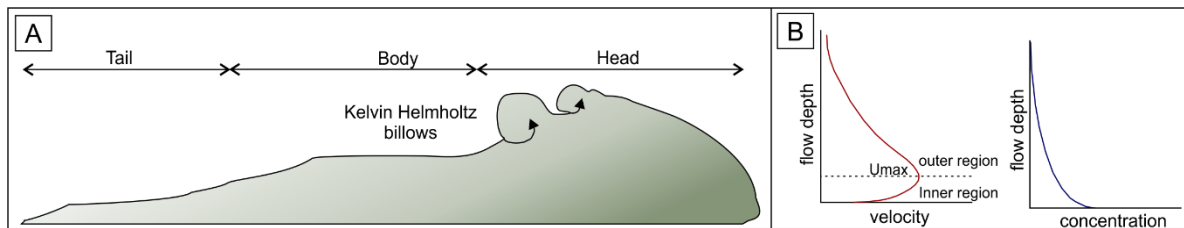


Figure 2.2 (A) Sketch of the horizontal structure of a turbidity current divided in the head, body and tail (modified from Hansen et al., 2015). (B) Typical velocity and density/concentration profiles in turbidity currents.

Experimental and natural turbidity currents have shown that their profiles vary vertically in density and velocity (Stacey and Bowen, 1988b; Xu et al., 2014; De Leeuw et al., 2016; Dorrell et al., 2019). A typical velocity profile is shown in Figure 2.2B which is characterized by an inner and an outer region divided by the velocity maximum (Kneller and Buckee, 2000). The velocity gradient in the inner region is positive and is dominated by basal drag; as it reaches the velocity maximum at a given height above the bed, the profile reverses to display a negative gradient in the outer region which is dominated by drag at the flow-ambient fluid interface. The velocity maximum height is dependent on frictional drag at the bed and drag at the flow-ambient fluid interface (Kneller et al., 1997), and it has been defined to occur at 0.2-0.3 times the current thickness based on experimental observations (Kneller et al., 1997; De Leeuw et al., 2016). In natural currents, velocity maximums were observed within 3-4 m above the seabed (Simmons et al., 2020).

The vertical density gradient is determined by the sediment in suspension (Stacey and Bowen, 1988a; Peakall et al., 2000). Sediment concentration is a critical parameter controlling turbidity current dynamics (Xu et al., 2014; Stevenson et al., 2018; Simmons et al., 2020). These thesis deals with turbulence-supported

turbidity currents with non-cohesive sediment that have less than 9% bulk sediment concentration (Bagnold, 1956; Mulder and Alexander, 2001; Talling et al., 2012). Coarse-grained particles are closer to the bed whilst fine-grained particles are distributed above, leading to stratification of the flow that is equivalent to a vertical gradient in sediment concentration (Dorrell et al., 2014) (e.g., turbidity current events observed in the Congo, Simmons et al., 2020). A typical concentration profile is shown in Figure 2.2B. Hence, the highest concentrations occur at the base of the flow and decrease upwards (Kneller and Buckee, 2000; Peakall et al., 2000). Theoretical and experimental analysis has shown that the variation in the vertical concentration and velocity gradients is not uniform for all flows (Wells and Dorrell, 2021) but varies for low- and high-concentration flows (Peakall et al., 2000; Cartigny et al., 2013) as well as for supercritical and subcritical flows and bed roughness (Sequeiros et al., 2010).

2.1.3.2 Flow states and evolution

Once a turbidity current is triggered, it experiences a complex evolution that involves three important flow states: erosion, deposition and possibly a period of autosuspension or complete bypass. These flow states have been widely investigated (Menard and Ludwick, 1951; Bagnold, 1962; Parker, 1982; Parker et al., 1987; Garcia, 1991, 1994; Middleton, 1993; Sequeiros et al., 2009; Pantin and Franklin, 2011; Amy and Dorrell, 2021), as the transition between one flow state to another controls the flow run-out, bed degradation or aggradation and the ultimate fate of turbidite deposits (Normark and Piper, 1991; Kneller, 1995, 2003).

Turbidity currents are often erosional near the site of initiation (often at submarine canyons (Daly, 1936; Kuenen, 1938)), hence, a state termed self-acceleration dominates. Self-accelerating currents increase in flow velocity and sediment concentration as they travel downslope due to sediment entrainment from the seabed dominating water entrainment (Parker et al., 1986; Sequeiros et al., 2009; Wells and Dorrell, 2021). This particular state of the flow is therefore dependant on the composition of the bed, i.e., an erodible bed, as well as the down-system slope gradient (Parker, 1982; Sequeiros et al., 2009). Generally, steep gradients have been thought of promoting long-distance sediment transport, hence transporting sediments from proximal to distal slopes (Normark and Piper, 1991), however, currents traveling 1000s of km over gentle slope gradients occur in the Labrador Sea (Klaucke et al., 1997).

As noted by Sequeiros et al., (2009), self-acceleration may precede autosuspension, a mechanism described by Bagnold (1962) where flows can

keep sediment in suspension, and therefore be self-sustained through the effect of turbulence. By definition, autosuspension is therefore equivalent to a bypassing current, which are further discussed in the following section.

An increase in concentration exceeding the flow capacity (Hiscott, 1994; Dorrell et al., 2013b) might suppress turbulence and promote a depositional flow. Another suggested factor controlling the deposition of sediment is the flow thickness, where thin currents are able to transport sand more effectively than thick currents (Normark and Piper, 1991). Other factors like slope gradient reductions can lead to slowing down the current and promoting deposition (Kneller, 1995).

2.1.3.3 Sediment bypass

Stevenson et al. (2015) offers a comprehensive review on sediment bypass by submarine gravity flows, including turbidity currents. Submarine gravity flows fully bypass sediment when all the sediment is transported beyond a fixed geographical point and deposited farther down-system (Stevenson et al., 2015). Therefore, sediment bypass is an important process in deepwater settings due to its key role in the distribution of sediment across shelf-to-basin slope profiles. The main controls on the amount of sediment bypassed and its stratigraphic expression have been proposed based on outcrop studies (Mutti and Normark, 1987; Amy et al., 2000; Gardner et al., 2003; Van der Merwe et al., 2014), examples from modern systems (Wynn et al., 2002; Stevenson et al., 2013, 2014), physical experiments (Cartigny et al., 2013; De Leeuw et al., 2018) and computational modelling (Bagnold, 1962; Leeder et al., 2005; Halsey et al., 2017; Amy and Dorrell, 2021). However, sediment bypass prediction using theoretical or numerical criteria is still challenging. Data integration and a model that takes into account the main factors controlling sediment bypass (i.e. grain size, slope, flow size and sediment concentration according to Stevenson et al., 2015) in deepwater systems, might have the potential to make predictions about the distribution of turbidity current deposits, including sandstone turbidites that may act as reservoirs in a hydrocarbon play (Pettingill, 2004), and may help de-risking bypass-related upslope pinchout stratigraphic traps (Amy, 2019; Counts et al., 2021).

2.1.3.3.1 Description based on geological observations

Key terms in sediment bypass have been suggested in both a process and stratigraphic context as: bypassing flows, partially bypassing flows and depositional flows (Stevenson et al., 2015). Bypassing flows transport their entire sediment load in suspension or traction beyond the point of observation and are related to complete sediment bypass zones and bypass-dominated zones,

resulting in no depositional record or erosion surfaces created by the bypassing current (Stevenson et al., 2015). Partially bypassing flows deposit a fraction of their sediment load downslope, resulting in thin deposits associated to bypass-dominated zones. This definition covers a broad range of flow states from bypassing most of their load to being almost depositional. Depositional flows generate thickest deposits at the point of observation compared to other areas along the flow pathway and are related to depositional zones (Stevenson et al., 2015).

The expression of sediment bypass varies depending on the scale of observation in stratigraphic and planform architectures, and site of occurrence (Stevenson et al., 2015). Submarine channels are volumetrically the most important sediment bypass conduits and previous workers have shown that bypass and its stratigraphic expression can vary parallel and perpendicular to the channel axis, depending on the degree of flow confinement (Stevenson et al., 2013; Stevenson et al., 2015). Channel-axis drapes can record sediment bypass from the lower axial part of the flow, whilst the channel-margin may record a lateral depositional record from the upper parts of the flow (Mutti and Normark, 1987; Stevenson et al., 2015). Other features such as composite erosion surfaces, scours, coarse-grained lag deposits and levee building are indicators of sediment bypass in channels (Stevenson et al., 2015). Mud draped erosion surfaces are interpreted to be the product of longitudinal variations in the flow, when the head of the turbidity current (Figure 2.2A) is erosive and bypassing and the tail (Figure 2.2A) deposits the fine-grained fraction as with fine-grained thin-bedded channel-base drapes (Mutti and Normark, 1987; Stevenson et al., 2015). At a seismic scale, composite channel-forms reveal repeated periods of initial incision, erosion and sediment bypass (Stevenson et al., 2015).

Channel-lobe transition zones at base-of-slope settings are also an important zone of sediment bypass, controlled by the flow size, grain size and by the change slope (Mutti and Normark, 1987; Stevenson et al., 2015; De Leeuw et al., 2018; Hodgson et al., 2022); they provide good potential for the development of detached lobes as updip pinchout stratigraphic traps (Straccia and Prather, 1999; Amy, 2019; Hansen et al., 2019; Counts et al., 2021).

2.1.3.3.2 Sediment bypass-related traps

Bypass-related stratigraphic upslope pinchouts are formed when sediment gravity flows completely bypass its sediment load in the proximal to mid slope and deposit downslope; hence, the change from bypass-erosion to deposition

constitutes a mechanism for the development of detached sands (Figure 2.3) (Amy, 2019; Counts et al., 2021).

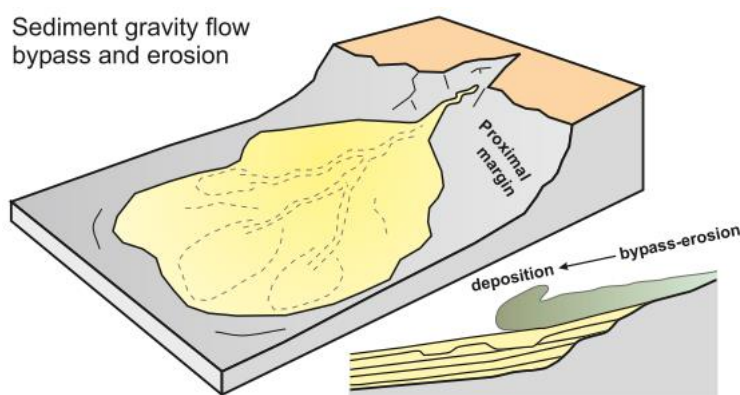


Figure 2.3 Schematic diagram illustrating how bypass and erosion by sediment gravity flows might form upslope turbidite pinchout traps in proximal upslope areas (adapted from Amy, 2019).

However, there is a high exploration risk associated with this trapping style, as reservoir sands might be connected with updip sands, which would result in hydrocarbon leakage via thief zones (e.g., Hansen et al., 2019). Furthermore, seismic resolution might not be good enough to resolve for thin units, leading to uncertainty on the pinchout location (Amy, 2019). Therefore, upslope pinchout traps are usually left as secondary exploration targets (Straccia and Prather, 1999; Stirling et al., 2018).

Outcrop and subsurface studies show that bypass surfaces in slope settings might allow the development of potential turbidite reservoir bodies detached from their feeder system (Straccia and Prather, 1999; Doré and Robbins, 2005; Horseman et al., 2014; Van der Merwe et al., 2014; Hansen et al., 2019; Counts et al., 2021). If sediment bypass continues over enough time for thick mudstones to develop, these may act as permeability barriers to prevent the updip leakage of hydrocarbons (Straccia and Prather, 1999; Van der Merwe et al., 2014; Amy, 2019). An example of a successful bypass-related oilfield is the Buzzard Field located in the Outer Moray Firth, UK North Sea (Doré and Robbins, 2005). The reservoir sands bypassed the slope due to a significant change in the slope angle and were deposited in a base of slope setting as detached turbidite lobes (Doré and Robbins, 2005). Similarly, the English Colony Field, California is a stratigraphic pinchout onto the mid slope along the Santa Margarita slope (Hewlett and Jordan, 1993). The transgressive marine mudstones provide a lateral and updip seal, although the seal is not as effective in the upper slope

position where the turbidite reservoirs are next to deltaic sandstones (Hewlett and Jordan, 1993).

Understanding the controls on sediment bypass is important to predict the integrity of bypass-related upslope pinchout traps (Figure 2.3) (Amy, 2019), as well as the potential location, extent and thickness of deposits associated with bypassing flows (Stevenson et al., 2015).

2.2 Submarine channels

2.2.1 Overview

Submarine channels constitute conduits in the continental slope and basin plain formed by the passage of erosional, bypassing or depositional turbidity currents and other sediment-laden gravity-driven underflows (Menard, 1955; Peakall and Sumner, 2015). Hence, submarine channels allow the transport of sediment from proximal to more distal settings and facilitate the development of submarine fans which represent some of the largest sediment accumulations on Earth (e.g., the Bengal Fan, Curray et al., 2003). Furthermore, they also permit the transport and represent areas of deposition of plastics (Kane and Clare, 2019; Zhong and Peng, 2021).

Submarine channels are economically important due to their potential to host hydrocarbons (Weimer and Slatt, 2004). Additionally, their geological record may preserve signals useful for the reconstruction of palaeoenvironments (Prins and Postma, 2000) and palaeoseismology (Goldfinger, 2011). Hence, the morphology, inception and evolution of submarine channels have been extensively studied through i) bathymetry datasets (sometimes integrated with shallow seismic profiles) (e.g., Pirmez and Flood, 1995; Babonneau et al., 2002; Bourget et al., 2008; Maier et al., 2011; Fildani et al., 2013; Covault et al., 2014; Wiles et al., 2017; Vendettuoli et al., 2019; Heijnen et al., 2020); 3D seismic datasets (e.g., Abreu et al., 2003; Deptuck et al., 2007; Gee and Gawthorpe, 2007; Cross et al., 2009; Mayall et al., 2010; Qin et al., 2016); bathymetry and 3D seismic integration (e.g., Jobe et al., 2015; Tek et al., 2021); exhumed channel deposits (e.g., Mutti and Normark, 1987; Gardner et al., 2003; Beaubouef, 2004; Hubbard et al., 2014), as well as through modelling (e.g., McHargue et al., 2011a; Sylvester et al., 2011).

In this work and throughout this thesis, the term 'channel' will be used for surficial channels that represent hydraulic conduits; whereas the term 'channel-form' will

be referred to subsurface channels that may represent a palaeo-hydraulic conduit or an element of higher hierarchy.

2.2.2 Morphology and evolution

The morphology of submarine channels vary in planform and cross-sectional shape across systems but share a longitudinal elongated planform morphology that can be either straight or sinuous and stretch as long as 1000's of kilometres (Wynn et al., 2007). Peakall and Sumner (2015) classified submarine channels into six types according to their distinct morphologies and occurrence (Figure 2.4): i) 'arteries and veins' of submarine fans (also defined as distributary channels, (e.g., Flood and Damuth, 1987), often connected to a river system at sea-level low-stand (e.g., the Bengal, Curray et al., 2003) and Amazon systems (Flood and Damuth, 1987)); ii) isolated deep-ocean channels not related to major fans (e.g., Klaucke et al., 1998); iii) axial channels in ocean trenches (e.g., Tek et al. 2021). The work of McArthur and Tek (2021) showed that the rate of sediment supply, the length and rugosity of the trench, and the subduction rate are the main controls on the development of trench-axial channels; iv) aggradational (e.g., Straub and Mohrig, 2008) or erosional slope channels; v) non-margin ocean channels not connected to a terrestrially derived sediment supply; and vi) canyon-confined slope channels. Most studied channels initiate in canyons (e.g., Fildani et al., 2006). Canyons are erosional, deep and steep features on the slope with V-shaped cross-sections that allow sediment transfer from shallow to deepwater (Daly, 1936; Shepard, 1981).

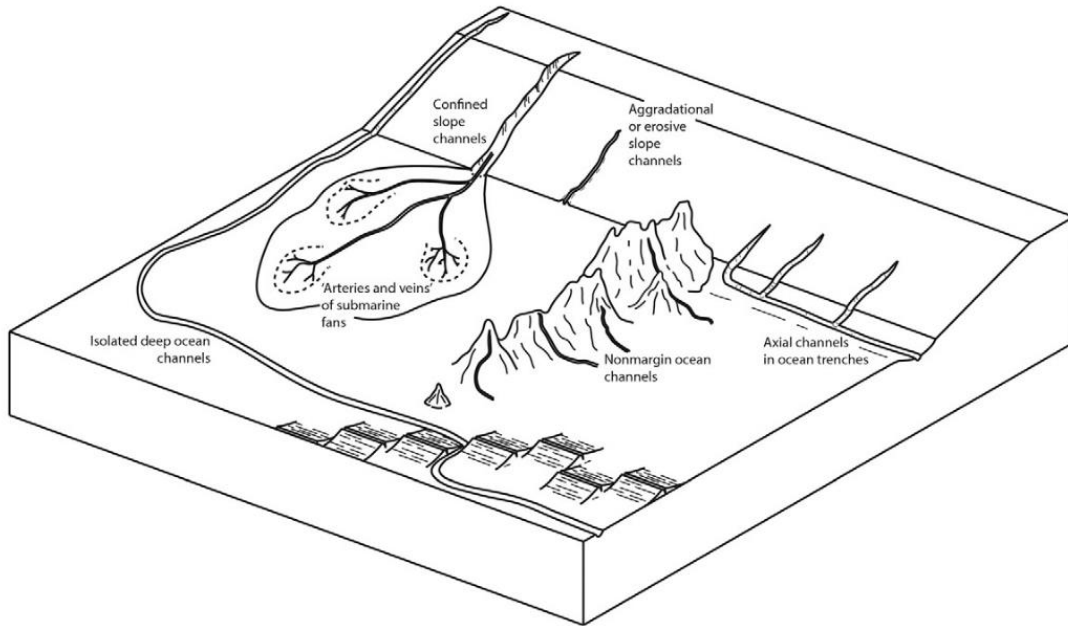


Figure 2.4 Submarine channel classification from Peakall and Sumner (2015) according to their morphology and occurrence in the continental slope and basin plain.

2.2.2.1 Cross-sectional morphology and longitudinal profile

Channels have a concave-up shape in cross-section that mainly evolves depending on the character of the turbidity currents traversing them (Figure 2.5). Channel depths typically vary from tens to hundreds of meters and channel widths vary from hundreds of meters to tens of kilometres (Konsoer et al., 2013).

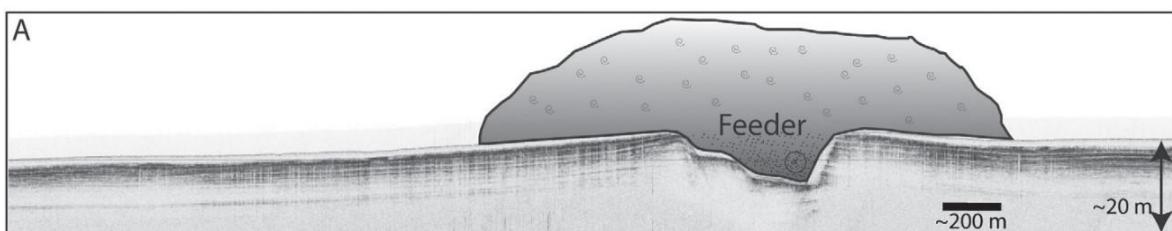


Figure 2.5 Compressed high-intensity radar pulse subbottom profile from the Lucia Chica channel system and schematic turbidity current (adapted from Maier et al. (2011)).

Their cross-sectional shape has been commonly defined as being either aggradational or erosional (Figure 2.6) (Kneller, 2003) although a combination of both has also been proposed (Pickering et al., 1995). Additionally, equilibrium channels (also termed 'at grade' or 'graded') have been defined, mainly based on their longitudinal profile (Pirmez et al., 2000; Kneller, 2003). The channel thalweg slope of equilibrium channels is thought to be in equilibrium with the currents traversing it, i.e., flows would not erode nor deposit sediment in the channel (Figure 2.6A). Therefore, there would not be channel aggradation nor

degradation (Kneller, 2003) or it would be very minimum (Pirmez et al., 2000), which would lead to a concave-up slope profile (Ferry et al., 2005) (Figure 2.6A). The concept of an equilibrium profile is more complex in settings with high syn-sedimentary deformation (Clark and Cartwright, 2011). Georgiopoulou and Cartwright (2013) showed that channels may establish an equilibrium profile if flows take the most energy efficient routes and flow power exceeds changes in the slope due to structural deformation.

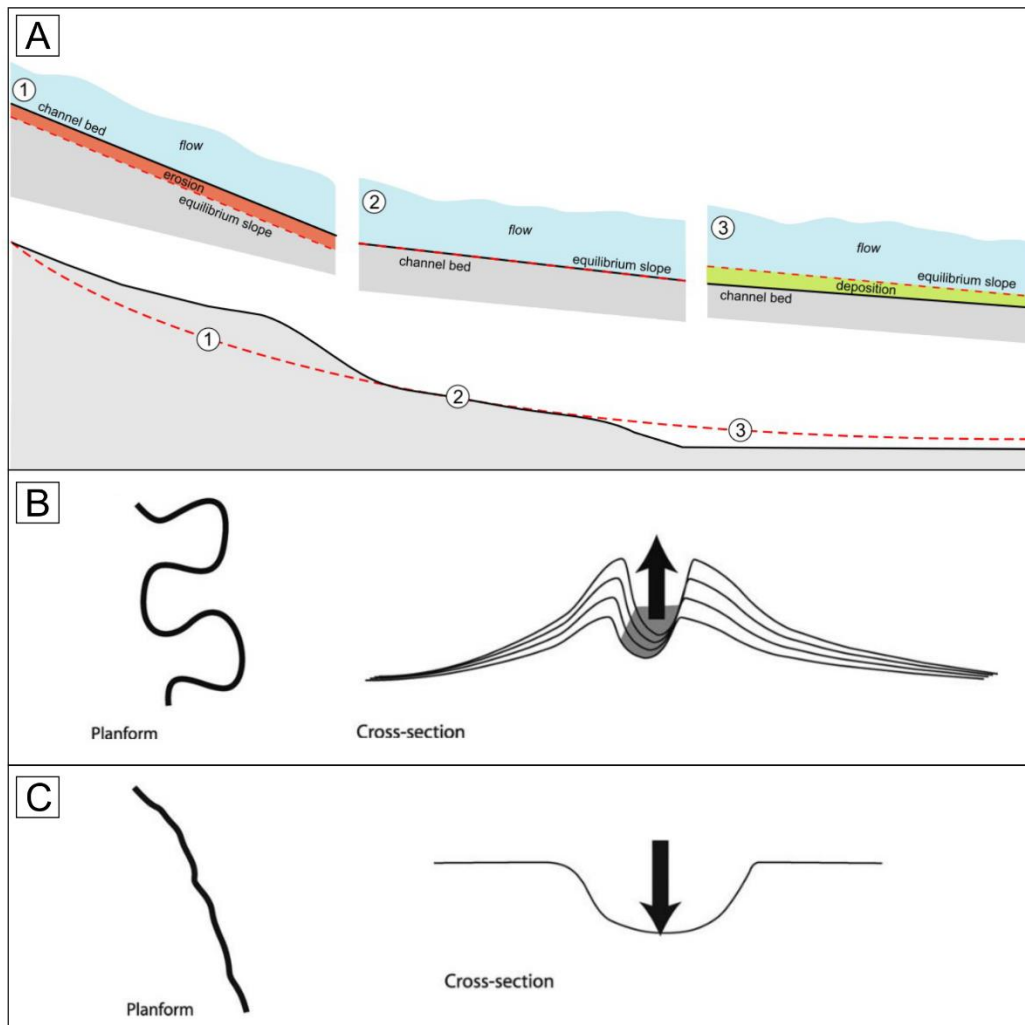


Figure 2.6 (A) Schematic diagram of a channel slope profile (solid line) and the theoretical equilibrium slope profile (dashed line) that is achieved over time through erosion (1) or deposition (2) (from Amy and Dorrell, 2021); (B) schematic illustration of an aggradational channel and its sinuous planform; (C) schematic illustration of an erosional channel and its straight planform (B and C adapted from Kneller, 2003).

Deviations from the equilibrium profile slope result in a change in the flow dynamics and channel morphology (Kneller, 2003). Aggradational channels may arise when the slope profile is below the theoretical equilibrium slope (e.g., Pirmez and Flood, 1995; Straub et al., 2012). Hence, the available

accommodation and depositional flows allow the channel to aggrade (Figure 2.6A and 2.6B). Furthermore, they often display sinuous planforms (Figure 2.6B). Deposition occurs both in the channel and in the overbank areas to retain flow confinement. Overbank deposition occurs through two different mechanisms: overspilling (or overbanking) (Figure 2.7A) and flow stripping (Figure 2.7B). Overspilling occurs when the flow exceeds the channel confinement, whereas during flow stripping, the flow is driven to the outer overbank area of a bend (Peakall et al., 2000). Hence, both mechanisms contribute to the construction of laterally extensive wedge-shaped architectures termed levees (Kane and Hodgson, 2011; Hansen et al., 2015). Multiple channels with associated bounding levees in the slope or basin floor are termed channel-levee systems (Hansen et al., 2015).

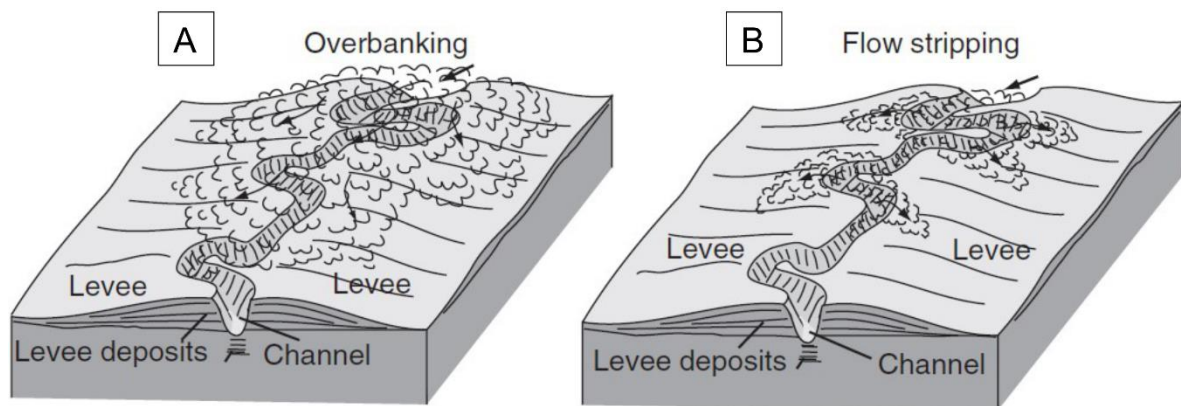


Figure 2.7 Block diagrams showing (A) overbanking or overspilling and (B) flow stripping by turbidity currents. Arrows indicate the flow direction (from Mulder, 2011).

When the slope profile is above a theoretical equilibrium that reduces accommodation and when erosion is greater than deposition (Figure 2.6A), then flows would degrade the channel bed and form erosional channels (Figure 2.6C) (Kneller, 2003). A key feature that differentiates erosional channels from aggradational channels is the absence of channel-bounding levees and possibly a straighter planform (often related to a short channel life) (Figure 2.6C) (Kneller, 2003). A change in flow conditions where deposition exceeds erosion contribute to the fill of this channel type.

These channel types form the basic building blocks of channel systems however, in their evolution they can become far more complex and both types (erosional and aggradational), a combination of both or one channel type evolving into the other (generally over longer time-scales) may be found in a given system (Mayall and Stewart, 2000; Gee and Gawthorpe, 2007; Janocko et al., 2013b).

2.2.2.2 Planform morphology - sinuosity

Most of the submarine channels shown in Figure 2.4 can potentially develop sinuous planform morphologies (Figure 2.8) (sinuosity >1.2 following Wynn et al., (2007)) similar to those observed in rivers. Submarine channels and rivers have been compared as they share features such as bend cut-offs, high sinuosity, point bars, scroll bars or meander belts (Kneller, 2003; Kolla et al., 2007). However, it has been recognized that there are significant differences in the flow processes, geometry and evolution between both submarine and subaerial channels (Peakall et al., 2000; Kolla et al., 2007; Wynn et al., 2007; Jobe et al., 2016, 2020).

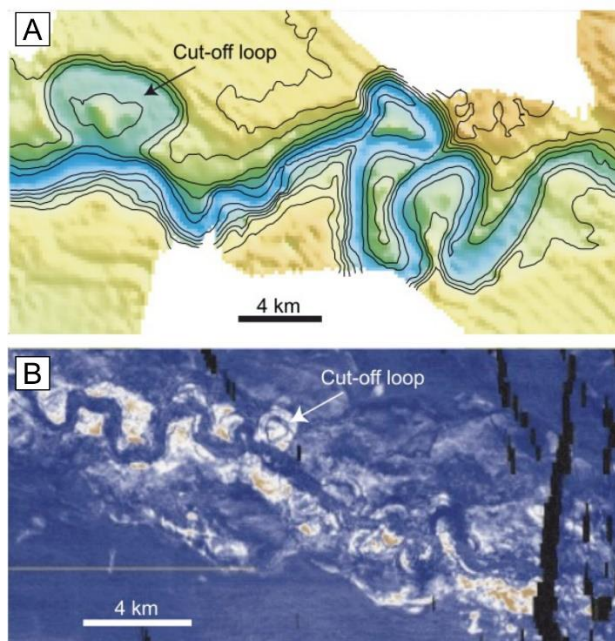


Figure 2.8 Examples of sinuous submarine channels. (A) Bathymetry image of a highly sinuous planform from Cap Timiris Canyon, offshore Mauritania, (B) root-mean-square seismic horizon slice from a sinuous subsurface channel, offshore West Africa; high amplitudes shown in red and low amplitudes in blue (adapted from Wynn et al., 2007).

The fundamental processes building aggradational sinuous channels have been explained by Peakall et al. (2000) through a three-stage model (Figure 2.9): Stage 1 describes a phase of lateral accumulation of channel thalweg deposits at bend apices, related to bend growth. In the depositional record, this translates into point-bar deposits with lateral-accretion surfaces (Abreu et al., 2003). Stage 2 describes an equilibrium phase where the channel vertically aggrades reaching a stable planform geometry and sediment bypass dominates. Stage 3 is defined by channel abandonment. Fining upward in channel fill deposits, plugging by debris-flow deposits or hemipelagic drapes characterised this phase. Although the three-stage model synthesises sinuous submarine channel evolution in a comprehensive way; the internal dynamics of turbidity currents at channel bends

may lead to sinuosity development that can be far more complex due to changes in the downstream and cross-stream flow velocity and density (Janocko et al., 2013a; Sumner et al., 2014; Peakall and Sumner, 2015), as well as the behaviour of secondary flow fields (Keevil et al., 2007; Peakall et al., 2007; Wells and Dorrell, 2021) and changes in flow dynamics due to Coriolis (Davarpanah Jazi et al., 2020).

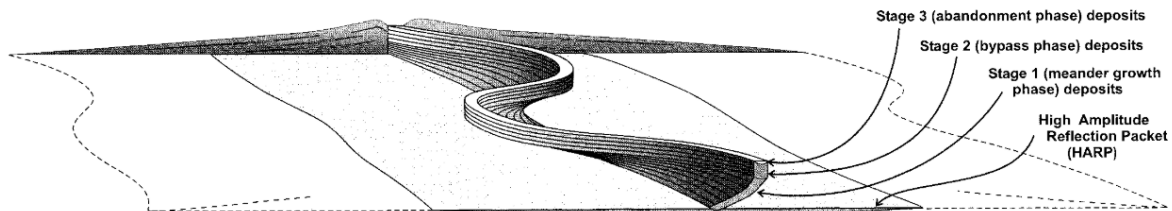


Figure 2.9 Conceptual diagram showing the three-stage model from Peakall et al. (2000) for the development of high sinuosity, aggradational submarine channels.

It has been of great interest to further understand the controls on the development of sinuosity in submarine channels given that variations in sinuosity have important implications for reservoir distribution and heterogeneity (Mayall et al., 2006). Clark et al. (1992) identified two end-members through the analysis of channel morphometrics (i.e. width, depth, meander radius of curvature and wavelength, peak sinuosity and valley slope gradients): i) the development of high-sinuosity promoted by low valley slope gradients and ii) low sinuosity channels linked to high valley slope gradients. They also suggested that a coarser bedload is linked to low sinuosity peak values than a suspended-dominated load, therefore the sediment type transported may also contribute to changes in sinuosity.

Peakall et al., (2012) highlighted that the relationship of sinuosity with slope gradient has been linked to a dominant grain size following Reading and Richards (1994). Therefore, the two end-member would result in: i) high-sinuosity low-gradient, fine-grained systems and ii) low-sinuosity, high gradient, coarse-grained systems. Furthermore, in contrast to the work of Clark et al. (1992), Peakall et al., (2012) demonstrated that the relationship between channel sinuosity and slope gradient was weak. Instead, they showed that there was a strong correlation between peak sinuosity and latitude. High-latitude systems correlated with low sinuosity channels whereas low-latitude systems with high sinuosity channels; they attributed these correlations to the effect of Coriolis force changing the three-dimensional intra-channel dynamics, which has been demonstrated in experiments on rotating flumes (Cossu and Wells, 2010, 2013; Cossu et al., 2010; Davarpanah Jazi et al., 2020).

Later, Sylvester and Pirmez (2019) demonstrated through an extensive analysis of individual channel bends that the latitudinal control in sinuosity was weak whereas the sinuosity-slope relationship was stronger, as initially proposed by Clark et al. (1992). Furthermore, Sylvester and Pirmez (2019) highlighted that the Coriolis force would only be important in large-scale channels such as the Northwest Atlantic Mid-Ocean Channel (NAMOC). Other controls on channel sinuosity have been related to the degree of sediment bypass and flow confinement, where a higher degree of bypass promotes inner-bend deposition and weakly bypassing flows deposit at the outer bend (Kane and McCaffrey, 2008).

It is important to note that variations in sinuosity can also be attributed to variations in sediment supply (Flood and Damuth, 1987; Babonneau et al., 2002), the seafloor topography (Mayall et al., 2006) and tectonics that modify the course of the channel (e.g., Cronin, 1995; Clark and Cartwright, 2011; Carter et al., 2016). Clark and Cartwright (2009) documented four types of channel-structure interactions using examples from aggradational channels however, they may also be found in channels where erosional flows dominate: i) confinement by pre-existing structures that constrains the channel course and limits lateral migration and sinuosity development as well as lateral extension of levees (Figure 2.10A); ii) diversion of the channel course due to obstruction of the flow pathway by a pre-existing (inactive) structure or series of structures. The channel is diverted around the structure and may resume its original downchannel course (Figure 2.10B); iii) deflection by an actively growing structure that causes a progressive shift towards the new topographic lows. The timing of channel development and deformations differentiates diversion from deflection. Active growth structures may also cause uplift and tilting of adjacent channel levees (Figure 2.10C); iv) blocking of channels by an actively growing structure orientated at a high angle to the flow pathway resulting in flow reflection and backfilling. Channel remnants may be preserved downstream of the blocking structure (Figure 2.10D).

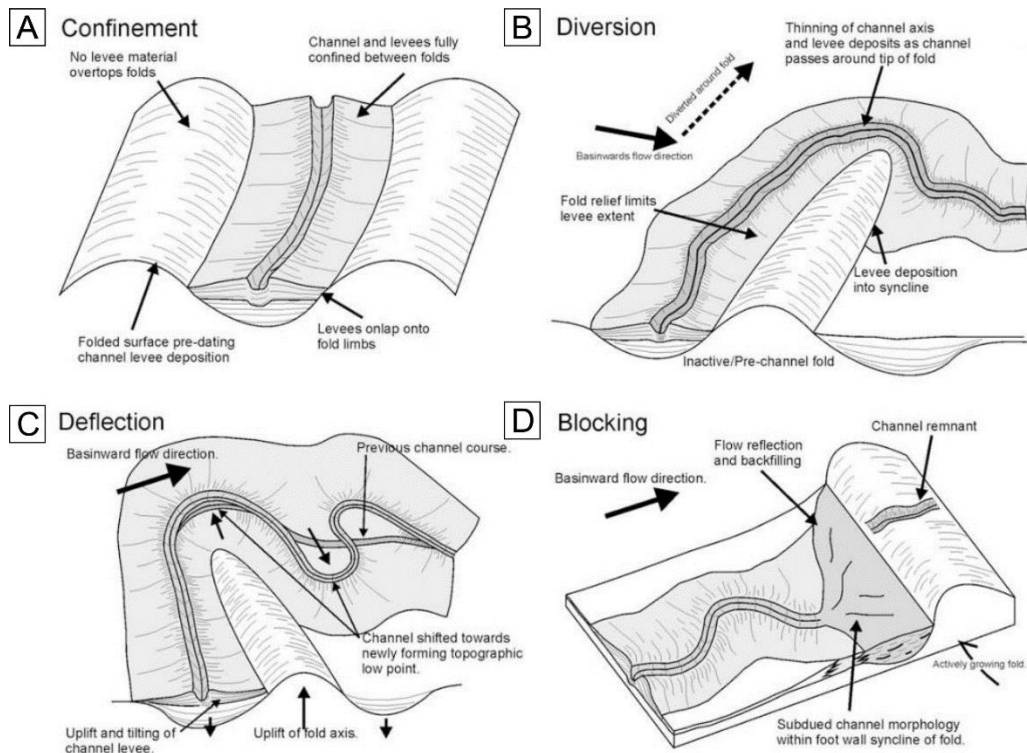


Figure 2.10 Diagrams illustrating the four end-member submarine channel-structure interactions (A) confinement by pre-existing structures, (B) diversion by inactive structural high, (C) deflection by and (D) blocking by an actively growing structure (from Clark and Cartwright, 2009).

Despite the advances, the controls on channel sinuosity are still a subject of debate and determining whether Coriolis forces hinder the development of sinuosity in submarine channels remains as an important research topic to address.

2.2.3 Subsurface channel-forms

Studies based on seismic reflection data have allowed great advancements in the understanding of submarine channel architecture and evolution. Subsurface observations have shown that channels commonly undergo a complex history of repeated periods of erosion, deposition and aggradation (Posamentier and Kolla, 2003; Mayall et al., 2006; Deptuck et al., 2007; Gee and Gawthorpe, 2007; Cross et al., 2009; Janocko et al., 2013b; Jobe et al., 2015; Qin et al., 2016; Tek et al., 2021). Stratigraphic analysis of channel-forms has shown that they are often confined within a major wide U-shaped erosional surface or a constructional surface that may be bounded by external levees (Figure 2.11) (*sensu* (Kane and Hodgson, 2011; Hansen et al., 2015)), whereas individual channel-forms within the major confining surface may be bounded by internal levees or depositional terraces (*sensu* (Kane and Hodgson, 2011; Hansen et al., 2015)).

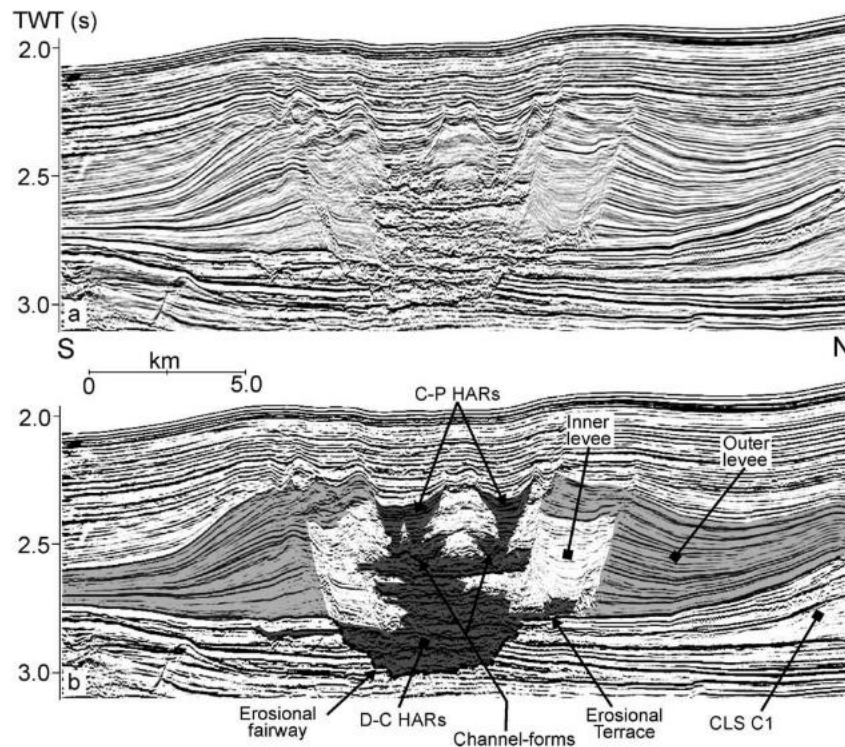


Figure 2.11 Uninterpreted and interpreted seismic profiles across a channel-levee system on the Indus Fan, Arabian Sea, with well-defined external (outer) and internal levees confining channel-forms that show discontinuous-chaotic high-amplitude reflectors (D-C HARs) or continuous-parallel high-amplitude reflectors (C-P HARs) (from Deptuck et al., 2003).

The deposits of turbidite channel-forms reflect changes in the volume and calibre of turbidity currents through multiple cycles of flow waxing and waning. The base of channel-floor deposits is often characterized by coarse-grained sediments (basal lags) that generate high-amplitude reflections (Mayall and Stewart, 2000; Posamentier and Kolla, 2003). McHargue et al. (2011b) suggested that flows are large and dense with coarse sediment in suspension, which promotes erosion during the waxing portion of a cycle. Conversely, less powerful, small, fine-grained depositional flows predominate during the waning phase (hence, generating fining-upwards grain-size profiles) and enhance overbank deposition. Furthermore, channels might undergo lateral and downdip migration producing lateral-accretion packages (LAPs) that appear as shingled reflections in seismic (Figure 2.12A) (Abreu et al., 2003). Channel migration might also occur through avulsion (Pirmez and Flood, 1995; Babonneau et al., 2002; Ortiz-Karpf et al., 2015), which can be differentiated from LAPs in seismic cross-sections due to its cut and fill pattern with subhorizontal reflections between dipping reflections (Figure 2.12B) (Abreu et al., 2003). Hence, confined individual channel-forms might also display different stacking patterns such as vertical or offset lateral stack (Figure 2.12C). Changes in channel evolution and infill may be driven by

allogenic factors such as changes in sea-level and climate (which influence the character of turbidity currents) or tectonics (Cronin, 1995; Mayall and Stewart, 2000; Abreu et al., 2003; Deptuck et al., 2007; Cross et al., 2009; Janocko et al., 2013b).

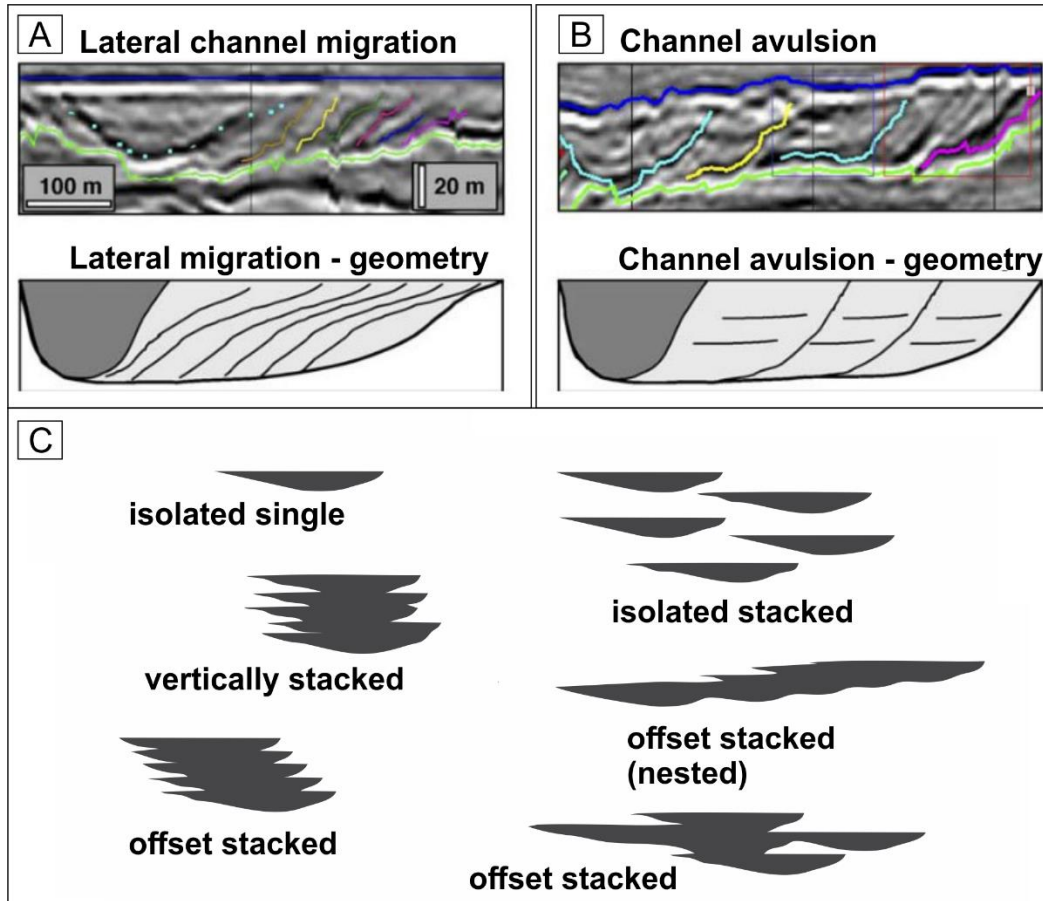


Figure 2.12 (A) Seismic cross-section showing shingled reflections product of lateral channel migration with a sketch of their geometry below; (B) Cut and fill patterns in seismic profile and sketch characteristic of channel avulsion (A and B are adapted from Abreu et al., 2003) (C) Stacking patterns of submarine channels (adapted from Pickering et al., 1995).

Hierarchical classifications have been developed to better characterize the channel-form deposits in terms of geometry, stacking patterns and scale (Cullis et al., 2018). One of the most used classifications is from Sprague et al. (2005) which divides channel-forms into six groups that increase in scale and complexity as: 1) channel storey, 2) channel-fill, 3) channel complex, 4) channel complex set, 5) channel complex system and 6) channel complex system set. Two hierarchical orders are used in this thesis, channel-fill (or channel element in McHargue et al., 2011b) and channel complex. A channel-fill is described as “*the volume of sediment deposited within a single cycle of channel-filling and abandonment*”. The height of channel fills is typically between 10-30 m and their

width between 300-500 m. Hence, this potentially constitutes the smallest channel-form identifiable in the seismic data used in Chapter 4 due to limits in vertical and horizontal seismic resolution. A channel complex is defined as ‘*two or more genetically-related channel-fills of similar architectural style*’. Sprague et al. (2005) highlights that the use of this channel-form hierarchy is independent of the channel sinuosity, channel fill type, aspect-ratio, or location. Cullis et al. (2018) offers a more detailed review on other hierarchical classifications for channel-forms.

2.3 Modelling of channelised turbidity currents from channel architecture

Much of the understanding of channelised turbidity currents has come from computational modelling techniques that study the dynamics and evolution of the current. By extension, this allows further understanding of changes in the morphology of submarine channels due to hydraulic changes in the currents that they confine. Most modelling techniques of channelised turbidity currents can be classified into the following categories according to the complexity of the governing equations and methods used to solve them: 1) Numerical methods that solve the Reynolds-averaged Navier-Stokes equations (often resolving over depth-averaged conditions) (e.g., Parker et al., 1986; Imran et al., 1999; Das et al., 2004; Groenenberg et al., 2009; Abd El-Gawad et al., 2012; Sequeiros, 2012; Janocko et al., 2013a; Dorrell et al., 2014; Ge et al., 2017; Kelly et al., 2019). 2) Numerical methods that solve the Navier-Stokes equations at all scales of motion such as large eddy or direct numerical simulation (e.g., Goodarzi et al., 2020). 3) Theoretical modelling based on different forms of the modified Chezy-type equation (Komar, 1973, 1977; Kneller, 2003; Konsoer et al., 2013; Stevenson et al., 2014; Li et al., 2018). 4) Theoretical modelling based on the channel geometry (Komar, 1969), where the extraction of channel morphometrics from various channel systems has helped to relate them to their forming flow processes (Komar, 1969; Bowen et al., 1984; Zeng et al., 1991; Stevenson et al., 2018). 5) Estimation of flow parameters from the grain size of turbidite deposits (Bowen et al., 1984; Komar, 1985; Zeng et al., 1991; Pirmez and Imran, 2003; Stevenson et al., 2014).

This part of the review focuses on the modelling technique number 4 which is directly related to the turbidity current modelling technique used in this thesis. Komar (1977), Middleton (1993), Kneller and Buckee (2000) and Parsons et al.,

(2007) offer more detailed reviews on the theory and applications of techniques 1 to 3.

2.3.1 The surface-slope equation

2.3.1.1 Theory

Komar (1969) introduced a theoretical prediction of turbidity current velocity based following observations from strong channel-levee asymmetry at high latitudes that was interpreted to be produced by a combination of the effect of Coriolis forces acting upon turbidity currents and the curvature-induced centrifugal force in channel bends. The Coriolis force, or Coriolis effect, is an inertial force that acts perpendicular to the direction of a moving body located in a rotating frame of reference. The acceleration of the Coriolis force is defined by the product of the Coriolis parameter, f and velocity, U : fU (Wells and Dorrell, 2021). On Earth, the Coriolis parameter is defined by $f = 2\Omega\sin\theta$, where Ω is the Earth's rotation rate and θ is the latitude; therefore, the Coriolis parameter is zero at the equator and increases with latitude. The effect of Coriolis upon turbidity currents is that of deflecting the bulk of the flow as it travels downchannel (Menard, 1955; Komar, 1969; Wells and Cossu, 2013); in the northern hemisphere, it deflects the bulk of the flow to the right (Figure 2.13A), creating higher right-hand side levees (looking downstream) (e.g., Komar, 1969; Hesse et al., 1987); whereas in the southern hemisphere, it deflects the flow to the left, creating higher left-hand side levees (e.g., Droz and Mougenot, 1987; Carter and Carter, 1988) (Figure 2.13B).

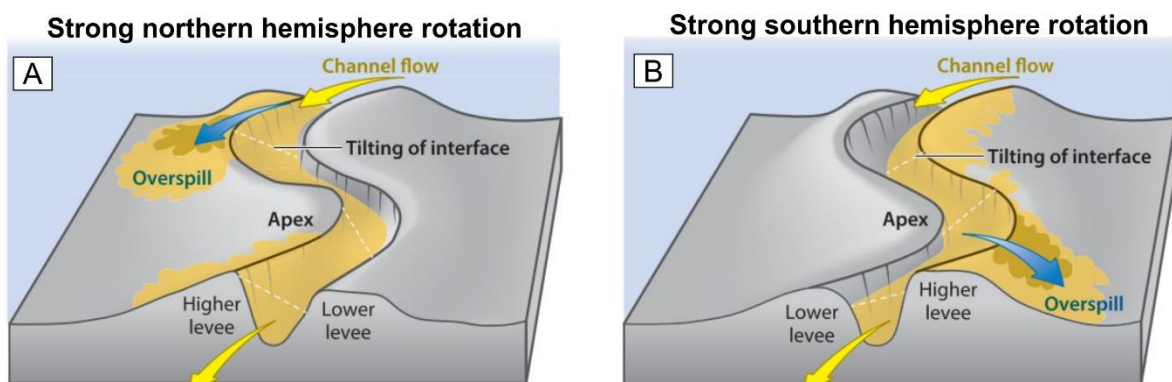


Figure 2.13 The Coriolis effect causes turbidity current deflection to the right under strong northern hemisphere rotation (A) and to the left under strong southern hemisphere rotation (B) looking downstream (adapted from Wells and Dorrell, 2021).

Komar (1969) recognised that the cross-channel slope (or tilt) arising from the channel-levee asymmetry could be used to estimate the velocity of turbidity currents under the assumption that the currents exactly fill the channel

confinement. Therefore, the observed cross-channel slope was used to approximate the pressure gradient force that results from the upper flow-ambient fluid interface slope through $g \frac{\Delta\rho}{\rho_t} \left(\frac{\Delta H}{W} \right)$, where g is gravity, $\Delta\rho$ is the excess density of the flow with respect to ambient water, ρ_t is the turbidity current density, ΔH the difference in levee height (Figure 2.14) and W the channel width (Figure 2.14). The centrifugal force is defined by $\frac{U^2}{r}$, where r is the bend radius of curvature (Figure 2.14), then, the surface-slope equation that balances the centrifugal and Coriolis force against the pressure force is written as (Komar, 1969)

$$\frac{U^2}{r} + fU = g \frac{\Delta\rho}{\rho_t} \left(\frac{\Delta H}{W} \right). \quad (2.1)$$

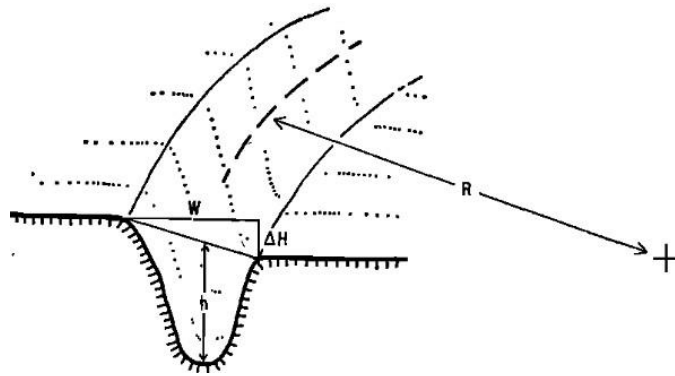


Figure 2.14 Parameters obtained from the channel morphology are used as inputs into the surface-slope equation (from Komar, 1969).

Equation (2.1) can also be applied to straight channel sections where $r \rightarrow \infty$ (Komar, 1969). Most parameters can be obtained from the channel morphology and only two unknowns remain, U and ρ_t (Komar, 1969). Komar (1969) calculated flow velocities in the Monterey channel assuming a range of lower and upper limits for the current density of $\sim 1,030 \text{ kg/m}^3$ to $1,180 \text{ kg/m}^3$ following the autosuspension criteria of Bagnold (1962), which derived velocities between 4 m/s and 20 m/s.

It is important to note that the momentum balance in Equation (2.1) calculates bulk flow properties, i.e., it does not account for vertical velocity and density variations in the flow (Stacey and Bowen, 1988a). It ignores mixing at the upper interface (Ellison and Turner, 1959), ambient water entrainment and drag at the bed (Parker et al., 1987), and bed slope which are critical parameters in the characterization of turbidity currents (Parker et al., 1987; Abad et al., 2011). Furthermore, it does not incorporate the effects of secondary circulation that arise at channel bends (Cossu and Wells, 2010; Sumner et al., 2014), and at straight

channel sections due to interactions of Coriolis force and pressure gradient force (Cossu et al., 2010).

2.3.1.2 Application to channel systems

After the definition and application of the surface-slope equation by Komar (1969), the equation has been applied to calculate bulk flow velocities in the Navy Fan (Bowen et al., 1984), the Bute Inlet (Zeng et al., 1991), the Knight Inlet (Ren et al., 1996), the NAMOC (Klaucke et al., 1997), the Amazon Channel (Pirmez and Imran, 2003) and to calculate the sediment concentration of the 1929 Grand Banks flow event (Stevenson et al., 2018) (Table 2.1).

Bowen et al. (1984) expressed the surface-slope equation in terms of the Froude number, Fr as

$$\left(\frac{fh}{U} + \frac{h}{R}\right) Fr^2 = \frac{\Delta H}{W}, \quad (2.2)$$

where

$$Fr^2 = \frac{S}{C_d + E}. \quad (2.3)$$

The Froude number describes the ratio of inertial to buoyancy forces and is used as an indicative of flow stability, hence flows are characterised as supercritical when $Fr > 1$ and subcritical when $Fr < 1$ (Ellison and Turner, 1959); the transition from supercritical to subcritical flow is characterised by a hydraulic jump (Sumner et al., 2013; Dorrell et al., 2016). E defines an ambient water entrainment coefficient, C_d the drag coefficient and S the bed downchannel slope. Hence, the description of the cross-flow momentum balance in terms of the Froude number allows to parameterize flow mixing, ambient water entrainment and drag at the bed which are not considered in Equation (2.1).

Bowen et al. (1984) analytically solved for turbidity current velocities in the mid Navy Fan using Equation (2.2) (Table 2.1) for a straight channel section ($r \rightarrow \infty$), which derived $U=0.32$ m/s and 0.23 m/s for $Fr^2 = 1$ and $Fr^2 = 0.75$, respectively. They argued that these velocity estimates were consistent with a sediment concentration of $3-4 \times 10^{-4}$ as estimated using an independent approach based on the sediment size (Bowen et al., 1984). Velocity values in the mid fan were also in agreement with a turbidity current that slowed down from the upper fan valley with $U=0.75$ m/s to the basin plain with $U=0.12$ m/s (based on grain size estimations) (Bowen et al., 1984).

Zeng et al. (1991) calculated mean flow velocities from the Bute Inlet using Equation (2.2) and the Froude numbers assumed by Bowen et al. (1984) (Table 2.1). Flow velocities decreased downstream from 4.24 m/s (upper reach) to 0.66

m/s (lower reach). Zeng et al. (1991) argued that the velocity of 4.24 m/s was too high compared to the downstream reaches and attributed the difference to uncertainties in the estimates of bank height difference ΔH and radius of curvature r which in turn depend on the quality and resolution of bathymetric maps. Nevertheless, the calculated flow parameters showed to be consistent with direct measurements from a flow event in May 1986 (Zeng et al., 1991), where mean flow velocity between stations 1 (upper reach) and 2 (mid-reach) yielded 3.35 m/s and between stations 2 and 3 (lower reach) yielded 0.75 m/s. Assuming that the currents in the Knight Inlet were similar to the Bute Inlet as they are geographically closed fjords, Ren et al. (1996) obtained comparable results with a maximum flow velocity of 4.06 m/s in the upper reach which decreased to 0.58-1.16 m/s in the lower reach. A Chezy-type equation (Middleton, 1966c) was used to estimate the current density ρ_t in both studies (Zeng et al., 1991; Ren et al., 1996) using the flow velocities estimated from the channel morphology. The calculated densities ranged from 1,028 to 1,048 kg/m³ in the Bute Inlet (Zeng et al., 1991) and from 1,024 to 1,048 kg/m³ in the Knight Inlet (Ren et al., 1996).

Equation (2.2) was also applied to the 'equilibrium channel' portion (~300 km long) of the NAMOC to calculate mean flow velocities. Estimated velocities ranged downstream from 0.86 to 0.05 m/s (Klaucke et al., 1997) suggesting decelerating turbidity currents. Klaucke et al. (1997) argued that the low velocities observed compared to the previous study of Komar (1969) (Table 2.1) could be due to the use of Equation (2.2), which avoided ambiguities in the selection of a turbidity current density. Furthermore, they highlighted that the bathymetry data in this study allowed to better constrain the channel geometry.

Pirmez and Imran (2003) estimated the mean flow velocity in the meander bends of the Amazon Channel (Table 2.1) assuming a range of turbidity current densities between 1040 to 1070 kg/m³ which are equivalent to a volume concentration of 0.6% to 2.5% respectively. The calculated velocities ranged between ~1.5-3.5 m/s in the uppermost reaches of the channel and decreased to ~0.5-1.5 m/s in the upper fan and the remaining channel length which was in agreement with velocity estimates from grain size and the downslope conservation method (Pirmez and Imran, 2003). Pirmez and Imran highlighted that the variation in flow velocities in each channel section was due to the assumed range on flow density, which in turn illustrated the sensitivity of the model to this parameter. This study constitutes the largest in terms of the application of Komar's method as they applied Equation (2.1) to 167 meander bends of which 121 gave valid solutions (Pirmez and Imran, 2003). Invalid solutions resulted at channel sections where the outer bank elevation was equal

to the inner bank (which led to velocities near zero) or slightly lower than the inner bank due to levee erosion (Pirmez and Imran, 2003), which highlights limitations to the application of this equation.

Stevenson et al. (2018) introduced an alternative way of applying Equation (2.1) with the estimation of the sediment concentration from the 1929 Grand Banks flow event (Piper and Aksu, 1987) (Table 2.1). The equation was applied to a channel bend in the South Branch of the Eastern Valley of the Grand Banks slope; whereas an independent approach using the downslope conservation method (Pirmez and Imran, 2003) was applied to straight channel sections (Stevenson et al., 2018). An advantage in this study was that the depth-averaged downstream velocities used as input into Equation (2.1) corresponded to velocities obtained from seafloor cable breaks, which reduced uncertainty in the outputs of sediment concentration. A key difference from other studies was that the estimation of the height difference of the flow (ΔH) between the outer and inner bend was taken from the erosional trimlines interpreted to represent the thickness of the high-concentration lower layer of the flow. The bulk sediment concentration calculated at the channel bend was $\sim 1.5\%$. Downstream of the channel bend, the downslope conservation method estimated sediment concentration values of up to $\sim 4.8\%$ in the South Branch. Stevenson et al. (2018) discussed that significant uncertainties arise in the downslope conservation method related to the estimation of the basal drag coefficient and ambient water entrainment which are not present in Equation (2.1).

Table 2.1 Summary of studies that used Komar (1969) surface-slope method to calculate bulk turbidity current properties. Columns for water entrainment and mixing list the reference to the equation used to parameterize each flow aspect.

Location	Parameter solved	Inferred solution method	Water entrainment	Mixing	Results	Reference
Monterey Channel	Flow velocity (Eq. 2.1)	Analytical	NA	NA	6 – 20 m/s	Komar (1969)
Navy Fan, offshore California*	Flow velocity (Eq. 2.2)	Analytical	Ellison and Turner (1959)	Ellison and Turner (1959)	0.23-0.32 m/s	Bowen et al. (1984)

Bute Inlet, British Columbia*	Flow velocity (Eq. 2.2)	Analytical	Ellison and Turner (1959)	Ellison and Turner (1959)	0.66- 4.25 m/s	Zeng et al. (1991)
Knight Inlet, British Columbia*	Flow velocity (Eq. 2.1)	Analytical	NA	Middleto n (1966c)	0.58- 4.06 m/s	Ren et al. (1996)
NAMOC, Labrador Sea	Flow velocity (Eq. 2.2)	Analytical	NA	Middleto n (1966b)	0.05- 0.86 m/s	Klaucke et al. (1997)
Amazon Channel	Flow velocity (Eq. 2.1)	Analytical	NA	NA	1.5-3.5 m/s 0.5-1.5 m/s	Pirmez and Imran (2003)
Grand Banks slope	Sediment concentrati on (Eq. 2.1)	Analytical	NA	NA	~1.5%	Stevenson et al. (2018)

NA: not applicable.

* Modelling also incorporated a coefficient to parameterized drag at the bed.

The application of the momentum balance developed by Komar (1969) (Equation 2.1) and its expression in terms of the Froude number given by Bowen et al. (1984) (Equation 2.2) have provided great insights into the character and evolution of turbidity currents based on the characteristics of their confining channels. Furthermore, the solution generally show good agreement with other approaches that recover flow conditions from grain size (Komar, 1985) or via Chezy-type equations (Middleton, 1966b; Komar, 1977).

Studies highlight that the use of Equation (2.2) reduces uncertainty in the selection of an appropriate flow density to solve for flow velocity; however, other types of uncertainty are introduced in terms of the selection of a Froude number. For example, Bowen et al. (1984) assumed that the flow had a $Fr = 1$ in most calculations, which might be unlikely as the flow responds to changes in the bed slope and ambient water entrainment (Ellison and Turner, 1959). Similarly, using the surface-slope equation to calculate sediment concentration would introduce great uncertainty when the flow velocity is not known or not well constrained. To

reduce this uncertainty, a better approach could constitute to jointly solve for the unknown parameters (e.g., flow velocity and Froude number or sediment concentration and Froude number) through numerical data fitting techniques instead of the analytical solution method used (Table 2.1), incorporating the effect of water entrainment and mixing at the upper part of the flow and drag at the bed which are critical parameters in the description of turbidity current dynamics (Ellison and Turner, 1959; Parker et al., 1986; Stacey and Bowen, 1988a; Middleton, 1993). However, as highlighted by Stevenson et al. (2018), some uncertainty is probably unavoidable as parameters such as the drag coefficient and ambient water entrainment are not well constrained by field data.

Chapter 3 A new modelling approach to sediment bypass prediction applied to the Hikurangi Margin, New Zealand

3.1 Abstract

Predicting when turbidity currents are erosional or depositional (i.e., leaving no depositional record vs. leaving a deposit) remains challenging. Here, observations from submarine channel morphology were combined with a new sediment transport model to derive thresholds for net erosional, equilibrium or net depositional flow and to predict how far turbidity currents can transport different grain size classes down-channel. The approach was applied to the modern Madden and Omakere channels, which traverse the Hikurangi subduction margin of the North Island of New Zealand. A bathymetric dataset was used to establish the downstream change of channel geometry. Taking account of centripetal and Coriolis forces, the surface slope equation was used to estimate variations in flow criticality, velocity and concentration along the channels. The approximated flow height of the current and the calculated sediment concentration were used as model inputs in order to estimate the potential distribution of sand in the system, assuming well-sorted and poorly-sorted sediment in suspension. The predicted sand distribution maps deposited by poorly-sorted flows in the channels show good agreement with RMS amplitude mapping of the seafloor. These results confirm that thicker flows, and those carrying well-sorted suspensions can bypass sediment over lower slopes than thinner flows and those carrying more poorly-sorted suspensions. The net erosion and net deposition thresholds derived from this study may help to guide and constrain predictions of potential sediment bypass zones in seafloor and subsurface systems, and hence better constrain the predicted *loci* of deposition.

3.2 Introduction

Deep-marine siliciclastic systems are volumetrically some of the most important sedimentary environments on the surface of the earth (Covault and Graham, 2010; Meiburg and Kneller, 2010; Talling et al., 2015). Submarine gravity currents (e.g. turbidity currents) transport sediment from shallow to deep-water, often developing complex depositional geometries (e.g. Richards and Bowman, 1998; Wynn et al., 2002; Booth et al., 2003; Gardner et al., 2003; Posamentier and Kolla, 2003; Deptuck et al., 2008; Ponce and Carmona, 2011; Dorrell et al., 2015; Spychala et al., 2017). Whether suspended sediment of a particular grain size is either transported up to the

maximum flow runout distance, or deposited at any particular location along the flow pathway plays a key role in: 1) the distribution of sediment across shelf-to-basin slope profiles (Normark, 1978; Mutti and Normark, 1987; Prather et al., 1998; Wynn et al., 2002; Hadler-Jacobsen et al., 2005; Carvajal and Steel, 2009; Pyles et al., 2011); 2) the reservoir quality of turbidite sandstones through fractionation of different grain size classes (Pyles and Jennette, 2009; Horseman et al., 2014; Marchand et al., 2015; Bell et al., 2018); and 3) the development of up-dip stratigraphic pinch-outs that trap hydrocarbon reservoirs (Straccia and Prather, 1999; Carruth, 2003; Prather, 2003; Doré and Robbins, 2005; Milton-Worssell et al., 2006; Horseman et al., 2014; Van der Merwe et al., 2014; Amy, 2019; Hansen et al., 2019). However, determining whether a turbidity current transports or deposits sediment remains challenging, despite recent work observing and monitoring turbidity currents (Vangriesheim et al., 2009; Xu et al., 2014; Paull et al., 2018; Zhang et al., 2018).

A theoretical model was used for the calculation of the threshold between net sediment erosion and net sediment deposition of turbidity currents to determine the grain sizes that might be transported or deposited along the Madden and Omakere slope channels of the Hikurangi Margin, New Zealand. The submarine slope represents an actively growing subduction wedge (Nicol et al., 2007; Barnes et al., 2010), with a series of trench-slope basins that are either supplied with sediment or starved, depending on the presence of slope channels (McArthur et al., 2020a). The flow properties of turbidity currents were calculated based on an assumed relationship to the morphology of their confining channels. The thresholds between erosion and deposition were calculated assuming flows carrying non-cohesive sediment of a range of grain size classes and grain size distributions, accounting for the capacity and competence of the flow, flow height and bulk sediment concentration. Furthermore, the results from the model are validated by geophysical and petrophysical information. Here, it is demonstrated that the grain size distribution in the flow has a large impact on sediment transport thresholds, therefore potentially controlling the sand distribution in the system.

3.2.1 Terminology

Despite its importance, there is no agreed definition of sediment bypass and bypassing flows between disciplines that study both associated sediment transport processes and products. In stratigraphic studies, *bypassing flow* or *bypass* have been broadly used for flows that partially or completely transport their sediment load beyond a point of observation (e.g. Lowe, 1982; Mutti and Normark, 1987; Amy et al., 2000; Cronin et al., 2005b; Kolla et al., 2007; Wynn et al., 2007; Carvajal and Steel, 2009; Talling et al., 2012; Stevenson et al., 2013; Sylvester et al., 2015). Furthermore, bypassing flow

has also been used to refer to erosional flows despite the fundamental differences (i.e. changes in flow capacity) between both flow types (e.g. Mutti and Normark, 1987; Wynn et al., 2002; Hubbard et al., 2014; Stevenson et al., 2015; Lang et al., 2017). In contrast, previous experimental and numerical studies have defined non-depositional flows as equilibrium, self-sustaining or autosuspending flows (Bagnold, 1962; Kneller, 2003; Sequeiros et al., 2009; Dorrell et al., 2018). These definitions describe a flow state where there is a net balance between sediment erosion and sediment deposition, and allows differentiation of non-equilibrium flow regimes (i.e., erosional versus depositional flow).

In an attempt to make a clear differentiation of bypassing flows in both process and stratigraphic contexts, the terms *bypassing flows*, *partially bypassing flows* and *depositional flows* have been suggested by Stevenson et al. (2015). These definitions provide a useful framework in stratigraphic terms to distinguish flows that transport their complete load from those that leave a deposit. However, in terms of process, the definition of depositional flows implies that there must be some bypassing fraction in suspension, which overlaps with the definition for partially bypassing flows. Therefore, for the purpose of this work, the following terminology is used which applies to the suspension load transported by channelized turbidity currents (Figure 3.1).

Erosional flows are non-equilibrium, under-capacity flows which entrain sediment into suspension and transport it beyond the point of observation. *Equilibrium flows* are flows at capacity, sediment deposition is balanced with erosion and allows for transport of their complete suspension load beyond the point of observation, resulting in absence both of a depositional record and of erosional features (e.g. Stevenson et al., 2013). *Depositional flows* are non-equilibrium flows that are over capacity and deposit a fraction of their suspended load whilst the remainder is further transported downstream. Here, *sediment bypass* refers to the process where sediment is transported beyond a point of observation by erosional flows, equilibrium flows or depositional flows. The terms *deposition* and *bypass* preceded by the grain size (e.g. sand deposition and silt bypass) will be used to differentiate the grain sizes that are simultaneously deposited and bypassed at the point of observation.

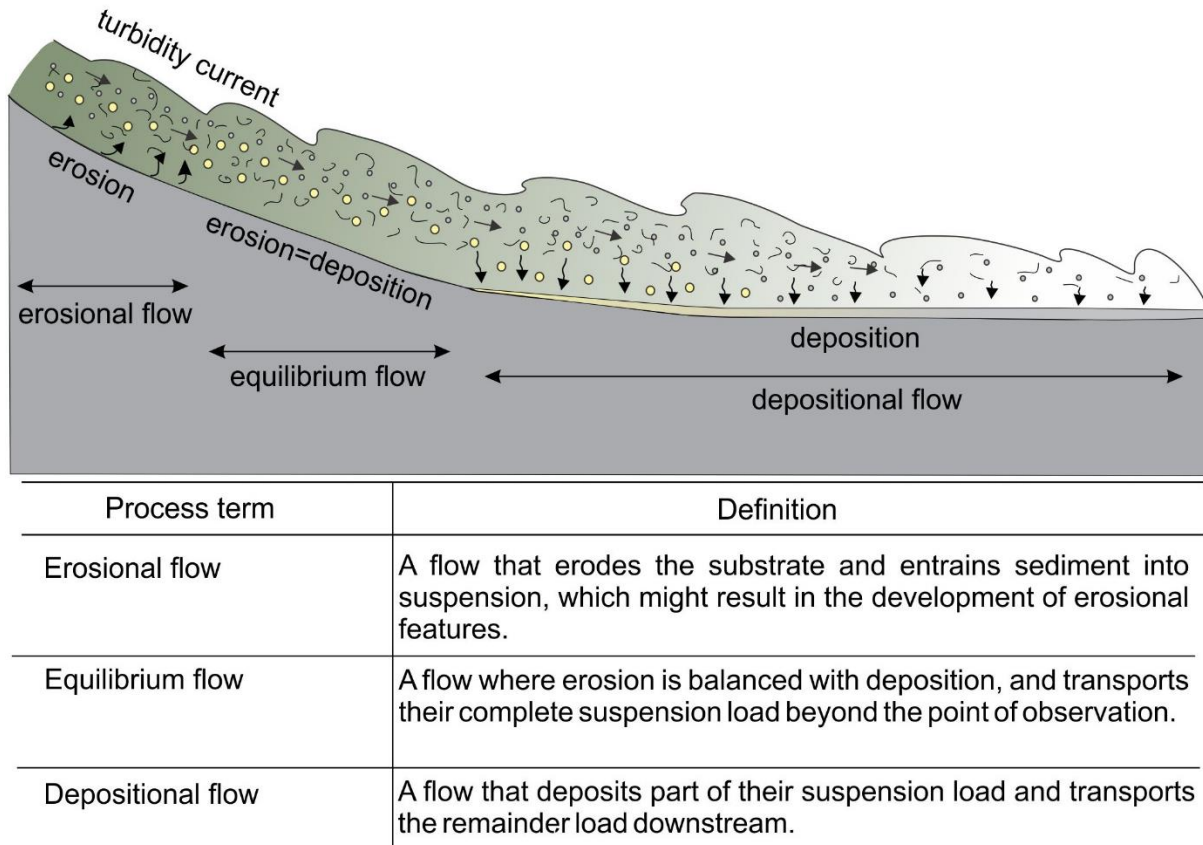


Figure 3.1 Process terminology used in this study for a channelized turbidity current.

3.3 Geological setting

The study area represents a growing subduction wedge on and offshore of the eastern margin of the North Island, New Zealand. The formation of the margin is the result of collision and oblique subduction of the Pacific Plate below the Australian Plate (Figure 3.2) (Ballance, 1976; Lewis and Bennett, 1985; Davey et al., 1986; Lewis and Pettinga, 1993; Nicol et al., 2007; Bland et al., 2015). The basin is limited to the east by the Hikurangi subduction trench and to the west by the axial ranges of the North Island (Ballance, 1976; Pettinga, 1982; Chanier and Ferriere, 1991; Nicol et al., 2007). The basin is dominated by NE-SW striking thrust faulting, sub-parallel to the trench axis (Lewis and Pettinga, 1993) and is divided into inner, mid and outer structural domains, each of which displays distinct deformation styles (Figure 3.2; McArthur et al., 2020a).

Hikurangi Margin subduction initiated in the late Oligocene, at c. 25 Ma (Ballance, 1976; Chanier and Ferriere, 1991; Nicol et al., 2007; Reyners, 2013); this convergence has created a series of elongate growth structures and trench-slope sub-basins, typically tens of kilometers long by kilometers wide (Lewis and Pettinga, 1993; Barnes et al., 2010; Bailleul et al., 2013; McArthur et al., 2020a). Continued compression to the present day has resulted in uplift and exhumation of the innermost trench-slope

sub-basins, which are exposed at outcrop (Bailleul et al., 2007), whilst the majority of the wedge remains submerged (Barnes et al., 2010). Therefore, the basin predominantly experienced marine conditions during the Neogene, with widespread deposition of mudstone and sandstone turbidites within bathymetric lows (Bailleul et al., 2007; Burgreen-Chan et al., 2016), whilst submarine canyons and channels incised ridges, acting as sediment conduits between sub-basins (McArthur and McCaffrey, 2019).

The present-day turbidite systems in the margin dominantly transport very-fine sand and silt (Barnes and Audru, 1999; Lewis and Pantin, 2002; Mountjoy et al., 2009; Wallace et al., 2019). The sedimentation rates, character of sedimentary pathways and subsequent fill of sub-basins varies throughout the subduction wedge, where a range of channels and submarine canyons are observed (Mountjoy et al., 2009; Bailleul et al., 2013; McArthur and McCaffrey, 2019). Channels in the northern and southern parts of the wedge potentially connect with the Hikurangi Channel (Figure 3.2) (Mountjoy et al., 2009). Channels in the central zone terminate in the mid-portion of the wedge delivering sediment to mid and outer trench-slope sub-basins (McArthur and McCaffrey, 2019). This variation in sediment distribution systems has been interpreted to result partly from the development of high-angle thrust faults forming steeper ridges in the northern and southern zones of the basin (McArthur et al., 2019). Other sediment transport processes in the basin include debris flows (Mountjoy and Micallef, 2012; McArthur et al., 2020a) and contour currents (Carter et al., 1996, 2004; Bailey et al., 2021), together with hemipelagic fallout.

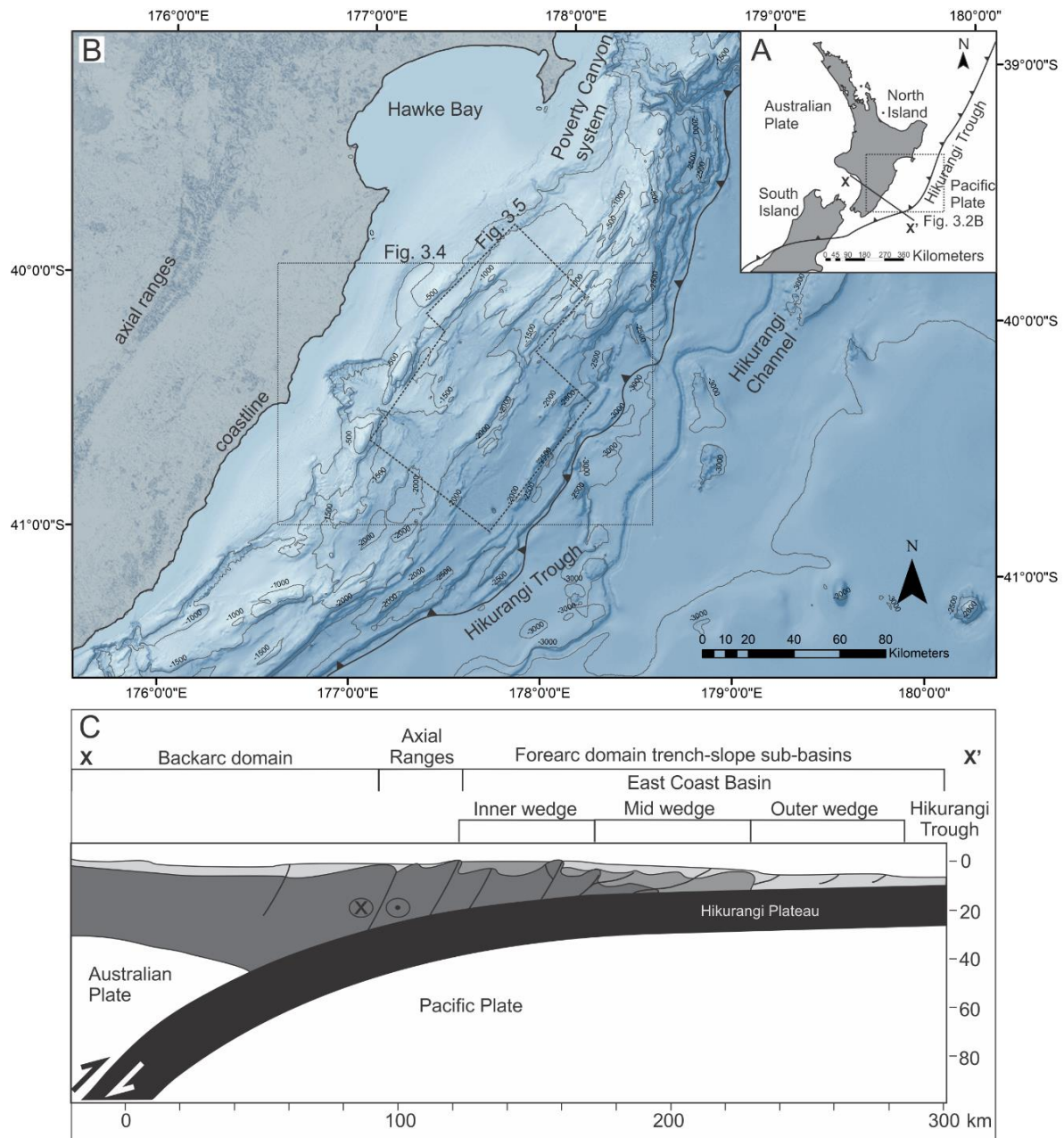


Figure 3.2 Study area. (A) The Hikurangi Margin is located on and offshore of the North Island, New Zealand and is limited to the east by the Hikurangi Trough and to the west by the axial ranges. (B) Offshore bathymetry map and bathymetric contours (500 m) of the study area (courtesy of the National Institute of Water and Atmospheric Research, New Zealand). (C) Regional cross-section across the Hikurangi subduction complex (after Nicol et al., 2007).

3.4 Methods

3.4.1 Datasets and morphological analysis

Bathymetric data of the Hikurangi Margin with a horizontal resolution of 100 m (provided by the National Institute of Water and Atmospheric Research, New Zealand)

were used to calculate the channel thalweg, and channel dimensions in the Madden and Omakere channels. Palm et al. (2021) showed using a statistical analysis of the horizontal errors in bathymetry datasets with 50 m and 100 m horizontal resolution that the latter is solid to undertake a morphological analysis and morphometrics extraction in submarine channels. The calculations were conducted using the Topotoolbox program in MATLAB, which enables landscape and drainage analysis of digital elevation models (Schwanghart and Kuhn, 2010). The channel thalwegs were calculated from landscape drainage and the bathymetric profiles were used to calculate the thalweg down-slope gradient (S).

Channel dimensions were measured from channel cross-sectional profiles as represented in Figure 3.3. The cross-sections in each channel were taken perpendicular to the channel thalweg approximately every 2 km downstream. In levee-bound channel sections, the mean channel height (\bar{H}) was calculated from the maximum (H) and minimum (h) levee crest heights, which represent the relief between the channel thalweg and the channel flank top (Figure 3.3). In sections where the channels were fully or partially ridge-confined, the erosional rim was used as a proxy for flow height and for the calculation of H , h and \bar{H} .

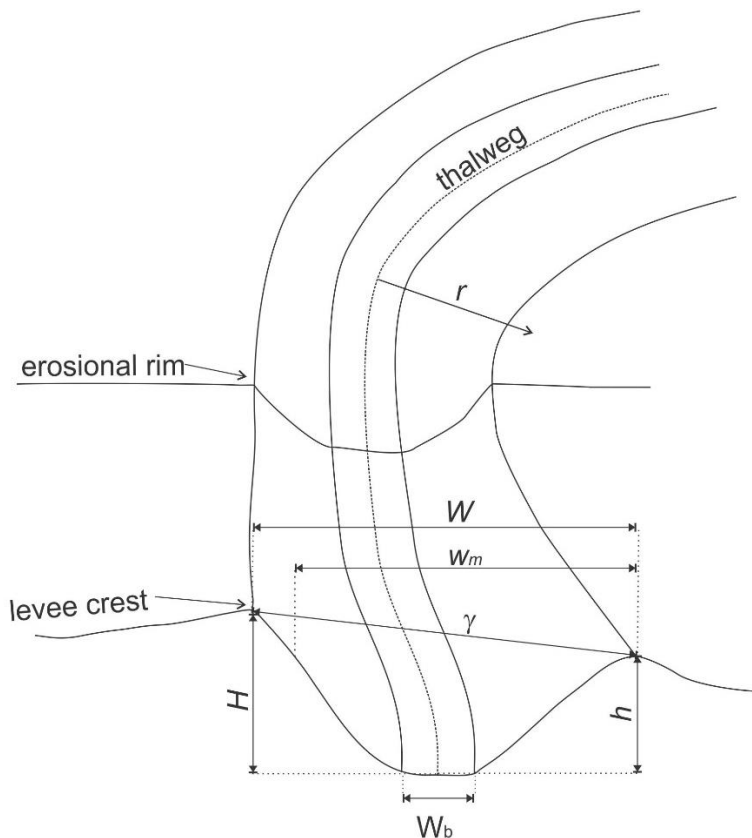


Figure 3.3 Sketch showing the morphometric parameters measured at channel bends, levee-bound channel cross-sections and erosional channel cross-sections of the Madden and Omakere channels.

The maximum channel width (W) represents the horizontal distance between the higher levee crest and the lower levee crest, whereas the minimum channel width (w_m) is the horizontal distance between the lower levee crest and the opposite channel wall. The mean channel width (\bar{W}) was calculated from the maximum (W) and minimum (w_m) channel widths (Figure 3.3). The width of the channel floor (W_b) (Figure 3.3) was measured perpendicular to the channel axis. The cross-channel slope (γ) was calculated from the horizontal (W) and vertical difference ($H - h$) of the levee crests or erosional rims, $\gamma = (H - h)/W$. The channel cross-sectional area (A) was calculated using Equation (3.1). The thalweg radius of curvature (r) (Figure 3.3; cf. Keevil et al., 2007) was measured at each channel bend.

$$A = \frac{W_b + W_m}{2} h + \frac{W_m}{2} (H - h). \quad (3.1)$$

The canyon-confined portion of the Madden Channel (Figure 3.4) was omitted in the analysis because estimates of the width and vertical channel relief do not permit estimation of flow properties where traversing flows are unlikely to overtop the erosional confinement (see below).

A 3D pre-stacked depth-migrated seismic dataset (acquired at broadband frequency in 2017) provided by WesternGeco Multiclient was used to map and generate the seafloor dip map using Schlumberger's Petrel© E&P software (Figure 3.5), and the root mean square (RMS) amplitude map of the shallow subsurface (<50 m). The dataset has an inline (NW-SE) spacing of 25 m and crossline (SW-NE) spacing of 12.5 m and a vertical resolution of 6.7 m. The vertical resolution was approximated through the calculation of the tuning thickness (Widess, 1973), using a wavenumber of 0.037m^{-1} calculated from the instantaneous frequency attribute map of the seafloor.

3.4.2 Turbidity current modelling

Downstream flow velocities and sediment concentration in the Madden and Omakere channels were calculated using the surface-slope equation from Komar (1969), and the relationship between the bed slope, densimetric Froude number and bed friction coefficient (Parker et al. 1987; Abad et al., 2011) that balances the gravitational force and drag force at the bed.

The surface-slope equation describes the balance of the Coriolis force, the centrifugal force produced at channel bends and the pressure gradient in a turbidity current assuming a bankfull flow (Komar, 1969), which can be used to reconstruct the flow properties of turbidity currents (e.g. Bowen et al., 1984; Klaucke et al., 1997; Pirmez and Imran, 2003; Stevenson et al., 2018). In clockwise flows in the Southern Hemisphere, the centrifugal and Coriolis forces are oriented towards the outer bank,

causing preferential overspill and cross-sectional channel relief asymmetry, where the left-hand side bank is higher (looking in a downstream direction) (Cossu and Wells, 2010; Dorrell et al., 2013a); whereas in anticlockwise flows, the forces are opposed. At high latitudes, in straight channel sections, cross-sectional channel asymmetry arises in the absence of centrifugal forces, due to Coriolis force alone (Cossu et al., 2010). The cross-channel slope (γ in Figure 3.3) is then used as a proxy of the superelevation of the boundary between the flow and the ambient fluid (Komar, 1969).

The momentum balance of the pressure gradient force, the Coriolis force and the centrifugal force across the channel (Komar, 1969; Stacey and Bowen, 1988a; Wells and Cossu, 2013) can be written as,

$$gRC\gamma = \pm fU + \frac{U^2}{r}, \quad (3.2)$$

where $g = 9.81 \text{ m/s}^2$ gravity; $R = \left(\frac{\rho_s}{\rho_f} - 1\right)$ is the submerged specific gravity (where $\rho_s = 2650 \text{ kg/m}^3$ is the density of quartz for the material in suspension, and $\rho_f = 1000 \text{ kg/m}^3$ is the density of the fluid); C , the bulk sediment concentration (vol./vol.); $\gamma = (H - h)/W$, the cross-channel slope (m/m); f , the Coriolis acceleration $f = 2\Omega \sin\theta$, where $-f$ for clockwise flows and $+f$ for anticlockwise flows, Ω is the Earth's rotation rate, and θ the latitude (values for $\theta = -40.5^\circ$ to -40.7° in the Madden Channel and -40.3° to -40.4° in the Omakere Channel); U , the downstream flow velocity in m/s; and r , the thalweg radius of curvature (m), in straight channel sections $r \rightarrow \infty$.

Equation (3.2) can be rewritten in terms of the Froude number, Fr , (Cossu and Wells, 2010; Wells and Dorrell, 2021) where $Fr = U/\sqrt{gRC\bar{H}}$ (Parker et al. 1987),

$$\gamma = Fr^2 \left(\frac{\pm f\bar{H}}{Fr\sqrt{gRC\bar{H}}} + \frac{\bar{H}}{r} \right), \quad (3.3)$$

where \bar{H} is the mean flow depth (m).

Further, using the model of Parker et al. (1987) which balances gravitational driving force with frictional drag at the bed, and through the entrainment of ambient water (e.g. Abad et al. 2011),

$$S = \frac{C_d + e_w \left(1 + \frac{Ri}{2}\right)}{Ri}, \quad (3.4)$$

where S is the calculated down-channel slope in m/m; $C_d = 0.0025$ (Abad et al., 2011; Konsoer et al., 2013), the drag coefficient, which is considered constant in the downstream direction for the calculated flows; Ri , the bulk Richardson number (which scales inversely with Fr^2 (Wells and Dorrell, 2020) which is a measure of mixing of the flow-ambient fluid interface (Parker et al., 1987; Abad et al., 2011),

$$Ri = \frac{gRC\bar{H}}{U^2} = \frac{1}{Fr^2}, \quad (3.5)$$

and e_w , the ambient water entrainment by mixing is parameterized using

$$e_w = \frac{0.00153}{0.0204 + Ri'} \quad (3.6)$$

a relation empirically derived by Parker et al. (1987) for turbidity currents.

A MATLAB script was written from scratch to model turbidity current properties using the founding Equations (3.3) to (3.10) (Appendix D). The script was developed to use a non-linear least squares MATLAB solver, *lsqnonlin*, to find solutions of C and Fr . Non-linear least squares is a numerical data-fitting technique that finds the optimal solution of unknown parameters for a given set of equations in an iterative process that minimizes the sum of squares (Dennis, 1977). A test of the nonlinear MATLAB solvers *fsolve* with the trust-region-dogleg algorithm (Powell, 1970), *lsqnonlin* with the Levenber-Marquardt (Moré, 1978) and the trust-region-reflective (Coleman and Li, 1996) algorithms showed that solutions converged to the same global minimum regardless of the algorithm of choice and starting point of the iterative process. Therefore, the non-linear least square solver (*lsqnonlin*) using the trust-region-reflective algorithm (Coleman and Li, 1996), with a tolerance point of 10^{-12} was used in this study.

Fr values were then used to calculate downstream flow velocities U in m/s using Equation (3.7) (Parker et al., 1987; Abad et al., 2011). The shear velocity u^* was calculated in m/s via Equation (3.8) (Parker et al., 1987; Abad et al., 2011); the flow discharge Q in m^3/s was calculated through Equation (3.9) and sediment discharge Q_s in kg/s with Equation (3.10) using the derived sediment concentration C :

$$U = Fr \sqrt{gRC\bar{H}}, \quad (3.7)$$

$$u^* = \sqrt{C_d} U, \quad (3.8)$$

$$Q = UA, \quad (3.9)$$

$$Q_s = QC. \quad (3.10)$$

The use of non-linear least squares analysis allows for improved estimations of bulk turbidity currents properties compared to previous work, where analyses do not jointly solve for Coriolis, gravitational and drag forces at straight channel sections and channel bends (e.g., Komar, 1969; Bowen et al., 1984; Pirmez and Imran, 2003; Stevenson et al., 2018).

The mean flow depth and bulk sediment concentration derived from this analysis were used as inputs into the sediment transport model to estimate the threshold between net sediment erosion and net deposition of turbidity currents.

3.4.3 Modelling of the net erosion and net deposition threshold for turbidity currents

A MATLAB script of the Flow-Power Flux-Balance type model developed by Dorrell et al. (2018) was used to model the threshold of erosion and deposition for the turbidity current conditions estimated for the Madden and Omakere channels. The model makes at-a-point predictions, and does not forward model the evolution of the currents nor the downdip transport of sediment in suspension (i.e. carried from source or eroded). In this analysis the average flow depths and sediment concentrations, calculated at each channel section from the surface-slope equation, were used to constrain the current hydrodynamics. The model incorporates the bulk capacity (maximum amount of sediment that can be transported in suspension by a turbulent flow), competence (particle class specific capacity) (Dorrell et al., 2013b), using a polydisperse description of sediment suspension. It has been shown that this model outperforms other particle laden flow models and is consistent with experimental and natural data (Dorrell et al., 2018; Amy and Dorrell, 2021).

For each particle class the threshold between a net erosional and a depositional flow is given by

$$\frac{C_i^-}{C_m} E_i = C_i^+ w_{si} \forall i, \quad (3.11)$$

where the total concentration of sediments at the bed is

$$\sum_{i=1}^N C_i^- = C_m, \quad (3.12)$$

where C_i^- is the grain size class concentration in the active layer of the bed that freely exchanges material with material transported as suspended load (Dorrell et al., 2013b), C_m is the packing concentration, C_i^+ is the grain size class concentration at the bed and w_{si} the particle settling velocity for each grain size class. Further, the description of the vertical distribution of suspended sediment concentration was determined by the mass conservation equation

$$w_s C_i(Z) = -k_s \frac{dC_i(Z)}{dZ}, \quad (3.13)$$

where $Z = z/L$ is the dimensionless flow depth, $k_s = ku^* L f(Z)$ is the eddy diffusivity which was assumed constant, therefore the flow length scale $L = \bar{H}/6$, and the Rouse number is defined by $\beta = 6 \frac{W_{si}}{ku_i^*}$ (Dorrell and Hogg, 2012), $k=0.4$ is the von Kármán constant; thus, the diffusion profile is given by

$$C_i(Z) = C_i^+ \left(\frac{1-e^{-\beta}}{\beta} \right). \quad (3.14)$$

The model incorporates a sediment entrainment function in which the power required to move sediment and incorporate it into suspension is proportional to the depth-averaged flow power:

$$E_i = \varepsilon \rho_f (gR\bar{H})^{-1} \Delta u_i^{*3}, \quad (3.15)$$

where $\varepsilon = 13.2$ (Dorrell et al., 2018) is an empirical parameter describing entrainment efficiency.

The characteristic grain size classes (d_{50}) used to solve Equation (3.11) to Equation (3.15) range from $\phi = 8$ to $\phi = -2$ (Wentworth scale; i.e., very fine silt to gravel). A log normal distribution derived from empirical data (Dorrell et al., 2018) was used to model grain size distribution, where a standard deviation $\sigma = 0$ represents a monodisperse suspension, a standard deviation $\sigma = 0.5$ is equivalent to a polydisperse suspension that is well-sorted (Folk, 1966) and a standard deviation $\sigma = 2$ is equivalent to one that is poorly-sorted (Folk, 1966). The slope gradient required to maintain equilibrium conditions for a given grain size and grain size distribution was calculated through Equation (3.4) and presented in m/m and degrees. Then, the slope values in m/m calculated for each down-channel section were plotted in the net erosion-deposition threshold plots.

3.5 Results

3.5.1 Madden canyon – channel morphology

The Madden Canyon is located downstream of the Madden Sub-basin where it incises the Madden Banks at water depths of ~1400 m. (Figure 3.4). The Madden Canyon has been classified as being detached from direct hinterland supply (McArthur and McCaffrey, 2019). The canyon head exhibits a funnel shape measuring ~9 km wide and exhibiting a V-shape morphology (Figure 3.4A and Figure 3.4B, cross section A1). Channel morphometrics can be found in Appendix A.1.

Given the changes in channel morphology and flow characteristics, the following division was established for the Madden Canyon - Channel:

- 1) The canyon-confined portion of the channel (not included in the turbidity current modelling, see methods) initiates from the Madden Banks breach-point (~1500 m water depth) to ~7 km downstream (~1800 m water depth) (Figure 3.4A and Figure 3.6A). A series of crescentic bedforms stepping basinward, and the steepest gradients of up to 3° are found in this section (Figure 3.5).
- 2) The upper reaches of the channel (~35 km long) (cross section A2, Figure 3.4B) comprise an area with an erosional terrace on the left bank (looking

downstream), characterized by slide scars of mass failures from over steepened walls (Figure 3.5), and a structurally confined levee on the right bank (Figure 3.5B). Sediment waves migrating in a SSW direction perpendicular to the channel thalweg are present on the outer external levees (cf. Hansen et al., 2015) and terraces have formed likely due to the inward collapse of the external levees (inset in Figure 3.5B). Knickpoints are observed in the canyon-confined portion as the channel crosses the axis of a tectonic fold and at the beginning of the upper reaches (Figure 3.5B). The average channel height in the upper reaches is 380 m (Figure 3.6B), the average channel width and area are 9.2 km and 1,899 km² respectively (Figure 3.6C). Slope gradients in this section increase and decrease downstream, ranging from 2° to 0.04° (Figure 3.6 A).

- 3) The Madden Channel - Porangahau section (~10 km long) comprises the area where the channel crosses the Porangahau Trough (cross-section A3, Figure 3.4B). Sediment waves are observed on the outer external levees of the right bank, migrating in a SSW direction perpendicular to the channel thalweg. On the left bank, sediment waves are also developed trending in a NNE direction. The levees have lower relief than those observed upstream in the upper reaches. Scours are present downstream on the channel floor (Figure 3.5B). Channel heights (average channel height is 31 m), widths (average is 3.11 km) and area (57.7 km²) are lower compared to the channel upper reaches (Figure 3.6B and Figure 3.6B). Slope gradients are gentler, ranging from 0.02° to 0.04° (Figure 3.6A).
- 4) The lower channel reaches (~20 km long) comprise the transect of the sub-basin between the Porangahau Ridge and the start of the Akitio Trough (cross section A4 and A5, Figure 3.4B). In this area, the channel is diverted by a growth ridge (cf. Clark and Cartwright, 2009), changing briefly to a trough-axial flow direction and limiting the left levee development (Figure 3.5B). Sediment waves are developed in the outer right levee where the channel is diverted by the ridge structure (Figure 3.5B). Then the channel changes its course again to resume a transverse orientation towards the Akitio Trough (Figure 3.5B). The average channel height in this section is 16 m, average width of 1.31 km and area of 17.1 km² (Figure 3.6B and Figure 3.6C). The slope gradients in the lower reaches also has recurring steep slopes (2°, 1.2°) followed by more gentle slopes as in the upper reaches (Figure 3.6A).
- 5) The Madden Channel terminates in the Akitio Trough, which exhibits a uniform surface (cross section A6, Figure 3.4B) with local emplacement of mass failure

deposits (Figure 3.5B). The lowest gradient of 0.01° is in this section (Figure 3.6A).

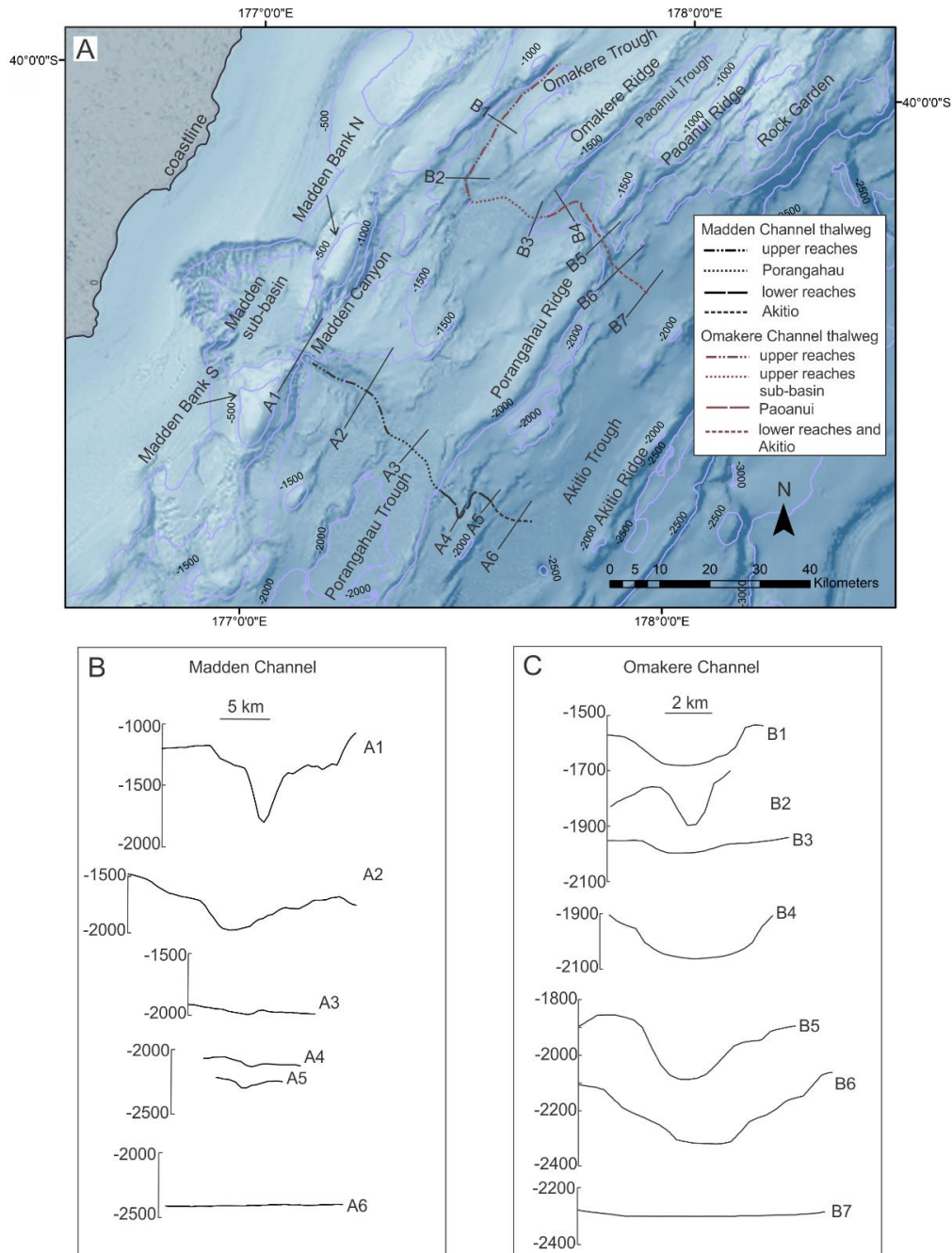


Figure 3.4 (A) The bathymetry map and bathymetric contours (500 m) courtesy of NIWA, show the Madden Channel and Omakere Channel systems. The channel thalweg line styles differentiate the sub-channel sections described in this study. (B) Selected cross-sectional profiles (with orientation looking downstream) of the Madden Channel highlighting the down-channel evolution from the canyon-confined portion (transect A1) to the Akitio Trough (transect A6). Transect location shown in A. (C) Selected cross-sectional profiles of the Omakere Channel from the channel upper reaches (transect B1) to the northern Akitio Trough (transect B7).

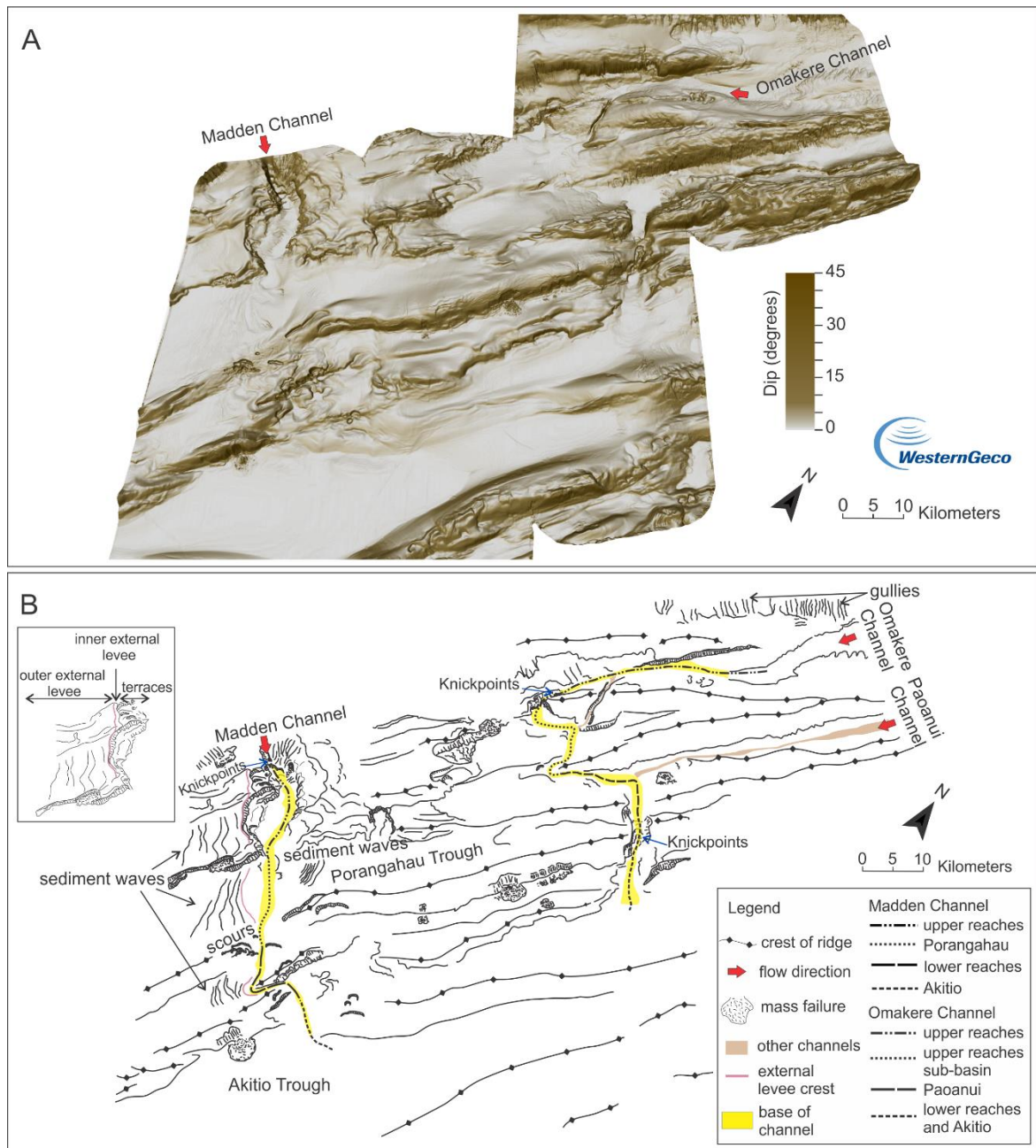


Figure 3.5 (A) Seafloor dip map of the Madden and Omakere channels derived from 3D seismic data provided by WesternGeco Multiclient. (B) Interpreted seafloor dip map showing morphological features of the channels resulted from tectonic and sedimentary processes. The interpretation of the crests of thrust-faulted bathymetric ridges is derived from Barnes et al. (2010).

3.5.2 Modelled turbidity current conditions in the Madden channel

The results from the turbidity current modelling in the Madden Channel are shown in Figure 3.6. The flow velocity and shear velocity in the upper reaches of the channel show the highest values fluctuating from 8-12 m/s (Figure 3.6D) and 0.4-0.6 m/s (Figure 3.6F), respectively. A drop in flow velocity to 3 m/s is observed at ~22 km decreasing gradually to 1.7 m/s in the last section of the upper reaches, then to 0.7

m/s in the Porangahau section and finally there is an increase up to 3.8 m/s in the lower reaches (Figure 3.6D). The calculated velocities are within the ranges of current velocities calculated from cable breaks and measured at submarine canyon systems (0.02 m/s - 19 m/s) (Talling et al., 2013). Fr numbers from 2 to 1.2 downstream of the upper reaches indicate super-critical flow conditions, which transition to sub-critical flow averaging 0.35. Flow deceleration and Fr values at this transition may indicate the development of an internal hydraulic jump causing suspension and mixing near the bed which allows sediment transport down-channel (Dorrell et al., 2016). The shear velocity decreases downstream to 0.15 m/s and 0.03 m/s in the upper reaches and Porangahau sections, respectively. Then, a slight increase in flow velocity (up to 4 m/s) and shear velocity (up to 0.2 m/s) occurs at ~48 km downstream in the lower reaches section. Supercritical flow conditions with Fr numbers from 1.9 to 1.6 prevail at the lower reaches as the channel passes through a steep area of structural confinement.

The calculated bulk sediment concentrations exhibit less fluctuations in the upper reaches and Porangahau sections with average values of 0.0074 v/v (0.7%) and 0.008 v/v (0.8%) (Figure 3.6G), respectively. A peak of 0.017 v/v (1.7%) occurs in the lower reaches at ~54 km downstream, the average sediment concentration in this section is of 0.009 v/v (0.9%). The flow discharge and sediment discharge (Figure 3.6H) display decreasing and increasing trends that parallel those seen in the flow velocities and Froude number. The average flow discharge and sediment discharge values in the upper reaches of the Madden Channel are 1.33×10^7 m³/s and 1.04×10^8 kg/s, respectively. In the Porangahau section, the average values reduce to 5.25×10^4 m³/s and 4.46×10^5 kg/s. The average flow discharge reduces to 5.14×10^4 m³/s in the lower reaches but the sediment discharge depicts an increment to 5.53×10^5 kg/s, reflecting the higher sediment concentrations shown in the same section in Figure 3.6G. These calculated flow conditions allow us to investigate for erosion, equilibrium or deposition along the channel profile.

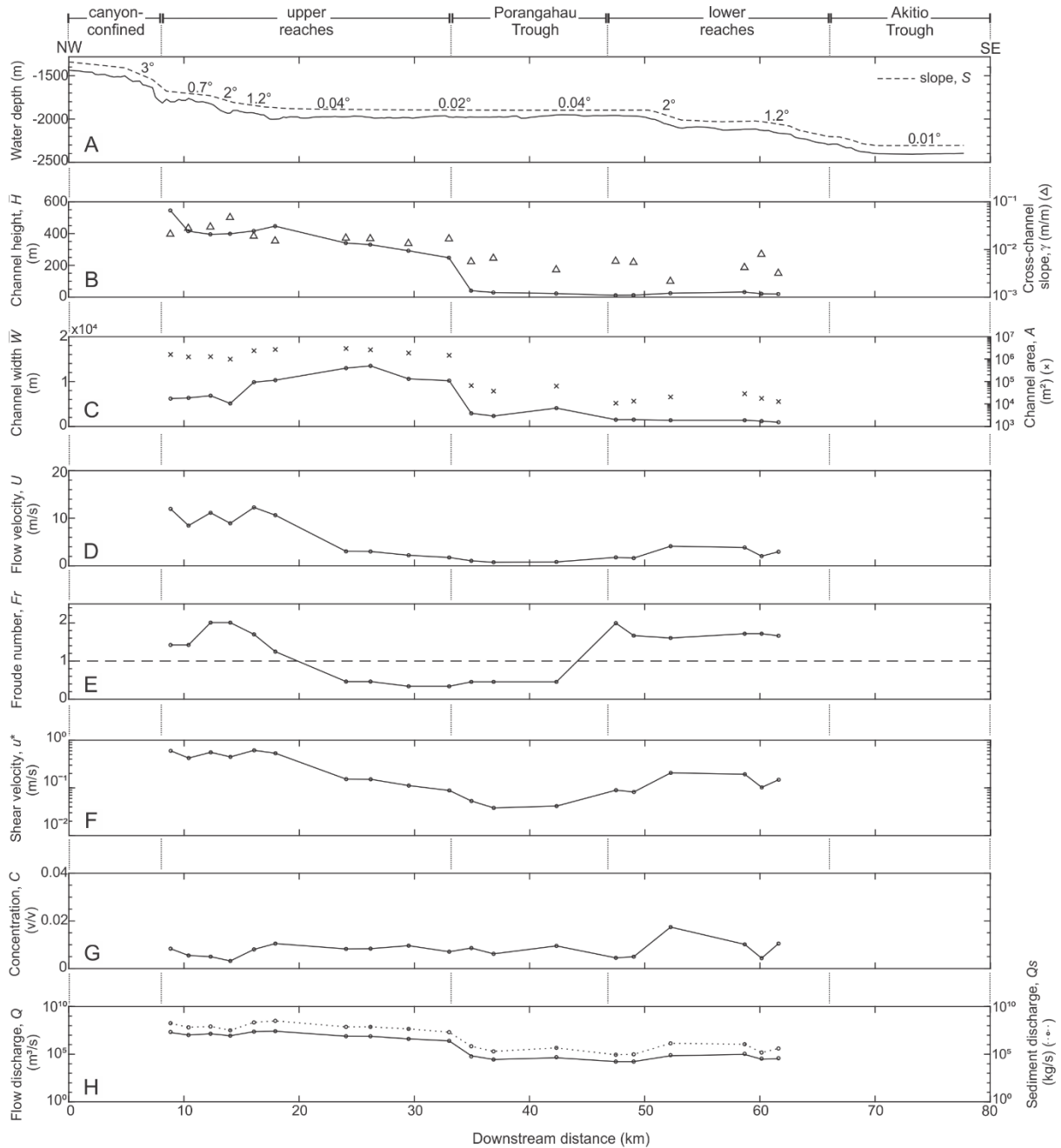


Figure 3.6 Calculated dimensions and turbidity current conditions in the Madden Channel from the upper reaches through the lower reaches section (sub-sections of the channel are shown at the top of the plots and differentiated with grey shading). (A) Channel thalweg depth profile (black solid line) and slope gradient profile (red dotted line) with values presented in degrees. (B) Average channel height profile (solid line) and cross-channel slope values (triangles). (C) Average channel width (solid line) and channel area (crosses). (D) Downstream turbidity current velocity profile. (E) Froude number profile, dashed line at 1 indicates the threshold between subcritical and supercritical flow. Downstream (F) shear velocity, (G) bulk sediment concentration, (H) flow discharge and sediment discharge profiles.

3.5.3 Omakere channel morphology

A series of gullies incising the shelf at ~70 km offshore Hawke Bay constitute conduits that feed the Omakere Channel (Figure 3.2). The Omakere Channel initiates as a trough axial channel in the Omakere Trough at ~1500 m water depth. It evolves into a transverse channel traversing troughs and eroding the Paoanui and Porangahau ridges and terminates in the Akitio Trough at ~2270 m water depth (Figure 3.4 and Figure 3.7A). Channel morphometrics can be found in Appendix A.2.

The following division is established for the Omakere Channel given its changes in morphology and flow characteristics:

- 1) The upper reaches of the Omakere Channel (~35 km long) initiate in the Omakere Trough and is confined by thrust-faulted NE-SW oriented ridges (Figure 3.4), which have limited the development of external levees. The channel exhibits a wide u-shape morphology in the first ~25 km (cross-section B1, Figure 3.4C), which evolves to a box-shape at the end of the upper reaches (cross-section B2, Figure 3.4C) likely due to down-channel tectonic confinement. Therefore, the channel area decreases from 552 km² to 57 km². Knickpoints developed in the most confined section (Figure 3.5B) before the channel is diverted into the upper reaches sub-basin. The average channel height in this section is 147 m, and average width of 3.96 km. There is a gentle slope of 0.09° followed by an increase up to 3° in the knickpoint area.
- 2) The section where Omakere Channel traverses the upper reaches sub-basin (~15 km long) starts as the channel is diverted to a NW-SE direction by the Omakere Ridge (Figure 3.4). The channel floor is smooth in this area. The average channel height decreases to 48 m due to loss of ridge-confinement as it enters the sub-basin and the average channel width increases to 6.14 km giving a wider U-shape morphology with subtle levee development (cross-section B3, Figure 3.4C). The slope gradient in this area is gentler (0.12°) and less variable compared to the upper reaches.
- 3) The Omakere Channel-Paoanui section (~21 km long) starts where the channel course is diverted into the Paoanui Trough and subsequently cross-cuts the Paoanui Ridge. The channel widens in the trough giving a U-shape (cross-section B4, Figure 3.4C), which narrows downslope as the channel height and ridge confinement increases (cross-section B5, Figure 3.4C). The average channel height and area are 190 m and 783 km², respectively. The slope gradient in this area increase with respect to the upper reaches sub-basin portion (Figure 3.7A).

- 4) The lower reaches and the Akitio sections of the Omakere Channel (~15 km long) comprise the area where the channel cross-cuts the northern portion of the Porangahau ridge and other downstream ridges to terminate in the northern portion of the Akitio Trough. A series of knickpoints are observed at the start of the lower reaches where the slope gradient is steep (2° , Figure 3.7A). The channel exhibits a box-shape as the channel widens due to loss of ridge confinement (cross-section B6, Figure 3.4C) and subsequently becomes unconfined in the Akitio Trough (cross-section B7, Figure 3.4C) where the slope decreases to 0.008° (Figure 3.7A).

3.5.4 Modelled turbidity current conditions in the Omakere channel

The flow velocity in the Omakere Channel decreases from 3.2 m/s average in the upper reaches to 1.8 m/s average velocity in the upper reaches sub-basin and increase downslope to 6.3 m/s in the Paoanui Trough, then to 12 m/s average in the lower reaches and drops to 0.6 m/s in the Akitio Trough (Figure 3.7D). As in the Madden Channel, the calculated velocity values for the Omakere Channel are within the ranges of current velocities observed at slope canyon systems (0.02 m/s - 19 m/s) (Talling et al., 2013). The shear velocity exhibits an average value of 0.09 m/s at the upper reaches sub-basin and peaks at 0.8 m/s in the lower reaches, followed by a decrease to 0.5 m/s as the flow reaches the Akitio Trough (Figure 3.7D). The flow is predominantly super-critical with phases of sub-critical flow at the start of the upper reaches and in the sub-basin, where slope gradients are gentler (Figure 3.7E).

The calculated bulk sediment concentration of the flow suggests more diluted flows at the upper reaches with average values of 0.004 v/v (0.4%), which increase down-channel in the Paoanui channel section and peaks at the lower reaches ~0.023 v/v (2.3%) (Figure 3.7G). As with the flow and shear velocities, the concentration drops in the Akitio Trough to ~0.003 v/v (0.3%). The flow and sediment discharge initiate with an average of 1.51×10^6 m³/s and 1.31×10^7 kg/s respectively in the upper reaches and increase down-channel to 3.98×10^6 m³/s and 7.87×10^7 kg/s (Figure 3.7H).

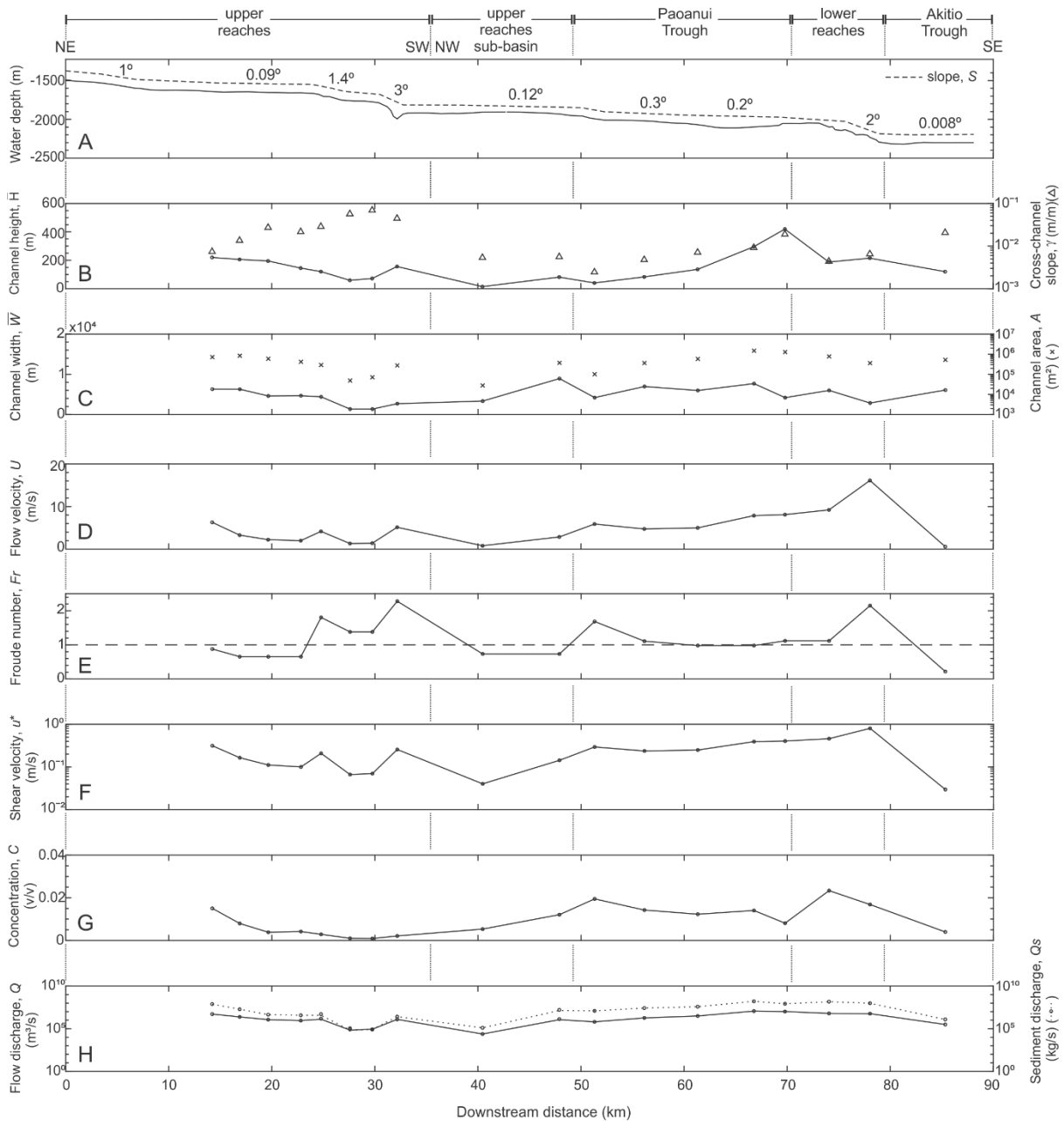


Figure 3.7 Calculated dimensions and turbidity current conditions in the Omakere Channel from the upper reaches through the Akitio Trough section (sub-sections of the channel are shown at the top of the plots and differentiated with blue shading). (A) Channel thalweg depth profile (black solid line) and slope gradient profile (white dotted line) with values presented in degrees. (B) Average channel height profile (solid line) and cross-channel slope values (triangles). (C) Average channel width (solid line) and channel area (crosses). (D) Downstream turbidity current velocity profile. (E) Froude number profile, dashed line at 1 indicates the threshold between subcritical and supercritical flow. Downstream (F) shear velocity, (G) bulk sediment concentration, (H) flow discharge and sediment discharge profiles.

3.5.5 Sediment bypass conditions in the Madden channel

3.5.5.1 Well-sorted flows

The thresholds for equilibrium conditions of the modelled flows traversing each channel section are shown from Figure 3.8A to Figure 3.8D. The contours represent the thresholds for well-sorted ($\sigma = 0.5$), moderately sorted ($\sigma = 1$) and poorly-sorted ($\sigma = 2$) sediment in suspension. For a given slope value (S), the grain sizes (ϕ) above a given threshold represent sediment bypass under erosional flow conditions and grain sizes below a given threshold represent deposition. Note that the variation in particle size distribution (log-normal standard deviation), flow height and down-slope channel gradient have an important effect on equilibrium.

The calculated flow of 380 m average height and 0.74% average sediment concentration traversing the steep slopes (2° , 1.2°) in the upper reaches (Figure 3.8A and Figure 3.8E) can transport grain size classes up to medium sand if they are suspended within a well-sorted flow ($\sigma = 0.5$). However, for the same flow conditions and sorting, the maximum grain size that can be maintained in suspension reduces to medium silt as the slope gradients become gentler in the upper reaches (0.04° , 0.2°). As the flow reaches the Porangahau section (Figure 3.8B and Figure 3.8E), the reduction in the average flow height to 31 m due to loss of flow confinement in the Porangahau Trough, and gentle slopes of 0.04° causes a reduction of the maximum grain size that can be transported in suspension to fine silt.

The steep slopes formed by the presence of the Porangahau Ridge at the start of the channel lower reaches cause an increase in the driving force of the flow, consequently increasing the flow velocity, shear velocity, bulk sediment concentration and discharge (Figure 3.6). These changes in flow suggest that down-channel erosion might occur. Although the sediment being eroded depends on the composition of the bed, it can be estimated that the maximum grain size class that can be transported in suspension is very fine sand, for the calculated flow conditions, assuming a well-sorted flow travelling through the lower reaches (positions 6 and 7 in Figure 3.8C and Figure 3.8D, respectively). The channel terminates in the Akitio Trough where flows become unconfined.

Although the flow conditions in the Akitio Trough could not be calculated in the absence of channels, from the slope values in the trough (0.01°) it is estimated that most of the grain size classes would become depositional except for the very fine silt (position 8, Figure 3.8D). Therefore, the maximum grain size that could be transported downstream by the modelled flows, from the upper reaches of the channel into the Akitio Trough, assuming a well-sorted sediment in suspension, is very fine silt.

3.5.5.2 Poorly-sorted flows

The equilibrium thresholds for poorly-sorted suspensions ($\sigma = 2$) occur at higher slope values for all grain size classes compared to flows carrying well-sorted suspensions ($\sigma = 0.5$). For the same flow conditions, the maximum grain size class that can be suspended in the flow and transported in the steep slopes (position 1, Figure 3.8A and Figure 3.8E) is very fine sand. However, it reduces to coarse silt (position 2, Figure 3.8A and Figure 3.8E), fine silt (position 3, Figure 3.8A and Figure 3.8E) and very fine silt (position 4, Figure 3.8A and Figure 3.8E) as the slope gradient decreases downstream.

As with the well-sorted case, the equilibrium threshold for poorly-sorted sediment in suspension in the Porangahau Trough suggest that all grain size classes would start to become depositional in this section (position 5, Figure 3.8B), partly due to the low slope gradients and the reduction in flow size. Slope gradients approximately above 0.1° would be required to keep the very fine sand in suspension.

The increase in flow, shear velocities and sediment flux at the start of the channel lower reaches suggest downstream erosion (Figure 3.6). When poorly-sorted material is eroded (assuming this characterizes the composition of the substrate), it can be estimated that the maximum grain size that can be kept in suspension is medium silt throughout the lower reaches (positions 6 to 8, Figure 3.8C and Figure 3.8D). Any sand-sized grains eroded would become depositional, limiting further transport into the Akitio Trough (Figure 3.8D).

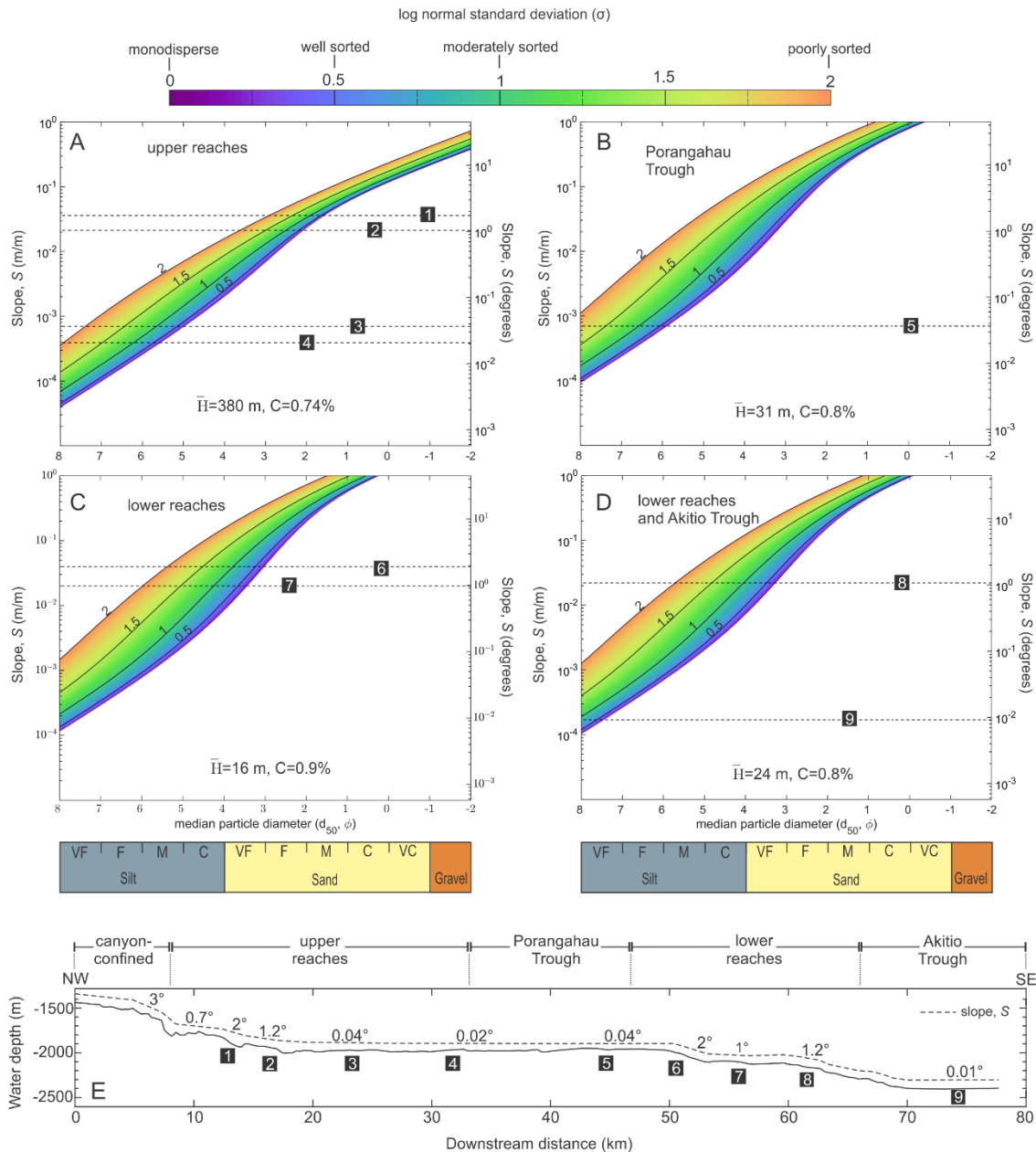


Figure 3.8 Plots showing the thresholds of equilibrium flow for the modelled turbidity current traversing each section of the Madden Channel. The thresholds vary from well-sorted ($\sigma = 0.5$) to poorly-sorted ($\sigma = 2$) sediment in suspension. For a given slope value (S), the grain sizes (ϕ) above a given threshold represent sediment bypass under erosional flow conditions and grain sizes below a given threshold represent deposition. The average flow height, \bar{H} , and average bulk sediment concentration, C , used for the calculation of the thresholds are shown in each plot for the (A) channel upper reaches (B) Porangahau Trough, (C) channel lower reaches and (D) channel lower reaches and Akitio Trough. (E) Channel thalweg depth profile. The numbers in black squares show the positions of the slope gradient values plotted in A-D.

3.5.6 Sediment bypass conditions in the Omakere channel

3.5.6.1 Well-sorted flows

The thresholds for equilibrium conditions of the modelled flows traversing each channel section are shown from Figure 3.9A to Figure 3.9D (see Well-sorted Flows section of the Madden Channel on how to interpret the plots). The flow conditions calculated at the upper reaches section, where slope gradients are gentle, show that the maximum grain size that can be kept in suspension is coarse silt (0.09° , position 1, Figure 3.9A). However, the maximum grain size increases downstream over the steep slopes at ~25-31 km (positions 2, and 3, Figure 3.9A) where the erosional flows can transport up to fine sand.

The increase in sediment concentration suggests an erosional flow down-channel from the upper reaches sub-basin (Figure 3.9B) to the lower reaches (Figure 3.9D), nevertheless, the different grain sizes that can be suspended within such erosional flows varies at each channel section due to the differences in flow height and variations in the slope gradient. As flows become less confined and smaller in the upper reaches sub-basin, the thresholds widen and the maximum grain size that can be maintained in suspension is coarse silt (position 4, Figure 3.9B). The slope gradient increases and maintains above 0.1° down-channel, flows increase in height in the Paoanui Trough (positions 5 and 6, Figure 3.9C) and the lower reaches (position 7, Figure 3.9D), therefore, the maximum grain size that can be suspended in these sections is fine sand.

As in the Madden Channel, the slope gradients in the Akitio Trough promote the deposition of most grain size classes (position 8, Figure 3.9D). Under well-sorted conditions, the maximum grain size that can be bypassed through the entire channel length and be deposited in the Akitio Trough is coarse silt.

3.5.6.2 Poorly-sorted flows

The thresholds for equilibrium flow conditions assuming poorly-sorted sediment in suspension ($\sigma = 2$) show that the maximum grain size class that can be transported through the upper reaches of the Omakere Channel is coarse silt (Figure 3.9A) which reduces to very fine silt in the upper reaches sub-basin (Figure 3.9B). Nevertheless, flows evolving downstream could transport larger grain sizes through erosional or equilibrium flows as they increase in height and sediment concentration. In the Paoanui Trough, the maximum grain size that can be kept in suspension is coarse silt (Figure 3.9C) which increases to fine sand over the steep slopes in the lower reaches (position 7, Figure 3.9D). All grain sizes are calculated to be deposited as flows enter the Akitio Trough (position 8, Figure 3.9D).

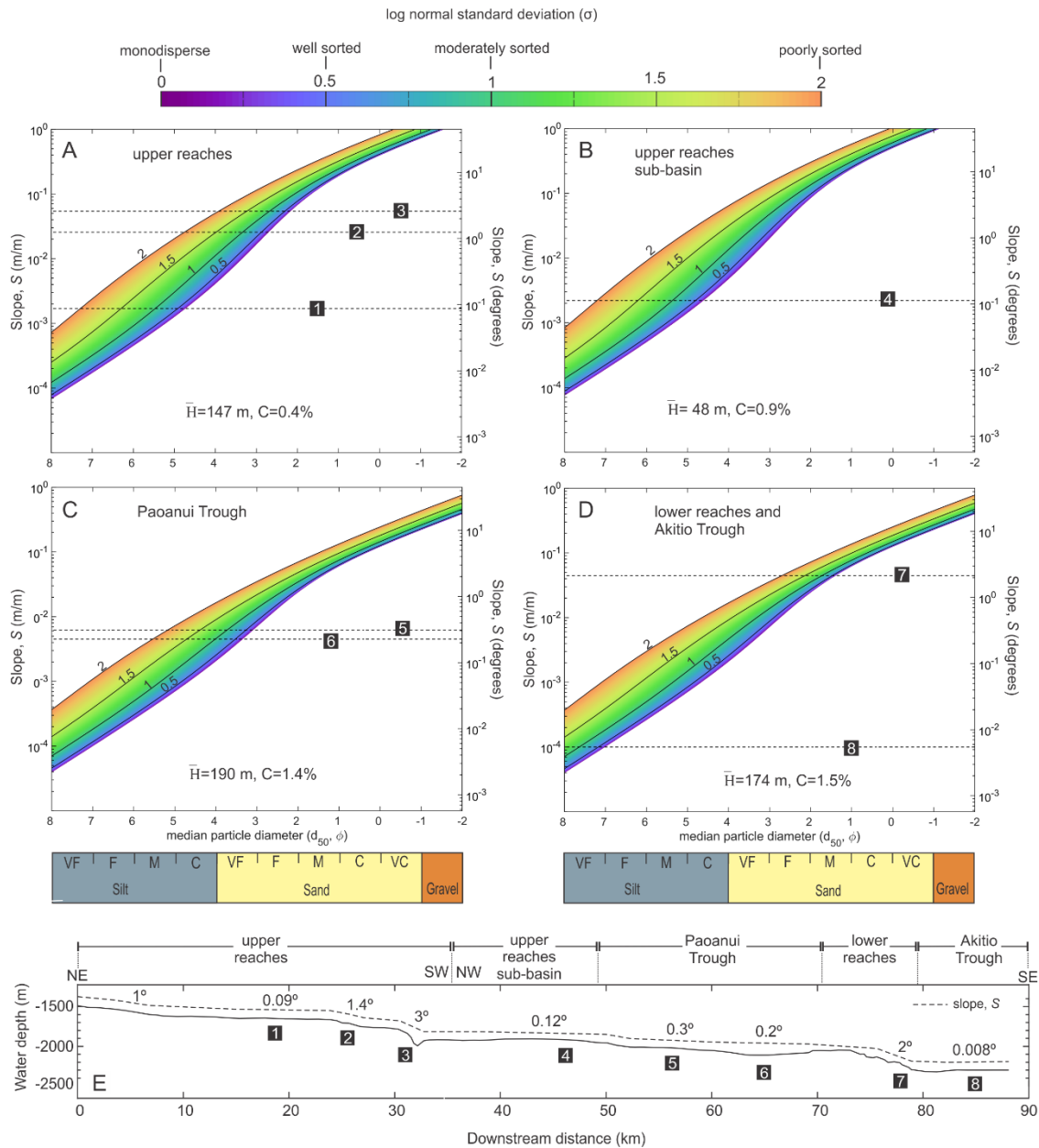


Figure 3.9 Plots showing the thresholds of equilibrium flow for the modelled turbidity current traversing the Omakere Channel. The thresholds vary from well-sorted ($\sigma = 0.5$) to poorly-sorted ($\sigma = 2$) sediment in suspension. For a given slope value (S), the grain sizes (ϕ) above a given threshold represent sediment bypass under erosional flow conditions and grain sizes below a given threshold represent deposition. The average flow height, \bar{H} , and average bulk sediment concentration, C , used for the calculation of the thresholds are shown in each plot for the (A) channel upper reaches (B) upper reaches sub-basin, (C) Paoanui Trough and (D) channel lower reaches and Akitio Trough. (E) Channel thalweg depth profile. The numbers in black squares show the positions of the slope gradient values plotted in A-D.

3.6 Discussion

3.6.1 Controls on sediment bypass and implications for sand distribution

Results here suggest that in order to achieve very fine sand bypass (or coarser grain sizes) by trough-axial flows into outboard troughs, shallow flows (< 50 m) require steeper gradients than thicker flows (> 140 m) under well-sorted and poorly-sorted conditions (Table 3.1). Furthermore, poorly-sorted flows require steeper gradients than well-sorted flows to achieve very fine sand (or coarser) bypass, given that wider particle size distributions promote vertical density stratification, hence, the magnitude of the shear stress in the flow must increase to maintain sediment in suspension and reach equilibrium (Dorrell et al., 2018). Therefore, the changes in the flow height, grain size distribution and slope gradient have an effect on the equilibrium thresholds for sediment bypass and on the distribution of sand in the channels (Figure 3.10).

Table 3.1 Slope gradient values required to bypass very fine sand for the flow properties calculated in the Madden and Omakere channels.

Flow height (m)	Slope gradient (°)		Bulk sediment concentration (%)
	<u>Well-sorted Flow</u> $\sigma = 0.5$	<u>Poorly-sorted Flow</u> $\sigma = 2$	
16	> 0.4	> 7	0.9
24	> 0.35	> 6	0.8
31	> 0.3	> 5	0.8
48	> 0.25	> 3	0.9
147	> 0.2	> 2.5	0.4
174	> 0.1	> 0.8	1.5
190	> 0.1	> 0.8	1.4
380	> 0.1	> 0.8	0.7

Assuming a well-sorted suspension of very fine sand and coarse silt, an equilibrium flow develops in the upper reaches of the Madden Channel, enhanced by thick flows and steep gradients. It may then become depositional as when reaching the

Porangahau Trough, an area of low confinement (hence the flow height reduces) and gentle slope gradients (Figure 3.10A). Therefore, very fine sand bypass into the lower reaches and Akitio Trough is limited and flows rely on erosion to entrain very fine sand into suspension, if available, to continue sediment transport downstream and deposit into the Akitio Trough (Figure 3.10C). Similarly, the very fine sand deposition in the Omakere Channel is more likely to occur in the Omakere Trough (upper reaches section of the channel) where, although flows are more confined than in the Porangahau section, it also constitutes an area of low gradient (Figure 3.10A). As in the Madden Channel, flows evolving downstream in the Omakere Channel must erode very fine sand in order to deposit it in the upper reaches sub-basin and Akitio Trough (Figure 3.10C).

Assuming a poorly-sorted suspension of very fine sand and very fine silt to medium silt, the wider grain size distribution promotes depositional flows with very fine sand deposition at the uppermost reaches of the Madden Channel and the Omakere Channel, and silt bypass down-channel (Figure 3.10B). If erosional flows entrain very fine sand, the smaller magnitude of the flows combined with a poorly-sorted suspension promote very fine sand deposition in the Madden and Omakere Channel sections as shown in Figure 3.10D. Therefore, only the finer silt fraction bypasses to the Akitio Trough.

The results are compared to the RMS amplitude map of the seafloor (Figure 3.10E), where high RMS amplitude responses indicative of high impedance contrast, are interpreted as sand-prone intervals, whereas low RMS amplitude responses indicate more homogeneous and finer-grained sediments (Hansen et al., 2017; McArthur et al., 2022b). The high RMS amplitude patterns indicate sandier deposits along the Madden and Omakere channel thalweg (Figure 3.10E), which are similar to the patterns projected for poorly-sorted flows that erode sand down-channel (Figure 3.10D). In the Madden Channel, higher RMS values along the channel thalweg are observed at the start of the upper reaches (Figure 3.10F), and in the lower reaches (Figure 3.10G) whereas low RMS values predominate in the Porangahau and Akitio Troughs. Furthermore, grain size analysis of drop cores in the Madden system have suggested poorly-sorted deposits from very fine silt to fine sand (McKeown, 2018). Drop core M1 located in the upper reaches (Figure 3.10E and 3.10F) records a series of poorly-sorted sediments, composed of interbedded very fine to coarse silt, silty fine sands and very fine sand beds (McKeown, 2018). Drop core M2 located in the Porangahau Trough (Figure 3.10E and 3.10F) also consists of poorly-sorted sediments, but only very fine to coarse silt beds were found here (McKeown, 2018). Sediments from drop core M3 located in the Akitio Trough (Figure 3.10E and 3.10G) are poorly-sorted, very fine to medium silt and sandy silt beds. Sediments of M1 and

M2 are in agreement with the deposits predicted from the model in the scenario shown in Figure 3.10D and the RMS amplitude map, suggesting these deposits might have been the product of poorly-sorted depositional flows with flow depths and bulk sediment concentrations comparable with the modelling. Samples were not available from the Omakere Channel, however RMS amplitude mapping can be used to examine our findings. Higher amplitude values are located in the upper reaches (Figure 3.10H), the Paoanui Trough (Figure 3.10I) and the lower reaches (Figure 3.10I), whereas lower amplitude values predominate in the upper reaches sub-basin and northern Akitio Trough, which shows good agreement with the patterns projected for poorly-sorted deposits in Figure 3.10D. Differences in the distribution of sand in the system might be due to other processes such as contour currents or bedload sediment transport which are not considered in the modelling.

The results show that flows can change from sand bypass to deposition depending on the characteristics of the turbidity current and that the bypass slope is not unique. Furthermore, the thresholds derived from this study might help constrain the conditions required to develop equilibrium flows over submarine slopes more generally. If a system has an up-dip slope of 0.25° , it would constitute a bypass slope for very fine sand when flows are approximately thicker than 140 m (Table 3.1) whereas, for the same slope gradient and flow thickness, sand would be deposited if poorly-sorted conditions prevail as they would require slope gradients above 0.8° to sustain bypass (Table 3.1). Thick flows (>140 m) with well-sorted sediment in suspension might aid the development of detached systems and possibly upslope pinch-outs, when up-dip slopes are above 0.1° . Poorly-sorted flows transporting sand might be depositional throughout the feeder channel, hence, either promoting the formation of attached systems or starved basins where only the finest grain sizes can be bypassed downstream, as observed in the studied channels (Figure 3.10).

The thresholds are dependent on the assumptions made on the modelling, therefore the thresholds for erosion, equilibrium and deposition might change for a different set of flow height and sediment concentration. However, the thresholds derived from these flow conditions might help guide and constrain interpretations of zones associated with equilibrium or depositional flows in study areas where the slope gradient, the grain size and grain size distribution are known such as in surface or subsurface deep-marine systems. Furthermore, this approach might allow us to predict areas of slope accommodation that may be starved or well supplied with sands and thus help constrain and predict sediment distributions.

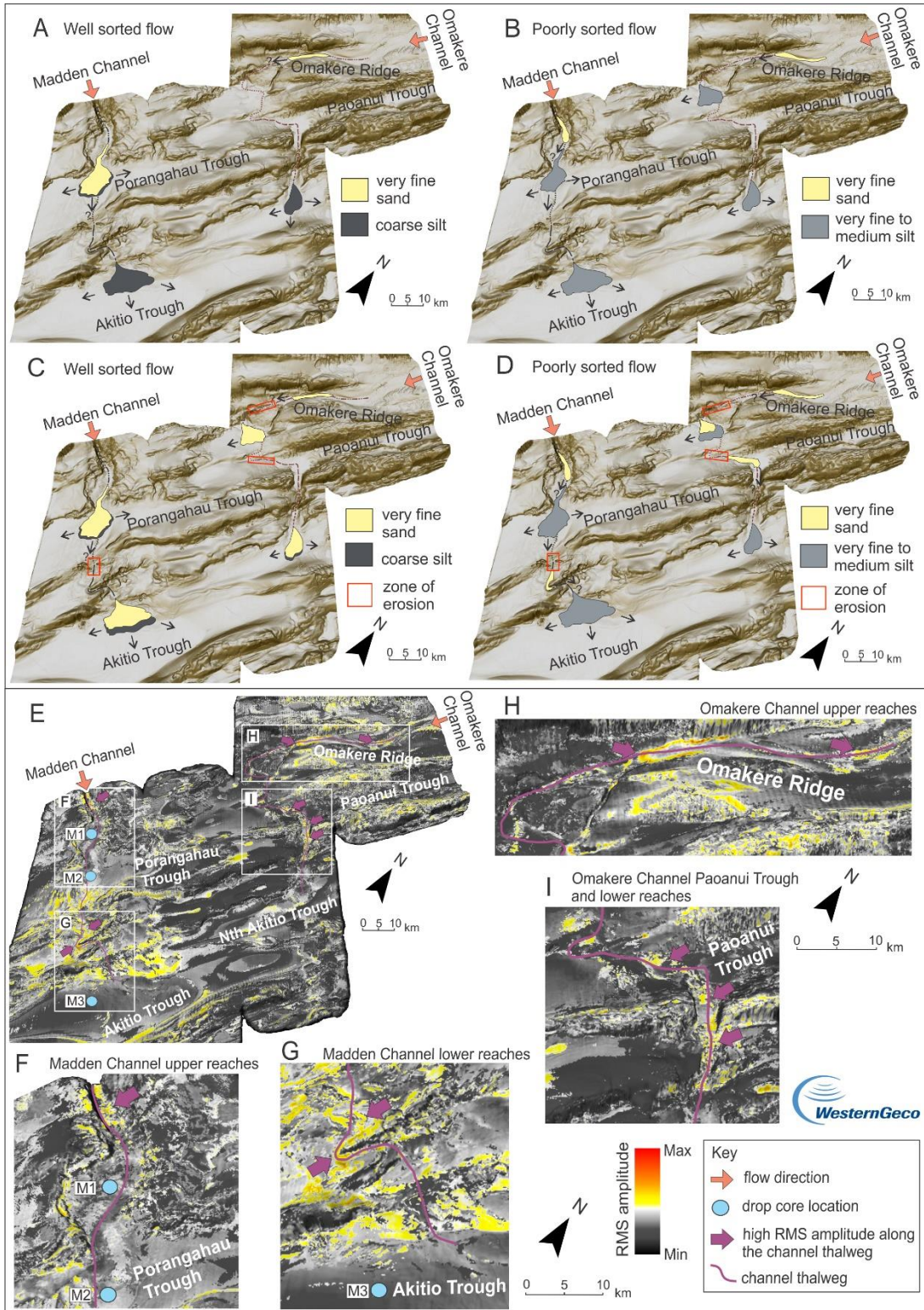


Figure 3.10 (A-D) Potential sand distribution maps of the Madden and Omakere Channel systems. The maps show the deposition from (A) a well-sorted turbidity current transporting very fine sand; (B) a poorly-sorted turbidity current transporting very fine sand and very fine sand to medium silt; (C) a well-sorted turbidity current transporting very fine sand and coarse silt, assuming downstream erosion of sand; (D) a poorly-sorted turbidity current transporting very fine sand and very fine sand to medium silt assuming downstream erosion of sand. (E) Root Mean Square (RMS) amplitude map of the seafloor with drop core locations M1-M3. High RMS amplitude values are interpreted to represent deposits with higher sand content. Low RMS amplitude responses are interpreted to represent soft homogeneous finer-grained deposits. Enlarged areas showing the RMS amplitude distribution of the (F) Madden Channel upper reaches and Porangahau sections, (G) Madden Channel lower reaches, (H) Omakere upper reaches and (I) Omakere Channel Paoanui and lower reaches sections.

3.7 Conclusions

Equilibrium thresholds were calculated to estimate sediment bypass in turbidity currents traversing the Madden and Omakere channels of the Hikurangi Margin using the surface-slope equation and Flow-Power Flux-Balance type model. This methodology allowed us to determine that sediment bypass in the channels is controlled by changes in the flow height (calculated from the channel morphology), by sediment sorting in the flow and by changes in the seafloor gradient. On this basis, maps for the potential distribution of very fine sand were derived, where deposits estimated from poorly-sorted flows show good agreement with the observations from the RMS amplitude map of the seafloor. The conditions required to achieve sand bypass derived from this study might serve to screen other flow pathways of the Hikurangi Margin and could be applied to other margins.

Chapter 4 Calculating deepwater palaeo-hydraulic conditions from subsurface channel architecture: a critical test using examples from the Hikurangi Margin, New Zealand

4.1 Abstract

Turbidity current modelling plays a key role in the understanding of submarine channel development. However, its subsurface applicability depends upon whether or not preserved channel-forms truly represent equilibrium palaeo-hydraulic conduits. Using high-resolution 3D seismic data, an offshore subsurface channel-form from the Hikurangi Margin, New Zealand was measured along a 32 km reach; up to ~65 m thick and ~883 m wide, it partly overlies a ~15 km long mass-transport deposit. To estimate the palaeo-hydraulic properties of traversing turbidity currents, the measured dimensions of the channel-form were used to condition a depth-averaged turbidity current model, capturing both transverse and down-channel forces. Assuming bankfull equilibrium conditions, the model yields plausible average flow sediment concentrations and downstream velocities of 0.04% and 0.44 m/s, respectively, with well-sorted sediment up to silt size capable of being suspended. At some bends, however, the modelled sediment concentrations exceed the 9% theoretical concentration limit for dilute turbidity currents; a steeper cross-channel slope than that derived from measured channel-form margin height differences is required for the concentrations to fall within this limit. The derivation of physically unrealistic flow properties might arise if the modelled channel-form is a compound channel, and therefore not a genuine hydraulic conduit. Additionally, if the channel was preserved at a point of immature evolution, or if its mass-transport deposit substrate prevented the development of an equilibrium channel morphology, the assumption of equilibrium conditions may fail. These new factors act in addition to previously recognized issues such as poor channel preservation or low seismic resolution in complicating palaeohydraulic analysis. Future studies should incorporate the effects of these additional factors on turbidite channel-forms in the subsurface. These factors may also impact palaeohydraulic studies in other terrestrial or planetary settings where compound channel forms may be developed or where equilibrium flow conditions cannot be assumed.

4.2 Introduction

Submarine channels are important conduits on the continental slope that convey sediment (Covault and Graham, 2010), organic carbon (Hage et al., 2020) and microplastics (Kane et al., 2020) from terrestrial and shallow marine environments into deeper water. Furthermore, many ancient channel systems constitute important hydrocarbon reservoirs (Mayall et al., 2006) or may be important for effective carbon capture storage (Marshall et al., 2016). The flow conditions of turbidity currents passing through these conduits, i.e., erosional vs. equilibrium vs. depositional, is an important control on the distribution of material downslope and on channel development and evolution (Pirmez and Imran, 2003; Hadler-Jacobsen et al., 2005; Stevenson et al., 2013; Dorrell et al., 2015).

Extensive research has been conducted to better understand channel inception, morphology and evolution using data from modern systems (Babonneau et al., 2010; Maier et al., 2013; Vendettuoli et al., 2019), subsurface examples (Deptuck et al., 2007; Cross et al., 2009; Tek et al., 2021) and those exposed at outcrop (Gardner et al., 2003; Hubbard et al., 2014; McArthur and McCaffrey, 2019). However, one of the greatest challenges is the difficulty of directly observing and measuring the processes that shape channels. Hydraulic modelling studies have advanced our understanding of the interplay between turbidity current activity and submarine channel development. Such models have been applied in theoretical settings (Das et al., 2004) and in modern channels (Abd El-Gawad et al., 2012; Covault et al., 2014; Dorrell et al., 2014; Crisóstomo-Figueroa et al., 2021); a limited number of studies has attempted to integrate morphological observations derived from seismic-reflection datasets with process modelling (e.g. Li and Gong, 2018; Li et al., 2018; Gong et al., 2020).

The application of hydraulic modelling techniques to subsurface channel-forms is likely subject to more limitations than their application to modern systems. For example, vertical and horizontal seismic resolution limitations may prevent the recognition and measurement of channel features (Deptuck et al., 2007), preventing application of the techniques at all. When channel forms can be observed, the risk that they might be compound features (i.e. channel complexes), and therefore not true palaeo-hydraulic conduits, must additionally be considered. In fact, the potential pitfalls related to the calculation of palaeo-hydraulic conditions using channel-forms observed in seismic data remain to be established; this is a critical consideration in the investigation of the development of ancient channel systems that has not been discussed in previous studies (e.g. Li et al., 2018; Gong et al., 2020).

To investigate the application of hydraulic modelling techniques to subsurface channel-forms, a high-resolution 3D seismic dataset from the Hikurangi Margin, offshore New Zealand was used. The seismic dataset images the subsurface Omakere Channel Complex (Figure 4.1). Interpretation of channel-forms herein allows application of a modelling technique that calculates equilibrium turbidity current conditions and assumes a relationship between hydraulic conditions and the morphology of their confining channels. The approach has been previously applied to the modern (surficial) Omakere Channel and validated with geophysical and petrophysical data (Crisóstomo-Figueroa et al., 2021, see also Chapter 3). Observations on the seismic stratigraphy of the channel-forms were integrated with turbidity current modelling to: 1) evaluate whether the studied channel-form may represent a palaeo-hydraulic conduit; a key test is whether modelled velocities and flow densities fall within plausible ranges for low-density turbulence dominated turbidity currents, < 20 m/s and $< 9\%$ respectively; (Bagnold, 1956; Talling et al., 2012); and 2) document the factors that might influence the calculation of palaeo-hydraulic conditions from subsurface channel-forms.

The results from this study highlight some of the challenges and limitations of applying current hydraulic modelling techniques to subsurface systems using a morphometric-based approach, which have not been always considered in earlier work (Li et al., 2018; Gong et al., 2020). Future studies should consider these limitations for an improved calculation of palaeo-hydraulic conditions which will lead to a better understanding of the evolution of ancient channel systems.

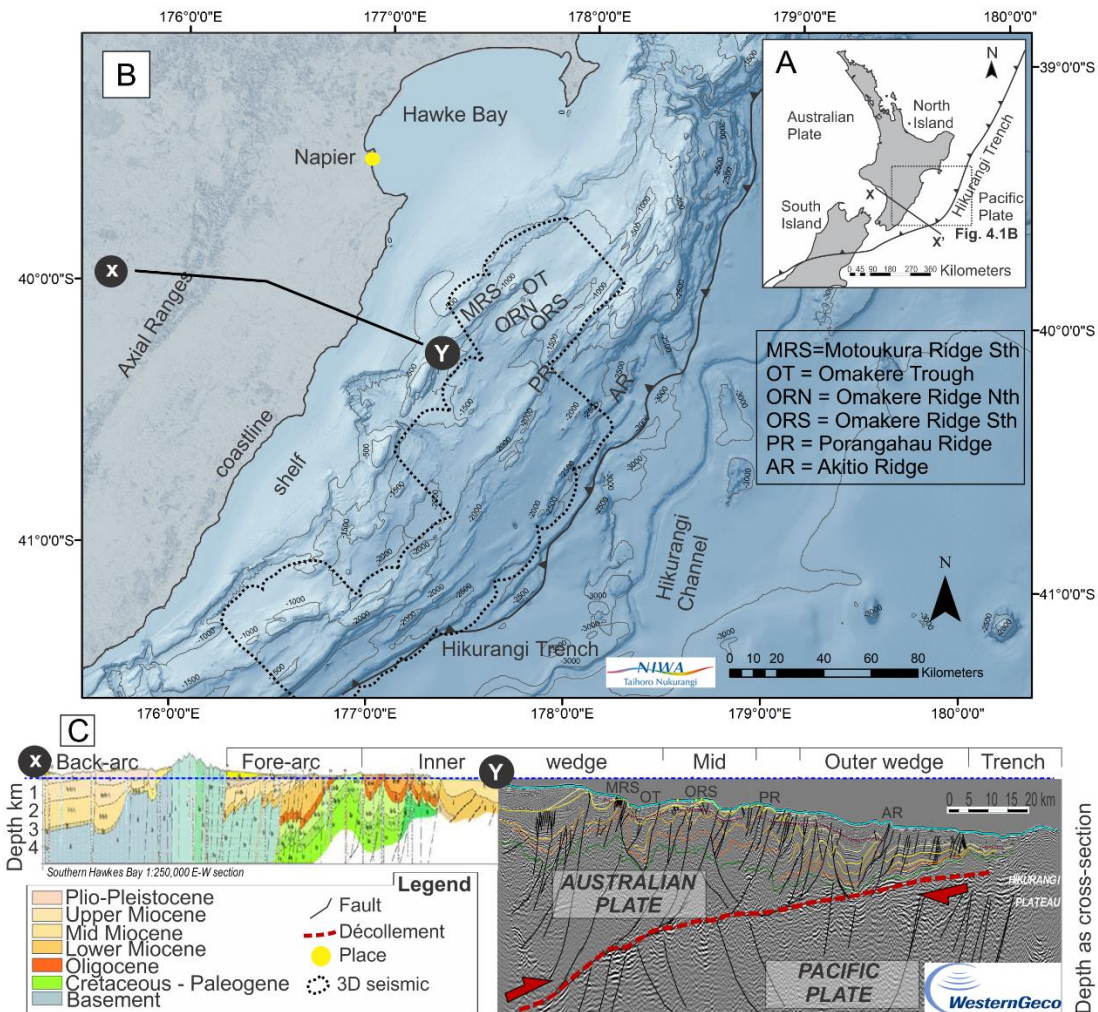


Figure 4.1 Study area. (A) The Hikurangi Margin is located on and offshore of the North Island, New Zealand. (B) Offshore bathymetry map and bathymetric contours (500 m) of the Hikurangi Margin (courtesy of the National Institute of Water and Atmospheric Research, New Zealand). The dashed black outline indicates the 3D seismic survey area. (C) Regional cross-section across the Hikurangi subduction complex (adapted from McArthur et al., 2022).

4.3 Geological setting

The study area is located on the actively growing subduction wedge of the Hikurangi Margin, offshore to the east of the North Island, New Zealand (Figure 4.1A). The margin is limited to the east by the Hikurangi subduction trench and to the west by the axial ranges of the North Island (Figure 4.1B) (Ballance, 1976; Pettinga, 1982; Chanier & Ferriere, 1991; Nicol et al., 2007). The onset of subduction of the Pacific Plate below the Australian plate initiated c. 25 Ma (Ballance, 1976; Chanier and Ferriere, 1991; Nicol et al., 2007; Reyners, 2013) the resultant fold and thrust belt created elongate NE-SW trench-slope basins,

typically tens of kilometers long by kilometers wide (Figure 4.1B and C) (Lewis & Pettinga, 1993; Barnes et al., 2010; Bailleul et al., 2013; McArthur et al., 2022).

Three stages of deformation occurred in the Neogene including: 1) a stage of significant compression, uplift and thrust nappe emplacement related to the onset of subduction in the Early Miocene (Chanier and Ferriere, 1991), 2) a mixed extensional and compressional phase in the Middle to Late Miocene (Chanier et al., 1999; Barnes et al., 2002) and 3) a phase of renewed margin compression from the Late Miocene onwards (Nicol and Beavan, 2003). Continuing compression to the present day has resulted in uplift and exhumation of the innermost trench-slope basins, which are exposed at outcrop (Bailleul et al., 2007; McArthur et al., 2022a), whilst the majority of the wedge remains submerged (Barnes et al., 2010).

The inner and middle domains of the wedge exhibit thick-skinned deformation, characterized by the reactivation of pre-subduction structures (Figure 4.1C, and Figure 4.2) (McArthur et al., 2020a). Deformation has migrated towards the trench through an outer structural domain exhibiting thin-skinned deformation (McArthur et al., 2020a), albeit with out of sequence thrust and fold emplacement (Chanier and Ferriere, 1991; Bailleul et al., 2013).

Due to the dominantly marine conditions experienced during the Neogene, the syn-subduction strata forming the offshore trench-slope basins comprise marine mudstones, turbidites, mass-transport deposits, carbonates and contourites (Figure 4.2) (Bailleul et al., 2007; Burgreen-Chan et al., 2016; McArthur and McCaffrey, 2019; Bailey et al., 2021; McArthur et al., 2021; Crisóstomo-Figueroa et al., 2021). Changes in sediment supply, sedimentary processes, timing and style of deformation control the different styles of trench-slope basin fill; this results in a complex lateral and longitudinal pattern of basin fill variation with time (McArthur et al., 2022a).

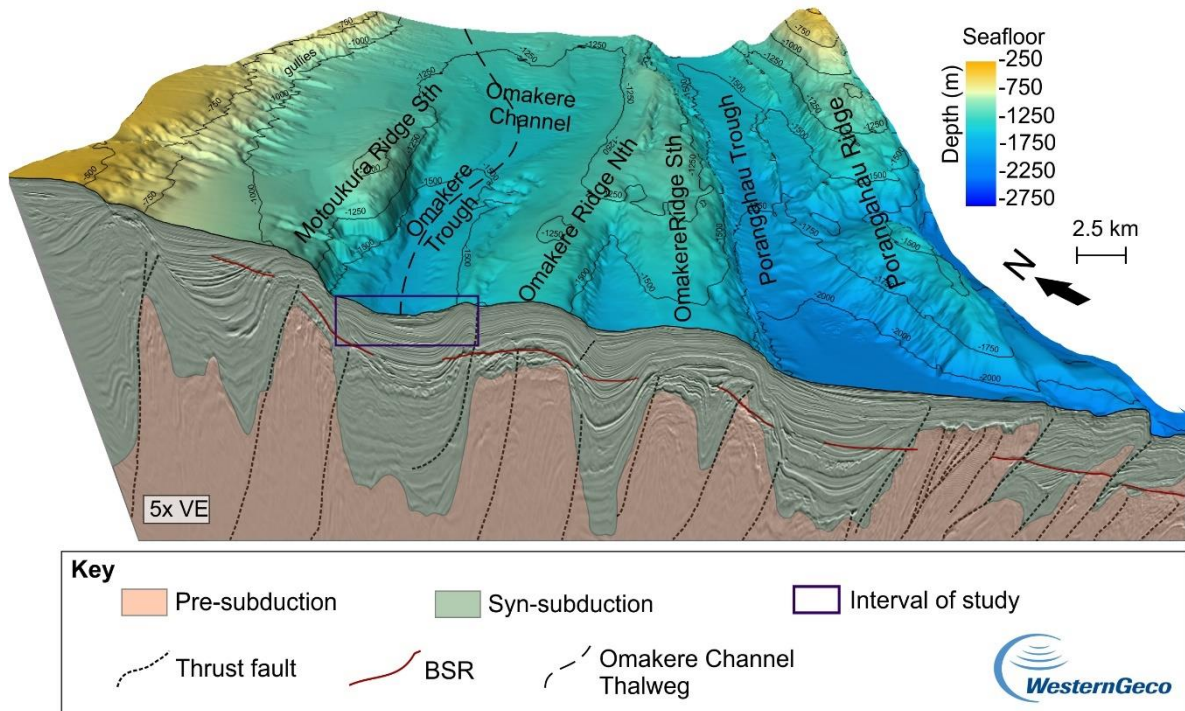


Figure 4.2 3D perspective view of the seafloor with corresponding seismic cross-section showing the structural style of the subduction wedge where the Omakere Trough is located. The studied interval of the Omakere Channel complex is found at depths of up to ~ 300 mbsf.

4.4 Study area

4.4.1 The Omakere Trough

The Omakere Trough is a NE-SW oriented trench-slope basin located south of Hawke Bay in the northern zone of the middle domain of the subduction wedge (Figure 4.1). It is approximately 70 km long and 12 km wide, being bounded to the north by a thrust-faulted anticline, here referred to as the Motoukura Ridge South, and to the south by the Omakere Ridge, which bifurcates forming Omakere Ridge North and Omakere Ridge South (Figure 4.2). This area is characterized by thick-skinned deformation and the development of steep ridges due to seamount subduction in the outer structural domain (Pecher et al., 2004). Channel formation is documented within the shallowest part of the syn-subduction fill (Figure 4.2) and therefore a ~300 m thick interval below the seafloor has been chosen as the focus of this study.

4.5 Dataset and methodology

4.5.1 Seismic dataset and interpretation

Depth-converted 3D seismic reflection data acquired at broadband frequency in 2017 and processed using pre-stacked Kirchhoff depth-migration by WesternGeco Multiclient was used. The seismic has an inline (NW-SE) spacing of 25 m and crossline (SW-NE) spacing of 12.5 m. The seismic volume covers 15,344 km² of the margin (Figure 4.1), with the area of interest in the northern part of the survey evaluated in this study covering 1,956 km². Vertical resolution within the first 50 metres below the sea floor (mbsf) is ca. 6.7 m (Crisóstomo-Figueroa et al., 2021) and decreases to ca. 8 m at ca. 500 mbsf. The vertical resolution at ca. 500 mbsf was approximated through the calculation of the tuning thickness (Widess, 1973) using a wavenumber of 0.031 m⁻¹, calculated using the instantaneous frequency attribute map obtained at this depth. Full stack data are displayed as zero-phase, SEG-Y reverse polarity, where a downward decrease in acoustic impedance is represented by a peak (positive amplitude).

Horizon mapping and attribute extraction and analysis were carried out in the cropped dataset using Schlumberger's Petrel© E&P and Eliis' Paleoscan™ software, with a focus on the interval that contains the Omakere Channel complex at ca. 350 mbsf. Paleoscan offers an automated horizon tracking system with a ModelGrid (Paumard et al., 2019) that compares wavelets trace-by-trace to link those that share similar geophysical responses. Based on their similarities and relative distance, auto-tracked horizons were generated from the Model Grid and then individually checked to ensure a consistent and accurate interpretation.

Seismic units and facies were defined based on changes in seismic geometry and character and the mapped horizons were used to generate volume- and surface-based seismic attributes to better constrain our interpretations of depositional elements. Attributes were extracted and used as follows: 1) root-mean-square (RMS) amplitude was used to identify amplitude variations within the channel complex, where high amplitude values are interpreted as sand-prone intervals and low amplitude values as more homogeneous and fine-grained sediments. The established relationship between the RMS response and the interpreted sediment type has been applied to the modern channels of the study area and validated by drop core data (Crisóstomo-Figueroa et al., 2021); 2) variance, a signal coherency based analysis that identifies discontinuities in the seismic, was mainly used to help identify and define mass transport deposits; 3) spectral decomposition, which transforms the seismic signal into its constituent frequencies, helped to better identify subtle channel-form features and aided the interpretation of the seismic geomorphology (Bacon et al., 2003).

4.5.2 Morphometric analysis

An interpreted horizon corresponding to the base of a channel-form within the complex was converted to a data points set in Petrel© and imported into the Topotoolbox program in MATLAB using a grid with 25 m spacing to locate the data points. Topotoolbox enables landscape and drainage analysis (Schwanghart and Kuhn, 2010); here it was used to perform the morphometric and depth-profile extraction from the imported horizon. The down-channel bed slope (S) was calculated from the extracted channel-form depth profile. Cross-sections were taken every 1 km perpendicular to the channel-form confinement and measurements were taken in each cross-section as represented in Figure 3.3 in Chapter 3.

4.5.3 Modelling of palaeo-hydraulic conditions

Using a modelling approach that has been applied to the modern (surficial) channels of the study area (Crisóstomo-Figueroa et al., 2021) the depth-averaged sediment concentration, C , Froude number, Fr , and flow velocity, U , for given subsurface channel-form were calculated to evaluate whether they might represent palaeo-hydraulic conduits. It was assumed that low-density turbidity currents dominated in the observed channel-forms, similar to the flows suggested in the modern channels (McKeown, 2018; Crisóstomo-Figueroa et al., 2021). The model estimated the bankfull hydraulic conditions for dilute, turbulence-dominated turbidity currents; hence, valid model solutions of bulk sediment concentration were interpreted to be below a 9% concentration threshold (Bagnold, 1956; Talling et al., 2012). The model used the surface-slope equation from Komar (1969) (Equation 4.1, below) and the relationship between the bed slope, Froude number, and bed friction coefficient (Parker et al., 1987; Abad et al., 2011) that balances the gravitational force and drag force at the bed (Equation 4.3).

The MATLAB script developed in Chapter 3 incorporating a nonlinear data-fitting MATLAB solver (*lsqnonlin*) was used to solve for the governing equations (4.2) to (4.9) and find optimal solutions of C and Fr , for a given channel-form morphology, jointly solving for both cross-channel forces (Equation 4.2) (Komar, 1969) and down-channel forces (Equation 4.3) (Abad et al., 2011).

Equation (4.1) describes the momentum balance of the pressure gradient force, the Coriolis force and the centrifugal force across a channel (Komar, 1969; Stacey and Bowen, 1988a; Wells and Cossu, 2013).

$$gRC\gamma = \pm fU + \frac{U^2}{r}, \quad (4.1)$$

where $g = 9.81 \text{ m/s}^2$ gravity; $R = (\rho_s/\rho_f - 1)$ is the submerged specific gravity (where $\rho_s = 2650 \text{ kg/m}^3$ is the density of quartz for the material in suspension, and $\rho_f = 1000 \text{ kg/m}^3$ is the density of the fluid); C , the bulk sediment concentration (vol./vol.); $\gamma = (H - h)/W$, the cross-channel slope (m/m), where H is the maximum, and h the minimum channel-form heights and W the channel-form width (Figure 3.3, Chapter 3); f , the Coriolis acceleration $f = 2\Omega \sin\theta$, where $-f$ applies for clockwise flows and $+f$ for anticlockwise flows, Ω is the Earth's rotation rate, and θ the latitude; U , the downstream flow velocity in m/s; and r , the thalweg radius of curvature (m), in straight channel-form sections $r \rightarrow \infty$.

Equation (4.1) can be rewritten in terms of the Froude number, Fr , (Cossu and Wells, 2010; Wells and Dorrell, 2021) where $Fr = U/\sqrt{gRC\bar{H}}$ (Parker et al. 1987),

$$\gamma = Fr^2 \left(\frac{\pm f \bar{H}}{Fr \sqrt{gRC\bar{H}}} + \frac{\bar{H}}{r} \right), \quad (4.2)$$

where \bar{H} is the average flow height (m) assumed to be in bankfull conditions, hence the flow height is equal to the average channel-form height.

Down-channel forces were calculated using the balance of gravitational driving force with frictional drag at the bed, and through the entrainment of ambient water following the model of Parker et al. (1987) (e.g. Abad et al. 2011),

$$S = \frac{C_d + e_w \left(1 + \frac{Ri}{2}\right)}{Ri}, \quad (4.3)$$

where S is the calculated down-channel slope in m/m; $C_d = 0.0025$ (Abad et al., 2011; Konsoer et al., 2013), the drag coefficient, which is considered constant in the downstream direction for the calculated flows; Ri , the bulk Richardson number, which scales inversely with Fr^2 (Wells & Dorrell, 2020), is a measure of mixing of the flow-ambient fluid interface (Parker et al., 1987; Abad et al., 2011),

$$Ri = \frac{gRC\bar{H}}{U^2} = \frac{1}{Fr^2}, \quad (4.4)$$

and e_w , the ambient water entrainment by mixing was defined using

$$e_w = \frac{0.00153}{0.0204 + Ri}, \quad (4.5)$$

a relation derived empirically by Parker et al. (1987) for turbidity currents.

Turbidity current velocities were then calculated using Equation (4.6) and the shear velocity u^* using Equation (4.7) (Parker et al., 1987; Abad et al., 2011).

$$U = Fr \sqrt{gRC\bar{H}}, \quad (4.6)$$

$$u^* = \sqrt{C_d} U. \quad (4.7)$$

The flow and sediment discharge were calculated using Equation (4.8) and (4.9) respectively,

$$Q = UA, \quad (4.8)$$

$$Q_s = QC. \quad (4.9)$$

where A is the channel-form area calculated using Equation (3.1).

4.5.3.1 Sensitivity Analysis

A sensitivity analysis of Equations (4.2) and (4.3) was conducted to identify the input parameters that have a greater influence on the calculations of C and Fr , by varying one parameter while keeping all other parameters fixed at a selected baseline value (Figure 4.3). The limits in parameter values describing channel morphology were set to cover the range displayed by modern submarine channels (Konsoer et al., 2013; Lemay et al., 2020) (Table 4.1). Baseline values were selected from measured morphometrics at a channel bend of the modern Omake Channel with an anticlockwise flow orientation (Table 4.1) following Crisóstomo-Figueroa et al. (2021).

Table 4.1 Parameters assessed in the sensitivity analysis of Equations 4.2 and 4.3.

Parameter	Baseline values	Range of values used when varied
Flow height, \bar{H}	40.5 m	10 to 300
Cross-channel slope, γ	2.0×10^{-3}	10^{-3} to 10^{-1}
Down-channel slope, S	2.09×10^{-2}	10^{-3} to 10^{-1}
Latitude, θ	-40.28°	-5° to -45°
Radius of curvature, r	2235.5 m	10^2 to 10^4 m

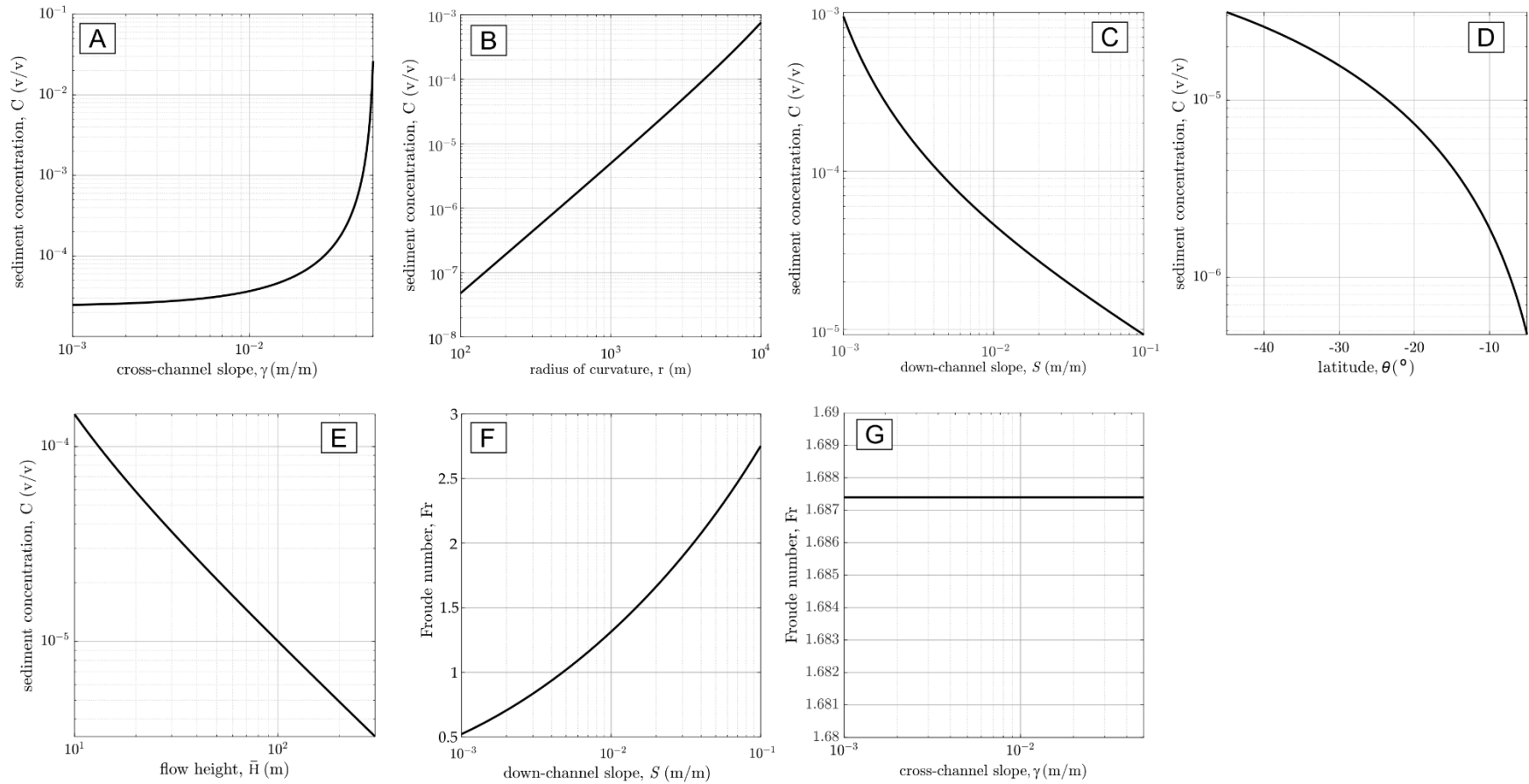


Figure 4.3 Plots showing the sensitivity of calculated values sediment concentration and Froude number to the input parameters to Equations (4.2) and (4.3). In each case, the parameter shown on the x axis was varied whilst the others remained fixed. Variations in sediment concentration are shown for varying (A) cross-channel slope, (B) radius of curvature, (C) down-channel slope, (D) latitude, and (E) flow height. Variations in Froude number are shown for varying (F) down-channel slope and (G) cross-channel slope.

4.5.4 Estimating the net erosion - net deposition threshold

A MATLAB script of the Flow-Power Flux-Balance type model developed by Dorrell et al. (2018) was used to compute the threshold of erosion and deposition for the estimated palaeo-hydraulic conditions. The Flow-Power Flux-Balance model has been applied to the modern (surficial) channels of the study area and validated by geophysical and petrophysical information (Crisóstomo-Figueroa et al., 2021). Therefore, if the subsurface channel-forms analysed here represent true palaeo-hydraulic conduits, results should be consistent with observations from RMS maps of the channel-forms, as was observed for the modern channels (Crisóstomo-Figueroa et al., 2021).

In this analysis, the bankfull flow heights, \bar{H} (assumed equal to the measured channel-form depth), and depth-averaged sediment concentrations, C , calculated with Equation (4.2) at each channel-form section were used to constrain the palaeo-hydrodynamics. The model does not forward model the evolution of currents, nor the downdip transport of sediment in suspension (whether carried from source or eroded). The model incorporates the bulk capacity (maximum amount of sediment that can be transported in suspension by a turbulent flow) and competence (particle class specific capacity) (Dorrell et al., 2013b), using a polydisperse description of sediment suspension. For each particle class the threshold between a net erosional and a depositional flow is given by

$$\frac{C_i^-}{C_m} E_i = C_i^+ w_{si} \forall i, \quad (4.10)$$

where the total concentration of sediments at the bed is

$$\sum_{i=1}^N C_i^- = C_m, \quad (4.11)$$

where C_i^- is the grain size class concentration of the i th particle size in the active layer of the bed that freely exchanges material with material transported as suspended load (Dorrell et al., 2013b), C_m is the packing concentration, C_i^+ is the grain size class concentration at the bed and w_{si} the particle settling velocity for each grain size class. Furthermore, the description of the vertical distribution of suspended sediment concentration was determined by the mass conservation equation (Soulsby, 1997)

$$w_s C_i(Z) = -k_s \frac{dC_i(Z)}{dZ}, \quad (4.12)$$

where $Z = z/L$ is the dimensionless flow height, where $z = \bar{H}$ (Dorrell & Hogg, 2012). The eddy diffusivity $k_s = ku^* LF(Z)$ was assumed constant, therefore the flow length

scale $L = \bar{H}/6$, and the Rouse number is defined by $\beta = 6 \frac{W_{si}}{ku_i^*}$ (Dorrell and Hogg, 2012), $k = 0.4$ is the von Kármán constant; thus, the diffusion profile is given by

$$C_i(Z) = C_i^+ \left(\frac{1 - e^{-\beta}}{\beta} \right). \quad (4.13)$$

The model incorporates a sediment entrainment function in which the power required to move sediment and incorporate it into suspension is proportional to the depth-averaged flow power:

$$E_i = \varepsilon \rho_f (gR\bar{H})^{-1} \Delta u_i^{*3}, \quad (4.14)$$

where $\varepsilon = 13.2$ is an empirical parameter describing entrainment efficiency (Dorrell et al., 2018).

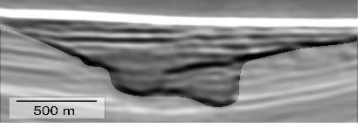
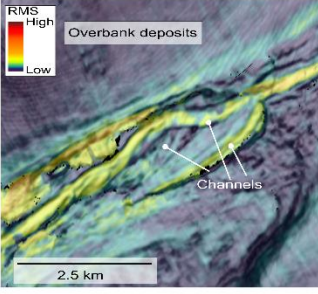
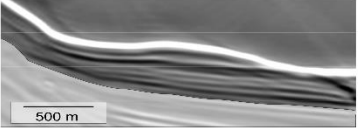
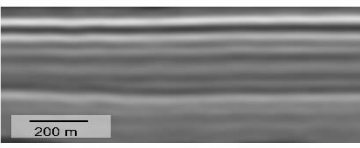
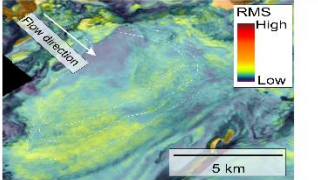
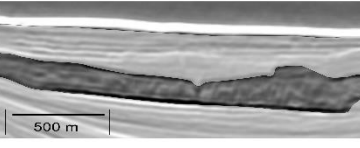
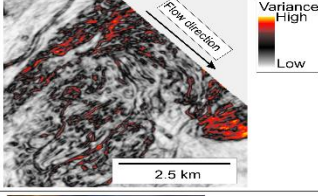
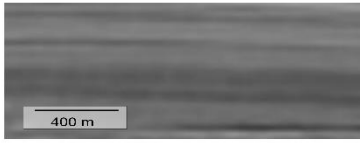
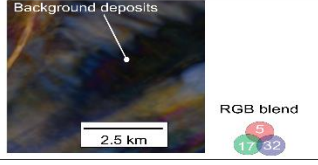
The grain size classes (d_{50}) used to solve Equation (4.10) to Equation (4.14) range from $\phi = 8$ to $\phi = -2$ (i.e., very fine silt to gravel on the Wentworth scale). A log normal distribution derived from empirical data (Dorrell et al., 2018) was used to model grain size distribution, where a standard deviation $\sigma = 0$ represents a monodisperse suspension, a standard deviation $\sigma = 0.5$ is equivalent to a polydisperse suspension that is well sorted (Folk, 1966) and a standard deviation $\sigma = 2$ is equivalent to one that is poorly sorted (Folk, 1966). The slope gradient required to maintain equilibrium conditions for a given grain size distribution was calculated with Equation (4.3); here presented in m/m and degrees. The down-channel slope, S , values calculated using the channel-form longitudinal depth profile were compared to the calculated equilibrium slope to assess the grain sizes that would erode, deposit or bypass the slope.

4.6 Results

4.6.1 Seismic facies and depositional elements in the Omake Trough

The analysis of the seismic stratigraphy and geomorphology allowed the recognition of five principal seismic facies within the Omake Trough. The facies are interpreted to be the product of different deepwater processes and represent the following depositional elements: 1) turbidite slope channel fill (SF1), 2) channel overbank deposits (SF2), 3) lobe deposits (SF3), 4) mass-transport deposits (SF4) and 5) background deposits (SF5) (Table 4.2).

Table 4.2 Deepwater depositional elements identified in the Omakeere Trough are based on their seismic cross-section character and geomorphology.

		Depositional elements				
Seismic facies		Seismic stratigraphy	Reflection character and geometry	Seismic geomorphology	Planform geometry	Interpretation
SF 1	Turbidite slope channel fill		Deposits confined within stacked, narrow (< 500 m) v-shaped to wide (> 2 km), up to 150 m deep, u-shaped channel-forms. Parallel to sub-parallel reflectors of variable amplitude. Occurring adjacent to SF2. They exhibit upper surfaces that are either flat and smooth related to deposits from SF2 or irregular due to erosion related to SF4.		Elongated planform geometry, up to 30 km long. They exhibit low sinuosity of ~1.25 and widths up to 2.8 km wide.	Interpreted as the fill of turbidite channels. Their basal fill may be formed by continuous high amplitude reflectors interpreted as sand-rich deposits. Intervals of low to moderate amplitude response are inferred to represent silt or mud-rich deposits. When stacked and confined within a major erosion surface they are interpreted as a channel complex (Abreu et al. 2003; Posamentier and Kolla 2003; Deptuck et al. 2007).
SF 2	Turbidite overbank deposits		Parallel to sub-parallel, transparent or low to moderate amplitude reflections that are continuous to semi-continuous and occur in packages that are either flat-topped or thin away from SF1. They can be up to 90 m thick, extending up to 2.2 km away from SF1, and may be spatially restricted or tilted when found adjacent to confining structures.		Low RMS amplitude, overbank sediment waves may develop	Interpreted as overbank deposits, product of turbidity currents overspilling the fine upper part of their sediment load. A low RMS response suggests a fine-grained composition of either silty or muddy sediments. When they occur adjacent to the channel complex they are interpreted as external overbank deposits. When found adjacent to individual channel-forms they are interpreted as internal overbank deposits (Posamentier and Kolla 2003; Hansen et al. 2015).
SF 3	Lobe deposits		Characterised by parallel to subparallel, continuous and moderate to high amplitude packages, which thin and onlap adjacent to confining structures in cross-section view. They can be up to 90 m thick, 14 km wide and 11 km long.		They are located down-dip of SF1 and may display a lobate or sheet-like geometry in planform view and most show a high amplitude RMS response.	Lobe deposits formed by unconfined depositional turbidity currents near turbidite channels mouth. The irregular RGB blend response and localised scour-like features downstream of the channel mouth suggest the development of channel-lobe-transition zones. The high RMS response suggests the presence of sand-rich deposits. These bodies are usually areally restricted by confining structures. (McArthur et al. 2012; Posamentier 2003; Prélart et al. 2010).
SF 4	Mass Transport Deposits		Occurs widely across the margin and displays chaotic, discontinuous reflections of transparent or low-to-moderate amplitude in cross-section. Coherent blocks and internal thrust structures are locally imaged within these intervals. This seismic facies often displays an erosional, rough basal surface, and an irregular high amplitude response at its upper surface, suggesting contrasting lithologies of adjacent deposits. Individual bodies can be up to 95 m thick, 15 km long and 12 km wide. These bodies are found adjacent to confining structures and either below or above SF1, SF2 and SF3.		Variable shape, irregular to lobate, with hummock relief, clasts or thrust faulting near its terminus. They exhibit high variance response and low RMS amplitude.	These deposits are interpreted to be the product of <i>en masse</i> gravitational sediment movement (Moscardelli et al. 2006; Posamentier and Martinsen, 2011; Hodgson et al. 2019).
SF 5	Background deposits		This seismic facies shows parallel to sub-parallel, low frequency, continuous to semi-continuous and low or transparent reflections in cross-section. It extends tens of kilometers and occurs widely throughout the trough.		Dark and continuous in RGB blend, low RMS amplitude.	This seismic facies is interpreted as mud-dominated background sediments deposited by pelagic and hemipelagic fallout or by mud-rich turbidity currents (McArthur et al. 2021a).

4.6.2 Seismic stratigraphy and geomorphology of the Omakere Channel Complex

The ~ 57 km long, up to 300 thick, and up to 4.8 km wide Omakere Channel complex is confined, running axially along the Omakere Trough (NE-SW), parallel to the Omakere Ridge, before being diverted ~ 90° towards the SE (Figure 4.4A and 4.4B). A systematic downdip variation in the geomorphology allowed subdivision of the long-profile of the channel complex into Areas 1, 2, and 3 (Figure 4.4C). These Areas comprise the focus of this study as they contain a well imaged channel-form, here referred to as channel-form A, (Figure 4.4C, 4.5A-D) which was selected to apply the flow modelling techniques described in the Methods.

4.6.2.1 Area 1

This area comprises the first ~12.5 km length of the interpreted channel complex (Figure 4.4). In cross-section view (Figure 4.5A), the base of the fill comprises an MTD (SF4), here referred to as MTD A (Figure 4.4) sourced from the upper slope to the north and extending ~15 km in a NNE-SW direction (Figure 4.6A). Channel-form A (SF1) (Figure 4.4C and 4.4A) is observed to have cut down into this MTD (Figure 4.5A and Figure 4.6A). In this area and throughout its length (Areas 1 to 3, Figure 4.4C), the fill of channel-form A shows a low RMS response, interpreted to reflect the presence of predominantly fine-grained deposits (Figure 4.6B). In planform view (Figure 4.4C), this channel shows a low sinuosity (~1.25). Higher in the stratigraphy of Area 1, a second channel-form is identified with associated internal overbank deposits (SF2) that overlie channel-form A (Figure 4.5A).

4.6.2.2 Area 2

This area extends for ~ 8.5 km in the channel direction with a thinner MTD (MTD B) at its base, which is overlain by thicker, vertically stacked channel-forms with associated internal overbank deposits (Figure 4.4; 4.5B). Here, channel-form A exhibits a straighter planform geometry and strongly deflects to the right, probably due to the presence of MTD B (Figure 4.6B and 4.6C), which potentially originated from local channel bank collapse. Knickpoints are preserved downdip (Figure 4.4C),

which contribute to an increase in the depth and width of the channel-form (Figure 4.5B).

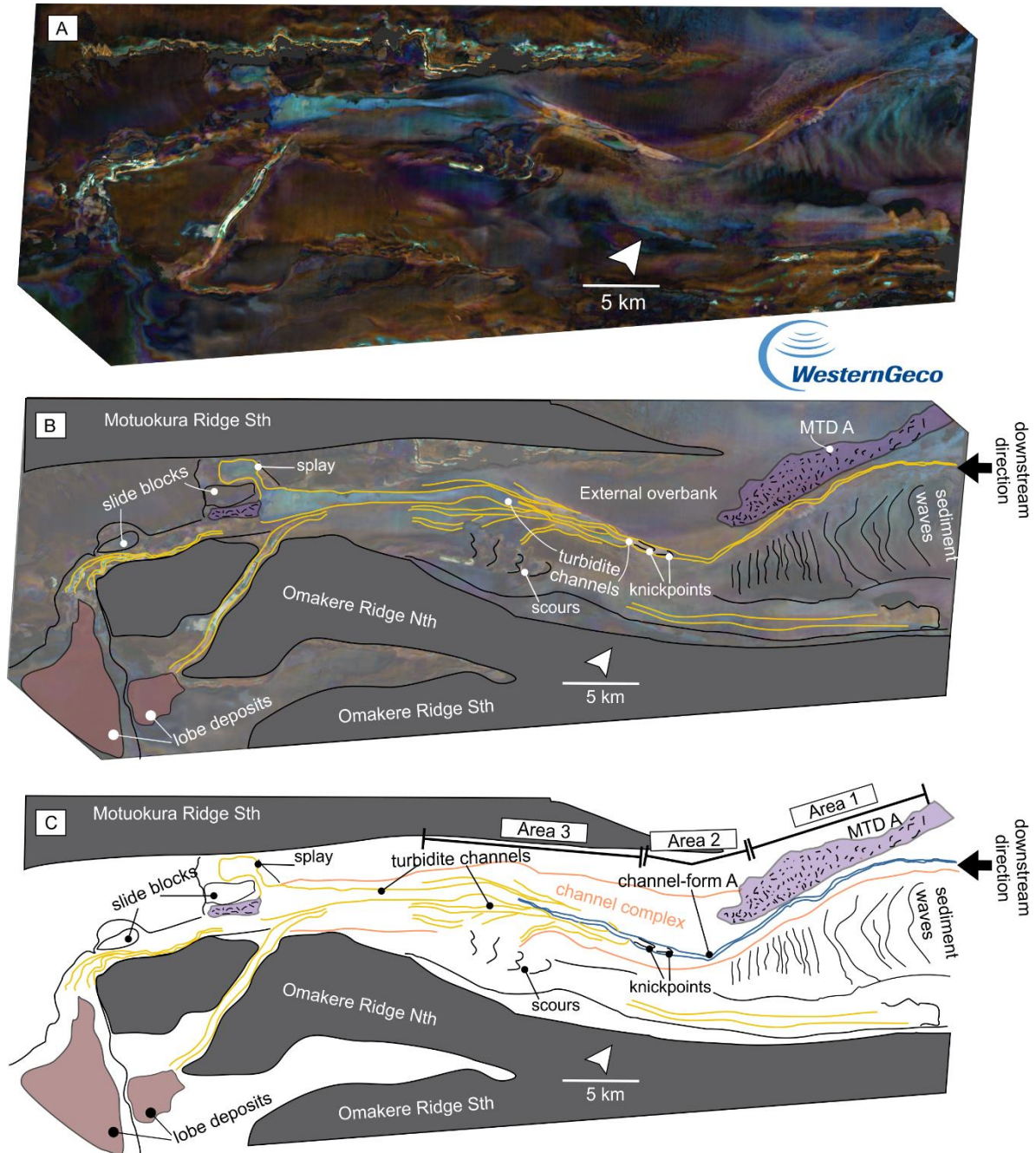


Figure 4.4 (A) Uninterpreted and (B) interpreted spectral decomposition maps and (C) interpretation of the Omakere Trough where the Omakere Channel Complex is located. See Figure 4.1 for map location.

4.6.2.3 Area 3

This area covers a ~16 km long stretch of the channel complex (Figure 4.4C). Here, laterally offset, stacked channel-forms with associated internal overbank deposits are confined within external overbank deposits that are thicker than those observed in Area 1 and 2 (Figure 4.5C). The arrangement of channel-forms in cross-section (Figure 4.5C and 4.5D) and planform view (Figure 4.4) suggest an area of channel avulsion and possibly the development of distributary channels in Area 3 (Figure 4.4, and 4.5C), some of which might have avulsed after the emplacement of MTD B (Figure 4.5C and 4.6C). Channel-forms become wider further downdip, vertically stacked and with less lateral offset (Figure 4.5D). As the structural confinement increases downdip, due to convergence of the Motuokura Ridge South and the Omakere Ridge North (Figure 4.4, Figure 4.5E), external overbank deposits are absent, likely due to the height of the turbidity current being lower than the structural confinement and / or flows becoming more depositional in this area. Here, channel-forms are thicker and wider, eroding deeper into pre-channel slope deposits (Figure 4.5E). In the distal portion of this area, reflector packages forming the channel fill are tilted towards the channel axis (Figure 4.5E) due to coeval sedimentation and structural ridge growth. A thicker deposit of MTD B is also observed in this section, extending over the complete Area 3 channel accommodation available at the time (Figure 4.6C) and is overlain by high amplitude channel fill deposits.

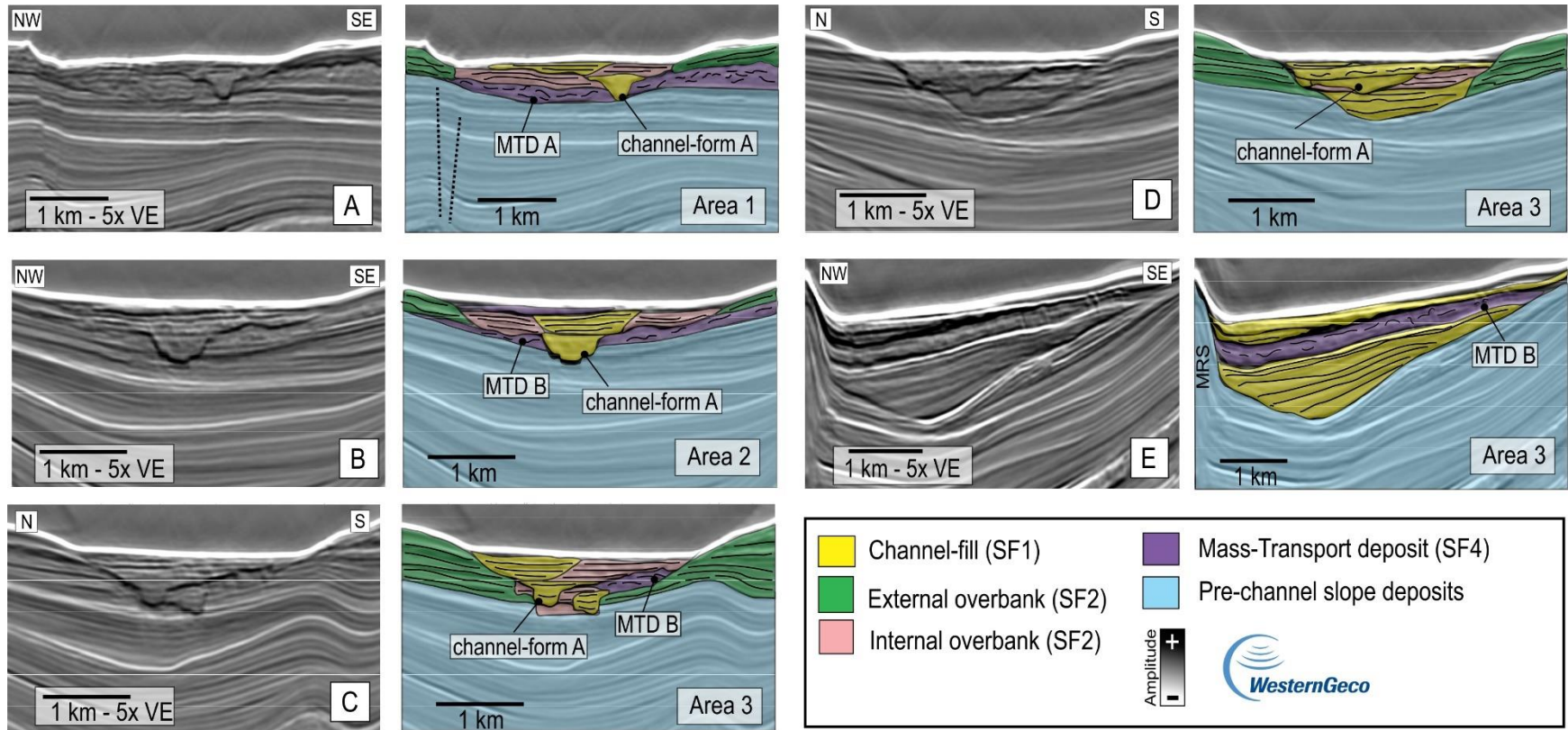


Figure 4.5 (A-E) Uninterpreted and corresponding interpreted cross-sections of the Omakere Channel Complex through Areas 1 to 3 based on the identified seismic facies and depositional elements.

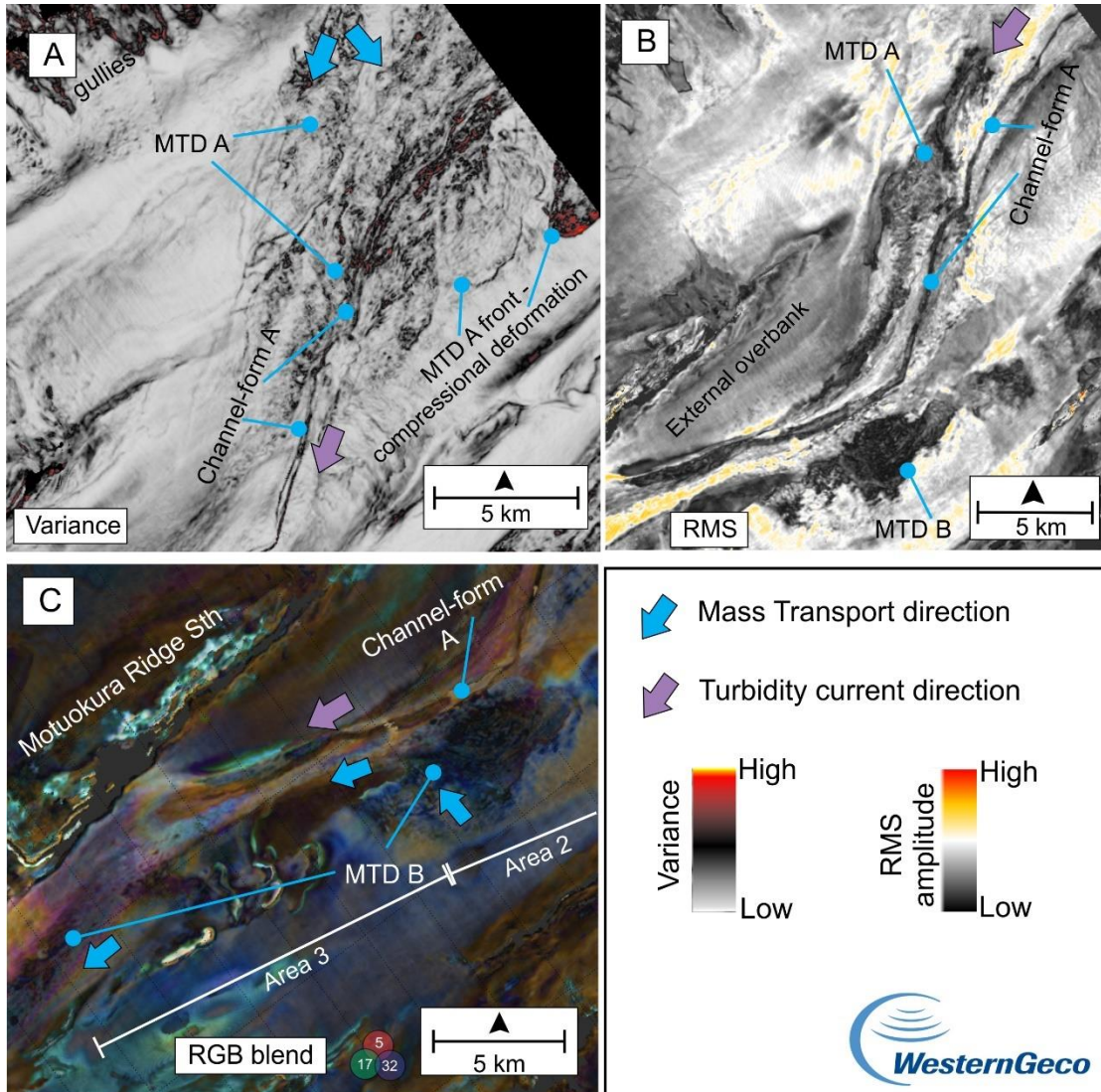


Figure 4.6 (A) MTD A located in Area 1 of the Omakere Channel Complex, (B) RMS amplitude map of channel-form A (C) MTD B, extending from Area 2 to Area 3.

4.6.3 Channel-form A morphometrics and flow modelling results

4.6.3.1 Channel-form morphometrics

Channel-form cross-sections (looking downstream) with the measured cross-channel slope, and a depth map with the cross-section locations are shown in Figure 5.7A; some of the cross-sections correspond to the locations of channel bends B1-B6, which are highlighted with grey bars in plots 7C-I. The channel depth long-profile and down-channel slope values are shown in Figure 4.7B, divided into the Areas 1-3. Channel-form morphometrics can be found in Appendix B.2.

Initially, channel-form cross-sections display narrow v-shaped morphologies with low to moderate overbank asymmetry, then progressively widen downstream to display u-shaped morphologies, with terrace-like or internal overbank deposits becoming evident (cf. Hansen et al., 2015) (Figure 4.7A). The down-channel slope increases from 0.2° to 1.1° (the steepest channel section) through Area 1 and decreases through Area 2 where the shallowest slopes (0.04°) are found (Figure 4.7B). The slope increases again in Area 3 up to values of 0.3° . Four of the six recognised channel bends occur in Area 1 where the channel exhibits a low sinuosity of up to 1.25 and radius of curvature ranging from 920 m (B2) to ~ 1.91 km (B4). The channel then exhibits a straighter planform, where one channel bend is developed in each of Areas 2 and 3, showing a radius of curvature of ~ 1.21 km in Area 2 and ~ 1.15 km in Area 3 (Figure 4.7B).

In Area 1, the channel-form is initially shallow: channel height is ~ 28 m on average in the first ~ 2 km (Figure 4.7C). Channel height increases downstream to average ~ 47 m over the last ~ 15 km of Area 1 (Figure 4.7C). Over the ~ 14 km of Area 2 channel heights increase to an average of ~ 58 m, then reduces to ~ 40 m along the 5 km of Area 3 (Figure 4.7C). Cross-channel slope values in Areas 1 and 2 vary in magnitude from 10^{-3} to 10^{-2} with an average slope value of 0.0179 m/m in Area 1, reducing to 0.0120 m/m in Area 2; values then increases to 0.0314 m/m in Area 3 (Figure 4.7C). The channel width and area also increase down-channel from Area 1 to Area 2 (Figure 4.7D), from an average width of ~ 290 m to ~ 597 m respectively, and average area from $\sim 6,698$ m² to $\sim 21,767$ m². Similar to channel depth trends, the channel width and area also decrease in Area 3 to an average channel width of ~ 459 m and area of $\sim 11,988$ m² (Figure 4.7D).

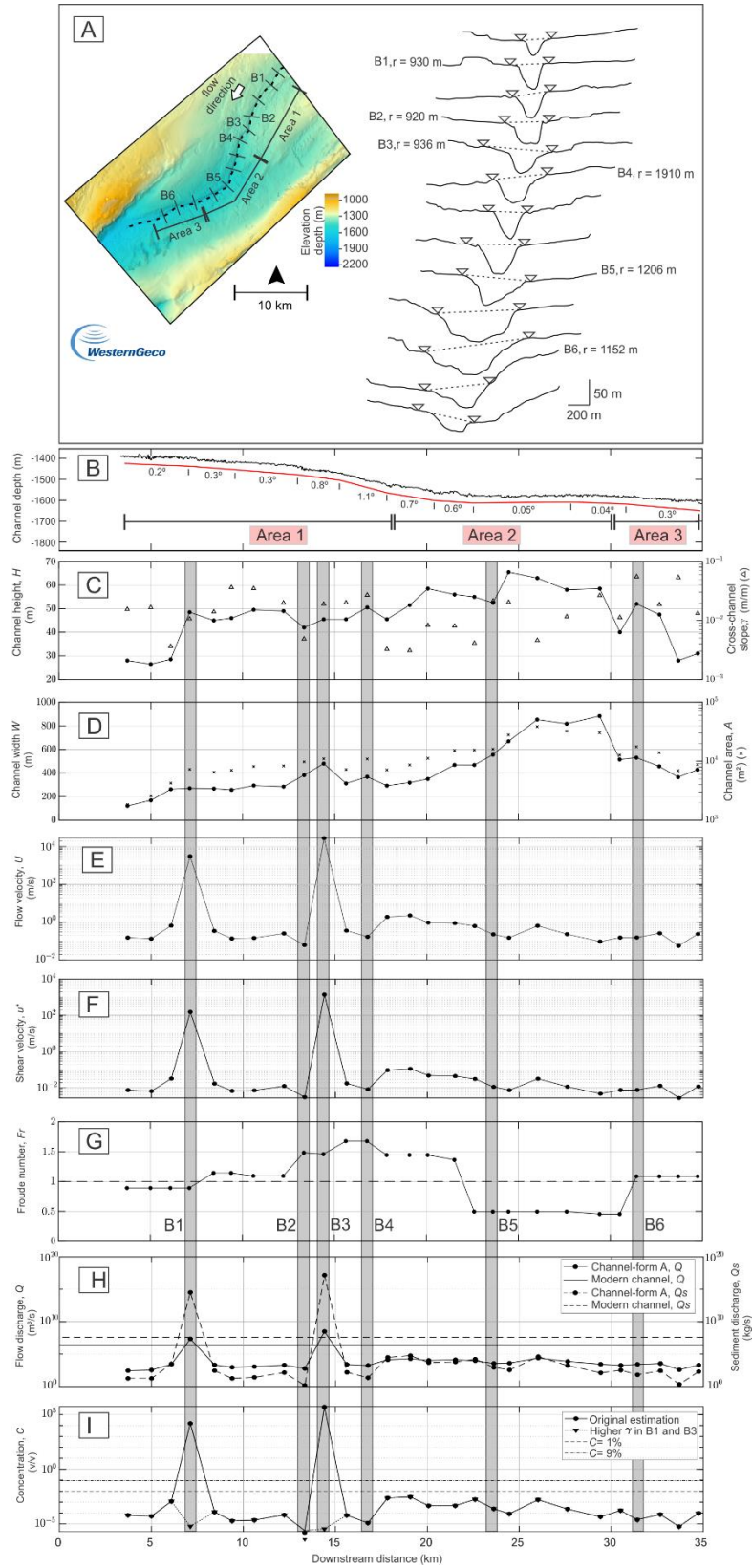


Figure 4.7 Morphology (A-D) and turbidity current modelling results (E-I) of channel-form A. (A) Palaeobathymetry and corresponding cross-sections (looking down-channel). (B) Channel-form thalweg depth profile and down-channel slope values shown in decimal degrees. (C) Mean channel-form height and cross-channel slope. (D) Channel-form width and area. (E) Downstream flow velocity. (F) Shear velocity. (G) Froude number; the dashed line at 1 indicates the threshold between sub-critical and super-critical flow. The labels B1-B6 and grey bars highlight the data points and results for channel-form bends. (H) Channel-form flow and sediment discharge; reference lines correspond to the average discharge calculated in the modern Omakere Channel from Crisóstomo-Figueroa et al. (2021). (I) Sediment concentration showing original estimations for channel-form A and estimations obtained from increasing γ one order of magnitude in B1 and B3.; the dashed line at 1% and 9% (0.09 v/v) indicates the theoretical limit for concentration values of turbidity currents (Bagnold, 1956; Talling et al., 2012).

4.6.3.2 Model sensitivity

To better understand what input parameters have a greater influence on the calculations of bulk sediment concentration, C , and Froude number, Fr , a sensitivity analysis was performed. The results are shown in Figure 4.3A to 4.3E for the calculation of C and Figure 4.3F and 4.3G for Fr . In these plots, the x axis shows the varied parameter in Equations (4.2) and (4.3), whilst other parameters were kept constant. Values of sediment concentration display the greatest variability with the cross-channel slope (Figure 4.3A) and the radius of curvature (Figure 4.3B). Increasing the cross-channel slope (or tilt of the upper part of the current) increases C by three orders of magnitude, and increasing the radius of curvature increases it by around four orders of magnitude. Decreasing latitude values from -45° to -5° (Southern Hemisphere) (Figure 4.3D) decreases C values by approximately two orders of magnitude and increasing flow height decreases C by approximately two orders of magnitude (Figure 4.3E) as flows become more dilute. The down-channel slope (Figure 4.3F) has the largest effect on the value of the Froude number; Fr values vary from 0.5 (subcritical on shallow slope values) to 2.7 (supercritical on steep slope values) as observed in other systems (Sequeiros, 2012). Varying other parameters did not cause significant variations in the calculated Froude number (e.g. Figure 4.3G).

4.6.3.3 Calculated palaeo-hydraulic conditions

Palaeo-hydraulic conditions (Figure 4.7E to 4.7I) were estimated using the morphometric parameters derived from channel-form A as input parameters in Equations (4.2) and (4.3). The analysis suggests that bankfull flows had velocities,

U , ranging from 0.056 m/s (Area 3) to 2.26 m/s (Area 2) (Figure 4.7E); these are similar to known velocities of turbidity currents in modern systems (Talling et al., 2013). Shear velocities, u^* , range from 0.027 m/s (Area 3) to 0.11 m/s (Area 2) (Figure 4.7F). Average down-channel flow velocities are \sim 0.39 m/s in Area 1, 0.6 m/s in Area 2 and 0.17 m/s in Area 3. Average flow velocity values exclude two calculated velocity values, at channel bends B1 and B3, which are physically implausible, exceeding 10^3 m/s.

Due to the changes in down-channel slope values shown in Figure 4.7B, changes in the computed Froude number are observed throughout the channel-form, where lower gradients at the start of Area 1 yield sub-critical calculated flow condition. Froude values change to super-critical downstream of channel bend B1 and continue to be >1 throughout this area and at the start of Area 2 (Figure 4.7G). A change to subcritical flow (<1) in Area 2 around channel bend B5 occurs as the down-channel slope decreases. This transition in flow criticality may well have caused a hydraulic jump, as has been observed in modern systems (Sumner et al. 2013, Dorrell et al. 2016); note there is an associated increase in the bankfull flow height, which is assumed to be equal to the bankfull channel-form depth (Figure 4.7C) together with flow deceleration in this portion of Area 2 (Figure 4.7 E). Area 3 shows a return to supercritical flow conditions as the down-channel slope increases (Figure 4.7G).

The discharge values of flow and sediment shown in Figure 4.7H reflect the flow characteristics described above, with average values of 2.574×10^3 m³/s and 3.216×10^3 kg/s in Area 1, which increase to 1.067×10^4 m³/s and 1.422×10^4 kg/s in Area 2, and subsequently decrease to 2.143×10^3 m³/s and 1.72×10^2 kg/s in Area 3. Discharge values obtained in channel-form A are lower than those estimated in the modern Omakere Channel with exception of B1 and B3 which reflect the peaks in flow velocity (Figure 4.7E) and sediment concentration (Figure 4.7I).

The calculated values of sediment concentration in channel-form A are shown in Figure 4.7I (Original estimation), where the dashed line 0.09 v/v (9%) indicates the theoretical upper limit for the bulk sediment concentration of dilute, turbulence-dominated turbidity currents (Bagnold, 1956; Talling et al., 2012). Because the techniques used here do not account for suppressed turbulence and grain-to-grain collisions, which become important above the 9% sediment concentration threshold (Bagnold, 1956; Talling et al., 2012), any calculated values higher than 9% are considered anomalous and not representative of the flows modelled in this study.

Sediment concentration ranges from 2.5×10^{-6} v/v (0.00025%) on channel bend B2 (Area 1) up to 0.0029 v/v (0.29%) in Area 2; overall these data are representative of dilute turbidity currents. The average concentration value in Area 1 is ~ 0.0003 v/v (0.03%), which slightly increases to an average of 0.0008 v/v (0.08%) in Area 2 and further reduces to 0.00007 v/v (0.007%) in Area 3. The computed average concentration values were used as input into the Flow-Power Flux-Balance model (see Methods), to estimate the sediment bypass conditions in the studied channel-form. Average C values do not include the peaks in sediment concentration that exceed the 9% threshold on channel bends B1 and B3. A number of factors may influence the modelling results at these two channel bends to produce values out of the normal known range for turbidity currents (see Figure 4.7E, 4.7F and 4.7I); these are evaluated in the discussion section below.

The sensitivity analysis shows that variations in the measured cross-channel slope, γ , and the radius of curvature, r , have the greatest impacts on C (Figure 4.3). Therefore, varying γ one order of magnitude lower and one order of magnitude higher at bends B1 and B3 showed that a steeper γ resulted in sediment concentration values below the 9% threshold (Figure 4.7I). Whereas, neither greater (up to 1910 m, equivalent to the largest measured r in B4) nor smaller (500 m) r values changed C to values below 9%.

4.6.3.4 Calculated sediment bypass conditions

Equilibrium modelled conditions for flows traversing channel-form A were calculated to show the range of grain sizes that could have been transported in suspension, and those grain sizes which would be deposited, at any section of the channel (Figure 4.8). The slope values, S , plotted in Figure 4.8A to 4.8C represent the measured down-channel slope in each Area (Figure 4.8D). Therefore, for a given S , the grain sizes ϕ above a given threshold would be bypassed under erosional flow conditions, whereas the grain sizes below a given threshold would be deposited. Assuming a log-normal sediment distribution, each contour represents a different position of this threshold, depending on whether the suspensions were monodisperse ($\sigma=0$), well sorted ($\sigma=0.5$), moderately sorted ($\sigma=1$) or poorly sorted ($\sigma=2$). This methodology has been applied to the seafloor channels on the Hikurangi Margin to assess the likely grain size range of suspended material bypassed through the channels (Crisóstomo-Figueroa et al., 2020).

For well-sorted suspended sediment ($\sigma = 0.5$), a flow with H of 47 m and C of 0.03% in Area 1 shows that at S values of $\sim 0.3^\circ$ (marker 1 in Figure 4.8A), the maximum grain size of loose sediment that can be entrained from the bed and maintained in suspension is medium silt, which increases to coarse silt as the down-channel slope increases through Area 1 (markers 2 and 3; Figure 4.8A) and at the start of Area 2 where steep slopes are maintained (marker 4, Figure 4.8B). The increase in calculated flow velocity, shear velocity and sediment concentration through these sections, as shown in Figure 4.7 supports the interpretation of flows being more capable of eroding and maintaining coarser grain sizes in suspension. Nevertheless, the maximum grain size that can be either eroded or bypassed is reduced further down Area 2 to medium silt (marker 5, Figure 4.8B). Thereafter, the maximum grain size transported reduces to fine silt (marker 6, Figure 4.8B) as the slope gradient is reduced and the flow decelerates. Despite the increase in slope gradient, fine silt remains the maximum grain size that can be transported in Area 3 as flows become more diluted (marker 7, Figure 4.8C).

The equilibrium thresholds show that a flow carrying poorly-sorted flow suspended sediment ($\sigma = 2$) would not have enough capacity to transport coarse grain sizes through the channel (Figure 4.8). Hence, the maximum grain size that can be transported in Area 1 is very fine silt (markers 1 to 3, Figure 4.8A), which would be deposited down-channel (markers 4 to 7, Figure 4.8B and C).

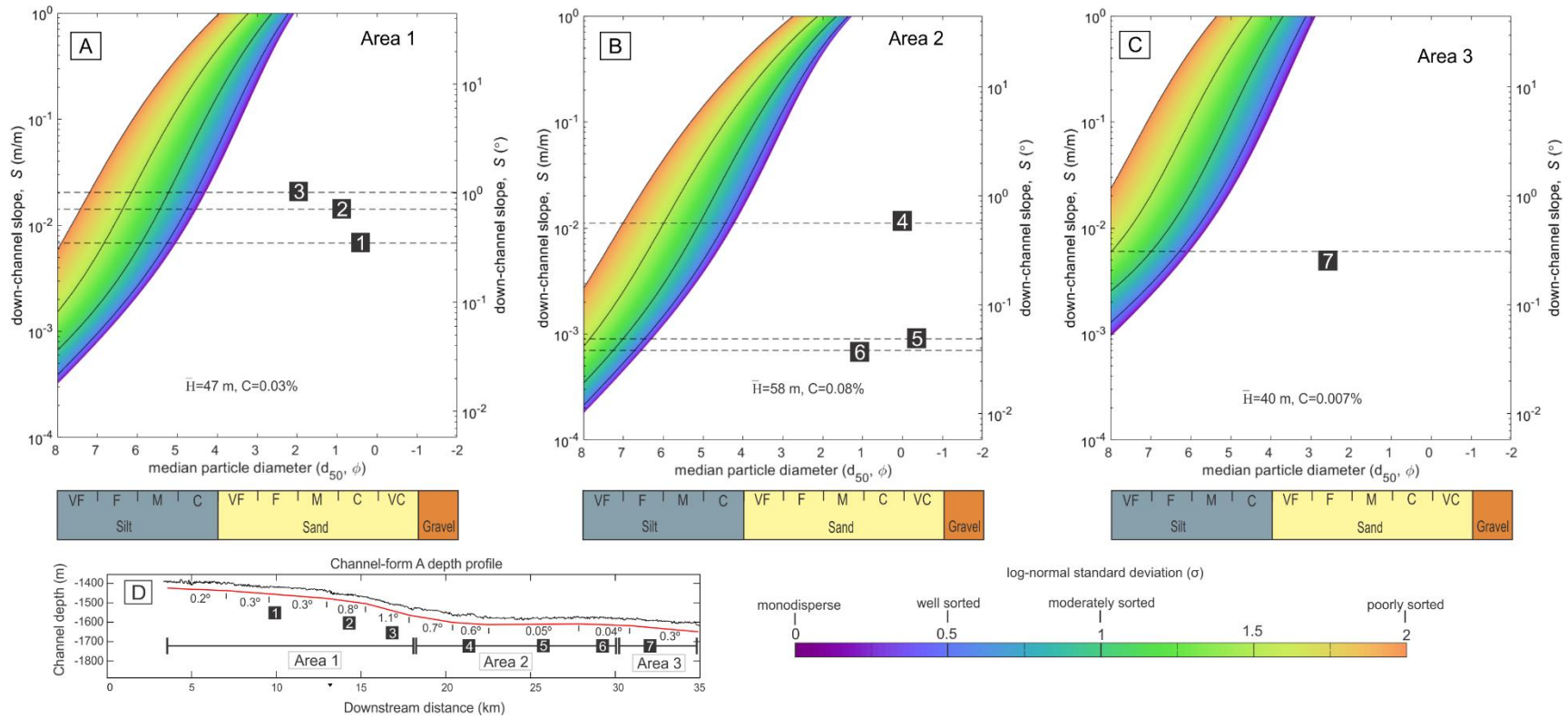


Figure 4.8 Equilibrium threshold plots calculated for channel-form A. The thresholds vary from well-sorted ($\sigma = 0.5$) to poorly-sorted ($\sigma = 2$) sediment in suspension. For a given slope value (S), the grain sizes (ϕ) above a given threshold represent sediment bypass under erosional flow conditions, and grain sizes below a given threshold represent deposition. The average flow height, \bar{H} , and average bulk sediment concentration, C , used for the calculation of the thresholds are shown in each plot for (A) Area 1, (B) Area 2 and (C) Area 3. (D) Channel-form A thalweg depth profile. The numbers in black squares show the positions of the slope gradient values plotted in A–C.

4.7 Discussion

4.7.1 Modelling as a critical test of the interpretation of subsurface channel-forms as palaeo-hydraulic conduits

4.7.1.1 Disequilibrium palaeo-hydraulic properties due to the presence of compound channel-forms

The calculation of palaeo-hydraulic conditions in subsurface channels has been previously undertaken. Li et al. (2018) estimated bankfull discharges from meandering subsurface channel-forms following the modelling approach of Konsoer et al. (2013), whereas Gong et al. (2020) used the Froude number approach from Sequeiros (2012) to estimate palaeo-flow conditions from straight subsurface channel geometries. Both studies interpreted the studied channel-forms as channel complexes, yet assumed that these geomorphic surfaces represented palaeo-hydraulic conduits. However, it is well documented in the literature that incision, construction and migration of individual channels in time and space may form compound surfaces that envelop the individual palaeo-hydraulic conduits and are larger in the cross-sectional area (Deptuck et al., 2007; Hodgson et al., 2016; Hubbard et al., 2020). Compound surfaces may therefore represent elements of higher hierarchy, such as channel complexes, that not only include submarine channel deposits but other depositional elements such as overbank deposits and MTDs, as observed in the Omakere Channel Complex (Figure 4.5). Calculations based on seismically-imaged channel-forms (cf. Li et al., 2018; Gong et al., 2020) may therefore yield outputs that are not representative of true palaeo-hydraulic conditions.

Channel-form A represents a shallow buried channel (< 300 mbsf) which might suggest that the imaged channel-form is more representative of the palaeo-hydraulic conduit. However, as shown in the modelling results of channel-form A, two channel bends (B1 and B3, Figure 4.7) show sediment concentration values that exceed by several orders of magnitude the 9% bulk sediment concentration theoretical threshold proposed for turbidity currents (Bagnold, 1956; Talling et al., 2012) (Figure 4.7I). Furthermore, results show that a cross-channel slope an order of magnitude larger than measured values provides sediment concentration values below the 9% threshold (Figure 4.7H). Therefore, it is interpreted that the channel morphometries at channel bends B1 and B3 are not representative of a palaeo-hydraulic conduit, but likely represent compound surfaces. Channel amalgamation

below seismic resolution could have produced a lower cross-channel slope than the true slope of an individual palaeo-hydraulic conduit, hence leading to sediment concentration overestimates.

The development of compound surfaces may have a more significant effect on the morphometrics, and thus modelling outputs, at channel bends where outer bend expansion occurs due to erosion (Kane and McCaffrey, 2008; Peakall and Sumner, 2015). Therefore, the preserved compound surface might yield a wider channel-form, with an overbank relief (e.g. B1 and B3 in channel-form A) and a radius of curvature that does not represent any palaeo-hydraulic conduit. Consequently, the model would not find a solution for sediment concentration values that are in equilibrium with the (compound) channel-form.

It follows that recovering palaeo-hydraulic conditions from subsurface submarine channels is likely more challenging than has been presented hitherto (e.g., Li and Gong, 2018; Li et al., 2018; Gong et al., 2020). Thus, previous calculations by Li et al. (2018) and Gong et al. (2020) might have yielded overestimates of palaeo-hydraulic properties (i.e. flow height, velocity and discharge) through the use of channel-complex morphometries as model inputs, given that the true palaeo-hydraulic conduits must have been smaller. Furthermore, the decrease in seismic resolution at greater burial depths would likely bring greater errors in the calculation of palaeo-hydraulic properties from imaged channel-forms.

4.7.1.2 Disequilibrium palaeo-hydraulic properties due to disequilibrium channel morphologies controlled by MTDs

Submarine channels may reach a stage in their evolution where their morphology is in equilibrium with the flows that they confine, hence allowing turbidity currents to transport sediment without aggrading or degrading the channel significantly (Pirmez et al., 2000; Kneller, 2003; Ferry et al., 2005). Therefore, equilibrium flow characteristics may be linked to a given equilibrium channel morphology with modelling techniques such as those used in this study. However, it has been shown that factors such as bed composition (e.g. MTD substrate), temporal changes in flow properties (Kneller, 2003) and tectonics (Georgiopoulou and Cartwright, 2013) may prevent submarine channels from reaching an equilibrium state.

Therefore, an alternative reason why the model does not find an equilibrium sediment concentration value (Figure 4.7i) is that channel-form A may represent a palaeo-hydraulic conduit with a disequilibrium channel morphology at bends B1 and

B3 (Figure 4.7A). The recalculated C in Figure 4.7I suggest that flows would need to build steeper cross-channel slopes, i.e. higher overbank asymmetries built through preferential overspill, in order to reach an equilibrium state with the channel morphology.

Achieving steeper overbank asymmetry in channel-form A may have been prevented by the flow confinement provided by MTD A (Figure 4.6A). MTD A exhibits a high variance response suggesting high internal deformation and heterogeneity, in the form of clasts (c.f. Ortiz-Karpf et al., 2017). Flow capture by MTDs and subsequent channel development has been documented in the Niger delta continental slope (Zhao et al., 2019); where strong confinement of flows by remnant blocks limited the formation of external levees, whereas weak MTD confinement allowed lateral channel migration, flow stripping and meander development. Also in the Taranaki Basin, New Zealand, inter-clast conduits have been established to result from flows travelling through blocky MTDs (Bull et al., 2020).

Strong MTD confinement at sections where B1 and B3 are located could have limited overspill needed to build steeper cross-channel slopes, therefore maintaining disequilibrium conditions. Alternatively, if flows exceeded the MTD confinement (i.e. overspilling and forming overbank deposits over the MTD, Figure 4.5A), the initial MTD confinement would have influenced the final cross-sectional shape of the channel-form, i.e., by forming an overbank relief that results in a cross-sectional area that possibly could not have been constructed solely by overspilling turbidity currents (B1 and B3, Figure 4.7A). Overbank modification by the MTD may therefore result in lower overbank asymmetry, which would lead to shallower cross-channel slope (γ) values than those that could have been derived by conventional overbank construction (Hansen et al., 2017). Therefore, this process may result in a channel relief and geometry that does not reflect an equilibrium state; anomalous calculated flow parameters could arise as a consequence (Figure 4.7I). In addition, the clast-rich MTD substrate may have played a role in limiting bed erosion, which is a key process to achieve equilibrium conditions (Kneller, 2003).

4.7.2 Comparing calculated modern to palaeo-hydraulic conditions in the Omakere Channel

Compound surfaces might have led to the development of channel-forms that do not represent palaeo-hydraulic conduits or MTD emplacement may limit the development of equilibrium channel morphologies, leading to overestimates of

sediment concentration in channel-form A (Figure 4.7). Nevertheless, the question arises as to why other channel bends and straight channel-form sections yield calculated palaeo-hydraulic values that are apparently well within accepted bulk sediment concentration (Figure 4.7I) and flow velocity values (Figure 4.7E) for turbidity currents. Realistic derived flow parameters and discharge values which are lower than those calculated in the modern Omakere Channel (Figure 4.7H) suggest that most of the channel-form could have represented the palaeo-hydraulic conduit and results from channel bends B1 and B3 (Figure 4.7) show that flows are locally out of equilibrium with the channel form these locations.

Hydraulic conditions calculated for the modern Omakere Channel (Figure 4.9A and 10B) (Crisóstomo-Figueroa et al., 2021) differ from those calculated for the subsurface (Figure 4.9C and 4.9D) (not considering any unrealistic flow values). The hydraulic conditions in the modern Omakere channel suggest thicker, denser and faster flows (Figure 4.9B) than the palaeo-hydraulic conditions in channel-form A (Figure 4.9D) (Crisóstomo-Figueroa et al., 2021, see Chapter 3).

Modern hydraulic conditions are predicted to bypass grain sizes up to coarse silt in flows carrying poorly-sorted material with sand grade material being deposited. This is consistent with sections where shallow RMS maps (Crisóstomo-Figueroa et al., 2021) suggest a sandy channel floor and where interbedded very fine sand and silt were retrieved in drop cores (Barnes et al., 2017). Palaeo-hydraulic conditions in channel-form A are calculated to represent the passage of shallow, dilute currents, that could transport up to coarse silt in well-sorted flows or very fine silt in poorly-sorted flows (Figure 4.9D). Therefore, if any sand was supplied to the system and transported as suspended load, it should have been deposited through Areas 1 to 3. However, the RMS map of channel-form A fill shows a low RMS amplitude response which is interpreted to represent a fine-grained dominated fill (Figure 4.6B) (following RMS interpretations from the modern channel validated by drop core data (Crisóstomo-Figueroa et al., 2021)). This suggests a disagreement between the estimated sedimentation predictions based on palaeo-hydraulic values and attribute maps of channel-form A, which might indicate that: 1) the disagreement is driven by the presence of a compound channel-form that hinders the recovery of true palaeo-hydraulic conditions; therefore, smaller channels with different morphometric attributes to those measured from the compound form might have acted as sand-bypass conduits and subsequently filled with fined-grained sediments. The identification of smaller scale channels might be hindered by seismic resolution

particularly at greater burial depths, as highlighted in other studies (Abreu et al., 2003). Alternatively, 2) the delivery of sand to downstream areas might have been promoted by bedload transport and sand-rich dense basal layers, which are not considered in these models. Therefore, the fill of channel-form A might represent a stage of the basin where dilute non-cohesive silty depositional flows (e.g. Strachan et al., 2016), such as those predicted with these models, predominated, hence deriving the observed RMS response.

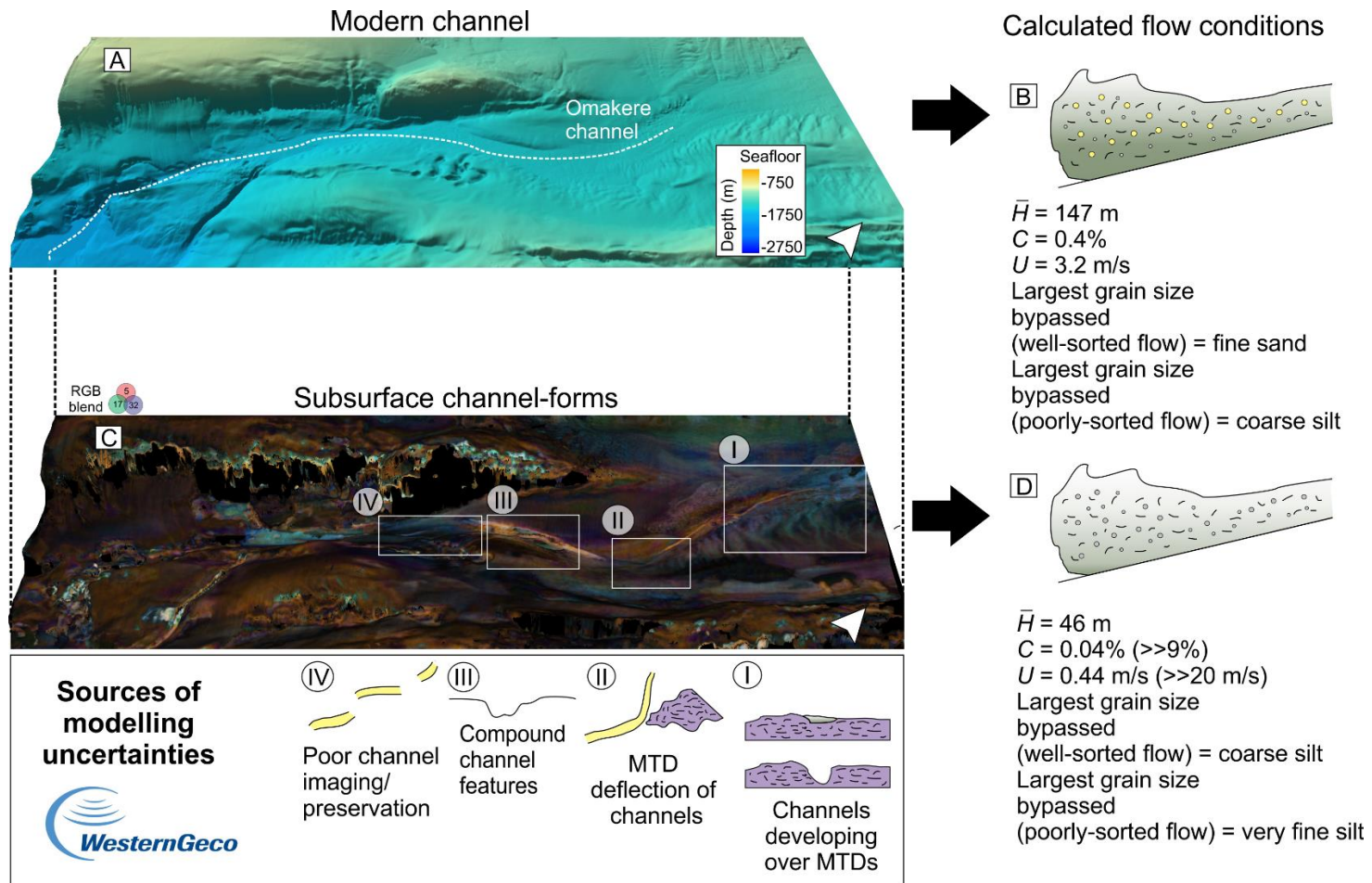


Figure 4.9 Subsurface vs surface modelling results and uncertainties. (A) Seafloor map of the Omakere Channel. (B) Calculated turbidity current conditions in the surficial channel (Crisóstomo-Figueroa et al., 2021). (C) Spectral decomposition map of the Omakere Channel Complex (see Figure 4.4 for the interpretation) showing the sources of modelling uncertainties in the subsurface. (D) Calculated turbidity current conditions in subsurface channel-form A.

4.7.3 Sources of modelling uncertainty and suggested solutions

These results show that the application of flow modelling techniques to subsurface channel-forms using a morphometrics-based approach is not straightforward; consequently, the identification of palaeo-hydraulic conduits through the techniques presented here remains challenging. Sources of modelling uncertainty that can be encountered in the subsurface include (Figure 4.9C): (I) channels developing over MTDs, (II) MTD deflection of channels (I and II both leading to the development of disequilibrium channel morphologies), (III) channel-forms that might represent compound channels, (IV) poor channel preservation, and (V) limitations associated with low seismic resolution.

Fine-scale analysis of exhumed submarine channel-fill has allowed differentiation between a compound channel-form and secondary channel-form surfaces that record the passage of turbidity currents (Hubbard et al., 2020). Therefore, differentiating between compound features in the subsurface and true palaeo-hydraulic conduits to confidently recover palaeo-hydraulic conditions in a system might require additional stratigraphic analysis using core data. Furthermore, a meta-data analysis approach (e.g. Cullis et al., 2019) contrasting morphometrics relationships from subsurface channel-forms (i.e. at different hierarchical levels) to their modern counterparts might help to constrain whether channel-forms observed in the subsurface are likely to represent palaeo-hydraulic conduits.

Identifying those channel-forms that represent good proxies for palaeo-hydraulic conduits is critical to analyse subsurface deepwater systems in terms of flow dynamics; this consideration likely applies to palaeo-hydraulic analyses in other environments and settings. Future studies aiming to integrate subsurface datasets with flow modelling techniques using a morphometrics-based approach (e.g. Komar, 1969; Sequeiros, 2012; Konsoer et al., 2013) should consider the examples and sources of uncertainty presented here.

4.8 Conclusions

In this study, 3D seismic reflection data interpretation of subsurface channel-forms in the Omakere Channel Complex, offshore New Zealand, are integrated with flow modelling techniques that use the channel-form morphometrics as input parameters to test whether the observed channel-forms might represent true equilibrium palaeo-hydraulic conduits. Results show that flow velocities and sediment concentrations

exceeded the theoretical limits for turbidity currents in some locations. This suggests that the observed channel-forms could be compound bodies or that they do not represent equilibrium channel morphologies, possibly due to the influence of the MTDs that form their immediate substrate. Differentiating between compound channel-forms and palaeo-hydraulic conduits within subsurface data is challenging, as is recognising whether preserved channel-forms were in equilibrium with traversing flows. These factors, together with difficulties arising from poor channel imaging and / or preservation constitute sources of modelling uncertainty in the calculation of palaeo-hydraulic conditions that may not apply to surficial channels. Modellers may be well advised to support interpretations of potential palaeo-hydraulic conduits through seismic facies analysis, core data (if available) and consideration of the channel-form burial depth. These modelling reservations may also apply in terrestrial or planetary settings where compound channel forms can be developed, and where the assumption of equilibrium flow conditions cannot be taken for granted.

Chapter 5 Modelling changes in the flow-ambient fluid interface tilt of turbidity currents: implications for the development of sinuous submarine channels

5.1 Introduction

Turbidity currents are a type of subaqueous flow that are driven by their excess density compared to the ambient fluid owing to suspended sediment (Talling et al., 2012). They can travel thousands of kilometres from shallow to deepwater settings and build channels that facilitate the transport of sediment (Piper and Normark, 2001), organic carbon (Hage et al., 2020) and pollutants (Zhong and Peng, 2021) (Figure 5.1). Submarine channels can develop sinuous planform morphologies, building deposits with complex architectural geometries (Peakall et al., 2007; Wynn et al., 2007); their reservoir potential makes channels of interest for hydrocarbon exploration (Abreu et al., 2003; Mayall et al., 2006) and for CO₂ storage (Marshall et al., 2016).

The geological and hydraulic factors controlling the development of submarine channel sinuosity have been a subject of intense debate (Clark et al., 1992; Peakall et al., 2000, 2012, 2013; Wynn et al., 2007; Kane and McCaffrey, 2008; Sylvester and Pirmez, 2019). Steep down-channel slope gradients and coarse-grained systems have been linked to the development of low sinuosity channels, with shallow gradients and fine-grained systems linked to the development of high sinuosity channels (Clark et al., 1992) (Figure 5.1). However, through the analysis of peak sinuosities from channels across the globe, Peakall et al. (2012) showed that the sinuosity-slope gradient relationship was weak, whereas the sinuosity-latitude relationship showed a stronger correlation. Furthermore, experimental work in rotating flumes has been interpreted to support the hypothesis that Coriolis forcing can impact turbidity current structure so as to hinder sinuosity development, and therefore that the latitudinal position of channels should be a strong control on the development of sinuosity (Cossu and Wells, 2010; Cossu et al., 2010; Wells and Cossu, 2013; Davarpanah Jazi et al., 2020). Consequently, low sinuosity channels are thought characteristic of high latitude areas where Coriolis forces are stronger (e.g., the Northwest Atlantic Mid-Ocean Channel (NAMOC), Klauke et al., 1997), whereas high sinuosity channels have been related to low latitudes where Coriolis forces are reduced (e.g., the Amazon Channel, Pirmez and Imran, 2003). However, based on the analysis of ancient turbidite channel systems of the Cerro Toro Formation in Chile, Cossu et al. (2015) suggested that smaller channels were less influenced by Coriolis forces.

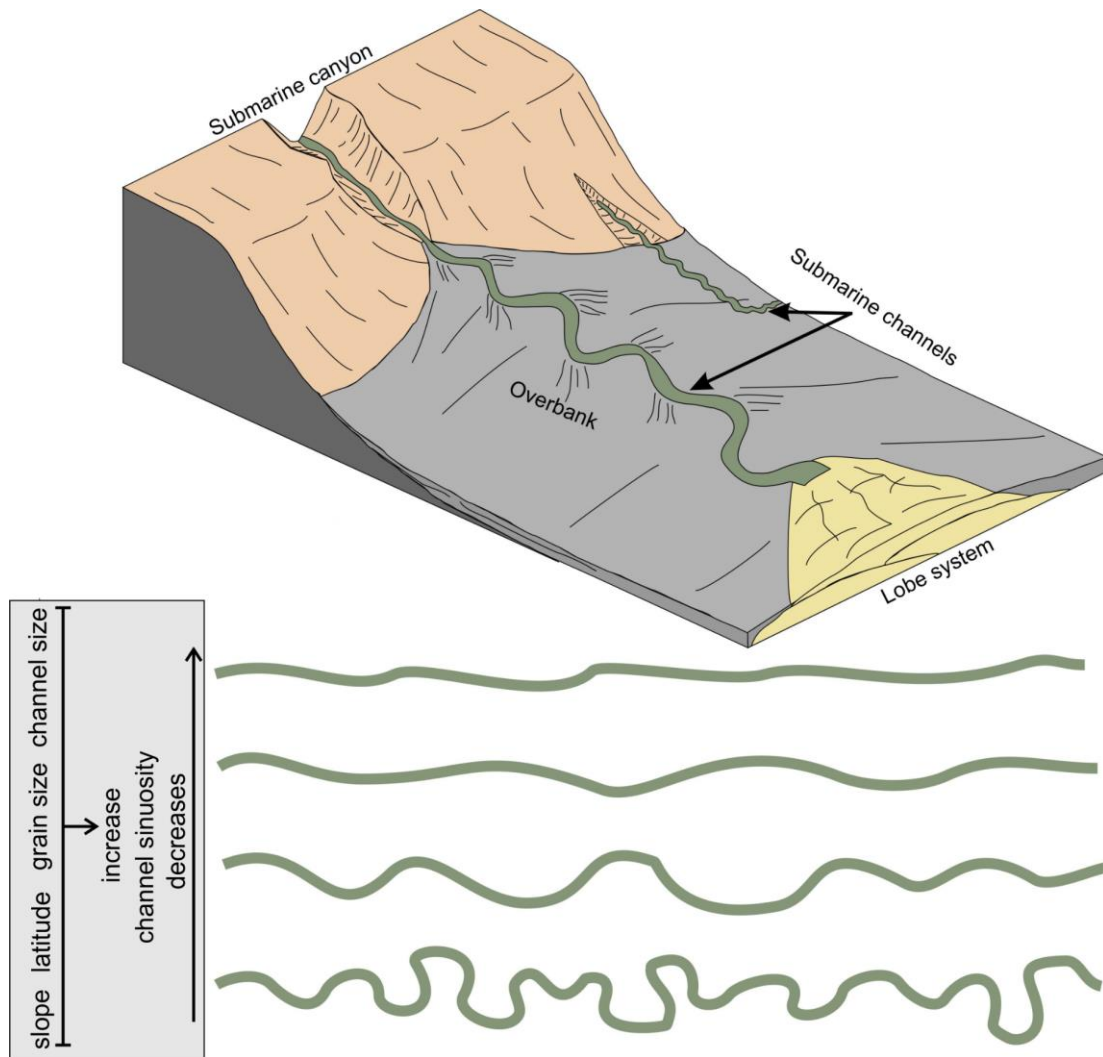


Figure 5.1 Schematic diagram of submarine channels on the slope and basin plain (adapted from Wells and Cossu, 2013) and proposed controls on the development of sinuosity in submarine channels (see text).

Laboratory experiments have shown that the Coriolis force can modify the three-dimensional structure of turbidity currents, including the flow-ambient fluid interface; around bends the orientation and slope of this surface depends on the interplay between Coriolis and centrifugal forces (Cossu and Wells, 2013; Wells and Dorrell, 2021). A key parameter used to evaluate whether Coriolis or centrifugal forces dominate is the Rossby number (Ro). Thus, under weak northern hemisphere rotation ($Ro \gg 1$) where Coriolis forcing is low, the balance between pressure and centrifugal forces dominates, resulting in an interface that alternates its tilt around successive bends, such that the interface always slopes toward the inner bank. (Figure 5.2A) (Cossu and Wells, 2010; Davarpanah Jazi et al., 2020). The velocity maximum and high-density core of the flow are co-located towards the outer bank (Davarpanah Jazi et al., 2020) and therefore they alternate channel sides between successive bends,

which promotes bend expansion and sinuosity development (Straub et al., 2008; Wells and Cossu, 2013).

Under strong northern hemisphere rotation ($Ro \approx 1$) (Figure 5.2B), anticlockwise flows have an equal force balance to anticlockwise flows with $Ro \gg 1$ (Figure 5.2A). In this case the tilting of the interface slopes towards the inner bank. However, experimental work has shown that steeper slopes are generated due to the effect of a stronger Coriolis force (Cossu and Wells, 2010). In clockwise flows, the Coriolis force deflects the bulk of the flow and causes a force balance rearrangement so that the Centrifugal and pressure forces oppose the Coriolis force (Figure 5.2B). Therefore, the flow interface is deflected and may slope instead towards the outer bank (Figure 5.2B) (Cossu and Wells, 2013). Furthermore, the velocity maximum is deflected towards the inner bend and the density core has been observed to be decoupled from the velocity field and remain directed towards the outer bend. This structure has been interpreted to diminish the potential for channels to develop sinuous bends, as there would be greater potential for erosion on the inner bend (Cossu and Wells, 2013; Davarpanah Jazi et al., 2020) and deposition on the outer bend where the maximum density is located (Davarpanah Jazi et al., 2020). Flow superelevation and overspill results in strong cross-sectional levee asymmetry, where the right levee is higher when looking in a downstream direction in northern hemisphere scenarios (Figure 5.2B) (Cossu and Wells, 2013; Dorrell et al., 2013a). The opposite force balances apply in the southern hemisphere, leading to higher left levees looking downstream.

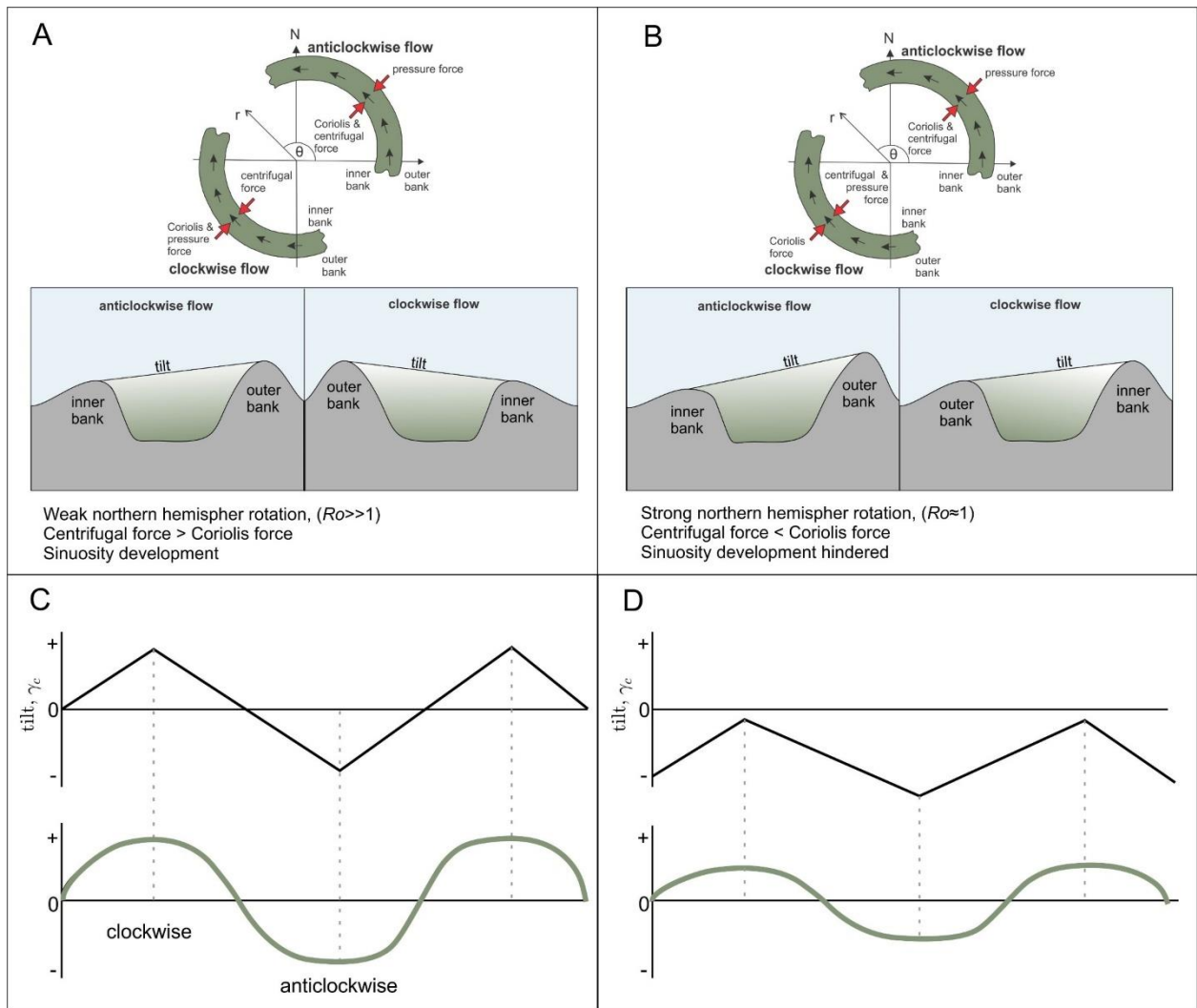


Figure 5.2 Changes in cross-channel forces due to Coriolis. Force balance and tilting under (A) weak northern hemisphere rotation and (B) strong northern hemisphere rotation; cross-sections looking in the downstream direction. (C) and (D) indicate the coordinate normal system used in the calculation of the tilt γ_c .

The role of Coriolis forces in channel sinuosity development was challenged by Sylvester et al., (2013) and Sylvester and Pirmez, (2019) who showed that high sinuosity channels are not exclusive to low latitude areas (e.g., the Danube Channel, Popescu et al., 2004) and that low sinuosity channels may also occur at low latitudes (e.g., the Tanzania Channel, Bourget et al., 2008). Using sinuosity measurements from individual bends from nine modern channel systems (in contrast to Peakall et al. 2012 who only used peak sinuosities), Sylvester and Pirmez (2019) showed that the latitude does not correlate well with sinuosity (i.e. contrary to the findings from Peakall et al. (2012)). They suggested that the Coriolis force was unlikely to have a big impact on the development of sinuosity in submarine channels and that it might only play a role in large scale channels at high latitude systems, such as the NAMOC.

In this chapter the slope of the flow-ambient fluid interface tilting was calculated using a modified version of the turbidity current modelling technique used in Chapters 3 and 4. Channel morphometrics from the NAMOC were extracted from the literature (Klaucke et al., 1997) and were used to test whether the modelling technique could be used with confidence to calculate areas of deflection of the flow-ambient fluid interface tilt due to Coriolis forces. One of the aims was to contribute to the debate on whether Coriolis forces control the development of sinuosity in submarine channels. If tilt modification is linked to the deflection of the velocity and density maxima within flows, promoting changes in erosion and deposition patterns (Davaranah Jazi et al., 2020), it may consequently hinder the development of channel sinuosity, as experimental observations suggest (Cossu and Wells, 2010; Wells and Cossu, 2013; Davaranah Jazi et al., 2020). Furthermore, through the solution of both cross- and downchannel forces, parameters such as latitude, radius of curvature, downchannel slope and depth-averaged flow properties can be evaluated under a broader set of conditions than experimental work can provide. Therefore, a second aim is to conduct a parametric study to assess the potential control of these parameters on the development of sinuous bends and to define the conditions that may or may not promote the modification of the flow-ambient fluid interface. A final aim is to re-assess the global submarine channel data compiled by Sylvester and Pirmez (2019) in light of the model predictions of conditions where Coriolis forces might exceed centrifugal forces; such analysis could provide an explanation of the observed sinuosity variations in modern channels across the globe.

5.2 Methods

5.2.1 Estimating the tilting of the flow-ambient fluid interface

The slope of the tilted flow-ambient fluid interface can be approximated through the surface-slope equation which describes the momentum balance of the pressure gradient force, the Coriolis force and the centrifugal force across a channel assuming depth averaged, bankfull flow conditions (Equation 5.1) (Komar, 1969)

$$gRC\gamma_c = \pm fU + \frac{U^2}{r}, \quad (5.1)$$

where $g = 9.81 \text{ m/s}^2$ gravity; $R = (\rho_s/\rho_f - 1)$ is the submerged specific gravity (where $\rho_s = 2650 \text{ kg/m}^3$ is the density of quartz for the material in suspension, and $\rho_f = 1000 \text{ kg/m}^3$ is the density of the fluid); C , the bulk sediment concentration (vol./vol.); γ_c = the slope of the flow-ambient fluid interface (m/m); f the Coriolis acceleration $f = 2\Omega \sin\theta$, where $-f$ applies for clockwise flows and $+f$ for anticlockwise flows, Ω is the Earth's

rotation rate, and θ the latitude; U , the downstream flow velocity in m/s; and r , the thalweg radius of curvature (m).

Equation (5.1) can be rewritten in terms of the Froude number, Fr , (Wells and Dorrell, 2021) where $Fr = U/\sqrt{gR\bar{C}\bar{H}}$ (Parker et al., 1987),

$$\gamma_c = Fr^2 \left(\frac{\pm f\bar{H}}{Fr\sqrt{gR\bar{C}\bar{H}}} + \frac{\bar{H}}{r} \right), \quad (5.2)$$

where \bar{H} is the average flow depth (m).

Down-channel forces can be calculated using the balance of gravitational driving force with frictional drag at the bed, and through the entrainment of ambient water following the model of Parker et al., (1987) (e.g., Abad et al. 2011),

$$S = \frac{C_d + e_w(1 + \frac{Ri}{2})}{Ri}, \quad (5.3)$$

where S is the down-channel slope in m/m; $C_d = 0.0025$ (Abad et al., 2011; Konsoer et al., 2013), the drag coefficient that, for simplicity, is considered constant in all calculations; Ri , the bulk Richardson number (which scales inversely with Fr^2 (Wells and Dorrell, 2020)) is a measure of mixing of the flow-ambient fluid interface (Parker et al., 1987; Abad et al., 2011),

$$Ri = \frac{gR\bar{C}\bar{H}}{U^2} = \frac{1}{Fr^2}, \quad (5.4)$$

and e_w , the ambient water entrainment by mixing is defined using

$$e_w = \frac{0.00153}{0.0204 + Ri}, \quad (5.5)$$

a relation derived empirically by Parker et al., (1987) for turbidity currents.

The MATLAB script developed in Chapter 3 incorporating a nonlinear least square MATLAB solver (*lsqnonlin*) was adapted to find optimal solutions of γ_c (while C remained fixed, see sections 5.2.2 to 5.2.4), and Fr , jointly solving for both cross-channel forces (Equation 5.2) (Komar, 1969) and down-channel forces (Equation 5.3) (Abad et al., 2011). The trust-region-reflective algorithm (Coleman and Li, 1996) was used in all computations with a tolerance point of 10^{-12} .

The degree to which turbidity currents are influenced by Coriolis forces can be determined by the dimensionless Rossby number (Wells and Dorrell, 2021)

$$Ro_R = \frac{U}{L_f}, \quad (5.6)$$

where L represents the horizontal length scale of the current, here $L = r$. Values of $Ro_R \gg 1$ describe a centrifugal dominated flow, while $Ro_R \approx 1$ describe flows where the Coriolis force dominates (Cossu and Wells, 2010; Wells and Dorrell, 2021).

A coordinate normal system was used to detect the deflection of the flow-ambient fluid interface γ_c due to Coriolis (Figure 5.2C and 5.2D); therefore, γ_c values derived from clockwise flows retained their sign whereas γ_c values derived from anticlockwise flows were multiplied by -1 (Figure 5.2C). The ratio γ_r is a measure of the tilting magnitude change between two consecutive bends.

5.2.2 Validating model tilt predictions with observed tilting in the NAMOC

The NAMOC is a large-scale, low sinuosity channel located in the Labrador Sea that displays a strong channel-levee asymmetry (Klaucke et al., 1997, 1998). The right-hand levee is consistently higher than the left levee despite changes in bend orientation, which has been attributed to the effect of Coriolis causing flow deflection and preferential overspill to the right-hand bank (Klaucke et al., 1997). Therefore, this channel constitutes a good field example to test the accuracy of the correspondence of computed model predictions of the ambient-fluid interface slope γ_c to the observed tilting of the channel levees, γ_m (assuming that the observed levee asymmetry is a proxy for the tilting of the flows travelling through the channel). Furthermore, morphometric measurements from the channel were analysed to evaluate the influence of the radius of curvature, downchannel slope and latitude on the observed changes in the tilt and sinuosity.

Channel bend morphometrics were obtained from Klaucke et al. (1995) and Klaucke et al. (1997), that cover an approximately 950 km long stretch of the channel ranging in latitude from 60° to 53° (Appendix C.1). Channel bend data (H , S , θ and r) were used as input parameters in Equations (5.2) and (5.3) to calculate γ_c ; while the channel levee tilt was calculated through $\gamma_m = \Delta H/w$ (Appendix C.1). Two data points from clockwise bends were omitted from the analysis due to documented levee collapses (red arrows in Figure 5.3A) (Klaucke et al., 1997). Levee collapses increase ΔH , thus making γ_m larger than the tilting expected from the effect of overspilling currents, invalidating comparisons of γ_c and γ_m .

Input values of C were estimated through

$$C = \frac{1}{R} \left(\frac{\rho_t}{\rho_f} - 1 \right), \quad (5.7)$$

where ρ_t is the current density (Konsoer et al., 2013). Klaucke et al., (1997) calculated that excess densities $\rho_t - \rho_f$ in the NAMOC ranged from 1 to 12 kgm⁻³ which, using Equation (5.7), are equivalent to C of 0.06% to 0.7%, respectively. Furthermore, a third value between the low and high C values was considered, where $C = 0.2\%$.

5.2.3 Calculating changes in the tilting due to hydraulic, morphological and latitudinal changes

Equations (5.2) to (5.5) were used to evaluate the degree to which changes in the Coriolis force, the turbidity current properties and the confining channel morphology impact changes in the tilting of the flow-ambient fluid interface that might lead to lateral flow deflection. For a turbidity current travelling through a channel with a decreasing downchannel slope (10^{-1} - 10^{-3} m/m) and a flow depth that decreases with distance (200-10 m), 27 different scenarios were evaluated. The input parameters of the first nine scenarios are shown in Table 5.1. Three fixed latitudes (5° , 35° and 55°), which are representative of channels located at low, mid and high latitudes, were chosen to evaluate the latitudinal effect. Three fixed radii of curvature (500 m, 3,000 m and 30,000 m) were used to evaluate the effect of changes in the scale of the bend. Three sediment concentrations were used to assess the effect of dilute vs. dense flows; $C = 0.02\%$ was used in scenarios 1 to 9. Scenarios 10-18 and 19-27 used the same input parameters shown in Table 5.1, except for the value of sediment concentration that was fixed at 0.2% and 2%, respectively.

Table 5.1 Input parameters used in the modelling of the flow-ambient fluid interface tilting.

Scenario	r (m)	Latitude θ ($^\circ$)	C (%)	H (m)	S (m/m)
1	500	5	Scenarios 1-9 0.02%	10-200	10^{-3} - 10^{-1}
2	3,000				
3	30,000				
4	500	35	Scenarios 10-18 0.2%		
5	3,000				
6	30,000				
7	500	55 $^\circ$	Scenarios 19-27 2%		
8	3,000				
9	30,000				

5.2.4 Calculating the downchannel transition slope

Lateral deflection of the flow-ambient fluid interface implies that before the deflection occurs, there is a balance of the Coriolis and centrifugal forces where the interface is

flat, then $\gamma_c = 0$ and $Ro_r = -1$ (Wells and Dorrell, 2021). Therefore, assuming a flat interface that represents the point of transition to flow deflection and setting $\gamma_c = 0$ in Equation (5.2), the downchannel slope S_T at which the transition occurs was approximated through Equation (5.3) and

$$Fr\sqrt{gRCH} = -fr, \quad (5.8)$$

where Fr values were used as inputs into Equation (5.3) through the relationship established in Equation (5.4) (Wells and Dorrell, 2020). Hence, S_T defines the minimum (threshold) downchannel slope needed in a channel for the development of sinuosity.

The calculation of S_T allows the evaluation of the conditions needed to achieve flow deflection over a wider range of latitudes, radius of curvature and flow conditions compared to those used in section 5.2.3. The *meshgrid* function in MATLAB was used to create three 2-D grids with vectors x and y to calculate contour plots of S_T and assess its variation as a function of r , C , H , and latitude θ . The range of r values shown in Table 5.2 was used as input in vector x for all the grids whereas vector y took the range of values from C , H and θ (Table 5.2) in the first, second and third grid, respectively. The number of datapoints in each vector was determined by a length, z , where $z=300$. Each 2-D grid produced was used as input into Equation (5.8) together with the baseline values for each parameter when not varied within the grid (Table 5.2).

Table 5.2 Input parameters in the calculation of S_T .

	r (m)	C (%)	H (m)	Latitude θ (°)
Range	90-65,000	0.01-1	5-300	3-90
Baseline value	-	0.2	100	35

Contours of S_T as a function of latitude and radius for different flow properties were produced and submarine channel data available from nine channels (i.e. Amazon, Danube, Knight Inlet, Monterey, NAMOC, Nile, Rhône, Tanzania and Zaire (Sylvester and Pirmez, 2019) were plotted to determine whether flow deflection due to Coriolis is likely in these systems. Furthermore, the assessment of whether the observed patterns in submarine channel sinuosity are strongly controlled by latitudinal effects

(Peakall et al., 2012) or by other parameters such as the slope, scale of the channel or flow properties (Sylvester and Pirmez, 2019) was carried out.

The digitized channel centrelines and the Python code of Sylvester and Pirmez (2019) were downloaded and run to extract channel sinuosities, radius of curvatures and latitudes from the nine systems. A summary of the channel data used and the downchannel slope of each system (extracted from the literature) is shown in Appendix C.2.

5.3 Results

5.3.1 NAMOC tilting and morphometric relationships

The first ~366 km stretch of the NAMOC is classified as the 'equilibrium channel' (zone 1, Figure 5.3A) while the remaining channel length in this dataset is classified as the 'modified equilibrium channel' (zone 2, Figure 5.3A) due to tributaries joining the NAMOC whose influence contribute to changes in the channel morphology (Klaucke et al., 1997). This part of the work was focused on analysing changes in the tilt and its relationship with sinuosity and other channel parameters, which were not included in the original work of Klaucke et al. (1997).

The NAMOC tilt and sinuosity display high variability throughout the channel length (Figure 5.3A). The tilt increases downchannel in zone 1 suggesting higher levee asymmetry than zone 2 which displays a decreasing trend. Two peaks above 0.008 m/m correspond to levee collapses in both zones (Klaucke et al., 1997). The sinuosity, si , has a trend that increases from a position at ~120 km (1.01) up to the point of transition between zone 1 and 2 (1.13) and continues with a decreasing trend but with some bends displaying sinuosities between 1.10 and 1.15 (Figure 5.3A).

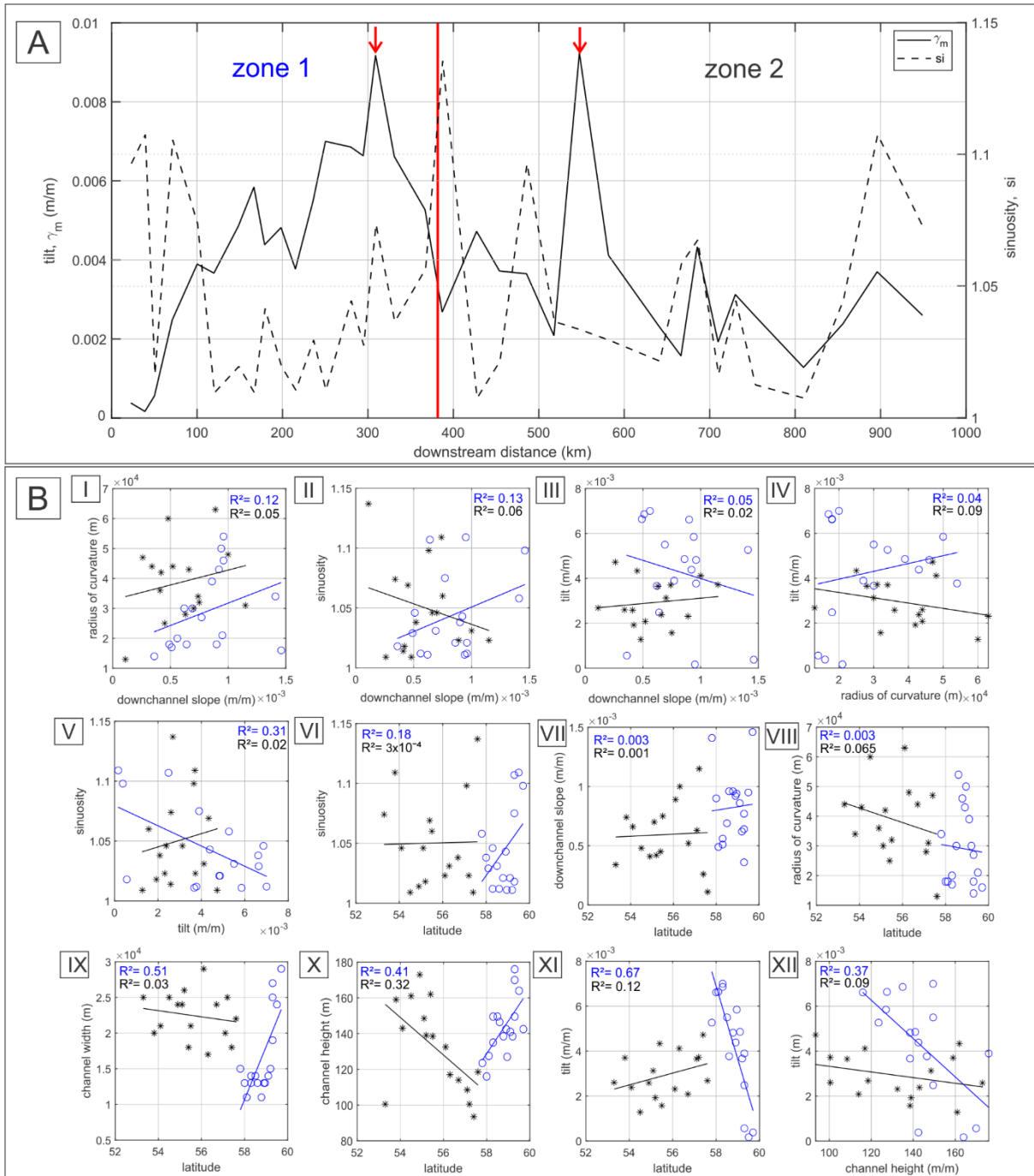


Figure 5.3 NAMOC morphometrics extracted from Klaucke et al., (1997). (A) Downchannel changes in the measured tilt and sinuosity. Zone 1 corresponds to the ‘equilibrium channel’ whereas zone 2 to the ‘modified equilibrium channel’. Red arrows indicate locations of levee collapse. (B) Morphometric relationships for each channel zone with calculated R^2 values. Blue circles correspond to data points from zone 1 and black asterisks to zone 2.

Scatter plots comparing different morphometric parameters against the tilt, sinuosity and latitude for each channel zone and their calculated R^2 values are shown in Figure 5.3B. R^2 values are higher in the equilibrium channel section (zone 1) than the

modified equilibrium channel where data are highly scattered in most cases (zone 2). Plots I, II and III in Figure 5.3B display weak relationships ($R^2 < 0.15$) in both zones for the downchannel slope against the radius of curvature, sinuosity and tilt, respectively. Plot IV shows the radius and the tilt have a weak relationship. The tilt against the sinuosity in V has a higher value of $R^2=0.31$ in zone 1, with the sinuosity decreasing as the tilt increases; zone 2 displays a weak relationship with an $R^2=0.02$. Plots VI, VII and VIII of latitude against sinuosity, downchannel slope and radius of curvature respectively, have weak relationships ($R^2 < 0.18$). The highest R^2 values are observed in zone 1 of Plots IX, X and XI of the latitude against the channel width, tilt and channel height respectively. Latitudes corresponding to zone 1 (between 58° and 60°) show a positive relationship with channel width (plot IX) and height (plot X) with R^2 values of 0.51 and 0.41, respectively. Both width and height decrease with decreasing latitude, i.e., in the case of the NAMOC, they decrease downchannel in zone 1. Channel width in zone 2 (plot IX) shows a negative but weak relationship with latitude; whereas channel height (plot X) also shows a negative but stronger relationship with $R^2=0.32$, where height increases with decreasing latitude. Latitude-tilt in zone 1 (plot XI) shows the strongest relationship with an $R^2=0.67$ where tilt increases with decreasing latitude, i.e., it increases downchannel as seen in Figure 5.3A; whereas the tilt in zone 2 has a positive but weaker relationship with latitude. Plot XII shows the relationship between channel height and tilt, where the tilt decreases with increasing height in both zones; however, zone 1 exhibits a higher R^2 value of 0.37.

5.3.2 Comparing model predictions of the tilt to the NAMOC tilting

The NAMOC tilt γ_c calculated as described in section 5.2.2 was compared against the measured tilt γ_m with the aim of testing whether the model captured the flow-ambient fluid interface in clockwise bends, as schematically shown in Figure 5.2. A positive clockwise γ_c result and a negative anticlockwise γ_c result (Figure 5.2C) indicates changes in tilting direction across successive bends. Negative clockwise γ_c results (Figure 5.2D) indicate that the flow is deflected such that the tilting would not alternate across bends. Modelling results for the three sediment concentrations in the NAMOC all show negative γ_c values (Figure 5.4A) (except for one single positive value at the start of $C=0.74\%$), hence clockwise flows are modelled to have a reversed tilt, suggesting that the flow is deflected for clockwise flows throughout the channel stretch (Figure 5.4A). The calculated reversed tilt agrees with the suggested flow deflection in the NAMOC due to Coriolis which has been proposed as a mechanism of producing right-hand side levees that are higher than left-hand side levees in both clockwise and anticlockwise flows (Klaucke et al., 1997; Wells and Cossu, 2013).

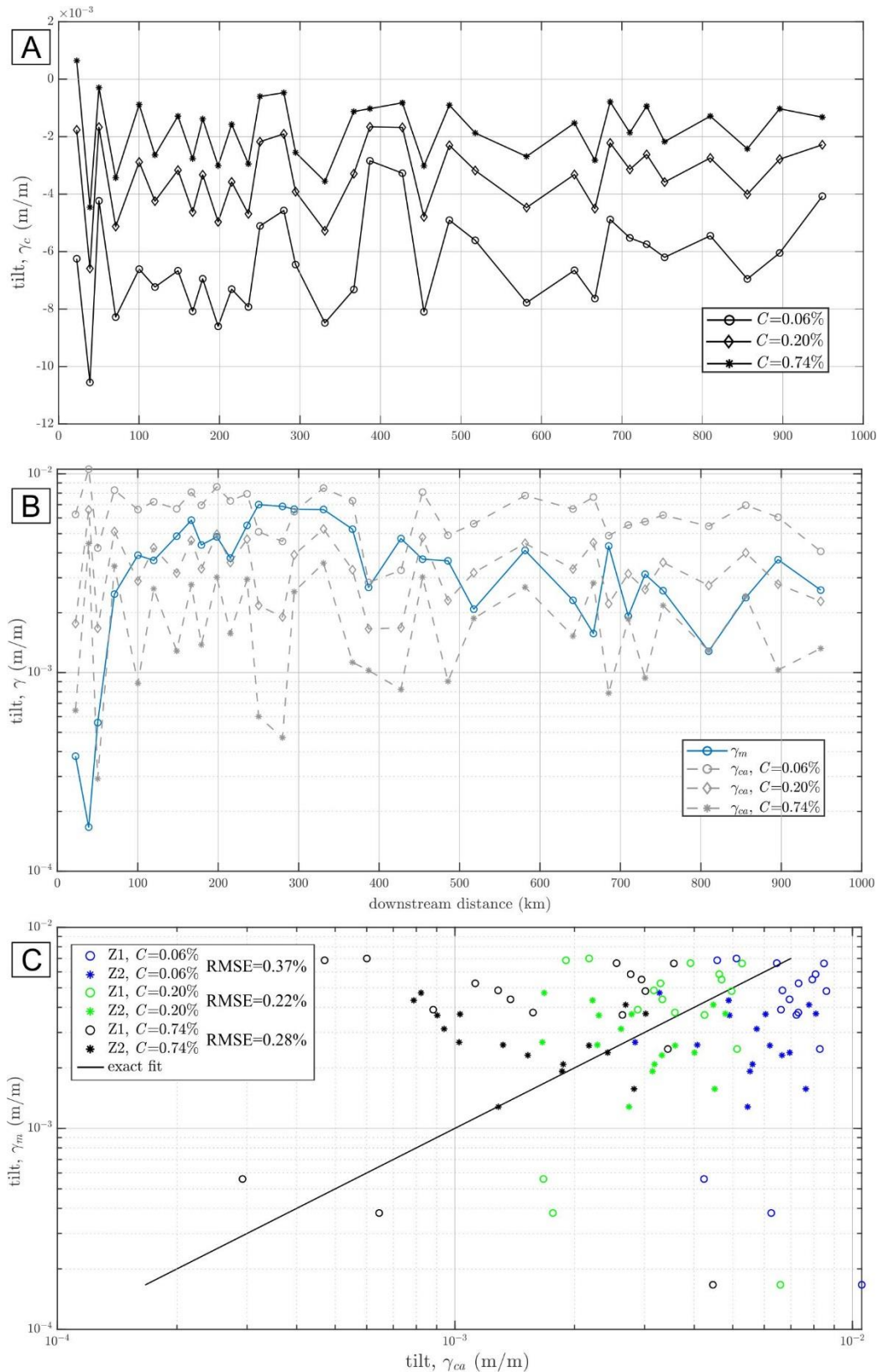


Figure 5.4 Changes in calculated turbidity current tilt for the NAMOC. (A) Calculated tilting from three different sediment concentrations. (B) Absolute values of the calculated tilting compared to the measured tilting. (C) Absolute calculated tilting against measured tilting. Data broken down into the sediment concentration and NAMOC zones defined in Methods.

The absolute slope values of the calculated tilt γ_{ca} compared to the channel tilt γ_m show that γ_m falls within the range of γ_{ca} for the proposed sediment concentrations (0.06% - 0.74%), except for the first three channel bends where γ_m is lower (Figure 5.4B). γ_m and γ_{ca} range from 10^{-3} to 10^{-2} , although some bends in the calculated flows with $C=0.74\%$ derive tilts less than 10^{-3} . Hence, γ_{ca} values suggest that dilute flows have steeper slopes than denser flows (Figure 5.4B).

A comparison of the predicted tilt γ_{ca} against the observed channel-levee tilt γ_m shows that calculations with 0.2% C produce the lowest RMSE error of 0.22%, followed by 0.74% C flows with 0.28% RMSE and 0.06% C flows produce an RMSE of 0.37% (Figure 5.4C).

These results shows that the model makes good predictions of areas of flow modification due to Coriolis forcing. This conclusion lends confidence to the results of the following section showing calculations of the variation of tilting under different channel and flow conditions; these are used to identify cases where significant deflection of the flow-ambient fluid interface might arise.

5.3.3 Variations in the tilting of the flow-ambient fluid interface

The results of the changes in the flow-ambient fluid interface as a function of the radius of curvature, latitude, downchannel slope and sediment concentration are shown in Figures 5.5 to 5.7. Saw-tooth patterns of γ_c follow the sign conventions established in section 5.2.1 (Figure 5.2C and 5.2D) with peaks corresponding to clockwise bends and troughs to anticlockwise bends. Positive peaks and negative troughs that produce a negative ratio γ_r indicate conditions where the slope of the tilt changes across bends (Figure 5.2A); whereas negative peaks and troughs that produce a positive γ_r suggest that the tilt in clockwise flows is reversed. Furthermore, $|\gamma_r| \cong 1$ indicates more stability in the slope magnitude of γ_c across bends whereas $1 \ll |\gamma_r| \ll 1$ suggests a less stable slope (indicated with blue bars in Figures 5.5 to 5.7).

Dilute flows with $C=0.02\%$ traversing bends with small radius of curvatures ($r = 500$ m) (Figure 5.5A, 5.5B and 5.5C) would not experience flow deflection at any latitude, due to the centrifugal force being greater than the Coriolis force ($Ro_R \gg 1$, Figure 5.8A). At low latitudes γ_r is ~ 1 (Figure 5.5A) and as the latitude increases, γ_r suggests less stability at shallow slopes (Figure 5.5B and 5.5C). In the three latitude examples for all radii of curvature, γ_c increases with downchannel slope and flow height (Figure, 5.5, 5.6, and 5.7).

Flows traversing bends with intermediate radii of curvature ($r = 3,000$ m) at low latitudes (Figure 5.5D) would not experience flow deflection ($|Ro_R| \gg 1$, Figure 5.8B),

however, the stability of the tilt decreases at shallow slopes. As the latitude increases to 35° (Figure 5.5E) and 55° (Figure 5.5F), the saw-tooth shape pattern becomes negative and the ratio becomes positive at shallow slopes, suggesting that flow deflection occurs at a given downchannel slope, i.e., the tilt transition slope S_T , where $|Ro_R| < 1$ (Figure 5.8B). The point of transition moves towards steeper slopes as the latitude increases (Figure 5.5F). Furthermore, the ratio shows that the stability of the tilt decreases near the transition point and stabilizes away from it (Figure 5.5E and 5.5F).

At larger radii of curvature ($r = 30,000$ m), flow deflection is observed at 5° (Figure 5.5G), 35° (Figure 5.5H), and 55° (Figure 5.5I) latitudes. The transition slope also moves towards steeper slopes from low to high latitudes. At 35° and 55° latitudes, positive γ_r values cover the entire downchannel slope range and $|Ro_R| \ll 1$ (Figure 5.8C).

The tilts of denser flows with $C=0.2\%$ (Figure 5.6) and 2% (Figure 5.7) show similar trends to those of dilute flows, where γ_c increases with downchannel slope and flow height. Also, at small radii of curvature (Figure 5.6A to 5.6C and Figure 5.7A to 5.7C) and at intermediate values ($r = 3,000$ m) at 5° latitude (Figure 5.6D and Figure 5.7D) flow deflection is not observed ($|Ro_R| \gg 1$, Figure 5.8A and 5.8B). Differences between dilute and denser flows are seen in areas of flow deflection. For flows with $C=0.2\%$ and $r = 3,000$ m (Figure 5.6D to 5.6F) zones of transition are observed only at 55° latitudes (Figure 5.6F), where the transition occurs at a shallower slope than its dilute equivalent (Figure 5.5F). The zone of transition in larger radii of curvature channels (Figure 5.6G to 5.6I) also occurs at shallower slopes compared to dilute flows. The tilt of flows with $C=2\%$ do not suggest flow deflection at any of the modelled latitudes when $r = 500$ m (Figure 5.7A to 5.7C) and $3,000$ m (Figure 5.7D to 5.7F), nor at 5° latitude when $r = 30,000$ m (Figure 5.7G). Flow deflection is only predicted at 35° and 55° latitudes for large radius (Figure 5.7H and 5.7I) and occurs at $|Ro_R| < 1.05$ (Figure 5.8D). Furthermore, $|Ro_R|$ for a given radius and latitude increases with C (Figure 5.8). Values of γ_r in denser flows are closer to 1, suggesting higher stability than in dilute flows.

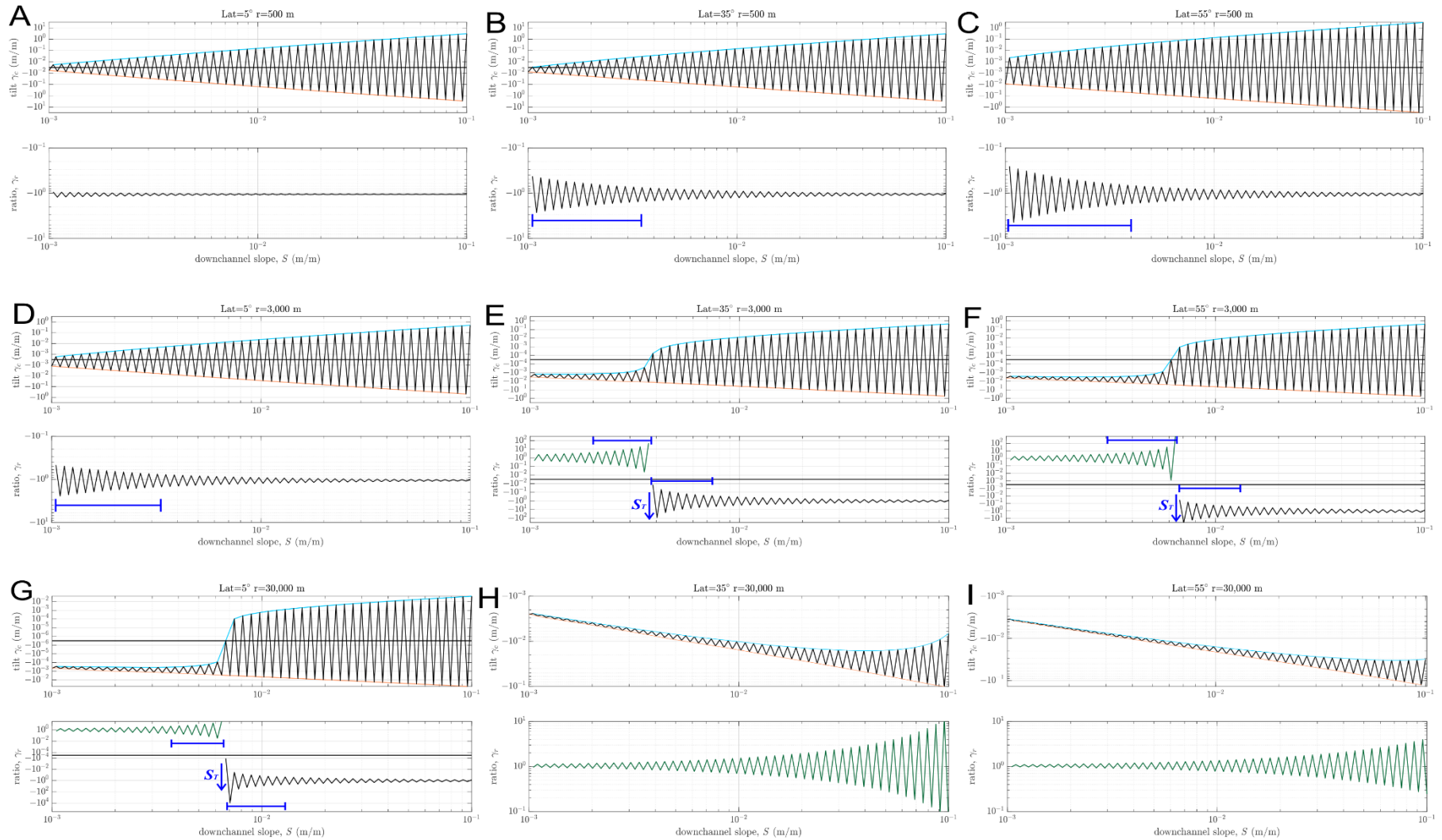


Figure 5.5 Calculated tilting γ_c and ratio γ_r at $C=0.02\%$. The latitude increases in each panel horizontally as 5° , 35° and 55° . (A-C) $r=500$ (D-F) $r=3$ km. (G-I) $r=30$ km. Vertical blue arrows indicate the tilting transition slope S_T . Horizontal bars indicate zones of tilting instability.

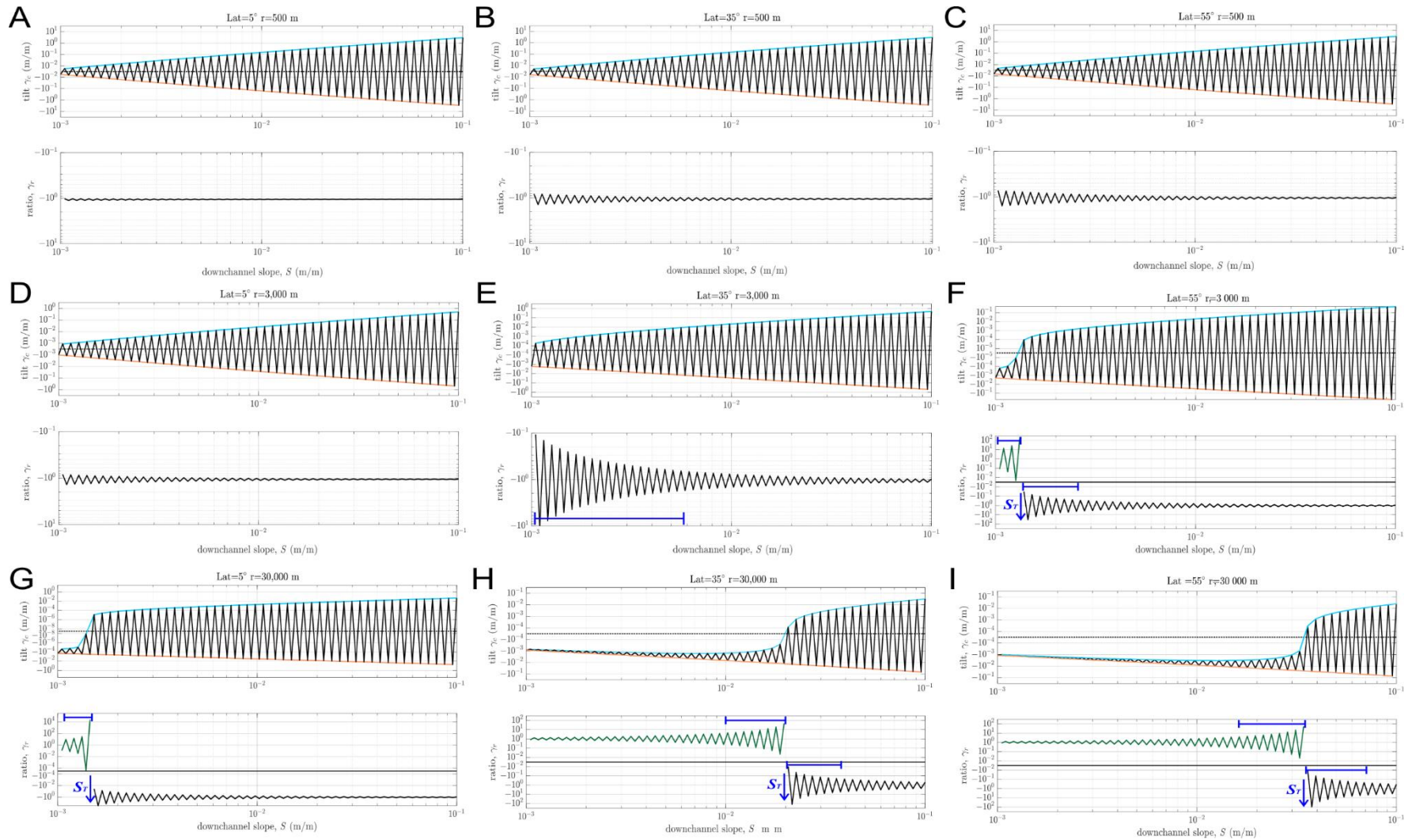


Figure 5.6 Calculated tilting γ_c and ratio γ_r at $C=0.2\%$. The latitude increases in each panel horizontally as 5° , 35° and 55° . (A-C) $r = 500$ (D-F) $r = 3$ km. (G-I) $r = 30$ km. Vertical blue arrows indicate the tilting transition slope S_T . Horizontal bars indicate zones of tilting instability.

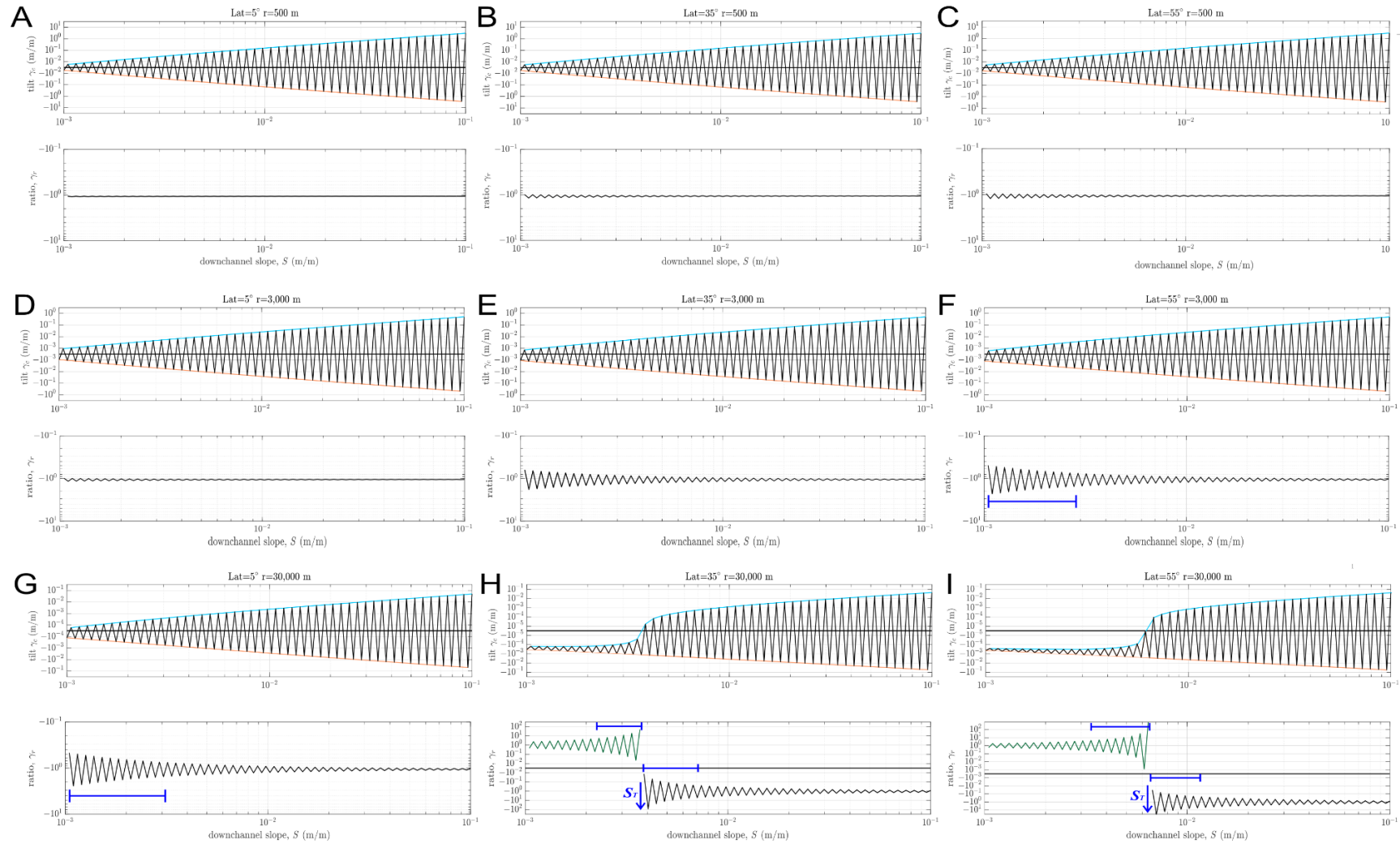


Figure 5.7 Calculated tilting γ_c and ratio γ_r at $C=2\%$. The latitude increases in each panel horizontally as 5° , 35° and 55° . (A-C) $r = 500$ (D-F) $r = 3$ km. (G-I) $r = 30$ km. Vertical blue arrows indicate the tilting transition slope S_T . Horizontal bars indicate zones of tilting instability.

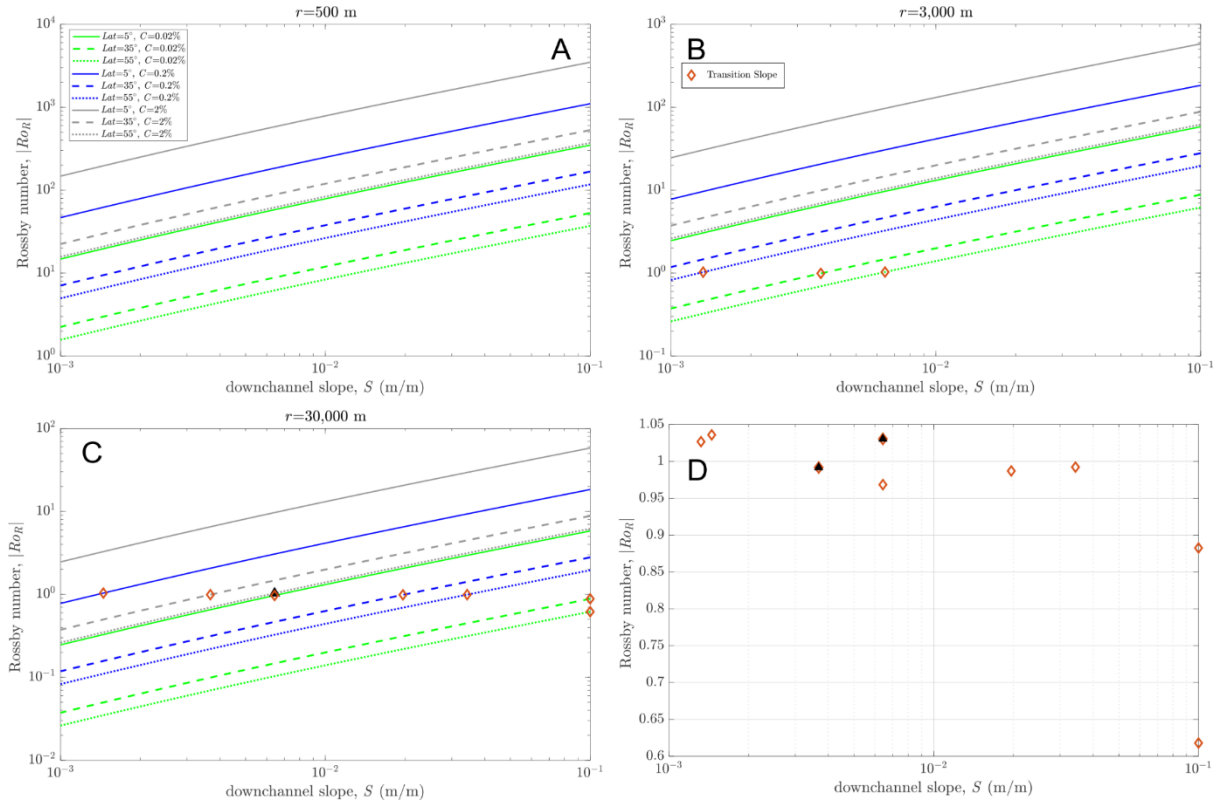


Figure 5.8 Calculated absolute Rossby number as a function latitude, sediment concentration and radius of curvature for (A) small, $r = 500$ m, (B) intermediate, $r = 3,000$ m and (C) large, $r = 30,000$ m, bends. Symbols show transition slopes. (D) Transition slopes observed for all modelling results of γ_c (see Figures 5.5 to 5.7).

5.3.4 Variations in the tilting transition slope S_T

The identification of flow deflection occurring at a specific downchannel transition slope, S_T motivated further investigation of where the transition might occur under a broader set of channel and flow conditions. Thereby, S_T values that would promote flow deflection were determined as a function of the scale of the bend, latitude and flow conditions.

S_T is proportional to the radius of curvature but inversely proportional to sediment concentration (Figure 5.9A). The transition slope increases with radius of curvature from $\sim 10^{-7}$ at $r = 300$ m to $\sim 10^{-2}$ at $r = 60,000$ for $C = 1\%$, therefore, small bends have lower transition slopes than large bends. As the flow density decreases, S_T increases up to $\sim 10^{-5}$ to $>10^0$ at small and large bends respectively. Dense flows have lower transition slopes than dilute flows for a given radius of curvature. Similarly, S_T increases with a decreasing flow height, where deep flows have lower transition slopes than shallow flows (Figure 5.9B). The variation of S_T with latitude shows that transition slopes are proportional to

latitude (Figure 5.9C). For a given radius, S_T increases as the latitude increases. Channels at low latitudes and small radius of curvature have the lowest transition slopes; whereas, large radius at high latitudes have the steepest. Furthermore, little change is observed in S_T contours at latitudes above 60° .

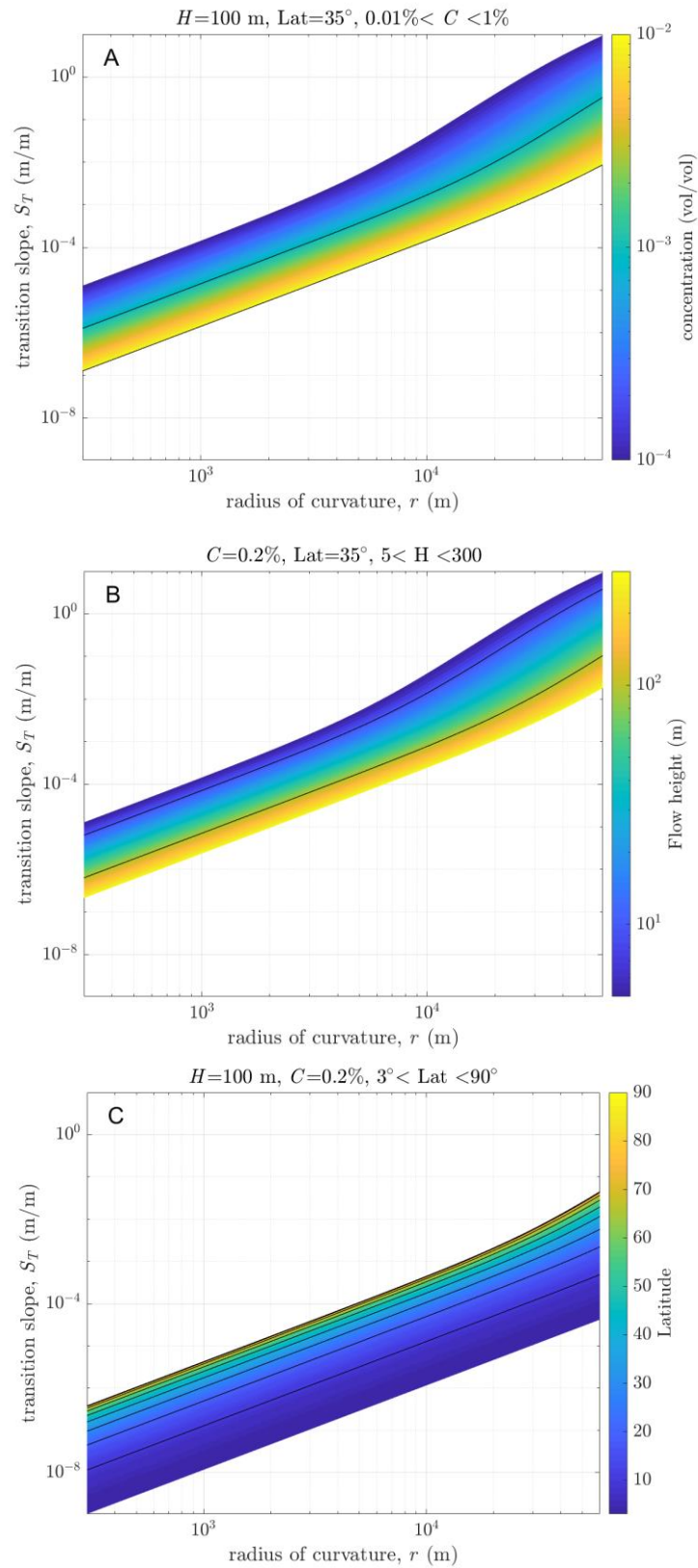


Figure 5.9 Changes in the calculated tilting transition slope S_T with (A) sediment concentration, (B) flow height and (C) latitude.

5.3.5 S_T and global submarine channel data

The latitude, sinuosity and radius of curvatures from nine submarine channels were obtained from Sylvester and Pirmez (2019): Amazon (Pirmez and Flood, 1995), Danube (Popescu et al., 2004), Knight Inlet (Ren et al., 1996), Monterey (Fildani and Normark, 2004), NAMOC (Klaucke et al., 1997), Nile (Migeon et al., 2010), RhôneRhône (Torres et al., 1997), Tanzania (Bourget et al., 2008) and Zaire (Babonneau et al., 2002) (Figure 5.10) (Appendix C.2). These channel systems span latitudes from 3° (Amazon) to 60° (NAMOC) and show the sinuosity for every channel bend (Figure 5.10A). The lowest sinuosities are observed in the Tanzania channel and NAMOC, with peak sinuosity of 1.11 and 1.15, respectively (Figure 5.10A, Appendix C.2). The RhôneRhône and Monterey channels follow with 1.62 and 2.35, respectively. The Danube, Zaire and Amazon channels have a peak sinuosities of 3.46, 3.5 and 4.1, respectively. Although most bends in the Knight Inlet have sinuosity values of less than 2.7, its peak sinuosity is 4.24; similarly, although most bends in the Nile channel are under 3.2, it has the highest sinuosity, of 4.7. The data spans radii of curvature of several orders of magnitude (from ~ 91 up to $\sim 14,800$ m) and shows that sinuosity decreases with increasing radius of curvature (Figure 5.10B).

Contour plots of calculated S_T vs latitude, plus the Sylvester and Pirmez (2019) channel data are shown in Figure 5.11. Data symbols correspond to the mean radius of curvature and vertical bars extend to the minimum and maximum radius of curvature measured. Coloured S_T contours match channel symbols according to the magnitude of their downchannel slope.

The values of the S_T contours increase as radius of curvature and latitude increase for all the flow conditions modelled (Figure 5.11A to Figure 5.11D). For the case of a deep and dilute current, most channels plot below their corresponding contour (Figure 5.11A). The mean radius of Tanzania is proximal to its contour (10^{-3}) whereas the NAMOC mean radius is located above it (10^{-4}) by one order of magnitude (Figure 5.11A). As the sediment concentration increases, the contours decrease for a given latitude and radius (Figure 5.11B). Therefore, channels plot further below their corresponding contour. S_T contours of a shallow and dense turbidity current show a similar relationship as those for deep and dilute (Figure 5.11C), where channels plot below their contours except for the NAMOC. As sediment concentration decreases, the contours increase for a given latitude and radius, and many channels plot close to or above their contour (Figure 5.11D).

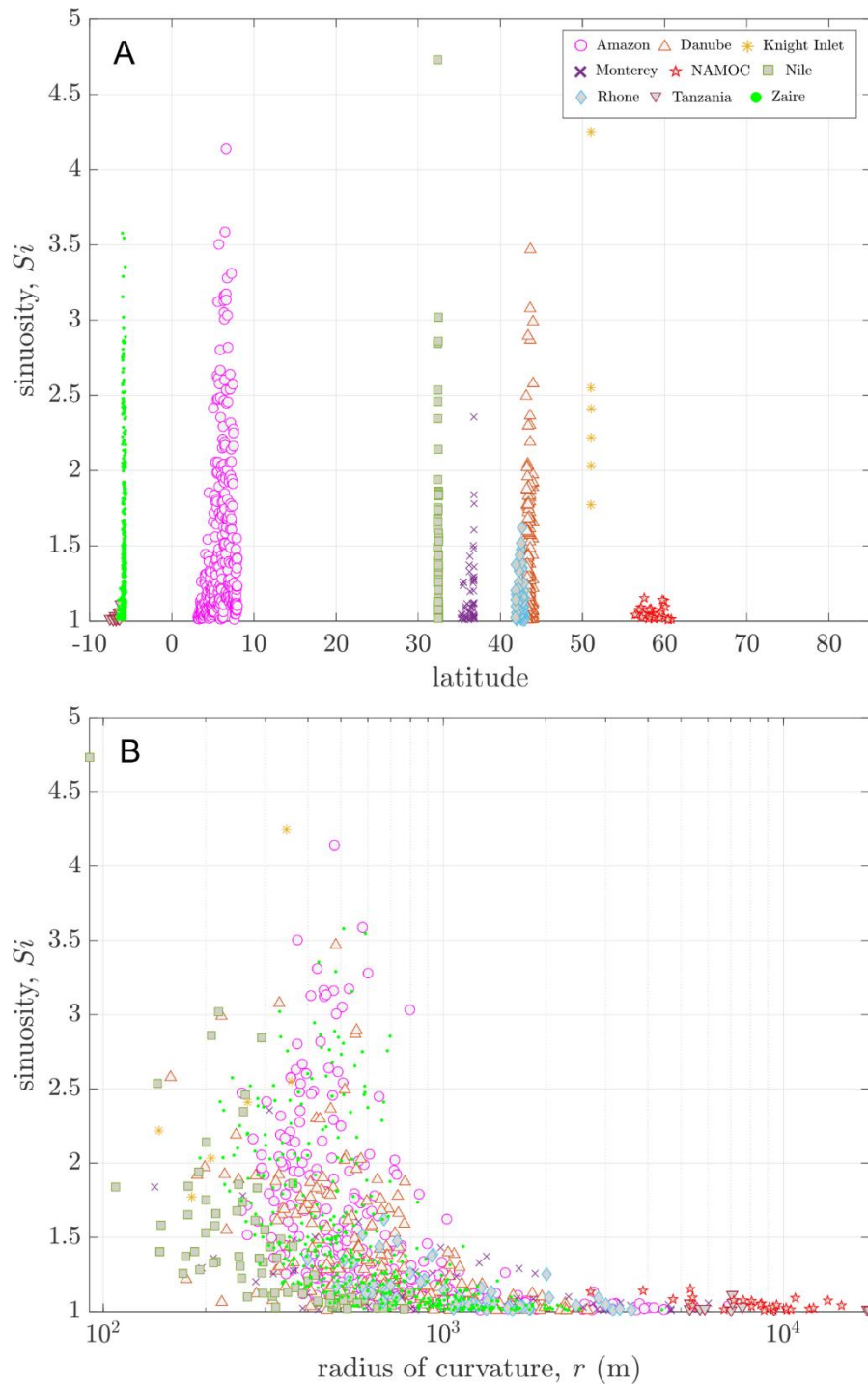


Figure 5.10 Global channel data extracted from Sylvester and Pirmez (2019).
 (A) Latitude versus sinuosity and (B) radius of curvature versus sinuosity.

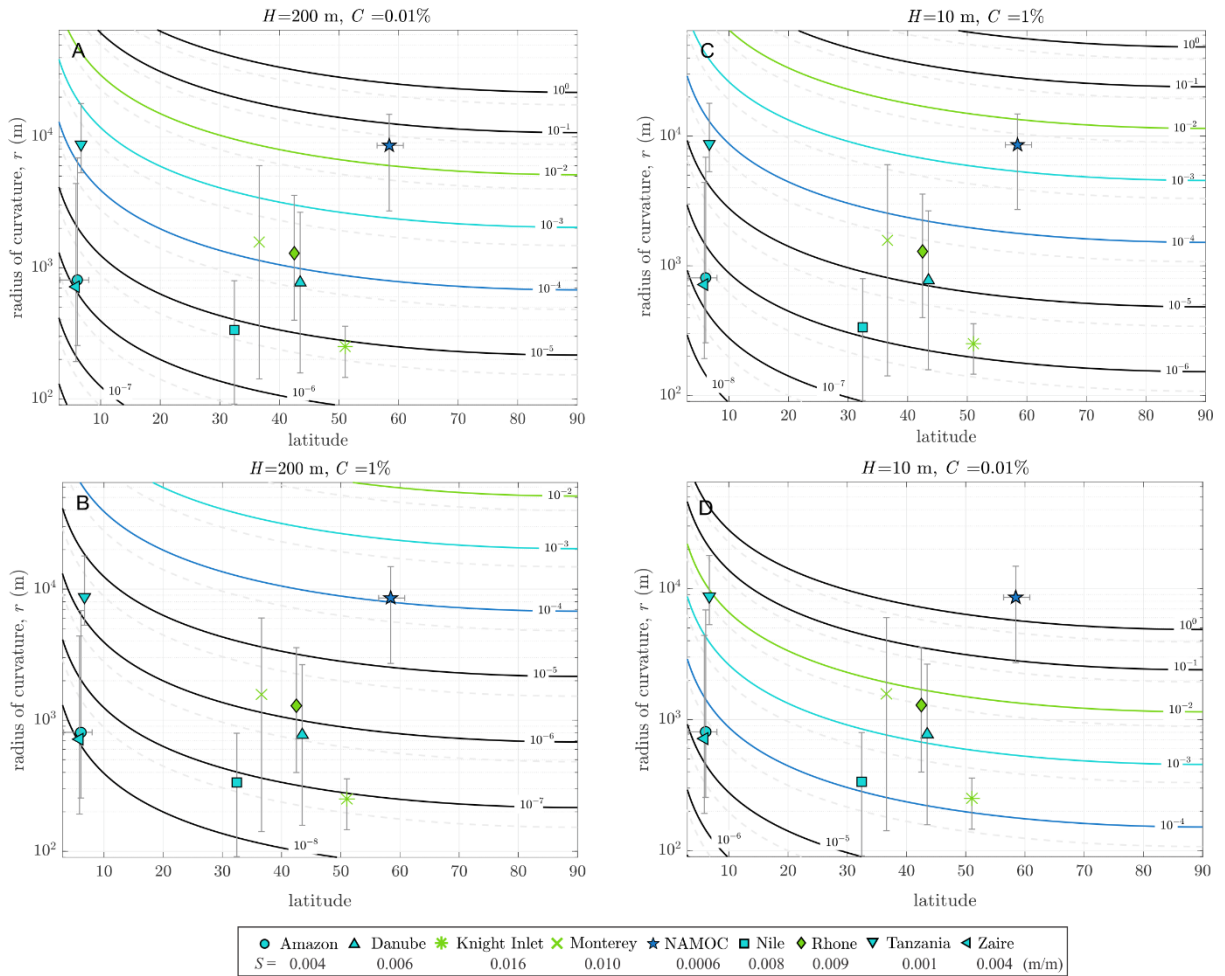


Figure 5.11 Contours of the tilting transition slope S_T co-plotted with seafloor channel data as a function of latitude and radius of curvature for (A) deep and dilute currents, (B) deep and dense currents, (C) shallow and dense currents and (D) shallow and dilute currents. Channel data from Sylvester and Pirmez (2019). Symbol colours correspond to the magnitude of the downchannel slope in each system.

5.4 Discussion

The work of Peakall et al. (2012), Cossu and Wells (2013), and Wells and Cossu (2013) hypothesized that reversals to the tilt of the interface, between the flow and ambient fluid of channelized turbidity currents, due to Coriolis forcing promotes the development of low sinuosity channels at high latitudes; whereas, the predominance of centrifugal forcing near the Equator promotes sinuous channel development. Furthermore, Peakall et al. (2012) proposed a 50° latitude cut-off for the development of high-sinuosity channels. However, Sylvester and Pirmez (2019) challenged the concept of latitudinal control and proposed that Coriolis forcing is unlikely to be responsible for the development of low sinuosity channels. Instead, they argued that the size of the channel has a more important

role in determining the impact of Coriolis rather than the latitudinal position. Sylvester and Pirmez (2019) suggested that the radius of curvatures in channels must be in the order of ~ 10 km or greater for Coriolis forcing to impact channel evolution.

The following sections discuss the observed controls on the changes in the tilting and S_T within the context of the current debate on whether a strong latitudinal control exists for the development of channel sinuosity.

5.4.1 Controls on the effect of Coriolis based on changes in the flow-ambient fluid interface tilting

The results from the changes in tilting suggest that both the latitudinal position and scale of the channel (here analysed through the radius of curvature) control the impact of Coriolis, providing that other conditions are met in terms of the downchannel slope and flow conditions (Figure 5.5 to 5.8). Dilute turbidity currents travelling over shallow slopes in large scale systems ($r = 30,000$) represent conditions where the Coriolis force more likely exceeds the centrifugal force (Figure 5.5), therefore promoting flow deflection that could limit bend expansion and sinuosity development, even at latitudes as low as 5° (Figure 5.5G); this value differs significantly from the 50° cut-off value proposed by Peakall et al. (2012). Dilute flows on shallow slopes would also experience flow deflection in mid-scale channels with $r = 3,000$ at 35° and 55° latitudes, which shows that the effect of Coriolis can be significant at radius of curvature much lower values than the ~ 10 km value proposed by Sylvester and Pirmez (2019).

The modelled conditions at 55° show that in small scale channels ($r = 500$), the Coriolis force cannot exceed the centrifugal force at any given downchannel slope. Hence, there is not an indication for flow deflection and sinuous channels may form. However, some of the examples that do not reflect a deflection of the tilting do suggest that the stability of the tilt is poor (Figure 5.5C). The lack of tilting stability translates into anticlockwise tilts being superelevated and clockwise tilts ≈ 0 due to the increase in Coriolis forcing (Wells and Dorrell, 2021). Therefore, Coriolis forces may shift the location of the velocity and density core before the upper interface is deflected, as experimental observations have shown (Davaranah Jazi et al., 2020). A measure of the early deflection may be approximated through the observation of tilt instabilities. Thus, areas of poor tilting stability found in both dilute and dense currents over shallow slopes at 35° and 55° latitudes might experience flow deflection. Furthermore, the observed tilting instability near S_T suggest that flow deflection might occur earlier than the results predict (Figures 5.5 to 5.7). In low latitudes, potential instability zones are

limited to mid-radius in dilute flows (Figure 5.5D) and large radius in dense flows (Figure 5.7G). Changes in γ_r also suggest that dense currents (Figure 5.7) can maintain a more stable tilting across bends (i.e., the effect of Coriolis is hampered), which explains the reduced occurrence of cases of flow deflection with flow density (Figure 5.7).

While the proposed 50° latitude and ~10 km radius cut-off values may seem high enough to assume that Coriolis would exceed centrifugal forces, the present results suggests that such thresholds may over-simplify the interplay between the effects of Coriolis and centrifugal forces.

5.4.2 Controls on S_T and implications for the development of sinuosity in submarine channels

The tilting transition slope S_T defines the minimum (threshold) downchannel slope needed in a system for sinuosity development and the analysis shows that it is dependent on flow conditions as well as the channel radius and latitude (Figure 5.9), rather than being solely controlled by latitude. If downchannel slopes in the system are steeper than their calculated threshold (i.e., the threshold for a given latitude, radius and flow conditions) sinuosity development would be promoted. In contrast, if the downchannel slope is lower than the threshold, sinuosity would be hindered by the effect of Coriolis. Therefore, the lower S_T values observed in low latitudes, small bends, dense and deep flows (Figure 5.9) equate to a lower threshold which would facilitate the development of sinuosity under these conditions. On the other hand, higher S_T values in large bends, dilute and shallow flows at high latitudes (Figure 5.9) are equivalent to higher thresholds that would make the development of sinuosity more difficult.

The changes on threshold conditions and the associated implications for the development of sinuosity may therefore provide an explanation to the important points raised by Sylvester and Pirmez (2019) on why the Nile, Danube and Knight Inlet have high sinuosity bends despite being located at high latitudes and why the low latitude Tanzania channel has a low sinuosity. Although the Nile and Knight Inlet are small scale channels (bends $< 10^{-3}$) with their threshold S_T between 10^{-7} to 10^{-4} for different flow conditions, the downchannel slopes in both systems are steep enough to exceed threshold conditions in all cases (Figure 5.11A-D), hence suggesting that the Coriolis force would not exceed the centrifugal force and therefore allowing for sinuosity development. The Nile and Knight Inlet (located above the 50° cut-off) have peak sinuosities > 4 (Figure 5.10). Therefore, in these cases the scale of the channels and slopes are stronger controls than the high latitudinal position. Similarly, centrifugal forces are stronger

than Coriolis forces in the Danube and Rhône channels as the threshold slope is exceeded by the channel slopes under most flow conditions (Figure 5.11A-C). Nevertheless, shallow and dilute flows traversing the larger channel bends (i.e., $>10^{-3}$) represent a scenario where flow deflection might occur due to Coriolis and therefore bend growth would be stopped or reduced (Figure 5.11D).

The downchannel slopes for other sinuous channels (i.e., Amazon, Zaire and Monterey) show that they exceed threshold conditions for most flows. Similarly to other channels, only shallow-dilute flows could experience flow deflection in Zaire and Monterey. However, this scenario might not happen in these channels as natural flow data from these settings have registered deeper flows with higher sediment concentration (Vangriesheim et al., 2009; Xu et al., 2014).

The low sinuosity Tanzania channel has a slope that is equivalent in magnitude to its low latitude but sinuous Amazon and Zaire equivalents. However, the Tanzania channel has bends that are an order of magnitude larger; therefore, its threshold S_T is higher, which makes the channel more prone to flow deflection than the Amazon and Zaire. The flow conditions that may suggest flow deflection in the channel, hence promoting low sinuosity are deep and dilute (Figure 5.11A) and shallow - dilute flows (Figure. 5.11 D). Deep and dilute flows in the Tanzania channel approximate threshold conditions therefore, tilt instability and flow deflection due to Coriolis may arise. On the other hand, shallow-dilute flows suggest flow deflection throughout the channel as channel slopes are lower than the channel threshold S_T . The Tanzania channel has a peak sinuosity of 1.1.

The NAMOC is the only channel in this data set consistently showing that the downchannel slopes do not exceed its calculated threshold S_T . The Coriolis force would exceed the centrifugal force throughout the channel length not only for its high latitudinal position but also for its large-scale bends and shallow slopes compared to other systems. This combination of factors potentially controlling sinuosity in the NAMOC might explain why individual morphometric relationships of channel sinuosity are weak (Figure 5.3) and why the NAMOC has very low sinuosity.

The calculation of S_T shows that the observed changes in channel sinuosity are not solely controlled by latitude, but by a combination of factors that would either promote or hinder bend growth. Also, this approach provides an explanation for high sinuosity channels being developed at high latitudes or low sinuosity channels near the equator. Furthermore, given that the latitude, radius and downchannel slope are parameters that can be easily approximated in a system,

the calculated S_T contours may be used to screen the likelihood of developing sinuous channels in other turbidite systems.

5.5 Conclusions

This work calculated the changes in the flow-ambient fluid interface of turbidity currents and derived the minimum tilting transition slope required in a system to develop sinuous bends, which allows the identification of areas of flow deflections and the definition of the conditions needed to achieve it. Following the aims set out in the Introduction (5.1), the conclusions are as follows:

1. The analysis of changes in the flow-ambient fluid interface of turbidity currents and the tilting transition slope thresholds show that end members solely based on latitude or bend radius, where high latitude channels are less sinuous than equatorial channels (Peakall et al., 2012) or on channel radius, where high radius channels are susceptible to Coriolis forcing (Sylvester and Pirmez, 2019) are limited in their capacity to capture the possible controls on channel sinuosity. Rather, a combination of factors including variations in downchannel slope, channel size, latitudinal position and flow conditions determine the tendency of channels to become sinuous. To reiterate: a single latitudinal (Peakall et al., 2012) or radius of curvature threshold (Sylvester and Pirmez, 2019) is not feasible, such that Coriolis forces would not always dominate under strong northern/southern hemisphere rotation, and, under a limited set of conditions, Coriolis might exceed centrifugal forces under weak northern/southern hemisphere rotation.
2. Conditions that would promote the development of sinuosity are deep and dense flows in small channels located in steep slope gradient systems at both low and high latitudes. Dilute and shallow flows in large channels located in low gradient systems at low and high latitudes have a diminished possibility of developing sinuous channel planforms.
3. The calculation of the tilting transition slope thresholds helps to explain the observed sinuosity variations in the analysed modern channels. Therefore, the thresholds may be applicable to other channels systems to determine whether for the given slope gradient, channel size, latitude and flow conditions (if known) the channel is likely to meander or straighten. By extension, if the channel evolution style can be constrained for such channels, then flow conditions might be estimated.

Chapter 6 Discussion and Conclusions

6.1 Implications for the formation of sand-detached systems and bypass-related upslope turbidite pinchouts

As discussed in the literature review and demonstrated in Chapter 3, sediment bypass is an important process in determining the distribution of deepwater deposits. Furthermore, sand bypass by erosional or equilibrium turbidity currents can promote the development of stratigraphic upslope pinchout traps (Amy, 2019; Counts et al., 2021). As hydrocarbon resources become more challenging to locate, upslope pinchouts traps can open up new plays and rejuvenate exploration in mature basins (Stoker et al., 2006; Stirling et al., 2018; Amy, 2019); furthermore, discoveries worldwide show that these plays can hold significant volumes of hydrocarbons (Newton and Flanagan, 1993; Montgomery, 1997; Doré and Robbins, 2005; Horseman et al., 2014). However, a confident estimation of the pinchout location is a common concern in hydrocarbon exploration (Straccia and Prather, 1999; Stirling et al., 2018).

Through a review of four producing fields with bypass-related upslope pinchout traps, Amy (2019) concluded that a steep palaeoslope, often related to faulting, in combination with a limited maximum grain size, i.e., finer than medium sand, are key elements for the successful formation of the trap, as they promote higher efficiency bypassing flows. Results from laboratory experiments of turbidity currents also support that the steepness of the slope is an important control on whether sand bodies are detached from the upper slope, and on the location of the upslope pinchout (Pohl et al., 2020a). Furthermore, both Amy (2019) and Pohl et al. (2020a) highlighted the need to better constrain the slopes and flow conditions needed to achieve sand bypass.

The modelling of sediment bypass in the modern channels of the Hikurangi Margin, New Zealand presented in Chapter 3 offer new insights into the conditions that promote sand bypass, expanding the experimental observations of Pohl et al. (2020a) in terms of the development of detached deposits from an upper slope. Pohl et al. (2020a) showed that steep (Figure 6.1A) and moderate (Figure 6.1B) upper slopes could be associated with downstream deposits that were detached from the upper slope, although, the decrease in upper slope steepness makes the upslope pinchout move updip (Figure 6.1B). A gentler upper slope gradient is associated with a deposit that is continuous in the upper

slope as the gradient is not steep enough to promote bypass of sediment there (Figure 6.1C).

The results obtained in Chapter 3 support the observations that steeper slopes promote sediment bypass (i.e., complete bypass of the sediment load), by erosional or equilibrium flows. However, it was also shown that what might constitute a bypass slope varied between flows, i.e., what constitutes a bypass slope for one set of flow conditions might be a depositional slope for a different set. Previous work has suggested that the flow volume, density and the amount of fine-grained sediment in suspension controls the efficiency of flows (Mutti, 1992; Al Ja'Aidi et al., 2004). Therefore, the present findings support the idea that the thickness of the flow and grain size distribution in suspension are likely factors that would control the development of an upslope pinchout in addition to the slope gradient. Also, it was found that the maximum grain size that could be bypassed was fine sand, which supports the conclusion of Amy (2019) that sediments finer than medium sand are needed for a successful trap development.

Certain cases in Figure 6.1A to 6.1C may then be further classified as more likely scenarios for bypass; i.e., those with flows with well-sorted sediment in suspension. Such flow conditions are shown to be more efficient in the bypass of fine or very fine sand, albeit with a decreasing likelihood of bypass as the upper slope gradient decreases (Figure 6.1C), e.g., over slopes lower than 0.2° for flows ~150 m thick (Table 3.1). As demonstrated in the Madden and Omakere channels (Chapter 3), shallow flows and poorly sorted sediment in suspension require steeper slopes to bypass sand. Hence, the location of an upslope pinchout would be located further updip under these flow conditions (Figure 6.1D and 6.1E). Recognizing that the location of the upslope pinchout may occur higher in the slope is important for the estimation of reservoir volumes given that wells that are drilled farther from the pinchout termination run the risk of leaving behind significant volumes of attic oil in the updip direction (Gardiner, 2006).

With a steep enough upper slope (e.g., above 5° for a ~30 m thick flow), sand would bypass the upper slope and deposit at the slope break (Figure 6.1D); as the upper slope decreases, deposits might then onlap onto the upper slope (Figure 6.1E) or be continuous (Figure 6.1F). Hence, cases A, B, D and E in Figure 6.1 may lead to the development of an upslope pinchout allowing for hydrocarbon accumulation providing that an effective seal is developed (Figure 6.1G) (e.g., the Buzzard field, Doré and Robbins, 2005). On the other hand, continuous sands have the risk of being connected to updip sands, forming “thief

zones” that allow for updip leakage of hydrocarbons (Figure 6.1H) (e.g., Hansen et al. 2019).

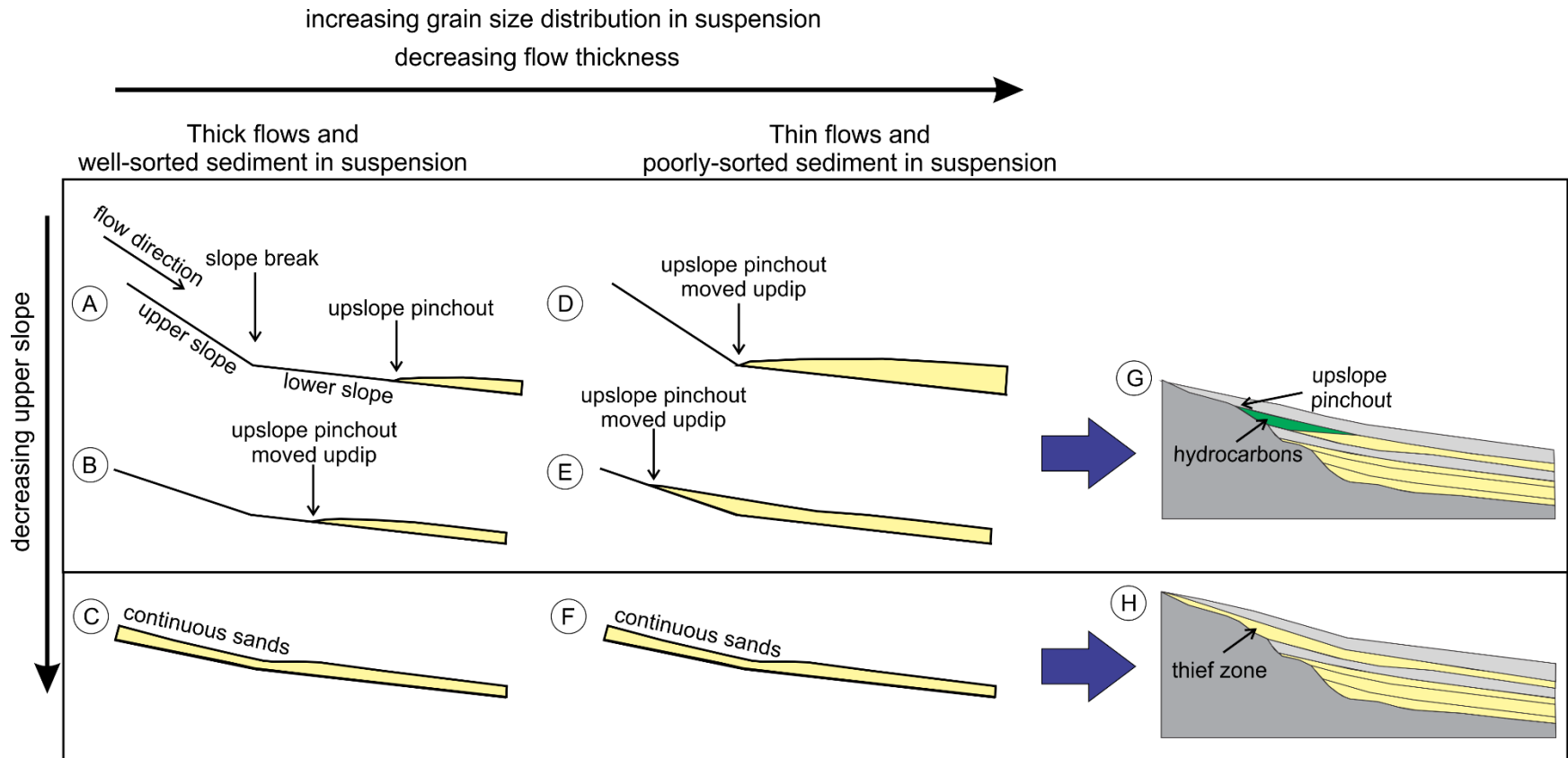


Figure 6.1 Schematic diagram showing the effect of changes in the upper slope gradient, flow thickness and grain size distribution in the formation of upslope pinchouts (A to F adapted from original sketches in Pohl et al., 2020a; G and H adapted from Amy, 2019).

6.2 Implications for sedimentation and erosion models based on Coriolis force changes

The results from modelling the changes of the upper flow-ambient fluid interface tilt and the downchannel slope at which the interface is deflected by Coriolis effects in Chapter 5 showed that the influence of the Coriolis force upon turbidity currents is not only dependant on the latitudinal position of the system but also on the size of the channel, the slope gradient of the system and the properties of the flow (i.e., height and concentration). These results therefore confirm that a more complex combination of factors control sinuosity than the two-end member systems previously proposed based on slope gradient/grain size (Clark et al., 1992) or latitude (Peakall et al., 2012; Wells and Cossu, 2013).

Patterns for sedimentation and erosion that could inhibit sinuosity development due to Coriolis forcing were first presented in Cossu and Wells (2013) and Wells and Cossu (2013), and more recently by Davarpanah Jazi et al. (2020) (Figure 6.2). This model proposes six scenarios showing changes in sedimentation patterns for traction-dominated flows and suspension fallout flows at high latitudes in the northern/ southern hemisphere where $|Ro_R| < 1$, and at the equator where $Ro_R = \infty$ (Figure 6.2). As discussed in Chapter 5, when the Coriolis force opposes and exceeds the centrifugal force, i.e., in clockwise bends in the northern hemisphere (Figure 6.2A and 6.2D) and anticlockwise bends in the southern hemisphere (Figure 6.2C and 6.2F), the locus of erosion is shifted to the inner bends and deposition to the outer bend which would tend to diminish lateral bend migration. In contrast, lateral bend migration is promoted through outer bend erosion and inner bend deposition when the Coriolis force is absent or low (Figure 6.2B and 6.2E).

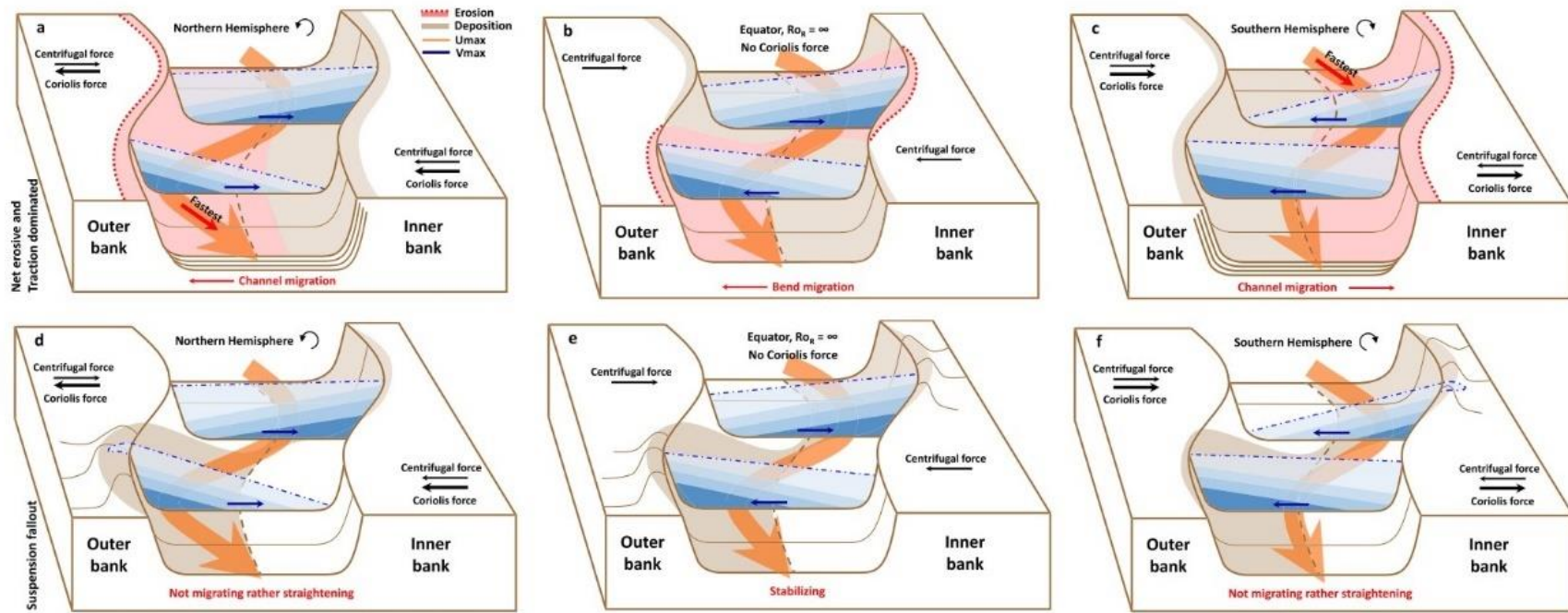


Figure 6.2 Block diagrams illustrating the changes in intrachannel sedimentation patterns due to Coriolis for (A-C) traction-dominated flows and (D-F) suspension fallout (Davaranah Jazi et al., 2020).

Given that the experiments were done using a fixed channel geometry, slope and flow density, the model of Davarpanah Jazi et al. (2020) shows the changes in sedimentation patterns simply as a function of latitude. Hence, the new results from Chapter 5 help to constrain under which additional sets of conditions such sedimentation patterns would be expected. Latitude, channel size (either calculated through the radius of curvature or channel width) and slope gradient constitute parameters that can be extracted or approximated in a system; therefore, it is possible to extend the model to constrain the sedimentation patterns in terms of these three parameters (for the northern hemisphere) in a 3D figure as shown in Figure 6.3.

The tendency for channels to become sinuous at high latitude increases from case 1 (large scale channel, low gradient) to case 4 (small scale channel, steep gradient) (Figure 6.3). Traction-dominated flow regimes that erode the right-hand side (left-hand side in the southern hemisphere) of the channel (looking downstream) due to a dominant Coriolis force would develop in cases 1 and 2 (large scale, steep gradient), hence promoting lateral channel migration without bend expansion (Cossu et al., 2015; Davarpanah Jazi et al., 2020) (Figure 6.3). In cases 3 (small scale, low gradient) and 4, the centrifugal forces dominate, therefore promoting outer bank erosion and inner bank deposition processes that develop sinuous channels (Abreu et al., 2003; Peakall et al., 2007). The models from Davarpanah Jazi et al. (2020) suggest that suspension fallout regimes would deposit sediment in the outer bank for all cases (Coriolis or centrifugal dominated) (Figure 6.2D, 6.2E, 6.2F); however, previous sedimentation models suggest that when the Coriolis force dominates, deposition from fallout occurs continuously on the right-hand side of the channel (and vice versa for the southern hemisphere) (Cossu and Wells, 2013; Wells and Cossu, 2013; Cossu et al., 2015) building higher right-hand side levees (e.g., Klauke et al. (1997); Boggild and Mosher (2021)).

At low latitudes, more sinuous bends would develop from case 5 (large scale channel, low gradient) to case 8 (small scale channel, steep gradient). In contrast to previous suggestions that the Coriolis force would only dominate at high latitudes, the results in Chapter 5 show that for conditions such as in case 5, Coriolis forces dominate, hence the sedimentation patterns would tend to diminish lateral bend migration (Figure 6.3). On the other hand, cases 6 (large scale channel, steep gradient), 7 (small scale channel, low gradient) and 8 are centrifugal force-

dominated, therefore, their sedimentation patterns enhance sinuosity development (Figure 6.3).

It is important to note that the sedimentation patterns presented in the 3D figure (Figure 6.3) might be modified by the properties of the flows. As shown in Chapter 5, the flow height and sediment concentration influence whether Coriolis force exceeds the centrifugal force. Deep and dense flows would enhance centrifugal force-dominated patterns, therefore, if these flow types initially dominate in cases such as 1, 2 and 5 in Figure 6.3, they might generate an initial perturbation for the development of sinuosity whereas, dilute and shallow flows, being more influenced by the Coriolis force, would act to limit the perturbation from continuing bend growth.

It is also important to highlight that the threshold downchannel slopes presented in Chapter 5 (Figure 5.11) as well as the sedimentation patterns shown in Figure 6.3 are applicable to areas or systems without a strong structural control as channel-structure interactions deviate the channel course, hence modifying (often locally increasing) channel sinuosity (Cronin, 1995; Clark and Cartwright, 2009).

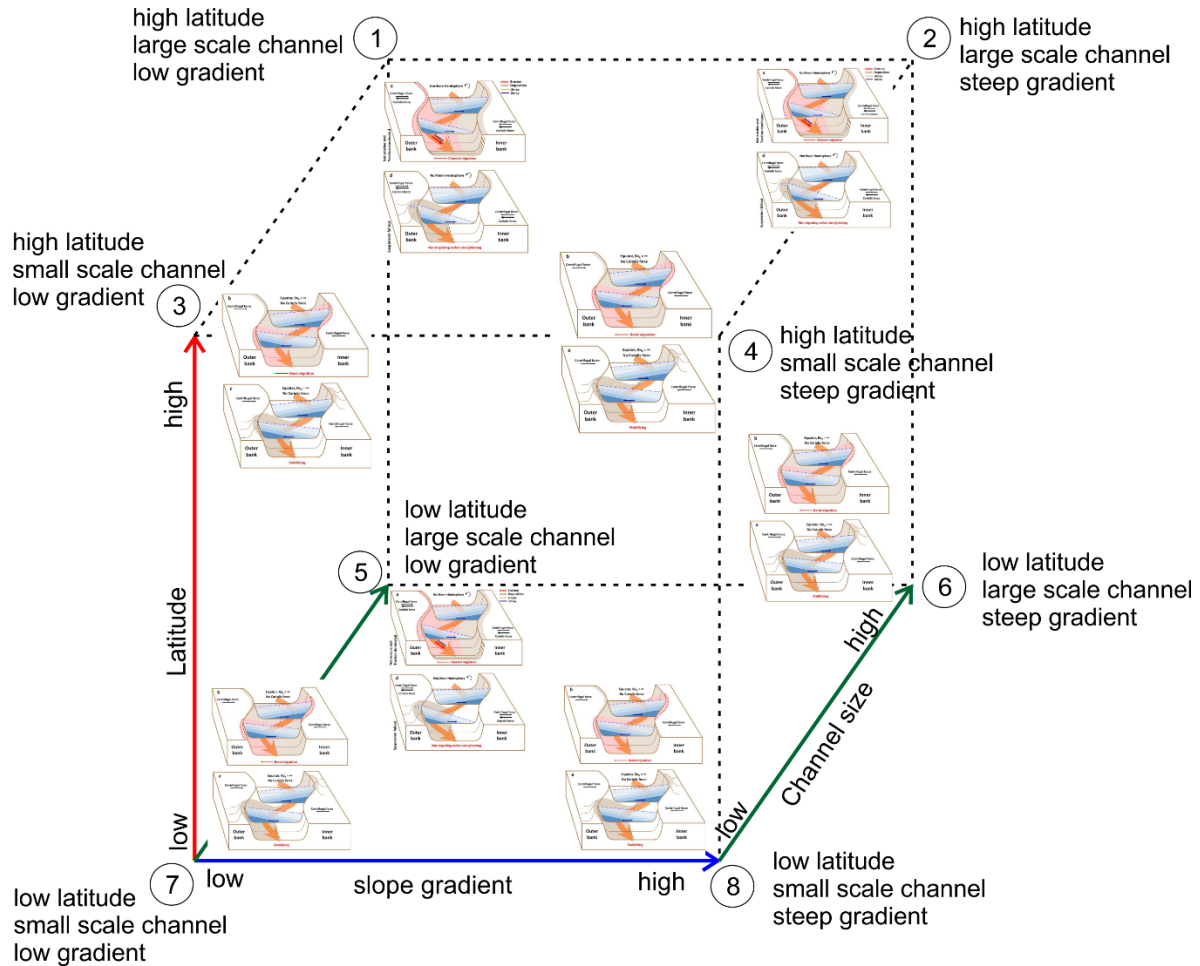


Figure 6.3 Schematic 3-dimensional diagram illustrating the expected sedimentation patterns at channel bends due to changes in the balance between Coriolis and centrifugal forces as a function of latitude, downchannel slope gradient and channel size (individual block diagrams are from Davarpanah Jazi et al., 2020).

6.3 Synthesis

This thesis is focused on the reconstruction of the physical properties of turbidity currents in modern channels (Chapters 3 and 5) and subsurface channel forms (Chapter 4).

The modelling results presented show the effect of the grain size distribution in suspension during sediment transport (Chapter 3), the challenges encountered in the application of the modelling approach to subsurface channel forms (Chapter 4) and the combination of factors that control the development of channel sinuosity (Chapter 5). Hence, adding new insights to an extensive body of knowledge on the

study of turbidity current dynamics using a numerical approach (e.g., Pirmez and Imran, 2003; Das et al., 2004; Konsoer et al., 2013; Kneller et al., 2016; Stevenson et al., 2018).

Here it is demonstrated that the application of turbidity current modelling techniques can help to better understand the dynamics of these critical processes in deepwater environments. However, it is important to recognize that limitations exist related to the parameters used as input into the governing equations. The parameters often must be assumed or approximated given the limited knowledge on the turbidity current characteristics in natural environments due to their intermittent nature and difficulty to be observed and monitored (Talling et al., 2013).

The following sections present an assessment of the parameters used in this thesis with the aims to highlight their challenges and uncertainties, as well as to demonstrate the influence on the interpretation of the flow height in the calculations, and finally, to offer recommendations on where the research efforts should be conducted to improve current modelling techniques.

6.3.1 Uncertainty in known and unknown parameters in the modelling of turbidity currents

The modelling approach used in this thesis to calculate turbidity current properties is based on the model of Komar (1969) (Equation 3.3) and Parker et al. (1987) (Equation 3.4) which describe the cross-channel forces and downchannel forces, respectively, that act upon a turbidity current as it travels through its confining channel. Furthermore, a Chézy equation (Middleton, 1966b; Komar, 1977) is used to calculate flow velocity (Equation 3.7). The models assume depth-averaged flows to simplify the mathematical description of the current dynamics, however, in nature, they can be far more complex due to the vertical variation in density and velocity, stratification and turbulence processes (Wells and Dorrell, 2021).

Estimates of turbidity current velocities, and more recently, sediment concentration (unknown parameters), based on depth-averaged hydrodynamic modelling, depend upon measurements of the values of morphological factors. In equations (3.3) and (3.4), the parameters such as the cross-channel slope, the flow height, the radius of curvature and the slope can be estimated from the channel morphology. However, the resulting flow conditions carry the uncertainty associated to the assumptions made during the extraction of these morphological values.

6.3.1.1 Flow height

One of the biggest uncertainties in modelling lies in the selection of an appropriate value of flow height. The height of turbidity currents in submarine channels is not well constrained as most measurements in natural settings come from canyon confined currents (Talling et al., 2013; Xu et al., 2014). Furthermore, the variability of the flow height within a system and among systems depend on factors such as the triggering mechanism of the current (Piper and Normark, 2009), the amount of water entrainment (Ellison and Turner, 1959) or waxing-waning cycles (McHargue et al. 2011); which are not always well known in a system, therefore making more difficult to constrain the flow height.

A common simplification made to overcome the uncertainty in modelling is to assume bankfull flows, i.e., with a height equivalent to the channel depth measured from the base of the channel to the levee crest, (e.g., Konsoer et al. 2013 and Chapter 3). Hence, the height of the levee crest constitutes the upper limit for the flow height. This assumption was applied to the channels analyzed in this thesis and although it proved to be useful as a first approximation of the flow conditions, it might not be representative of all flows given that they may exceed (Mohrig and Buttles, 2007; Straub et al., 2008) or be shallower than their confining channel (Mohrig and Buttles, 2007). Hence, sedimentation patterns different to those analysed in Chapters 3 and 4 would likely differ for flows that are, for example, half bankfull. Furthermore, it was demonstrated in Chapter 4 that there is more uncertainty in applying the interpretations of bankfull flows to subsurface channel-forms than in modern channels as they may represent compound forms rather than single palaeohydraulic conduits. Additional challenges may be encountered in areas where levees are not preserved (i.e., due to breaching of levees or levee collapse), either in modern or ancient systems. Hence, these areas would not constitute reliable sites for the extraction of morphological values to estimate flow conditions.

Another factor to consider in the selection of the flow height is the nature of the Chézy equation (originally formulated for open-channel flows (Chanson, 2004) that was applied to the studied channels in this thesis (Chapters 3 and 4) and that has been applied in other systems (e.g., Bowen et al., 1984; Ren et al., 1996; Pirmez and Imran, 2003; Stevenson et al., 2018). As introduced in Chapter 2, turbidity currents exhibit a vertical variation in their velocity profile where the velocity maximum (U_{max}) defines the inner (lower) and outer (upper) region (Figure 2.2). The lower region shares characteristics with open-channel flows with a positive velocity gradient and where near-wall effects are important; hence, formulations such as the

law-of-the-wall can be applied to this region (Kneller et al., 1997, 1999) and the height of the velocity maximum (H_{max}) can be used as input into equations (3.3) and (3.7) (e.g., Stevenson et al., 2018).

Although H_{max} in natural currents is not well constrained (i.e., representing another source of uncertainty in the selection of the flow height), values derived from experiments are between 0.2 and 0.3 times the total flow thickness (Kneller et al., 1997; De Leeuw et al., 2016). To test the effect of using H_{max} instead of bankfull flows in the Madden Channel (Chapter 3, Figure 3.4), the flow height has been reduced using H_{max} proportions of to $0.2H$, $0.25H$ and $0.3H$.

Figure 6.4A shows that both the flow velocity and sediment concentration increase, which potentially reflects the higher bulk values that would be observed towards the bed. The difference among the velocity of the bankfull flow and the different proportions of U_{max} is not uniform throughout the channel section. The average velocity values increase up to ~54% ($0.2H$) down to ~42 km and up to ~128% in the remaining channel length, i.e., they are significantly different to the original estimation of bankfull conditions. The non-uniform variation reflects the change from subcritical to a supercritical faster flow at ~42 km and shows the latter are more sensitive to the assumptions of flow height using this approach.

The sediment concentrations at different proportions of U_{max} show a significant increase of up to 169% (one order of magnitude) (Figure 6.4B), however, in contrast to the velocity, the difference among the U_{max} proportions throughout the channel length remains constant.

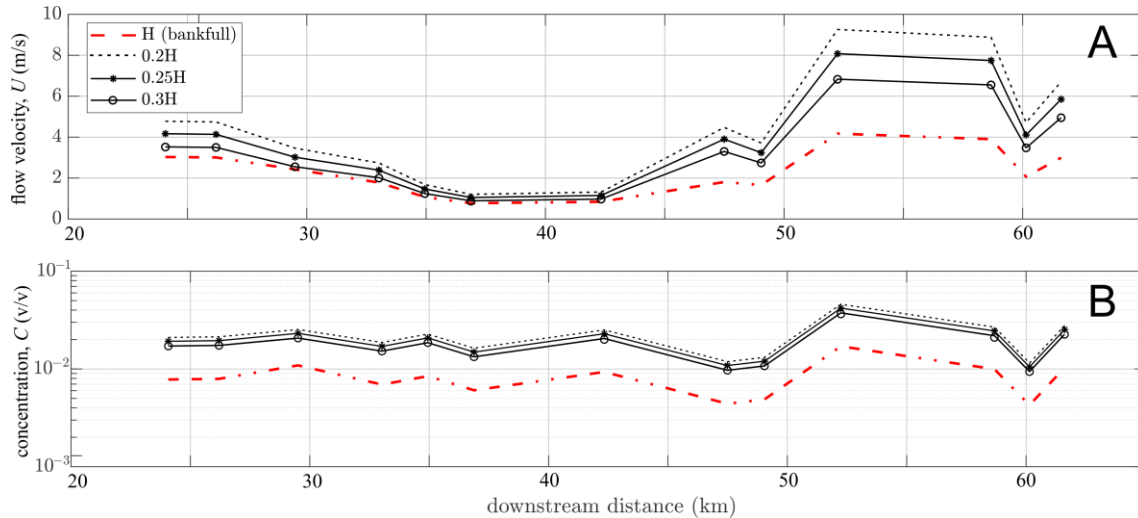


Figure 6.4 (A) Changes in flow velocity and (B) sediment concentration with variations in the height of the velocity maximum.

6.3.1.2 Turbidity current interface tilting (cross-channel slope)

The cross-channel slope is a parameter used in equation (3.3) that represents the tilting of the turbidity current-ambient fluid interface (Komar, 1969). Similarly to the calculation of bankfull flow heights, the levees are used to make an approximation of the cross-channel slope. Hence, in chapters 3 and 4 it was assumed, following Komar (1969), that the cross-channel (levee) asymmetry of the studied channels was a proxy for the flow tilting. However, this assumption carries an important uncertainty as the levee asymmetry might not be equal to the tilting in real flows. Measurements of the cross-sectional flow properties in natural channels have shown that the flow tilting is rarely equal to the cross-channel asymmetry (Parsons et al., 2010; Sumner et al., 2014), particularly for superelevated flows at channel bend apexes (Straub et al., 2008). Therefore, the tilting slope in real flows may be higher (or possibly lower in other cases) than the gradient suggested by the channel geometry.

As the sensitivity analysis presented in Chapter 4 showed, the cross-channel slope has a big influence in the calculation of the sediment concentration, as it may modify the concentration by several orders of magnitude (Figure 4.3). Furthermore, the modelling of the tilting in Chapter 5 shows that its variability is multifactorial. Given the lack of solid knowledge on the variations of the interface tilting in natural flows, the approximations through the channel-levee asymmetry might constitute the best guess. Further investigations on the variations and controls of the interface tilting

would be needed to better constrain this parameter, ideally through the observations of cross-sectional channel profiles of density and velocity from natural currents.

6.3.1.3 Drag coefficient

Turbidity currents experience drag at the bed and water entrainment at the upper interface as they travel downchannel (Parker et al., 1986; Kneller et al., 2016). The amount of drag and rates of entrainment influence the velocity of the current as well as the height of the velocity maximum (Kneller and Buckee, 2000). Despite the importance of both parameters in the determination of the current properties, they are not yet well constrained by field measurements.

The input values used in turbidity current modelling are based on drag values observed in rivers (Konsoer et al., 2013) or are estimated through formulations based on grain size in open channel flows (e.g., Stevenson et al. 2018). However, other factors such as the bedform types or biota influence the drag at the bed. Furthermore, as shown in Chapter 4, turbidity currents may run through MTD or contourite fields which lead to changes in bed roughness.

Due to such uncertainties and to the lack of robust alternative approaches to estimating the drag coefficient in submarine environments, a constant value of drag coefficient ($Cd = 0.0025$) which lies within common ranges used in turbidity current modelling (0.0025 – 0.005) (Pirmez and Imran, 2003; Konsoer et al., 2013; Stevenson et al., 2018) was chosen in this thesis.

To evaluate the impact of different drag coefficients in the calculations and following up the analysis on using H_{max} in the Madden Channel, values of $Cd = 0.0020$ and $Cd = 0.0050$ were used to model flows at $H_{max} = 0.25H$ (see Figure 6.4).

The velocity increases with a decreasing value of drag (Figure 6.5A). A decrease of the value originally used by 0.0005 causes an average increase in velocity of 12%, whereas the double of the original value increases the average velocity by 29%. The model does not capture changes in sediment concentration with drag coefficient (Figure 6.5B) which might be explained by a very small control of the Froude number (Fr) on the sediment concentration as Fr is the parameter linking the drag coefficient to concentration in equation (3.3). However, as shown in the calculations of Stevenson et al. (2018) from the Grand Banks flow, an increase from 0.003 to 0.0045 in the drag coefficient caused an increase in sediment concentration from 1% to up to 3%.

It is also important to highlight that the drag coefficient is not likely to be constant throughout the channel length, therefore, more variability downstream of the flow velocity and concentration would be expected as the characteristics of the bed change (Wells and Dorrell, 2021).

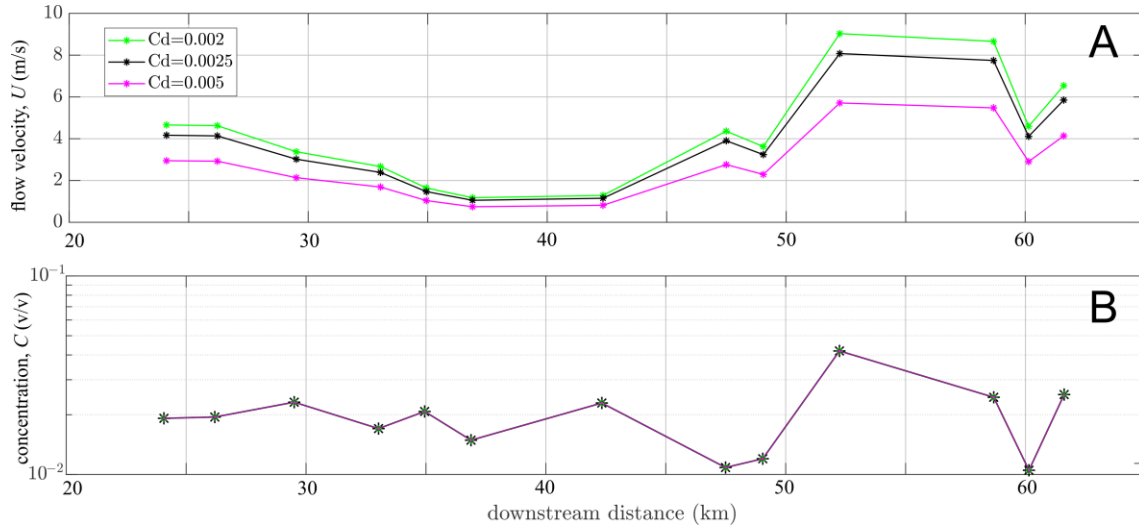


Figure 6.5 Changes in (A) flow velocity and (B) sediment concentration with variations in the drag coefficient.

6.3.1.4 Ambient water entrainment

Turbidity currents experience ambient fluid entrainment at the upper interface which may result in dilution of the current and flow thickening (Ellison and Turner, 1959). The relationships used to parameterize water entrainment (e_w) in turbidity current modelling have been derived from experiments for fully confined flows using relationships that are dependent on the Richardson number as it defines the stability of the upper interface, (Parker et al., 1987, equation (3.6)) or dependent on the downchannel slope for gradients $\sim 0.6^\circ$ (e.g., Pirmez and Imran, 2003; Stevenson et al., 2018). These formulations imply that some degree of entrainment occur throughout the flow duration, with a higher entrainment rate in supercritical flows compared to subcritical flows of entrainment for the duration of the flow; however, this assumption need consideration given that modelling approaches have shown that under certain flow conditions, the upper interface is stable with very low rates of water entrainment (2-3 order of magnitude lower than empirical relations suggest) or that it may then become negligible (Traer et al., 2015; Kneller et al., 2016).

Following the observations on negligible entrainment rates from Traer et al. (2015) using the relationship of Parker et al. (1986,1987), it is likely that the flows modelled in the Madden and Omakere Channels would exhibit higher flow velocities due to the lack of drag at the upper interface.

As with the estimations of the previous parameters discussed, constraining the empirical relations of water entrainment by field data is needed to reduce the uncertainty in the application of these relations to the calculation of flow conditions using submarine channel morphologies.

6.3.2 General recommendations

Many of the uncertainties in the input parameters are a consequence of the limited knowledge in the flow dynamics of natural turbidity currents during the early development of the pioneering equations used to characterise them (e.g., Ellison and Turner, 1959; Middleton, 1966; Komar, 1969, 1977; Parker et al., 1986; Stacey and Bowen, 1988; Kneller, 1995). The understanding of turbidity currents and their confining channels has increased partly thanks to the advances in the technology of the equipment used in experimental (Straub et al., 2008; De Leeuw et al., 2018; Davarpanah Jazi et al., 2020) and natural settings, as well as the computational advances to model them (Janocko et al., 2013a; Dorrell et al., 2014; Traer et al., 2015; Stevenson et al., 2018; Howlett et al., 2019; Goodarzi et al., 2020). However, many of the relationships and assumptions used before these advances are still used in current modelling approaches. This highlights a need to focus research efforts into the re-evaluation of parameters extrapolated from subaerial settings (e.g., drag coefficient) and re-assessment of empirical parameters (e.g., water entrainment) either through more robust experimental approaches or through flow monitoring in natural settings (ideally in submarine channels).

Also, as highlighted in section 6.3.1.1, increasing research focused on direct monitoring in submarine channels would also benefit the understanding of the relationship of the flow height, and the cross-channel slope relative to the channel geometry. Following the sensitivity analysis presented in Chapter 4 and the analysis of the effect of the different proportions of H_{max} , it is suggested that the flow height and cross-channel slope (tilting) need more careful investigation/ value extraction, for the analysis of turbidity currents. A well understanding of the uncertainty from the input parameters and the governing equations remains important to make more

accurate estimations of sediment transport rates and overall evolution of turbidity currents and deep-marine systems.

6.4 Conclusions

6.4.1 Summary

This thesis has presented an investigation of channelized turbidity currents dynamics through the application of theoretical models to surficial (Chapter 3), subsurface (Chapter 4) and theoretical (Chapter 5) channel architecture. A novel methodology was presented to calculate bulk turbidity current properties by using a non-linear least squares minimization method to solve for cross-channel forces using the surface-slope equation of Komar (1969), and downchannel forces using the relationship established by Parker et al. (1987). This approach offers more robust solutions of sediment concentration, flow criticality and velocity than were achieved by previous studies that analytically solved the cross-slope equation for the calculation of turbidity current properties in other channel systems. The solution of both cross- and downchannel forces coupled with the Flow-Power Flux-Balance theoretical sediment transport model was shown to derive good estimations of sediment bypass conditions in surficial channels. However, the application of the modelling techniques proved to be more challenging in subsurface systems. Hence, more caution is needed in calculating palaeo turbidity current conditions with models that use inputs based on subsurface channel form geometries. A third application of the surface-slope equation (Komar, 1969) and its solution through non-linear least squares proved the versatility of the modelling technique by estimating changes in upper-interface tilt of turbidity currents due to Coriolis, to give insights into whether the Coriolis force is a strong control in the development of submarine channel sinuosity.

Conclusions specific to each data chapter are presented below.

6.4.2 Chapter 3

Sediment bypass by turbidity currents is a key process in the distribution of sediment in deep-marine systems. Nevertheless, predicting the conditions of sediment bypass (i.e. through erosional, equilibrium or depositional flows) has remained challenging as prior sediment transport models did not collectively consider the principal factors governing sediment bypass (i.e. grain size distribution, flow height, competence, capacity, slope gradient and sediment

concentration). Using 100 m horizontal resolution bathymetric data and high-resolution 3D seismic data of the Hikurangi Margin, New Zealand, morphometric data were extracted from two submarine slope channels and applied in a modelling approach that 1) provides more robust estimations of turbidity current velocity and bulk sediment concentration and 2) incorporated the principal factors controlling sediment bypass through use of a flow-power flux-balance type sediment transport model. In this chapter it was demonstrated that the flow height, slope gradient and grain-size distribution in the flow jointly determine the down-dip patterns of turbidite deposits. Thick flows (>140 m) with well or poorly-sorted suspensions require lower slope gradients to bypass sand than thinner flows. Furthermore, well-sorted suspensions can completely bypass over lower slopes than can more poorly-sorted suspensions of equivalent flow height and bulk sediment concentration. Only fine-grained sediments from very fine silt to very fine sand were likely to be bypassed through sections of the channel lengths. The projected sedimentation patterns from poorly-sorted flows were shown to be in good agreement with observations from the RMS map of the seafloor and drop core data that described poorly-sorted deposits with mostly silty deposits and grain sizes up to fine sand.

Knowledge of the conditions under which turbidity currents bypass sediment increases understanding of the sedimentary processes in deep-marine systems and constrains interpretations of turbidite deposits on modern and/or ancient systems. Furthermore, such results provide insights into the potential implications for the formation of bypass-related upslope pinchouts. The upper slope gradient together with the characteristics of the current (i.e. flow height and sorting) determine the likelihood for the development of detached sands from a potential updip feeder system.

6.4.3 Chapter 4

Hydraulic modelling of turbidity currents plays a key role in the understanding of submarine channel systems. However, the application of modelling techniques to subsurface channels can be challenging where channel-forms observed in the subsurface might represent compound geomorphological features instead of genuine palaeo-hydraulic conduits. In chapter 4, high-resolution 3D seismic data was integrated with depth-averaged turbidity current modelling to estimate palaeo-hydraulic properties in subsurface channel-forms from the Hikurangi Margin, offshore New Zealand. It was tested whether the observed subsurface channel-forms represented the true palaeo-hydraulic conduit and the analysis allowed for the

documentation of sources of uncertainty that might not arise in modern channels. It was found that at some channel-bends, sediment concentrations exceeded the 9% theoretical concentration for dilute turbidity currents which suggested that the observed channel-forms either: i) represented compound bodies or ii) did not correspond to equilibrium channel-forms, possibly due to having a complex MTD substrate. Therefore, this data chapter showed that such factors constitute sources of modelling uncertainty that must be considered in addition to previously known limitations related to poor channel preservation or low seismic resolution. Furthermore, the findings may also be useful in other physical and planetary systems where recognition and measurement of palaeo-hydraulic conduits is challenging.

6.4.4 Chapter 5

A critical challenge in deepwater sedimentology is to define the factors that control the development of submarine channel sinuosity. Studies based upon laboratory experiments and observations from channel peak sinuosities have hypothesized that the Coriolis force is a key control, as it modifies the 3D structure of turbidity currents when it is greater than the centrifugal force at high latitudinal positions. However, the proposed latitudinal control has been debated over the years and instead it was argued that the size of the channel was more important in defining whether Coriolis forces dominate (see Peakall et al., 2012; Wells and Cossu, 2013 and Syvester and Pirmez, 2019).

The work in Chapter 5 showed a novel methodology to solve for the upper interface tilting of turbidity currents using the cross-slope equation from Komar (1969) to determine if Coriolis forces are a dominant control on the development of channel sinuosity. Furthermore, the threshold downchannel slope at which centrifugal forces would dominate in a system, hence allowing for the development of sinuous channel bends was calculated. The results suggested that the Coriolis force becomes significant due to a combination of factors controlled by the size of the channel, the slope gradient and flow conditions instead of solely being dependant on latitude or channel size. Thick and dense flows travelling over small scale channels and steep down-channel gradients were shown to be less susceptible to flow modification due to Coriolis forcing, even at high latitudes. On the other hand, thin and dilute flows in large scale channels at gentle gradients showed more susceptibility to be modified by Coriolis forces in low to high latitudes. Moreover, the analysis of the threshold downchannel slopes helped to provide an explanation for observed high sinuosity channels at high latitudes such as the Knight Inlet and Danube channels, as well as

to low sinuosity channels in high latitudes such as the Tanzania channel. Also, the current models of changes in intrachannel sedimentation patterns due to Coriolis were extended to incorporate each of latitude, channel size and slope gradient following the findings from the modelling.

6.5 Recommendations for future research

The following recommendations for future work arise from the findings presented in this thesis:

1. Turbidity current modelling coupled with sediment transport modelling in chapter 3 revealed that the grain size distribution in suspension was a key factor in determining flow efficiency, where well-sorted flows are more efficient than poorly-sorted flows in bypassing sediment through erosional or equilibrium flow regimes. Given that the models use depth-averaged theory, it is recommended that further investigation of the vertical and longitudinal variation of channelized turbidity currents with poorly-sorted vs well-sorted suspensions is performed through laboratory experiments to examine the difference in the mechanics of both flow types over varying slopes and flow heights and further test whether poorly-sorted suspensions require more flow power to bypass sediment.
2. To further evaluate the performance of the combined modelling technique presented in chapter 3 in modern systems, it is recommended its application to channels where sedimentation and flow processes are better constrained through repeat seafloor surveying and turbidity current monitoring (e.g. Heijnen et al., 2022) which will ultimately help constrain uncertainties in the model estimations.
3. The equilibrium thresholds presented in chapter 3 and 4 are specific to the calculated flow conditions in the channels of the Hikurangi Margin. A more global approach could be achieved through further modelling of equilibrium thresholds using a set of flow depths and sediment concentrations that capture the full variability of turbidity currents. Such thresholds might be used as predictive tools of sediment bypass in other systems. Furthermore, by expanding the analysis of the slopes required for sand bypass, a screening technique could be also developed to identify whether an area may indicate effective bypass-related stratigraphic trapping through the evaluation of the palaeoslope profile and predominant grain size in the system. Screening

techniques extract, isolate and identify a compound or group of components in a sample that indicate if they are above or below an established threshold, which is usually done in a few steps to assist rapid decision-making. Therefore, they have been used as predictive tools in industries including, but not limited to the oil and gas sector (Fugelli and Olsen, 2005).

4. The results in Chapter 4 suggest that modelling approaches could be applied to assess whether channel-forms observed in the subsurface represent the true palaeo-hydraulic conduit or whether they represent compound channel-forms. The identification of compound channel forms based on hydraulic reasoning may provide an additional constraint on the recognition of submarine channel hierarchy (Cullis et al., 2018). This is because compound channel-forms represent elements of higher hierarchical levels and their definition in seismic has been challenging due to limitations in seismic resolution and also due to the wide variety of hierarchical schemes established with the aim to simplify the interpretation and description of deepwater elements (Cullis et al., 2018). If such an approach can be developed it could be integrated with seismic interpretation techniques to help to better constrain channel architecture and facies distributions.
5. In chapter 4, a sensitivity analysis varying one variable at a time was conducted to determine the influence of each model input to the overall model outputs. It is recommended that a more robust sensitivity analysis is performed such as Global sensitivity Analysis using programming packages like SALib, which allow the complete parameter space and co-variance of model inputs to be tested (e.g., Lyons et al., 2019). A full multivariate analysis should incorporate the effects of the uncertainty distributions for each of the parameters that contributes to the calculation of flow properties. This testing approach is particularly recommended if the model is applied using subsurface channel architecture as it will allow investigation of which the variables need more careful investigation/ value extraction for the calculation of palaeo turbidity currents.
6. Following the findings from chapter 4 on channels developing over MTD fields, it is concluded that further work is needed to better understand turbidity current-MTD substrate interaction, possibly through laboratory experiments. A better understanding of how rugose MTD substrates modify turbidity current evolution will help to determine whether current hydrodynamic modelling techniques are suitable for these scenarios; if they are, they would help to

better constrain input parameters when modelling confined or unconfined currents over MTD substrates. On the other hand, if they prove not to be suitable, it could open up new areas of research for the development of new theoretical or numerical modelling techniques.

7. To further evaluate the performance of the model in calculating the upper-interface tilt of turbidity currents it is recommended to repeat the workflow applied to the NAMOC in other channel systems where the tilting of the channel-levees is well constrained. Possible candidates are the Amazon channel (Pirmez and Imran, 2003) or the Knight Inlet (Ren et al., 1996).
8. Following up from point 7, a fixed sediment concentration was chosen for calculating the upper interface tilting of the currents traversing the NAMOC in chapter 5. The model can be adapted to solve for both the tilting and sediment concentration to determine potential zones for erosion and deposition and whether changes in the channel morphometrics might be associated with changes in sediment concentration.
9. Chapter 5 presented the results of a tilting transition slope calculated analytically. Future work can focus on the development of a numerical solution of the transition slope that would more robustly estimate the minimum slope needed for the development of channel sinuosity. This could be achieved through the incorporation of a secondary iterative process in the solution of Equations (5.2) and (5.3) that finds the point of transition.
10. A final recommendation is that work should be conducted to assess the effect of grain size and grain size distribution in the models for the estimation of channel sinuosity, and for numerical solution of the tilting transition slope, jointly calculating for both the tilting and sediment concentration.

References

- Abad, J.D., Sequeiros, O.E., Spinewine, B., Pirmez, C., Garcia, M.H., and Parker, G., 2011, Secondary current of saline underflow in a highly meandering channel: experiments and theory: *Journal of Sedimentary Research*, v. 81, p. 787–813, doi:10.2110/jsr.2011.61.
- Abd El-Gawad, S., Cantelli, A., Pirmez, C., Minisini, D., Sylvester, Z., and Imran, J., 2012, Three-dimensional numerical simulation of turbidity currents in a submarine channel on the seafloor of the Niger Delta slope: *Journal of Geophysical Research: Oceans*, v. 117, p. 1–16, doi:10.1029/2011JC007538.
- Abreu, V., Sullivan, M., Pirmez, C., and Mohrig, D., 2003, Lateral accretion packages (LAPs): an important reservoir element in deep water sinuous channels: *Marine and Petroleum Geology*, v. 20, p. 631–648, doi:10.1016/j.marpetgeo.2003.08.003.
- Amy, L.A., 2019, A review of producing fields inferred to have upslope stratigraphically trapped turbidite reservoirs: trapping styles (pure and combined), pinchout formation and depositional setting: *American Association of Petroleum Geologists Bulletin*, v. 103, p. 2861–2889, doi:10.1306/02251917408.
- Amy, L., and Dorrell, R., 2021, Equilibrium sediment transport by dilute turbidity currents: Comparison of competence-based and capacity-based models: *Sedimentology*, v. 69, p. 624–650, doi:10.1111/sed.12921.
- Amy, L., Kneller, B., and McCaffrey, W., 2000, Evaluating the links between turbidite characteristics and gross system architecture: upscaling insights from the turbidite sheet-system of Peïra Cava, SE France, *in* Weimer, P., Slatt, R.M., and Coleman, J. eds., *Deep Water Reservoirs of the World: 20th Annual*, Houston, TX, p. 1–15, doi:10.5724/gcs.00.15.0001.
- Azpiroz-Zabala, M., Cartigny, M.J.B., Talling, P.J., Parsons, D.R., Sumner, E.J., Clare, M.A., Simmons, S.M., Cooper, C., and Pope, E.L., 2017, Newly recognized turbidity current structure can explain prolonged flushing of submarine canyons: *Science Advances*, v. 3, p. 1–12, doi:10.1126/sciadv.1700200.
- Babonneau, N., Savoye, B., Cremer, M., and Bez, M., 2010, Sedimentary architecture in meanders of a submarine channel: detailed study of the present Congo Turbidite Channel (Zaiango Project): *Journal of Sedimentary Research*, v. 80, p. 852–866, doi:10.2110/jsr.2010.078.
- Babonneau, N., Savoye, B., Cremer, M., and Klein, B., 2002, Morphology and architecture of the present canyon and channel system of the Zaire deep-sea fan: *Marine and Petroleum Geology*, v. 19, p. 445–467, doi:10.1016/S0264-8172(02)00009-0.
- Bacon, M., Simm, R., and Redshaw, T., 2003, *3D Seismic interpretation*: Cambridge University Press, 225 p.

- Bagnold, R.A., 1966, An Approach to the Sediment Transport Problem from General Physics: Geological Survey Professional Paper, v. 422–I, p. I1–I37.
- Bagnold, R.A., 1962, Auto-suspension of transported sediment; turbidity currents: Proceedings of the Royal Society of London. Series A, Mathematical and Physical Sciences, v. 265, p. 315–319.
- Bagnold, R.A., 1956, The flow of cohesionless grains in fluids: Royal Society of London, Philosophical Transactions, Series A, v. 249, p. 235–297, doi:10.1098/rsta.1956.0020.
- Bailey, W.S., McArthur, A.D., and McCaffrey, W.D., 2021, Distribution of contourite drifts on convergent margins: Examples from the Hikurangi subduction margin of New Zealand: Sedimentology, v. 68, p. 294–323, doi:10.1111/sed.12779.
- Bailleul, J., Chanier, F., Ferrière, J., Robin, C., Nicol, A., Mahieux, G., Gorini, C., and Caron, V., 2013, Neogene evolution of lower trench-slope basins and wedge development in the central Hikurangi subduction margin, New Zealand: Tectonophysics, v. 591, p. 152–174, doi:10.1016/j.tecto.2013.01.003.
- Bailleul, J., Robin, C., Chanier, F., Guillocheau, F., Field, B., and Ferriere, J., 2007, Turbidite systems in the inner forearc domain of the Hikurangi convergent margin (New Zealand): New constraints on the development of trench-slope basins: Journal of Sedimentary Research, v. 77, p. 263–283, doi:10.2110/jsr.2007.028.
- Ballance, P.F., 1976, Evolution of the Upper Cenozoic Magmatic Arc and plate boundary in northern New Zealand: Earth and Planetary Science Letters, v. 28, p. 356–370, doi:10.1016/0012-821X(76)90197-7.
- Barnes, P.M. et al., 2017, Tangaroa TAN1613 Voyage Report: Using sedimentary core records to unravel the earthquake of the Hikurangi Subduction Zone:, https://www.niwa.co.nz/static/web/Vessels/TAN1613-Voyage-Report_Hikurangi-Subduction-Zone-web.pdf.
- Barnes, P.M., and Audru, J.C., 1999, Quaternary faulting in the offshore Flaxbourne and Wairarapa Basins, southern Cook Strait, New Zealand: New Zealand Journal of Geology and Geophysics, v. 42, p. 349–367, doi:10.1080/00288306.1999.9514851.
- Barnes, P.M., Lamarche, G., Bialas, J., Henrys, S., Pecher, I., Netzeband, G.L., Greinert, J., Mountjoy, J.J., Pedley, K., and Crutchley, G., 2010, Tectonic and geological framework for gas hydrates and cold seeps on the Hikurangi subduction margin, New Zealand: Marine Geology, v. 272, p. 26–48, doi:10.1016/j.margeo.2009.03.012.
- Beaubouef, R.T., 2004, Deep-water leveed-channel complexes of the Cerro Toro Formation, Upper Cretaceous, southern Chile: American Association of Petroleum Geologists Bulletin, v. 88, p. 1471–1500, doi:10.1306/06210403130.
- Bell, D., Kane, I.A., Pontén, A.S.M., Flint, S.S., Hodgson, D.M., and Barrett, B.J., 2018, Spatial variability in depositional reservoir quality of deep-water channel-

- fill and lobe deposits: *Marine and Petroleum Geology*, v. 98, p. 97–115, doi:10.1016/j.marpetgeo.2018.07.023.
- Bland, K.J., Uruski, C.I., and Isaac, M.J., 2015, Pegasus Basin, eastern New Zealand: A stratigraphic record of subsidence and subduction, ancient and modern: *New Zealand Journal of Geology and Geophysics*, v. 58, p. 319–343, doi:10.1080/00288306.2015.1076862.
- Boggild, K., and Mosher, D.C., 2021, Turbidity currents at polar latitudes: A case study of NP-28 channel in the Amundsen Basin, Arctic Ocean: *Marine Geology*, v. 440, p. 106571, doi:10.1016/j.margeo.2021.106571.
- Booth, J.R., Dean, M.C., DuVernay, A.E., and Styzen, M.J., 2003, Paleobathymetric controls on the stratigraphic architecture and reservoir development of confined fans in the Auger Basin: central Gulf of Mexico slope: *Marine and Petroleum Geology*, v. 20, p. 563–586, doi:10.1016/j.marpetgeo.2003.03.008.
- Bourget, J., Zaragosi, S., Garlan, T., Gabelotaud, I., Guyomard, P., Dennielou, B., Ellouz-Zimmermann, N., and Schneider, J.L., 2008, Discovery of a giant deep-sea valley in the Indian Ocean, off eastern Africa: The Tanzania channel: *Marine Geology*, v. 255, p. 179–185, doi:10.1016/j.margeo.2008.09.002.
- Bowen, A.J., Normark, W.R., and Piper, D.J.W., 1984, Modelling of turbidity currents on Navy Submarine Fan, California Continental Borderland: *Sedimentology*, v. 31, p. 169–185, doi:10.1002/9781444304473.ch2.
- Bull, S., Browne, G.H., Arnot, M.J., and Strachan, L.J., 2020, Influence of Mass Transport Deposit (MTD) surface topography on deep-water deposition: an example from a predominantly fine-grained continental margin, New Zealand: *Geological Society, London, Special Publications*, v. 500, p. 147–171.
- Burgreen-Chan, B., Meisling, K.E., and Graham, S., 2016, Basin and petroleum system modelling of the East Coast Basin, New Zealand: a test of overpressure scenarios in a convergent margin: *Basin Research*, v. 28, p. 536–567, doi:10.1111/bre.12121.
- Cantero, M.I., Shringarpure, M., and Balachandar, S., 2012, Towards a universal criteria for turbulence suppression in dilute turbidity currents with non-cohesive sediments: *Geophysical Research Letters*, v. 39, p. 1–5, doi:10.1029/2012GL052514.
- Carruth, A.G., 2003, The Foinaven Field, Blocks 204/19 and 204/24a, UK North Sea: *Geological Society Memoir*, v. 20, p. 121–130, doi:10.1144/GSL.MEM.2003.020.01.10.
- Carter, L., and Carter, R.M., 1988, Late Quaternary development of left-bank-dominant levees in the Bounty Trough, New Zealand: *Marine Geology*, v. 78, p. 185–197, doi:10.1016/0025-3227(88)90108-9.
- Carter, R.M., Carter, L., and McCave, I.N., 1996, Current controlled sediment deposition from the shelf to the deep ocean: The Cenozoic evolution of circulation through the SW Pacific gateway: *International Journal of Earth*

- Sciences, v. 85, p. 438–451, doi:10.1007/s005310050087.
- Carter, L., Carter, R.M., and McCave, I.N., 2004, Evolution of the sedimentary system beneath the deep Pacific inflow off eastern New Zealand: *Marine Geology*, v. 205, p. 9–27, doi:10.1016/S0025-3227(04)00016-7.
- Carter, R.C., Gani, M.R., Roesler, T., and Sarwar, A.K.M., 2016, Submarine channel evolution linked to rising salt domes, Gulf of Mexico, USA: *Sedimentary Geology*, v. 342, p. 237–253, doi:10.1016/j.sedgeo.2016.06.021.
- Carter, L., Gavey, R., Talling, P.J., and Liu, J.T., 2014, Insights into submarine geohazards from breaks in subsea telecommunication cables: *Oceanography*, v. 27, p. 58–67, doi:10.5670/oceanog.2014.40.
- Cartigny, M.J.B., Eggenhuisen, J.T., Hansen, E.W.M., and Postma, G., 2013, Concentration-dependent flow stratification in experimental high-density turbidity currents and their relevance to turbidite facies models: *Journal of Sedimentary Research*, v. 83, p. 1046–1064, doi:10.2110/jsr.2013.71.
- Carvajal, C., and Steel, R., 2009, Shelf-edge architecture and bypass of sand to deep water: Influence of shelf-edge processes, sea level, and sediment supply: *Journal of Sedimentary Research*, v. 79, p. 652–672, doi:10.2110/jsr.2009.074.
- Chanier, F., and Ferriere, J., 1991, From a passive to an active margin: tectonic and sedimentary processes linked to the birth of an accretionary prism (Hikurangi margin, New Zealand): *Bulletin - Societe Geologique de France*, v. 162, p. 649–660, doi:10.2113/gssgfbull.162.4.649.
- Chanson, H., 2004, *The Hydraulics of Open Channel Flow: An Introduction*, doi:10.1061/(asce)0733-9429(2001)127:3(246).
- Clark, I.R., and Cartwright, J.A., 2009, Interactions between submarine channel systems and deformation in deepwater fold belts: Examples from the Levant Basin, Eastern Mediterranean sea: *Marine and Petroleum Geology*, v. 26, p. 1465–1482, doi:10.1016/j.marpetgeo.2009.05.004.
- Clark, I.R., and Cartwright, J.A., 2011, Key controls on submarine channel development in structurally active settings: *Marine and Petroleum Geology*, v. 28, p. 1333–1349, doi:10.1016/j.marpetgeo.2011.02.001.
- Clark, J.D., Kenyon, N.H., and Pickering, K.T., 1992, Quantitative analysis of the geometry of submarine channels: Implications for the classification of submarine fans: *Geology*, v. 20, p. 633–636.
- Coleman, T.F., and Li, Y., 1996, An interior, trust Region approach for nonlinear minimization subject to bounds: *Society for Industrial and Applied Mathematics Journal on Optimization*, v. 6, p. 418–445.
- Cossu, R., and Wells, M.G., 2010, Coriolis forces influence the secondary circulation of gravity currents flowing in large-scale sinuous submarine channel systems: *Geophysical Research Letters*, v. 37, p. 1–6, doi:10.1029/2010GL044296.

- Cossu, R., and Wells, M.G., 2013, The evolution of submarine channels under the influence of Coriolis forces: Experimental observations of flow structures: *Terra Nova*, v. 25, p. 65–71, doi:10.1111/ter.12006.
- Cossu, R., Wells, M.G., and Peakall, J., 2015, Latitudinal variations in submarine channel sedimentation patterns: The role of coriolis forces: *Journal of the Geological Society*, v. 172, p. 161–174, doi:10.1144/jgs2014-043.
- Cossu, R., Wells, M.G., and Whlin, A.K., 2010, Influence of the Coriolis force on the velocity structure of gravity currents in straight submarine channel systems: *Journal of Geophysical Research*, v. 115, p. 1–15, doi:10.1029/2010JC006208.
- Counts, J.W., Amy, L.A., Georgiopolou, A., and Haughton, P., 2021, A review of sand detachment in modern deep marine environments: Analogues for upslope stratigraphic traps: *Marine and Petroleum Geology*, v. 132, p. 1–15, doi:10.1016/j.marpetgeo.2021.105184.
- Covault, J.A., and Graham, S.A., 2010, Submarine fans at all sea-level stands: Tectono-morphologic and climatic controls on terrigenous sediment delivery to the deep sea: *Geology*, v. 38, p. 939–942, doi:10.1130/G31081.1.
- Covault, J.A., Kostic, S., Paull, C.K., Ryan, H.F., and Fildani, A., 2014, Submarine channel initiation, filling and maintenance from sea-floor geomorphology and morphodynamic modelling of cyclic steps: *Sedimentology*, v. 61, p. 1031–1054, doi:10.1111/sed.12084.
- Covault, J.A., Sylvester, Z., Ceyhan, C., and Dunlap, D.B., 2021, Giant meandering channel evolution, Campos deep-water salt basin, Brazil: *Geosphere*, v. 17, p. 1–21, doi:10.1130/ges02420.1.
- Crisóstomo-Figueroa, A., McArthur, A.D., Dorrell, R.M., Amy, L., and McCaffrey, W.D., 2021, A new modelling approach to sediment bypass prediction applied to the East Coast Basin, New Zealand: *Geological Society of America Bulletin*, v. 133, p. 1734–1748, doi:10.1130/B35687.1.
- Cronin, B.T., 1995, Structurally-controlled deep sea channel courses: Examples from the Miocene of southeast Spain and the Alboran Sea, southwest Mediterranean: *Geological Society Special Publication*, v. 94, p. 115–135, doi:10.1144/GSL.SP.1995.094.01.10.
- Cronin, B.T., Çelik, H., Hurst, A., and Turkmen, I., 2005, Mud prone entrenched deep-water slope channel complexes from the Eocene of eastern Turkey: *Geological Society Special Publication*, v. 244, p. 155–180, doi:10.1144/GSL.SP.2005.244.01.10.
- Cross, N.E., Cunningham, A., Cook, R.J., and Taha, A., 2009, Three-dimensional seismic geomorphology of a deep-water slope-channel system: The Sequoia field, offshore west Nile Delta, Egypt: *American Association of Petroleum Geologists Bulletin*, v. 93, p. 1063–1086, doi:10.1306/05040908101.
- Cullis, S., Colombera, L., Patacci, M., and McCaffrey, W.D., 2018, Hierarchical classifications of the sedimentary architecture of deep-marine depositional

- systems: *Earth-Science Reviews*, v. 179, p. 38–71, doi:10.1016/j.earscirev.2018.01.016.
- Cullis, S., Patacci, M., Colombera, L., Bührig, L., and McCaffrey, W.D., 2019, A database solution for the quantitative characterisation and comparison of deep-marine siliciclastic depositional systems: *Marine and Petroleum Geology*, v. 102, p. 321–339, doi:10.1016/j.marpetgeo.2018.12.023.
- Curry, J.R., Emmel, F.J., and Moore, D.G., 2003, The Bengal Fan: Morphology, geometry, stratigraphy, history and processes: *Marine and Petroleum Geology*, v. 19, p. 1191–1223, doi:10.1016/S0264-8172(03)00035-7.
- Daly, R.A., 1936, Origin of submarine canyons: *American Journal of Science*, v. s5-31, p. 401–420.
- Das, H.S., Imran, J., Pirmez, C., and Mohrig, D., 2004, Numerical modeling of flow and bed evolution in meandering submarine channels: *Journal of Geophysical Research*, v. 109, p. 1–17, doi:10.1029/2002JC001518.
- Davarpanah Jazi, S., Wells, M.G., Peakall, J., Dorrell, R.M., and Thomas, R.E., 2020, Influence of Coriolis force upon bottom boundary layers in a large - scale gravity current experiment : Implications for evolution of sinuous deep - water channel systems: *Journal of Geophysical Research: Oceans*, v. 125, p. 1–30, doi:10.1029/2019JC015284.
- Davey, F.J., Hampton, M., Childs, J., Fisher, M.A., Lewis, K., and Pettinga, J.R., 1986, Structure of a growing accretionary prism, Hikurangi margin, New Zealand.: *Geology*, v. 14, p. 663–666.
- Dennis, J.E.J., 1977, Nonlinear least squares, *in* Jacobs, D. ed., *The state of the art in numerical analysis*, Academic Press (New York), p. 269–312.
- Deptuck, M.E., Piper, D.J.W., Savoye, B., and Gervais, A., 2008, Dimensions and architecture of late Pleistocene submarine lobes off the northern margin of East Corsica: *Sedimentology*, v. 55, p. 869–898, doi:10.1111/j.1365-3091.2007.00926.x.
- Deptuck, M.E., Steffens, G.S., Barton, M., and Pirmez, C., 2003, Architecture and evolution of upper fan channel-belts on the Niger Delta slope and in the Arabian Sea: *Marine and Petroleum Geology*, v. 20, p. 649–676, doi:10.1016/j.marpetgeo.2003.01.004.
- Deptuck, M.E., Sylvester, Z., Pirmez, C., and O'Byrne, C., 2007, Migration-aggradation history and 3-D seismic geomorphology of submarine channels in the Pleistocene Benin-major Canyon, western Niger Delta slope: *Marine and Petroleum Geology*, v. 24, p. 406–433, doi:10.1016/j.marpetgeo.2007.01.005.
- Doré, G., and Robbins, J., 2005, The Buzzard Field, *in* *Petroleum Geology: North-West Europe and Global Perspectives-Proceedings of the 6th Petroleum Geology Conference*, p. 241–252.
- Dorrell, R.M., Amy, L.A., Peakall, J., and McCaffrey, W.D., 2018, Particle size distribution controls the threshold between net sediment erosion and

- deposition in suspended load dominated flows: *Geophysical Research Letters*, v. 45, p. 1443–1452, doi:10.1002/2017GL076489.
- Dorrell, R.M., Burns, A.D., and McCaffrey, W.D., 2015, The inherent instability of leveed seafloor channels: *Geophysical Research Letters*, v. 42, p. 4023–4031, doi:10.1002/2015GL063809.
- Dorrell, R.M., Darby, S.E., Peakall, J., Sumner, E.J., Parsons, D.R., and Wynn, R.B., 2013a, Superelevation and overspill control secondary flow dynamics in submarine channels: *Journal of Geophysical Research: Oceans*, v. 118, p. 3895–3915, doi:10.1002/jgrc.20277.
- Dorrell, R.M., Darby, S.E., Peakall, J., Sumner, E.J., Parsons, D.R., and Wynn, R.B., 2014, The critical role of stratification in submarine channels: Implications for channelization and long runout of flows: *Journal of Geophysical Research: Oceans*, v. 119, p. 2620–2641, doi:10.1002/2014JC009807. Received.
- Dorrell, R.M., and Hogg, A.J., 2012, Length and time scales of response of sediment suspensions to changing flow conditions: *Journal of Hydraulic Engineering*, v. 138, p. 430–439, doi:10.1061/(ASCE)HY.1943-7900.0000532.
- Dorrell, R.M., Hogg, A.J., and Pritchard, D., 2013b, Polydisperse suspensions: Erosion, deposition, and flow capacity: *Journal of Geophysical Research: Earth Surface*, v. 118, p. 1939–1955, doi:10.1002/jgrf.20129.
- Dorrell, R.M., Peakall, J., Darby, S.E., Parsons, D.R., Johnson, J., Sumner, E.J., Wynn, R.B., Özsoy, E., and Tezcan, D., 2019, Self-sharpening induces jet-like structure in seafloor gravity currents: *Nature Communications*, v. 10, p. 1–10, doi:10.1038/s41467-019-09254-2.
- Dorrell, R.M., Peakall, J., Sumner, E.J., Parsons, D.R., Darby, S.E., Wynn, R.B., Özsoy, E., and Tezcan, D., 2016, Flow dynamics and mixing processes in hydraulic jump arrays: Implications for channel-lobe transition zones: *Marine Geology*, v. 381, p. 181–193, doi:10.1016/j.margeo.2016.09.009.
- Droz, L., and Mougnot, D., 1987, Mozambique upper fan: origin of depositional units: *American Association of Petroleum Geologists Bulletin*, v. 71, p. 1355–1365, doi:10.1306/703c8079-1707-11d7-8645000102c1865d.
- Ellison, T.H., and Turner, J.S., 1959, Turbulent entrainment in stratified flows: *Journal of Fluid Mechanics*, v. 6, p. 423–448, doi:10.1017/S0022112059000738.
- Ferry, J.N., Mulder, T., Parize, O., and Raillard, S., 2005, Concept of equilibrium profile in deep-water turbidite systems: Effects of local physiographic changes on the nature of sedimentary process and the geometries of deposits: *Geological Society Special Publication*, v. 244, p. 181–193, doi:10.1144/GSL.SP.2005.244.01.11.
- Field, B.D., and Uruski, C.I., 1997, Cretaceous-Cenozoic geology and petroleum systems of the East Coast region, New Zealand: *Institute of Geological & Nuclear Sciences*, v. 1.

- Fildani, A., Hubbard, S.M., Covault, J.A., Maier, K.L., Romans, B.W., Traer, M., and Rowland, J.C., 2013, Erosion at inception of deep-sea channels: *Marine and Petroleum Geology*, v. 41, p. 48–61, doi:10.1016/j.marpetgeo.2012.03.006.
- Fildani, A., and Normark, W.R., 2004, Late Quaternary evolution of channel and lobe complexes of Monterey Fan: *Marine Geology*, v. 206, p. 199–223, doi:10.1016/j.margeo.2004.03.001.
- Fildani, A., Normark, W.R., Kostic, S., and Parker, G., 2006, Channel formation by flow stripping: Large-scale scour features along the Monterey East Channel and their relation to sediment waves: *Sedimentology*, v. 53, p. 1265–1287, doi:10.1111/j.1365-3091.2006.00812.x.
- Flood, R.D., and Damuth, J.E., 1987, Quantitative characteristics of sinuous distributary channels on the Amazon Deep-Sea Fan.: *Geological Society of America Bulletin*, v. 98, p. 728–738, doi:10.1130/0016-7606(1987)98<728:QCOSDC>2.0.CO;2.
- Folk, R., 1966, A review of grain-size parameters: *Sedimentology*, v. 6, p. 73–93.
- Fugelli, E.M.G., and Olsen, T.R., 2005, Screening for deep-marine reservoirs in frontier basins: Part 1 - Examples from offshore mid-Norway: *American Association of Petroleum Geologists Bulletin*, v. 89, p. 853–882, doi:10.1306/02110504029.
- Garcia, M.H., 1994, Depositional turbidity currents laden with poorly sorted sediment: *Journal of Hydraulic Engineering*, v. 120, p. 1240–1263.
- Garcia, B.M., 1991, Entrainment of bed sediment into suspension: *Journal of Hydraulic Engineering*, v. 117, p. 414–435.
- Gardiner, A.R., 2006, The variability of turbidite sandbody pinchout and its impact on hydrocarbon recovery in stratigraphically trapped fields, *in* Allen, M.R., Goffey, G.P., Morgan, R.K., and Walker, I.M. eds., *The deliberate search for the stratigraphic trap*. Geological Society, London, Special Publications, The Geological Society of London, v. 254, p. 267–287, doi:10.1144/GSL.SP.2006.254.01.14.
- Gardner, M.H., Borer, J.M., Melick, J.J., Mavilla, N., Dechesne, M., and Wagerle, R.N., 2003, Stratigraphic process-response model for submarine channels and related features from studies of Permian Brushy Canyon outcrops, West Texas: *Marine and Petroleum Geology*, v. 20, p. 757–787, doi:10.1016/j.marpetgeo.2003.07.004.
- Ge, Z., Nemeč, W., Gawthorpe, R.L., and Hansen, E.W.M., 2017, Response of unconfined turbidity current to normal-fault topography: *Sedimentology*, v. 64, p. 932–959, doi:10.1111/sed.12333.
- Gee, M.J.R., and Gawthorpe, R.L., 2007, Early evolution of submarine channels offshore Angola revealed by three-dimensional seismic data: *Geological Society Special Publication*, v. 277, p. 223–235, doi:10.1144/GSL.SP.2007.277.01.13.

- Georgiopoulou, A., and Cartwright, J.A., 2013, A critical test of the concept of submarine equilibrium profile: *Marine and Petroleum Geology*, v. 41, p. 35–47, doi:10.1016/j.marpetgeo.2012.03.003.
- Goldfinger, C., 2011, Submarine paleoseismology based on turbidite records: *Annual Review of Marine Science*, v. 3, p. 35–66, doi:10.1146/annurev-marine-120709-142852.
- Gong, C., Li, D., Qi, K., and Xu, H., 2020, Flow processes and sedimentation in a straight submarine channel on the qiongdongnan margin, northwestern South China Sea: *Journal of Sedimentary Research*, v. 90, p. 1372–1388, doi:10.2110/JSR.2020.68.
- Goodarzi, D., Sookhak Lari, K., Khavasi, E., and Abolfathi, S., 2020, Large eddy simulation of turbidity currents in a narrow channel with different obstacle configurations: *Scientific Reports*, v. 10, p. 1–16, doi:10.1038/s41598-020-68830-5.
- Groenenberg, R.M., Sloff, K., and Weltje, G.J., 2009, A high-resolution 2-DH numerical scheme for process-based modeling of 3-D turbidite fan stratigraphy: *Computers and Geosciences*, v. 35, p. 1686–1700, doi:10.1016/j.cageo.2009.01.004.
- Hadler-Jacobsen, F., Johannessen, E.P., Ashton, N., Henriksen, S., Johnson, S.D., and Kristensen, J.B., 2005, Submarine fan morphology and lithology distribution: A predictable function of sediment delivery, gross shelf-to-basin relief, slope gradient and basin topography, *in* *Petroleum Geology: North-West Europe and Global Perspectives-Proceedings of the 6th Petroleum Geology Conference*, v. 6, p. 1121–1145, doi:10.1144/0061121.
- Hage, S. et al., 2020, Efficient preservation of young terrestrial organic carbon in sandy turbidity-current deposits: *Geology*, v. 48, p. 882–887, doi:10.1130/G47320.1.
- Halsey, T.C., Kumar, A., Perillo, M.M., and Stansby, P.K., 2017, Sedimentological regimes for turbidity currents: Depth-averaged theory: *Journal of Geophysical Research: Oceans*, v. 122, p. 5260–5285, doi:10.1002/2016JC012635.Received.
- Hansen, L.A.S., Callow, R.H.T., Kane, I.A., Gamberi, F., Rovere, M., Cronin, B.T., and Kneller, B.C., 2015, Genesis and character of thin-bedded turbidites associated with submarine channels: *Marine and Petroleum Geology*, v. 67, p. 852–879, doi:10.1016/j.marpetgeo.2015.06.007.
- Hansen, L.A.S., Hodgson, D.M., Pontén, A., Bell, D., and Flint, S., 2019, Quantification of basin-floor fan pinchouts: Examples from the Karoo Basin, South Africa: *Frontiers in Earth Science*, v. 7, p. 1–20, doi:10.3389/feart.2019.00012.
- Hansen, L., Janocko, M., Kane, I., and Kneller, B., 2017, Submarine channel evolution, terrace development, and preservation of intra-channel thin-bedded turbidites: Mahin and Avon channels, offshore Nigeria: *Marine Geology*, v.

- 383, p. 146–167, doi:10.1016/j.margeo.2016.11.011.
- Haughton, P., Davis, C., McCaffrey, W., and Barker, S., 2009, Hybrid sediment gravity flow deposits - Classification, origin and significance: *Marine and Petroleum Geology*, v. 26, p. 1900–1918, doi:10.1016/j.marpetgeo.2009.02.012.
- Heerema, C.J. et al., 2020, What determines the downstream evolution of turbidity currents? *Earth and Planetary Science Letters*, v. 532, p. 1–11, doi:10.1016/j.epsl.2019.116023.
- Heezen, B.C., and Ewing, M., 1952, Turbidity currents and submarine slumps, and the 1929 Grand Banks earthquake: *American Journal of Science*, v. 250, p. 849–873.
- Heijnen, M.S. et al., 2022, Fill, flush or shuffle: How is sediment carried through submarine channels to build lobes? *Earth and Planetary Science Letters*, v. 584, p. 1–14, doi:10.1016/j.epsl.2022.117481.
- Heijnen, M.S. et al., 2020, Rapidly-migrating and internally-generated knickpoints can control submarine channel evolution: *Nature Communications*, v. 11, p. 1–15, doi:10.1038/s41467-020-16861-x.
- Hesse, R., Chough, S.K., and Rakofsky, A., 1987, The Northwest Atlantic Mid-Ocean Channel of the Labrador Sea. V. Sedimentology of a giant deep-sea channel: *Canadian Journal of Earth Sciences*, v. 24, p. 1595–1624, doi:10.1139/e87-155.
- Hewlett, J.S., and Jordan, D.W., 1993, Stratigraphic and combination traps within a seismic sequence framework, Miocene Stevens turbidites, Bakersfield Arch, California, *in* *Recent Applications of Siliciclastic Sequence Stratigraphy*, p. 135–162.
- Hiscott, R.N., 1994, Loss of capacity, not competence, as the fundamental process governing deposition from turbidity currents: *Journal of Sedimentary Research*, v. A64, p. 209–214.
- Hodgson, D.M., Kane, I.A., Flint, S.S., Brunt, R.L., and Ortiz-Karpf, A., 2016, Time-transgressive confinement on the slope and the progradation of basin-floor fans: implications for the sequence stratigraphy of deep-water deposits: *Journal of Sedimentary Research*, v. 86, p. 73–86, doi:10.2110/jsr.2016.3.
- Hodgson, D.M., Peakall, J., and Maier, K.L., 2022, Submarine channel mouth settings: processes, geomorphology, and deposits: *Frontiers in Earth Science*, v. 10, p. 1–20, doi:10.3389/feart.2022.790320.
- Horseman, C., Ross, A., and Cannon, S., 2014, The discovery and appraisal of Glenlivet: a West of Shetlands success story, *in* Cannon, S. and Ellis, D. eds., *Hydrocarbon exploration to exploitation West of Shetlands*. Geological Society, London, Special Publications, The Geological Society of London, v. 397, p. 131–144, doi:10.1144/SP397.10.
- Howlett, D.M., Ge, Z., Nemec, W., Gawthorpe, R.L., Rotevatn, A., and Jackson,

- C.A.L., 2019, Response of unconfined turbidity current to deep-water fold and thrust belt topography: Orthogonal incidence on solitary and segmented folds: *Sedimentology*, p. 2425–2454, doi:10.1111/sed.12602.
- Hubbard, S.M., Covault, J.A., Fildani, A., and Romans, B.W., 2014, Sediment transfer and deposition in slope channels: Deciphering the record of enigmatic deep-sea processes from outcrop: *Bulletin of the Geological Society of America*, v. 126, p. 857–871, doi:10.1130/B30996.1.
- Hubbard, S.M., Jobe, Z.R., Romans, B.W., Covault, J.A., Sylvester, Z., and Fildani, A., 2020, The stratigraphic evolution of a submarine channel: Linking seafloor dynamics to depositional products: *Journal of Sedimentary Research*, v. 90, p. 673–686, doi:10.2110/jsr.2020.36.
- Imran, J., Parker, G., and Pirmez, C., 1999, A nonlinear model of flow in meandering submarine and subaerial channels: *Journal of Fluid Mechanics*, v. 400, p. 295–331, doi:10.1017/S0022112099006515.
- Islam, M.A., and Imran, J., 2008, Experimental modeling of gravity underflow in a sinuous submerged channel: *Journal of Geophysical Research*, v. 113, p. 1–15, doi:10.1029/2007JC004292.
- Al Ja'Aidi, O.S., McCaffrey, W.D., and Kneller, B.C., 2004, Factors influencing the deposit geometry of experimental turbidity currents: Implications for sand-body architecture in confined basins: *Geological Society Special Publication*, v. 222, p. 45–58, doi:10.1144/GSL.SP.2004.222.01.04.
- Janocko, M., Cartigny, M.B.J., Nemeč, W., and Hansen, E.W.M., 2013a, Turbidity current hydraulics and sediment deposition in erodible sinuous channels: Laboratory experiments and numerical simulations: *Marine and Petroleum Geology*, v. 41, p. 222–249, doi:10.1016/j.marpetgeo.2012.08.012.
- Janocko, M., Nemeč, W., Henriksen, S., and Warchoł, M., 2013b, The diversity of deep-water sinuous channel belts and slope valley-fill complexes: *Marine and Petroleum Geology*, v. 41, p. 7–34, doi:10.1016/j.marpetgeo.2012.06.012.
- Jobe, Z.R., Howes, N.C., and Auchter, N.C., 2016, Comparing submarine and fluvial channel kinematics: Implications for stratigraphic architecture: v. 44, p. 931–934, doi:10.1130/G38158.1.
- Jobe, Z.R., Howes, N.C., Straub, K.M., Cai, D., Deng, H., Laugier, F.J., Pettinga, L.A., Shumaker, L.E., Owen, A., and Hodgson, D.M., 2020, Comparing aggradation, super-elevation, and avulsion frequency of submarine and fluvial channels: *Frontiers in Earth Science*, v. 8, p. 1–22, doi:10.3389/feart.2020.00053.
- Jobe, Z.R., Sylvester, Z., Parker, A.O., Howes, N., Slowey, N., and Pirmez, C., 2015, Rapid Adjustment of Submarine Channel Architecture To Changes In Sediment Supply: *Journal of Sedimentary Research*, v. 85, p. 729–753, doi:10.2110/jsr.2015.30.
- Kane, I.A., and Clare, M.A., 2019, Dispersion, accumulation, and the ultimate fate of microplastics in deep-marine environments: A review and future directions:

- Frontiers in Earth Science, v. 7, p. 1–27, doi:10.3389/feart.2019.00080.
- Kane, I.A., Clare, M.A., Miramontes, E., Wogelius, R., Rothwell, J.J., Garreau, P., and Pohl, F., 2020, Seafloor microplastic hotspots controlled by deep-sea circulation: *Science*, v. 368, p. 1140–1145, doi:10.1126/science.aba5899.
- Kane, I.A., and Hodgson, D.M., 2011, Sedimentological criteria to differentiate submarine channel levee subenvironments: Exhumed examples from the Rosario Fm. (Upper Cretaceous) of Baja California, Mexico, and the Fort Brown Fm. (Permian), Karoo Basin, S. Africa: *Marine and Petroleum Geology*, v. 28, p. 807–823, doi:10.1016/j.marpetgeo.2010.05.009.
- Kane, I.A., and McCaffrey, W.D., 2008, Controls on sinuosity evolution within submarine channels: *Geology*, v. 36, p. 287–290, doi:10.1130/G24588A.1.
- Keevil, G.M., Peakall, J., and Best, J.L., 2007, The influence of scale, slope and channel geometry on the flow dynamics of submarine channels: *Marine and Petroleum Geology*, v. 24, p. 487–503, doi:10.1016/j.marpetgeo.2007.01.009.
- Kelly, R.W., Dorrell, R.M., Burns, A.D., and McCaffrey, W.D., 2019, The Structure and Entrainment Characteristics of Partially Confined Gravity Currents: *Journal of Geophysical Research: Oceans*, v. 124, p. 2110–2125, doi:10.1029/2018JC014042.
- Khripounoff, A., Vangriesheim, A., Babonneau, N., Crassous, P., Dennielou, B., and Savoye, B., 2003, Direct observation of intense turbidity current activity in the Zaire submarine valley at 4000 m water depth: *Marine Geology*, v. 194, p. 151–158, doi:10.1016/S0025-3227(02)00677-1.
- Klaucke, I., 1995, The submarine drainage system of the Labrador Sea: Result of glacial input from the Laurentide Ice sheet: McGill University, 247 p.
- Klaucke, I., Hesse, R., and Ryan, W.B.F., 1997, Flow parameters of turbidity currents in a low-sinuosity giant deep-sea channel: *Sedimentology*, v. 44, p. 1093–1102, doi:10.1111/j.1365-3091.1997.tb02180.x.
- Klaucke, I., Hesse, R., and Ryan, W.B.F., 1998, Seismic stratigraphy of the Northwest Atlantic Mid-Ocean Channel: growth pattern of a mid-ocean channel-levee complex: *Marine and Petroleum Geology*, v. 15, p. 575–585, doi:10.1016/S0264-8172(98)00044-0.
- Kneller, B., 1995, Beyond the turbidite paradigm: Physical models for deposition of turbidites and their implications for reservoir prediction: *Geological Society Special Publication*, v. 94, p. 31–49, doi:10.1144/GSL.SP.1995.094.01.04.
- Kneller, B., 2003, The influence of flow parameters on turbidite slope channel architecture: *Marine and Petroleum Geology*, v. 20, p. 901–910, doi:10.1016/j.marpetgeo.2003.03.001.
- Kneller, B.C., Bennett, S.J., and McCaffrey, W.D., 1997, Velocity and turbulence structure of density currents and internal solitary waves: Potential sediment transport and the formation of wave ripples in deep water: *Sedimentary Geology*, v. 112, p. 235–250, doi:10.1016/S0037-0738(97)00031-6.

- Kneller, B.C., Bennett, S.J., and McCaffrey, W.D., 1999, Velocity structure, turbulence and fluid stresses in experimental gravity currents: *Journal of Geophysical Research: Oceans*, v. 104, p. 5381–5391, doi:10.1029/1998jc900077.
- Kneller, B., and Buckee, C., 2000, The structure and fluid mechanics of turbidity currents: A review of some recent studies and their geological implications: *Sedimentology*, v. 47, p. 62–94, doi:10.1046/j.1365-3091.2000.047s1062.x.
- Kneller, B., Nasr-Azadani, M.M., Radhakrishnan, S., and Meiburg, E., 2016, Long-range sediment transport in the world's oceans by stably stratified turbidity currents: *Journal of Geophysical Research: Oceans*, v. 121, p. 8608–8620, doi:10.1002/2016JC011978.Received.
- Kolla, V., Posamentier, H.W., and Wood, L.J., 2007, Deep-water and fluvial sinuous channels-Characteristics, similarities and dissimilarities, and modes of formation: *Marine and Petroleum Geology*, v. 24, p. 388–405, doi:10.1016/j.marpetgeo.2007.01.007.
- Komar, P.D., 1977, Computer simulation of turbidity current flow and the study of deep-sea channels and fan sedimentation, *in* Goldberg, E.D., McCave, I.N., O'Brien, J.J., and Steele, J.H. eds., *The Sea: Ideas and Observations on Progress in the Study of the Seas*, John Wiley, New York, p. 603–621, -.
- Komar, P.D., 1973, Continuity of turbidity current flow and systematic variations in deep-sea channel morphology: *Bulletin of the Geological Society of America*, v. 84, p. 3329–3338, doi:10.1130/0016-7606(1973)84<3329:COTCFA>2.0.CO;2.
- Komar, P.D., 1969, The channelized flow of turbidity currents with application to Monterey deep-sea fan channel: *Journal of Geophysical Research*, v. 74, p. 4544–4558.
- Komar, P.D., 1985, The hydraulic interpretation of turbidites from their grain sizes and sedimentary structures: *Sedimentology*, v. 32, p. 395–407, doi:10.1111/j.1365-3091.1986.tb00547.x.
- Konsoer, K., Zinger, J., and Parker, G., 2013, Bankfull hydraulic geometry of submarine channels created by turbidity currents: Relations between bankfull channel characteristics and formative flow discharge: *Journal of Geophysical Research: Earth Surface*, v. 118, p. 216–228, doi:10.1029/2012JF002422.
- Kuenen, P.H., 1938, Density Currents in connection with the problem of Submarine Canyons: *Geological Magazine*, v. 75, p. 241–249, doi:10.1017/S0016756800089627.
- Lang, J., Brandes, C., and Winsemann, J., 2017, Erosion and deposition by supercritical density flows during channel avulsion and backfilling: Field examples from coarse-grained deepwater channel-levée complexes (Sandino Forearc Basin, southern Central America): *Sedimentary Geology*, v. 349, p. 79–102, doi:10.1016/j.sedgeo.2017.01.002.
- Leeder, M.R., Gray, T.E., and Alexander, J., 2005, Sediment suspension dynamics

- and a new criterion for the maintenance of turbulent suspensions: *Sedimentology*, v. 52, p. 683–691, doi:10.1111/j.1365-3091.2005.00720.x.
- De Leeuw, J., Eggenhuisen, J.T., and Cartigny, M.J.B., 2016, Morphodynamics of submarine channel inception revealed by new experimental approach: *Nature Communications*, v. 7, p. 1–7, doi:10.1038/ncomms10886.
- De Leeuw, J., Eggenhuisen, J.T., Sychala, Y.T., Heijnen, M.S., Pohl, F., and Cartigny, M.J.B., 2018, Sediment volume and grain-size partitioning between submarine channel-levee systems and lobes: An experimental study: *Journal of Sedimentary Research*, v. 88, p. 777–794, doi:10.2110/jsr.2018.46.
- Lemay, M., Grimaud, J., Cojan, I., Rivoirard, J., and Ors, F., 2020, Geomorphic variability of submarine channelized systems along continental margins : Comparison with fluvial meandering channels: *Marine and Petroleum Geology*, v. 115, p. 1–17, doi:10.1016/j.marpetgeo.2020.104295.
- Lewis, K.B., and Bennett, D.J., 1985, Structural patterns on the Hikurangi margin: an interpretation of new seismic data.:
- Lewis, K.B., and Pantin, H.M., 2002, Channel-axis, overbank and drift sediment waves in the southern Hikurangi Trough, New Zealand: *Marine Geology*, v. 192, p. 123–151, doi:10.1016/S0025-3227(02)00552-2.
- Lewis, K.B., and Pettinga, J.R., 1993, The emerging, imbricate frontal wedge of the Hikurangi Margin: *Sedimentary Basins of the World*, v. 2, p. 225–250.
- Li, L., and Gong, C., 2018, Gradual transition from net erosional to net depositional cyclic steps along the submarine distributary channel thalweg in the Rio Muni Basin: A joint 3-D seismic and numerical approach: *Journal of Geophysical Research: Earth Surface*, v. 123, p. 2087–2106, doi:10.1029/2017JF004513.
- Li, L., Gong, C., and Steel, R.J., 2018, Bankfull discharge as a key control on submarine channel morphology and architecture: Case study from the Rio Muni Basin, West Africa: *Marine Geology*, v. 401, p. 66–80, doi:10.1016/j.margeo.2018.04.010.
- Lowe, D.R., 1982, Sediment gravity flows: II. Depositional models with special reference to the deposits of high-density turbidity currents.: *Journal of Sedimentary Petrology*, v. 52, p. 279–297.
- Lyons, N., Val, P., Albert, J., Willenbring, J., and Gasparini, N., 2019, Topographic controls on divide migration, stream capture, and diversification in riverine life: *Earth Surface Dynamics Discussions*, p. 1–29, doi:10.5194/esurf-2019-55.
- Maier, K.L., Fildani, A., Paull, C.K., Graham, S.A., McHargue, T.R., Caress, D.W., and McGann, M., 2011, The elusive character of discontinuous deep-water channels: New insights from Lucia Chica channel system, offshore California: *Geology*, v. 39, p. 327–330, doi:10.1130/G31589.1.
- Maier, K.L., Fildani, A., Paull, C.K., McHargue, T.R., Graham, S.A., and Caress, D.W., 2013, Deep-sea channel evolution and stratigraphic architecture from inception to abandonment from high-resolution Autonomous Underwater

- Vehicle surveys offshore central California: *Sedimentology*, v. 60, p. 935–960, doi:10.1111/j.1365-3091.2012.01371.x.
- Marchand, A.M.E., Apps, G., Li, W., and Rotzien, J.R., 2015, Depositional processes and impact on reservoir quality in deepwater Paleogene reservoirs, US Gulf of Mexico: *American Association of Petroleum Geologists Bulletin*, v. 99, p. 1635–1648, doi:10.1306/04091514189.
- Marshall, J.D., Tucker, O.D., and Lovelock, C.E., 2016, Goldeneye: Modelling a depleted field for carbon capture – how much uncertainty is left? *Petroleum Geoscience*, v. 22, p. 37–45, doi:10.1144/petgeo2014-072.
- Mayall, M., Jones, E., and Casey, M., 2006, Turbidite channel reservoirs-Key elements in facies prediction and effective development: *Marine and Petroleum Geology*, v. 23, p. 821–841, doi:10.1016/j.marpetgeo.2006.08.001.
- Mayall, M., Lonergan, L., Bowman, A., James, S., Mills, K., Primmer, T., Pope, D., Rogers, L., and Skeene, R., 2010, The response of turbidite slope channels to growth-induced seabed topography: *American Association of Petroleum Geologists Bulletin*, v. 94, p. 1011–1030, doi:10.1306/01051009117.
- Mayall, M., and Stewart, I., 2000, The architecture of turbidite slope channels, *in* *Deep Water Reservoirs of the World: 20th Annual Research Conference*, p. 578–586.
- McArthur, A.D., Bailleul, J., Chanier, F., Clare, A., and McCaffrey, W.D., 2022a, Lateral, longitudinal, and temporal variation in trench-slope basin fill: examples from the Neogene Akitio sub-basin, Hikurangi Margin, New Zealand: *New Zealand Journal of Geology and Geophysics*, v. 65, p. 105–140, doi:10.1080/00288306.2021.1977343.
- McArthur, A.D., Bailleul, J., Claussmann, B., Wunderlich, A., and McCaffrey, W.D., 2021, Deformation-sedimentation feedback and the development of anomalously thick aggradational turbidite lobes: Outcrop and subsurface examples from the Hikurangi Margin, New Zealand: v. 91, 362–389 p., doi:10.2110/JSR.2020.013.
- McArthur, A.D., Claussmann, B., Bailleul, J., Clare, A., and McCaffrey, W.D., 2020a, Variation in syn-subduction sedimentation patterns from inner to outer portions of deep-water fold and thrust belts: examples from the Hikurangi subduction margin of New Zealand: *Geological Society, London, Special Publications*, v. 490, p. 285–310, doi:10.1144/sp490-2018-95.
- McArthur, A.D., Crisóstomo-Figueroa, A., Wunderlich, A., Karvelas, A., and McCaffrey, W.D., 2022b, Sedimentation on structurally complex slopes: Neogene to recent deep-water sedimentation patterns across the central Hikurangi subduction margin, New Zealand: *Basin Research*, p. 1–31, doi:10.1111/bre.12686.
- McArthur, A.D., Kane, I., Bozetti, G., Hansen, L., and Kneller, B.C., 2020b, Supercritical flows overspilling from bypass-dominated submarine channels and the development of overbank bedforms: *The Depositional Record*, v. 6, p.

21–40, doi:10.1002/dep2.78.

- McArthur, A.D., and McCaffrey, W.D., 2019, Sedimentary architecture of detached deep-marine canyons: Examples from the East Coast Basin of New Zealand: *Sedimentology*, v. 66, p. 1067–1101, doi:10.1111/sed.12536.
- McArthur, A.D., and Tek, D.E., 2021, Controls on the origin and evolution of deep-ocean trench-axial channels: *Geology*, v. 49, p. 833–888, doi:10.1130/G48612.1.
- McHargue, T., Pyrcz, M., Sullivan, M.D., Clark, J., Fildani, A., Levy, M., Drinkwater, N., Posamentier, H.W., Romans, B.W., and Covault, J.A., 2011a, Event-based modeling of turbidite channel fill, channel stacking pattern, and net sand volume, *in* *Outcrops Revitalized*: Tools, Techniques and Applications, SEPM Society for Sedimentary Geology, p. 163–173, doi:10.2110/sepmcsp.10.163.
- McHargue, T., Pyrcz, M.J., Sullivan, M.D., Clark, J.D., Fildani, A., Romans, B.W., Covault, J.A., Levy, M., Posamentier, H.W., and Drinkwater, N.J., 2011b, Architecture of turbidite channel systems on the continental slope: Patterns and predictions: *Marine and Petroleum Geology*, v. 28, p. 728–743, doi:10.1016/j.marpetgeo.2010.07.008.
- McKeown, M.C., 2018, Understanding the physical sedimentology of the modern Madden Canyon distributary system, New Zealand: University of Auckland, 1–135 p.
- Meiburg, E., and Kneller, B., 2010, Turbidity currents and their deposits: *Annual Review of Fluid Mechanics*, v. 42, p. 135–156, doi:10.1146/annurev-fluid-121108-145618.
- Menard, H.W.J., 1955, Deep-sea channels, topography and sedimentation: *Bulletin of the American Association of Petroleum Geologists*, v. 39, p. 236–255.
- Menard, H.W.J., and Ludwick, J.C., 1951, Applications of hydraulics to the study of marine turbidity currents: *Society of Economic Paleontologists and Mineralogists Special Publication*, v. 2, p. 2–13.
- Van der Merwe, W.C., Hodgson, D.M., Brunt, R.L., and Flint, S.S., 2014, Depositional architecture of sand-attached and sand-detached channel-lobe transition zones on an exhumed stepped slope mapped over a 2500 km² area: *Geosphere*, v. 10, p. 1076–1093, doi:10.1130/GES01035.1.
- Middleton, G. V., 1966a, Experiments on density and turbidity currents: I. Motion of the head: *Canadian Journal of Earth Sciences*, v. 3, p. 523–546, doi:10.1139/e67-025.
- Middleton, G. V., 1966b, Experiments on density and turbidity currents: II. Uniform flow of density currents: *Canadian Journal of Earth Sciences*, v. 3, p. 627–637, doi:10.1139/e67-025.
- Middleton, G. V., 1993, Sediment deposition from turbidity currents: *Annual Review of Earth & Planetary Sciences*, v. 21, p. 89–114,

doi:10.1146/annurev.ea.21.050193.000513.

- Middleton, G. V., 1966c, Small-scale models of turbidity currents and the criterion for auto-suspension: *Journal of Sedimentary Petrology*, v. 36, p. 202–208.
- Migeon, S., Ducassou, E., Le Gonidec, Y., Rouillard, P., Mascle, J., and Revel-Rolland, M., 2010, Lobe construction and sand/mud segregation by turbidity currents and debris flows on the western Nile deep-sea fan (Eastern Mediterranean): *Sedimentary Geology*, v. 229, p. 124–143, doi:10.1016/j.sedgeo.2010.02.011.
- Milton-Worsell, R.J., Stoker, S.J., and Cavill, J.E., 2006, Lower Cretaceous deep-water sandstone plays in the UK Central Graben, *in* Allen, M.R., Goffey, G.P., Morgan, R.K., and Walker, I.M. eds., *The deliberate search for the stratigraphic trap*. Geological Society, London, Special Publications, The Geological Society of London, v. 254, p. 169–186, doi:10.1144/GSL.SP.2006.254.01.09.
- Mohrig, D., and Buttles, J., 2007, Deep turbidity currents in shadow channels: *Geology*, v. 35, p. 155–158, doi:10.1130/G22716A.1.
- Montgomery, S.L., 1997, Permian Bone Spring Formation: Sandstone play in the Delaware Basin Part I—Slope: *American Association of Petroleum Geologists Bulletin*, v. 81, p. 1239–1258.
- Moré, J.J., 1978, The Levenberg-Marquardt algorithm: Implementation and theory, *in* *Numerical Analysis*, Springer, Berlin, Heidelberg, p. 105–116, doi:10.1007/BFb0067700.
- Mountjoy, J.J., Barnes, P.M., and Pettinga, J.R., 2009, Morphostructure and evolution of submarine canyons across an active margin: Cook Strait sector of the Hikurangi Margin, New Zealand: *Marine Geology*, v. 260, p. 45–68, doi:10.1016/j.margeo.2009.01.006.
- Mountjoy, J.J., and Micallef, A., 2012, Polyphase emplacement of a 30 km³ blocky debris avalanche and its role in slope-gully development, *in* *Submarine mass movements and their consequences*, p. 213–222.
- Mulder, T., 2011, Gravity processes and deposits on continental slope, rise and abyssal plains, *in* *Developments in Sedimentology*, Elsevier B.V., v. 63, p. 25–125, doi:10.1016/B978-0-444-53000-4.00002-0.
- Mulder, T., and Alexander, J., 2001, The physical character of subaqueous sedimentary density flow and their deposits: *Sedimentology*, v. 48, p. 269–299, doi:10.1046/j.1365-3091.2001.00360.x.
- Mutti, E., 1992, *Turbidite sandstones: Agip S.p.A.*, 275 p., -.
- Mutti, E., and Normark, W.R., 1987, Comparing examples of modern and ancient turbidite systems: problems and concepts, *in* *Marine Clastic Sedimentology: Concepts and Case Studies*, p. 1–38, doi:10.1007/978-94-009-3241-8_1.
- Nakajima, T., and Kneller, B.C., 2013, Quantitative analysis of the geometry of submarine external levées: *Sedimentology*, v. 60, p. 877–910,

doi:10.1111/j.1365-3091.2012.01366.x.

- Newton, S.K., and Flanagan, K.P., 1993, The Alba field: evolution of the depositional model, *in* *Petroleum Geology of Northwest Europe: Proceedings of the 4th Conference*, p. 161–171, doi:10.1144/0040161.
- Nicol, A., and Beavan, J., 2003, Shortening of an overriding plate and its implications for slip on a subduction thrust, central Hikurangi Margin, New Zealand: *Tectonics*, v. 22, p. 1–14, doi:10.1029/2003tc001521.
- Nicol, A., Mazengarb, C., Chanier, F., Rait, G., Uruski, C., and Wallace, L., 2007, Tectonic evolution of the active Hikurangi subduction margin, New Zealand, since the Oligocene: *Tectonics*, v. 26, p. 1–24, doi:10.1029/2006TC002090.
- Normark, W.R., 1978, Fan valleys, channels, and depositional lobes on modern submarine fans: characters for recognition of sandy turbidite environments: *American Association of Petroleum Geologists Bulletin*, v. 62, p. 912–931, doi:10.1306/c1ea4f72-16c9-11d7-8645000102c1865d.
- Normark, W.R., and Piper, D.J.W., 1991, Initiation processes and flow evolution of turbidity currents: implications for the depositional record, *in* *From Shoreline to Abyss: Contributions in Marine Geology in Honor of Francis Parker Shepard*, SEPM Society for Sedimentary Geology, p. 207–230.
- Ortiz-Karpf, A., Hodgson, D.M., Jackson, C.A.-L., and McCaffrey, W.D., 2017, Influence of seabed morphology and substrate composition on mass-transport flow processes and pathways: Insights from the Magdalena Fan, offshore Colombia: *Journal of Sedimentary Research*, v. 87, p. 189–209, doi:10.2110/jsr.2017.10.
- Ortiz-Karpf, A., Hodgson, D.M., and McCaffrey, W.D., 2015, The role of mass-transport complexes in controlling channel avulsion and the subsequent sediment dispersal patterns on an active margin: The Magdalena Fan, offshore Colombia: *Marine and Petroleum Geology*, v. 64, p. 58–75, doi:10.1016/j.marpetgeo.2015.01.005.
- Palm, F.A., Peakall, J., Hodgson, D.M., Marsset, T., Silva Jacinto, R., Dennielou, B., Babonneau, N., and Wright, T.J., 2021, Width variation around submarine channel bends: Implications for sedimentation and channel evolution: *Marine Geology*, v. 437, p. 106504, doi:10.1016/j.margeo.2021.106504.
- Pantin, H.M., and Franklin, M.C., 2011, Improved experimental evidence for autosuspension: *Sedimentary Geology*, v. 273, p. 46–54, doi:10.1016/j.sedgeo.2011.02.002.
- Parker, G., 1982, Conditions for the ignition of catastrophically erosive turbidity currents: *Marine Geology*, v. 46, p. 307–327.
- Parker, G., Fukushima, Y., and Pantin, H., 1986, Self-accelerating turbidity currents: *Journal of Fluid Mechanics*, v. 171, p. 145–181, doi:10.1017/S0022112086001404.
- Parker, G., Garcia, M., Fukushima, Y., and Yu, W., 1987, Experiments on turbidity

- currents over an erodible bed: *Journal of Hydraulic Research*, v. 25, p. 123–147, doi:10.1080/00221688709499292.
- Parsons, J.D., Friedrichs, C.T., Traykovski, P.A., Mohrig, D., Imran, J., Syvitski, J.P.M., Parker, G., Puig, P., Buttles, J.L., and Garca, M.H., 2007, The mechanics of marine sediment gravity flows: Continental Margin Sedimentation: From Sediment Transport to Sequence Stratigraphy IAS Special Publication, v. 37, p. 275–337, doi:10.1002/9781444304398.ch6.
- Parsons, D.R., Peakall, J., Aksu, A.E., Flood, R.D., Hiscott, R.N., Beşiktepe, Ş., and Moulard, D., 2010, Gravity-driven flow in a submarine channel bend: Direct field evidence of helical flow reversal: *Geology*, v. 38, p. 1063–1066, doi:10.1130/G31121.1.
- Paull, C.K. et al., 2018, Powerful turbidity currents driven by dense basal layers: *Nature Communications*, v. 9, p. 1–9, doi:10.1038/s41467-018-06254-6.
- Paumard, V., Bourget, J., Durot, B., Lacaze, S., Payenberg, T., George, A.D., and Lang, S., 2019, Full-volume 3D seismic interpretation methods: A new step towards high-resolution seismic stratigraphy: *Interpretation*, v. 7, p. B33–B47, doi:10.1190/INT-2018-0184.1.
- Peakall, J., Amos, K.J., Keevil, G.M., William Bradbury, P., and Gupta, S., 2007, Flow processes and sedimentation in submarine channel bends: *Marine and Petroleum Geology*, v. 24, p. 470–486, doi:10.1016/j.marpetgeo.2007.01.008.
- Peakall, J., Kane, I.A., Masson, D.G., Keevil, G., Mccaffrey, W., and Corney, R., 2012, Global (latitudinal) variation in submarine channel sinuosity: *Geology*, v. 40, p. 11–14, doi:10.1130/G32295.1.
- Peakall, J., McCaffrey, B., and Kneller, B., 2000, A process model for the evolution, morphology, and architecture of sinuous submarine channels: *Journal of Sedimentary Research*, v. 70, p. 434–448, doi:10.1306/2dc4091c-0e47-11d7-8643000102c1865d.
- Peakall, J., and Sumner, E.J., 2015, Submarine channel flow processes and deposits: A process-product perspective: *Geomorphology*, v. 244, p. 95–120, doi:10.1016/j.geomorph.2015.03.005.
- Peakall, J., Wells, M.G., Cossu, R., Kane, I.A., Masson, D.G., Keevil, G.M., Mccaffrey, W.D., and Corney, R.K.T., 2013, Global (latitudinal) variation in submarine channel sinuosity: Reply: *Geology*, doi:10.1016/j.
- Pecher, I.A., Henrys, S.A., and Zhu, H., 2004, Seismic images of gas conduits beneath vents and gas hydrates on ritchie ridge, Hikurangi Margin, New Zealand: *New Zealand Journal of Geology and Geophysics*, v. 47, p. 275–279, doi:10.1080/00288306.2004.9515054.
- Pettinga, J.R., 1982, Upper cenozoic structural history, coastal southern Hawke's Bay, New Zealand: *New Zealand Journal of Geology and Geophysics*, v. 25, p. 149–191, doi:10.1080/00288306.1982.10421407.
- Pettingill, H.S., 2004, 2. Global overview of deepwater exploration and production,

- in* Petroleum Systems of Deepwater Settings, Society of Exploration Geophysics, p. 2-19-2–56, doi:10.1306/st571314c2.
- Pettingill, H.S., and Weimer, P., 2002, Worldwide deepwater exploration and production: Past, present and future, *in* Offshore Technology Conference, p. 371–376, doi:10.4043/14024-ms.
- Pickering, K.T., Clark, J.D., Smith, R.D.A., Hiscott, R.N., Ricci Lucchi, F., and Kenyon, N.H., 1995, Architectural element analysis of turbidite systems, and selected topical problems for sand-prone deep-water systems: Atlas of Deep Water Environments, p. 1–10, doi:10.1007/978-94-011-1234-5_1.
- Piper, D.J.W., and Aksu, A.E., 1987, The source and origin of the 1929 grand banks turbidity current inferred from sediment budgets: *Geo-Marine Letters*, v. 7, p. 177–182, doi:10.1007/BF02242769.
- Piper, D.J.W., and Normark, W.R., 2009, Processes that initiate turbidity currents and their influence on turbidites: A marine geology perspective: *Journal of Sedimentary Research*, v. 79, p. 347–362, doi:10.2110/jsr.2009.046.
- Piper, D.J.W., and Normark, W.R., 2001, Sandy fans from Amazon to Hueneme and beyond: *American Association of Petroleum Geologists Bulletin*, v. 85, p. 1407–1438.
- Pirmez, C., Beaubouef, R.T., Friedmann, S.J., and Mohrig, D.C., 2000, Equilibrium profile and baselevel in submarine channels: Examples from Late Pleistocene systems and implications for the architecture of deepwater reservoirs, *in* Deep Water Reservoirs of the World: 20th Annual Research Conference, p. 782–805.
- Pirmez, C., and Flood, R.D., 1995, Morphology and structure of Amazon Channel: *Proceedings of the Ocean Drilling Program, 155 Initial Reports*, v. 155, p. 23–45, doi:10.2973/odp.proc.ir.155.103.1995.
- Pirmez, C., and Imran, J., 2003, Reconstruction of turbidity currents in Amazon Channel: *Marine and Petroleum Geology*, v. 20, p. 823–849, doi:10.1016/j.marpetgeo.2003.03.005.
- Pohl, F., Eggenhuisen, J.T., Cartigny, M.J.B., Tilston, M.C., Leeuw, J. De, and Hermidas, N., 2020a, The influence of a slope break on turbidite deposits : An experimental investigation: *Marine Geology*, v. 424, p. 1–11, doi:10.1016/j.margeo.2020.106160.
- Pohl, F., Eggenhuisen, J.T., Kane, I.A., and Clare, M.A., 2020b, Transport and burial of microplastics in deep-marine sediments by turbidity currents: *Environmental Science and Technology*, v. 54, p. 4180–4189, doi:10.1021/acs.est.9b07527.
- Ponce, J.J., and Carmona, N.B., 2011, Miocene deep-marine hyperpycnal channel levee complexes, Tierra del Fuego, Argentina: Facies associations and architectural elements, *in* Slatt, R.M. and Zavala, C. eds., *Sediment transfer from shelf to deep water—Revisiting the delivery system*, The American Association of Petroleum Geologists, p. 75–93,

doi:10.1306/13271351St613439.

- Pope, E.L. et al., 2022, First source-to-sink monitoring shows dense head controls sediment flux and runout in turbidity currents: *Science Advances*, v. 8, p. 1–16.
- Popescu, I., Lericolais, G., Panin, N., Normand, A., Dinu, C., and Le Drezen, E., 2004, The Danube submarine canyon (Black Sea): Morphology and sedimentary processes: *Marine Geology*, v. 206, p. 249–265, doi:10.1016/j.margeo.2004.03.003.
- Posamentier, H.W., and Kolla, V., 2003, Seismic geomorphology and stratigraphy of depositional elements in deep-water settings: *Journal of Sedimentary Research*, v. 73, p. 367–388, doi:10.1306/111302730367.
- Powell, M.J.D., 1970, A Fortran Subroutine for Solving Systems of Nonlinear Algebraic Equations.:
- Prather, B.E., 2003, Controls on reservoir distribution, architecture and stratigraphic trapping in slope settings: *Marine and Petroleum Geology*, v. 20, p. 529–545, doi:10.1016/j.marpetgeo.2003.03.009.
- Prather, B.E., Booth, J.R., Steffens, G.S., and Craig, P.A., 1998, Classification, lithologic calibration, and stratigraphic succession of seismic facies of intraslope basins, deep-water Gulf of Mexico: *American Association of Petroleum Geologists Bulletin*, v. 82, p. 701–728.
- Prins, M.A., and Postma, G., 2000, Effects of climate, sea level, and tectonics unraveled for last deglaciation turbidite records of the Arabian Sea: *Geology*, v. 28, p. 375–378, doi:10.1130/0091-7613(2000)28<375:EOCSLA>2.0.CO;2.
- Pyles, D.R., and Jennette, D.C., 2009, Geometry and architectural associations of co-genetic debrite-turbidite beds in basin-margin strata, Carboniferous Ross Sandstone (Ireland): Applications to reservoirs located on the margins of structurally confined submarine fans: *Marine and Petroleum Geology*, v. 26, p. 1974–1996, doi:10.1016/j.marpetgeo.2009.02.018.
- Pyles, D.R., Syvitski, J.P.M., and Slatt, R.M., 2011, Defining the concept of stratigraphic grade and applying it to stratal (reservoir) architecture and evolution of the slope-to-basin profile: An outcrop perspective: *Marine and Petroleum Geology*, v. 28, p. 675–697, doi:10.1016/j.marpetgeo.2010.07.006.
- Qin, Y., Alves, T.M., Constantine, J., and Gamboa, D., 2016, Quantitative seismic geomorphology of a submarine channel system in SE Brazil (Espírito Santo Basin): Scale comparison with other submarine channel systems: *Marine and Petroleum Geology*, v. 78, p. 455–473, doi:10.1016/j.marpetgeo.2016.09.024.
- Rabouille, C. et al., 2019, Carbon and silica megasink in deep-sea sediments of the Congo terminal lobes: *Quaternary Science Reviews*, v. 222, p. 1–7, doi:10.1016/j.quascirev.2019.07.036.
- Reading, H.G., and Richards, M., 1994, Turbidite systems in deep-water basin margins classified by grain size and feeder system: *American Association of Petroleum Geologists Bulletin*, v. 78, p. 792–822, doi:10.1306/a25fe3bf-171b-

11d7-8645000102c1865d.

- Ren, P., Bornhold, B.D., and Prior, D.B., 1996, Seafloor morphology and sedimentary processes, Knight Inlet, British Columbia: *Sedimentary Geology*, v. 103, p. 201–228, doi:10.1016/0037-0738(95)00090-9.
- Reyners, M., 2013, The central role of the Hikurangi Plateau in the Cenozoic tectonics of New Zealand and the Southwest Pacific: *Earth and Planetary Science Letters*, v. 361, p. 460–468, doi:10.1016/j.epsl.2012.11.010.
- Richards, M., and Bowman, M., 1998, Submarine fans and related depositional systems II: Variability in reservoir architecture and wireline log character: *Marine and Petroleum Geology*, v. 15, p. 821–839, doi:10.1016/S0264-8172(98)00042-7.
- Schwanghart, W., and Kuhn, N.J., 2010, TopoToolbox: A set of Matlab functions for topographic analysis: *Environmental Modelling and Software*, v. 25, p. 770–781, doi:10.1016/j.envsoft.2009.12.002.
- Sequeiros, O.E., 2012, Estimating turbidity current conditions from channel morphology: A Froude number approach: *Journal of Geophysical Research: Oceans*, v. 117, p. 1–19, doi:10.1029/2011JC007201.
- Sequeiros, O.E., Naruse, H., Endo, N., Garcia, M.H., and Parker, G., 2009, Experimental study on self-accelerating turbidity currents: *Journal of Geophysical Research: Oceans*, v. 114, p. 1–26, doi:10.1029/2008JC005149.
- Sequeiros, O.E., Spinewine, B., Beaubouef, R.T., Sun, T., García, M.H., and Parker, G., 2010, Characteristics of velocity and excess density profiles of saline underflows and turbidity currents flowing over a mobile bed: *Journal of Hydraulic Engineering*, v. 136, p. 412–433, doi:10.1061/(ASCE)HY.1943-7900.0000200.
- Shepard, F.P., 1981, Submarine canyons: multiple causes and long-time persistence.: *American Association of Petroleum Geologists Bulletin*, v. 65, p. 1062–1077, doi:10.1306/03b59459-16d1-11d7-8645000102c1865d.
- Simmons, S.M., Azpiroz-Zabala, M., Cartigny, M.J.B., Clare, M.A., Cooper, C., Parsons, D.R., Pope, E.L., Sumner, E.J., and Talling, P.J., 2020, Novel acoustic method provides first detailed measurements of sediment concentration structure within submarine turbidity currents: *Journal of Geophysical Research: Oceans*, v. 125, p. 1–24, doi:10.1029/2019JC015904.
- Soulsby, R.L., 1997, *Dynamics of marine sands: A manual for practical applications*: Thomas Telford, 249 p.
- Sprague, A., Garfield, T., and Goulding, F., 2005, Integrated slope channel depositional models: the key to successful prediction of reservoir presence and quality in offshore West Africa, *in* E-Exitep 2005, Colegio de Ingenieros Petroleros de México, p. 1–13, doi:-.
- Spychala, Y.T., Hodgson, D.M., Prélat, A., Kane, I.A., Flint, S.S., and Mountney, N.P., 2017, Frontal and lateral submarine lobe fringes: Comparing

- sedimentary facies, architecture and flow processes: *Journal of Sedimentary Research*, v. 87, p. 75–96, doi:10.2110/jsr.2017.2.
- Stacey, M.W., and Bowen, A.J., 1988a, The vertical structure of density and turbidity currents: theory and observations: *Journal of Geophysical Research*, v. 93, p. 3528–3542, doi:10.1029/JC093iC04p03528.
- Stacey, M.W., and Bowen, A.J., 1988b, The vertical structure of turbidity currents and a necessary condition for self-maintenance: *Journal of Geophysical Research*, v. 93, p. 3543–3553, doi:10.1029/JC093iC04p03543.
- Stevenson, C.J., Feldens, P., Georgiopoulou, A., Schönke, M., Krastel, S., Piper, D.J.W., Lindhorst, K., and Mosher, D., 2018, Reconstructing the sediment concentration of a giant submarine gravity flow: *Nature Communications*, v. 9, p. 1–7, doi:10.1038/s41467-018-05042-6.
- Stevenson, C.J., Jackson, C.A.-L., Hodgson, D.M., Hubbard, S.M., and Eggenhuisen, J.T., 2015, Deep-water sediment bypass: *Journal of Sedimentary Research*, v. 85, p. 1058–1081, doi:10.2110/jsr.2015.63.
- Stevenson, C.J., Talling, P.J., Sumner, E.J., Masson, D.G., Frenz, M., and Wynn, R.B., 2014, On how thin submarine flows transported large volumes of sand for hundreds of kilometres across a flat basin plain without eroding the sea floor: *Sedimentology*, v. 61, p. 1982–2019, doi:10.1111/sed.12125.
- Stevenson, C.J., Talling, P.J., Wynn, R.B., Masson, D.G., Hunt, J.E., Frenz, M., Akhmetzhanov, A., and Cronin, B.T., 2013, The flows that left no trace: Very large-volume turbidity currents that bypassed sediment through submarine channels without eroding the sea floor: *Marine and Petroleum Geology*, v. 41, p. 186–205, doi:10.1016/j.marpetgeo.2012.02.008.
- Stirling, E.J., Fugelli, E.M.G., and Thompson, M., 2018, The edges of the wedges: A systematic approach to trap definition and risking for stratigraphic, combination and sub-unconformity traps, *in* *Petroleum Geology of NW Europe: 50 years of learning - Proceedings of the 8th Petroleum Geology Conference*, p. 273–286, doi:10.1144/PGC8.19.
- Stoker, S.J., Gray, J.C., Haile, P., Andrews, I.J., and Cameron, T.D.J., 2006, The importance of stratigraphic plays in the undiscovered resources of the UK Continental Shelf, *in* Allen, M.R., Goffey, G.P., Morgan, R.K., and Walker, I.M. eds., *The deliberate search for the stratigraphic trap*. Geological Society, London, Special Publications, The Geological Society of London, v. 254, p. 153–167, doi:10.1144/GSL.SP.2006.254.01.08.
- Straccia, J.R., and Prather, B.E., 1999, Stratigraphic traps in deep-water turbidite reservoirs at the base of depositional slope, *in* *Society of Petroleum Engineers, Offshore Europe Conference, SPE*,.
- Strachan, L.J., Bostock, H.C., Barnes, P.M., Neil, H.L., and Gosling, M., 2016, Non-cohesive silt turbidity current flow processes; insights from proximal sandy-silt and silty-sand turbidites, Fiordland, New Zealand: *Sedimentary Geology*, v. 342, p. 118–132, doi:10.1016/j.sedgeo.2016.06.017.

- Straub, K.M., and Mohrig, D., 2008, Quantifying the morphology and growth of levees in aggrading submarine channels: *Journal of Geophysical Research*, v. 113, p. 1–20, doi:10.1029/2007JF000896.
- Straub, K.M., Mohrig, D., McElroy, B., Buttles, J., and Pirmez, C., 2008, Interactions between turbidity currents and topography in aggrading sinuous submarine channels: A laboratory study: *Bulletin of the Geological Society of America*, v. 120, p. 368–385, doi:10.1130/B25983.1.
- Straub, K.M., Mohrig, D., and Pirmez, C., 2012, Architecture of an aggradational tributary submarine-channel network on the continental slope offshore Brunei Darussalam: *SEPM Special publication*, p. 13–30.
- Sumner, E.J., Peakall, J., Dorrell, R.M., Parsons, D.R., Darby, S.E., Wynn, R.B., McPhail, S.D., Perrett, J., Webb, A., and White, D., 2014, Driven around the bend: Spatial evolution and controls on the orientation of helical bend flow in a natural submarine gravity current: *Journal of Geophysical Research : Oceans*, v. 119, p. 898–913, doi:10.1002/2013JC009563.
- Sumner, E.J., Peakall, J., Parsons, D.R., Wynn, R.B., Darby, S.E., Dorrell, R.M., McPhail, S.D., Perrett, J., Webb, A., and White, D., 2013, First direct measurements of hydraulic jumps in an active submarine density current: *Geophysical Research Letters*, v. 40, p. 1–5, doi:10.1002/2013GL057862.
- Sylvester, Z., Cantelli, A., and Pirmez, C., 2015, Stratigraphic evolution of intraslope minibasins: Insights from surface-based model: *American Association of Petroleum Geologists Bulletin*, v. 99, p. 1099–1129, doi:10.1306/01081514082.
- Sylvester, Z., and Pirmez, C., 2019, Latitudinal Changes in the Morphology of Submarine Channels: Reevaluating the Evidence for the Influence of the Coriolis Force: *SEPM Special Publications*, v. 108, p. 82–92, doi:10.2110/sepm.sp.108.02.
- Sylvester, Z., Pirmez, C., and Cantelli, A., 2011, A model of submarine channel-levee evolution based on channel trajectories: Implications for stratigraphic architecture: *Marine and Petroleum Geology*, v. 28, p. 716–727, doi:10.1016/j.marpetgeo.2010.05.012.
- Sylvester, Z., Pirmez, C., Cantelli, A., and Jobe, Z.R., 2013, Global (latitudinal) variation in submarine channel sinuosity: Comment: *Geology*, v. 41, p. e287, doi:10.1130/G33548C.1.
- Symons, W.O., Sumner, E.J., Paull, C.K., Cartigny, M.J.B., Xu, J.P., Maier, K.L., Lorenson, T.D., and Talling, P.J., 2017, A new model for turbidity current behavior based on integration of flow monitoring and precision coring in a submarine canyon: *Geology*, v. 45, p. 367–370, doi:10.1130/G38764.1.
- Talling, P.J. et al., 2015, Key future directions for research on turbidity currents and their deposits: *Journal of Sedimentary Research*, v. 85, p. 153–169, doi:10.2110/jsr.2015.03.
- Talling, P.J., Masson, D.G., Sumner, E.J., and Malgesini, G., 2012, Subaqueous

- sediment density flows: Depositional processes and deposit types: *Sedimentology*, v. 59, p. 1937–2003, doi:10.1111/j.1365-3091.2012.01353.x.
- Talling, P.J., Paull, C.K., and Piper, D.J.W., 2013, How are subaqueous sediment density flows triggered, what is their internal structure and how does it evolve? Direct observations from monitoring of active flows: *Earth-Science Reviews*, v. 125, p. 244–287, doi:10.1016/j.earscirev.2013.07.005.
- Tek, D.E., Mearthur, A.D., Poyatos-Moré, M., Colombera, L., Patacci, M., Craven, B., and Mccaffrey, W.D., 2021, Relating seafloor geomorphology to subsurface architecture: How mass-transport deposits and knickpoint-zones build the stratigraphy of the deep-water Hikurangi Channel: *Sedimentology*, v. 68, p. 3141–3190, doi:10.1111/sed.12890.
- Torres, J., Droz, L., Savoye, B., Terentieva, E., Cochonat, P., Kenyon, N.H., and Canals, M., 1997, Deep-sea avulsion and morphosedimentary evolution of the Rhône Fan Valley and Neofan during the Late Quaternary (north-western Mediterranean Sea): *Sedimentology*, v. 44, p. 457–477, doi:10.1046/j.1365-3091.1997.d01-36.x.
- Traer, M., Fildani, A., McHargue, T., and Hilley, G.E., 2015, Simulating depth-averaged, one-dimensional turbidity current dynamics using natural topographies: *Journal of Geophysical Research: Earth Surface*, v. 120, p. 1485–1500, doi:10.1002/2013JF002871.Received.
- Vangriesheim, A., Khripounoff, A., and Crassous, P., 2009, Turbidity events observed in situ along the Congo submarine channel: *Deep-Sea Research Part II: Topical Studies in Oceanography*, v. 56, p. 2208–2222, doi:10.1016/j.dsr2.2009.04.004.
- Vendettuoli, D. et al., 2019, Daily bathymetric surveys document how stratigraphy is built and its extreme incompleteness in submarine channels: *Earth and Planetary Science Letters*, v. 515, p. 231–247, doi:10.1016/j.epsl.2019.03.033.
- Wallace, L.M., Saffer, D.M., Barnes, P.M., Pecher, I.A., Petronotis, K.E. LeVay, L., and Expedition 372/375 Scientists, 2019, Hikurangi Subduction Margin coring, logging, and observatories: *Proceedings of the International Ocean Discovery Program*, v. 372B/375, p. 1–15, doi:https://doi.org/10.14379/iodp.proc.372B375.2019.
- Weimer, P., and Slatt, R.M., 2004, 6. Deepwater Reservoir Elements: Channels and their Sedimentary Fill, *in* *Petroleum Systems of Deepwater Settings*, Society of Exploration Geophysics, p. 6-171-6–276, doi:10.1190/1.9781560801955.ch4.
- Wells, M.G., and Cossu, R., 2013, The possible role of Coriolis forces in structuring large-scale sinuous patterns of submarine channel – levee systems: *Philosophical transactions of the Royal Society A*, v. 371, p. 1–19.
- Wells, M.G., and Dorrell, R.M., 2021, Turbulence processes within Turbidity Currents: *Annual Review of Fluid Mechanics*, v. 53, p. 59–83, doi:https://doi.org/10.1146/annurev-fluid-010719- 060309.

- Widess, M.B., 1973, How thin is a thin bed? *Geophysics*, v. 38, p. 1176–1180.
- Wiles, E., Green, A., Watkeys, M., and Jokat, W., 2017, The Zambezi Channel: A new perspective on submarine channel evolution at low latitudes: *Geomorphology*, v. 286, p. 121–132, doi:10.1016/j.geomorph.2017.02.014.
- Wynn, R.B., Cronin, B.T., and Peakall, J., 2007, Sinuous deep-water channels: Genesis, geometry and architecture: *Marine and Petroleum Geology*, v. 24, p. 341–387, doi:10.1016/j.marpetgeo.2007.06.001.
- Wynn, R.B., Kenyon, N.H., Masson, D.G., Stow, D.A.V., and Weaver, P.P.E., 2002, Characterization and recognition of deep-water channel-lobe transition zones: *American Association of Petroleum Geologists Bulletin*, v. 86, p. 1441–1462.
- Xu, J.P., Sequeiros, O.E., and Noble, M.A., 2014, Sediment concentrations, flow conditions, and downstream evolution of two turbidity currents, Monterey Canyon, USA: *Deep-Sea Research Part I: Oceanographic Research Papers*, v. 89, p. 11–34, doi:10.1016/j.dsr.2014.04.001.
- Zeng, J., Lowe, D.R., Prior, D.B., Wiseman, W.J.J., and Bornhold, B.D., 1991, Flow properties of turbidity currents in Bute Inlet, British Columbia: *Sedimentology*, v. 38, p. 975–996, doi:10.1111/j.1365-3091.1991.tb00367.x.
- Zhang, Y., Liu, Z., Zhao, Y., Colin, C., Zhang, X., Wang, M., Zhao, S., and Kneller, B., 2018, Long-term in situ observations on typhoon-triggered turbidity currents in the deep sea: *Geology*, v. 46, p. 675–678, doi:10.1130/G45178.1.
- Zhao, X., Qi, K., Patacci, M., Tan, C., and Xie, T., 2019, Submarine channel network evolution above an extensive mass-transport complex : A 3D seismic case study from the Niger delta continental slope: *Marine and Petroleum Geology*, v. 104, p. 231–248, doi:10.1016/j.marpetgeo.2019.03.029.
- Zhong, G., and Peng, X., 2021, Transport and accumulation of plastic litter in submarine canyons—The role of gravity flows: *Geology*, v. 49, p. 581–586, doi:10.1130/G48536.1.

Appendix A Submarine channel data from Chapter 3

A.1 Madden Channel morphometrics

Table A.1 Channel morphometrics used as input parameters in the turbidity current modelling for the Madden Channel. Values of 99999 correspond to straight channel sections.

Average channel height \bar{H} (m)	Slope gradient S (°)	Cross-channel slope γ (m/m)	Latitude θ (degrees)	Radius of curvature r (m)	Channel width W (m)
546	0.720	0.021	-40.5	99999	6,190
415	0.720	0.028	-40.5	99999	6,355
395.5	2.060	0.030	-40.5	99999	6,842
399	2.060	0.047	-40.5	99999	5,115.5
416.5	1.226	0.019	-40.5	99999	9,855.5
447	0.495	0.015	-40.5	99999	10,295.5
340.5	0.044	0.017	-40.5	7109	12,979.5
330.5	0.044	0.017	-40.6	99999	13,481
292	0.022	0.013	-40.6	99999	10,586.5
248	0.022	0.017	-40.6	99999	10,183
40.5	0.042	0.006	-40.66	99999	2,911
29	0.042	0.007	-40.68	99999	2,327.5
22.5	0.042	0.004	-40.7	99999	4,080.5
11.5	2.015	0.006	-40.73	99999	1,495.5
12.5	1.155	0.005	-40.75	99999	1,511
24.5	1.048	0.002	-40.76	824	1,374
32	1.264	0.004	-40.77	99999	1,377
21	1.264	0.008	-40.77	99999	1,187
19.5	1.146	0.003	-40.78	99999	934

A.2 Omakere Channel morphometrics

Table A.2 Channel morphometrics used as input parameters in the turbidity current modelling for the Omakere Channel. Values of 99999 correspond to straight channel sections.

Average channel height	Slope gradient	Cross-channel slope	Latitude	Radius of curvature	Channel width
\bar{H} (m)	S (°)	γ (m/m)	θ (degrees)	r (m)	W (m)
220	0.197	0.007	-40.33	99999	6,312
206	0.095	0.014	-40.32	99999	6,287.5
195	0.095	0.027	-40.31	99999	4,618
145	0.095	0.022	-40.31	99999	4,677
120.5	1.473	0.029	-40.29	99999	4,397.5
59	0.660	0.057	-40.27	2324	1,348
72	0.660	0.069	-40.24	99999	1,350.5
156	3.091	0.044	-40.23	99999	2,701.5
14.5	0.126	0.005	-40.22	99999	3,341.5
81.5	0.126	0.006	-40.24	99999	8,939.5
40.5	1.196	0.002	-40.28	2235.5	4,209
83	0.358	0.005	-40.26	99999	6,963.5
136	0.259	0.007	-40.24	99999	5,977.5
295.5	0.259	0.009	-40.25	99999	7,686.5
419.5	0.366	0.019	-40.27	99999	4,197
187.5	0.366	0.004	-40.29	99999	5,992
215	2.562	0.007	-40.31	99999	2,861.5
120	0.008	0.021	-40.35	99999	6,081

Appendix B Channel-form data from Chapter 4

B.1 Channel-form A morphometrics

Table B.1 Channel morphometrics used as input parameters in the turbidity current modelling for channel-form A. Values of 99999 correspond to straight channel sections.

Average channel height	Slope gradient	Cross-channel slope	Latitude	Radius of curvature	Channel width
\bar{H} (m)	S (°)	γ (m/m)	θ (degrees)	r (m)	W (m)
28	0.004	0.015	-39.79	99999	121.35
26.5	0.004	0.017	-39.79	99999	168.95
28.5	0.004	0.004	-39.8	99999	262.35
48.5	0.004	0.011	-39.81	929.7	270.5
45	0.007	0.014	-39.82	99999	267.6
46	0.007	0.036	-39.82	99999	257
49.5	0.006	0.035	-39.83	99999	293.85
49	0.006	0.020	-39.83	99999	284.6
42	0.014	0.005	-39.84	920	381.55
45.5	0.014	0.019	-39.85	935.5	480
45.5	0.020	0.020	-39.86	99999	311.45
50.5	0.020	0.027	-39.86	1909.5	367.8
45.5	0.013	0.003	-39.87	99999	292.55
51.5	0.013	0.003	-39.88	99999	318.3
58.5	0.013	0.008	-39.89	99999	349.45
56	0.011	0.008	-39.9	99999	468.55
55	0.001	0.004	-39.91	99999	468
52.5	0.001	0.021	-39.92	1205.5	554.65
65.5	0.001	0.020	-39.93	99999	668.6
63	0.001	0.005	-39.94	99999	852.95
58	0.001	0.012	-39.95	99999	817.6
58.5	0.001	0.027	-39.95	99999	883
40	0.001	0.011	-39.95	99999	514.4
52	0.006	0.063	-39.96	1151.5	530.15

47.5	0.006	0.019	-39.96	99999	456.4
28	0.006	0.051	-39.97	99999	364.45
31	0.006	0.013	-39.97	99999	428.15

Appendix C Submarine channel data used in Chapter 5

C.1 NAMOC morphometrics

Table C.1 Parameters extracted from Klaucke et al., (1997) that were used in the calculations of the NAMOC tilting.

Downstream distance	Average channel height H (m)	Downchannel slope S (m/m)	Latitude θ (degrees)	Radius of curvature r (m)	Levee height difference ΔH (m)	Channel-levee tilt γ_m (m/m)	Channel width W (m)
22.6	142.5	0.00146	59.700	16000	11	0.000379	29000
39	164	0.00095	59.500	21000	4	0.000167	24000
50.2	170	0.00036	59.3	14000	14	0.00056	25000
71	149.5	0.00064	59.3	18000	67	0.002481	27000
100.2	176	0.00077	59.3	27000	74	0.003895	19000
119.8	138.5	0.00062	59.2	30000	55	0.003667	15000
148.4	141	0.00086	59.1	39000	68	0.004857	14000
166.6	127	0.00094	58.95	50000	76	0.005846	13000
179.1	142.5	0.00092	58.9	43000	57	0.004385	13000
198.3	138.5	0.00096	58.78	46000	53	0.004818	11000
215.1	146.5	0.00096	58.6	54000	49	0.003769	13000
235.9	149.5	0.00069	58.5	30000	77	0.0055	14000
250.3	149.5	0.00056	58.3	20000	91	0.007	13000
279.9	135	0.00051	58.3	17000	96	0.006857	14000
294.5	127.5	0.00049	58.1	18000	73	0.006636	11000
308.9	126.5	0.00022	58.11	18000	101	0.009182	11000
330.9	116	0.0009	58	18000	86	0.006615	13000
366.9	123.5	0.00141	57.8	34000	79	0.005267	15000
386.9	118.5	0.00011	57.6	13000	59	0.002682	22000
427.2	93.5	0.00026	57.4	47000	85	0.004722	18000

454	100.5	0.00115	57.2	31000	93	0.00372	25000
485.6	108.5	0.00063	57.1	28000	73	0.00365	20000
517.7	114	0.00052	56.7	44000	50	0.002083	24000
547.5	159.5	0.00069	56.5	34000	157	0.009235	17000
581.5	117	0.001	56.3	48000	70	0.004118	17000
641	132.5	0.00089	56.1	63000	67	0.00231	29000
666.4	138.5	0.00075	55.5	32000	33	0.001571	21000
685.4	162	0.00045	55.4	25000	78	0.004333	18000
709.8	139	0.00042	55.2	42000	50	0.001923	26000
730	148.5	0.0007	55.1	30000	75	0.003125	24000
753	173	0.00041	54.9	36000	62	0.002583	24000
809.8	161	0.00048	54.5	60000	32	0.00128	25000
855.8	143	0.00066	54.1	43000	50	0.002381	21000
896	159	0.00074	53.8	34000	74	0.0037	20000
949	100.5	0.00034	53.3	44000	65	0.0026	25000

C.2 Global channel data

Table C.2 Summary of data used from nine submarine channel systems. r , θ and S_i were obtained from Sylvester and Pirmez (2019).

Channel	Location	Radius of curvature r (m) Minimum-maximum	Radius of curvature r (m) Mean	Latitude θ (°)	Sinuosity S_i Maximum	Downchannel slope S (m/m)	S reference
Amazon	Offshore Brazil	255-6,866	807	3.17- 7.99	4.1	0.004	Pirmez and Flood (1995)
Danube	Black Sea	157-2650	771	43.14- 44.03	3.46	0.006	Popescu et al. (2004)
Knight Inlet	British Columbia	145-357	250	51.02- 51.05	4.24	0.016	Ren et al. (1996)
Monterey	Offshore Central California	141-6015	1571	35.20- 36.80	2.35	0.010	Clark et al. (1992)

NAMOC	Labrador Sea	2711-14822	8560	56.39-60.80	1.15	0.0006	Klaucke et al. (1997)
Nile	Mediterranean Sea	91-795	335	32.36-32.48	4.7	0.008	Migeon et al. (2010)
Rhone	Mediterranean Sea	398-3573	1289	41.83-43	1.62	0.009	Clark et al. (1992)
Tanzania	Indian Ocean, Eastern Africa	5304-17890	8711	(-6.22) - (-7.53)	1.11	0.001	Bourget et al. (2008)
Zaire	Offshore west Africa	192-4389	716	(-5.5) - (-6.6)	3.5	0.004	Babonneau et al. (2002)

Appendix D MATLAB code for turbidity current modelling

D.1 Script

```
% predefined parameters
%%%%%%%%%%%%%%%%%%%%%%%%%%%%%%%%%%%%%%%%%%%%%%%%%%%%%%%%%%%%%%%%%%%%%%%%
g = 9.81;%gravity
Cd = 1/20^2;%basal friction coefficient
ps = 2650;%density of suspended particle
pf = 1000; %density of ambient fluid
R = ps/pf-1;%submerged grav
W = 7.2921150*1e-5;%earth's rotation rate
%%%%%%%%%%%%%%%%%%%%%%%%%%%%%%%%%%%%%%%%%%%%%%%%%%%%%%%%%%%%%%%%%%%%%%%%
%%%%%%%%%%%%%%%%%%%%%%%%%%%%%%%%%%%%%%%%%%%%%%%%%%%%%%%%%%%%%%%%%%%%%%%%
M =TS1hmax25; %matrix with input parameter
N = length(M(:,1));
for n=1:N
    % parameters to define for each transect
    %%%%%%%%%%%%%%%%%%%%%%%%%%%%%%%%%%%%%%%%%%%%%%%%%%%%%%%%%%%%%%%%%%%%%%%%%
    y(n) = M(n,1);%distance
    h(n) = M(n,2);%flow height
    S(n) = tand(M(n,3));%slope
    dhdr(n) = M(n,4);%tilt
    Lat(n) = M(n,5);%latitude
    pm(n) = M(n,6);%coriolis orientation
    r(n) = M(n,7);%radius of curvature
    A(n) = M(n,8);%area of channel
    wi(n) = M(n,9);%channel width
    Fro(n) = sqrt(S(n)/Cd);
```

```

%      co(n) = -
2*W*sind(Lat(n))/dhdr(n)*h(n)/sqrt(g*R*h(n));
      co(n) = ((-
2*W*sind(Lat(n))*Fro(n)*h(n))^2)/(dhdr(n)^2*g*R*h(n));
%      co(n) = ((-
2*W*sind(Lat(n))*r(n))^2)/(Fro(n)^2*g*R*h(n));
      xo      = [co(n),Fro(n)];

%%%%%%%%%%%%%%%%%%%%%%%%%%%%%%%%%%%%%%%%%%%%%%%%%%%%%%%%%%%%%%%%%%%%%%%%
%%%%%%%%%%%%%%%%%%%%%%%%%%%%%%%%%%%%%%%%%%%%%%%%%%%%%%%%%%%%%%%%%%%%%%%%
%      options =
optimoptions('fsolve','Display','iter','tolfun',1e-
12,'tolx',1e-12);
%      [x,exitflag,output] = fsolve(@(x)
vc(x,h(n),S(n),dhdr(n),Lat(n),r(n),pm(n),Cd,g,R,W),xo,optio
ns);
      options =
optimoptions('lsqnonlin','Display','iter','tolfun',1e-
12,'tolx',1e-12);
      [x,exitflag,output] = lsqnonlin(@(x)
vc(x,h(n),S(n),dhdr(n),Lat(n),r(n),pm(n),Cd,g,R,W),xo,[],[]
,options);
      c(n) = x(1);%concentration
      Fr(n) = x(2);%Froude
      u(n) = Fr(n)*sqrt(g*R*c(n)*h(n));%velocity

end
Qtc=u.*A; %flow discharge
Qstc=c.*Qtc;%sediment discharge
us = sqrt(Cd).*u;%shear velocity

```

D.2 Function

```

function F = vc(x,h,S,dhdr,Lat,r,pm,Cd,g,R,W)
c = x(1);
Fr = x(2);
Ri = 1/Fr^2;
f = 2*W*sind(Lat);

E = 0.00153/(0.0204 + Ri); % Abad Eq 9
eq1 = (Cd + E*(1+Ri/2))/Ri-S; % Abad Eq 47
gravitational force - drag balance
if r<99999
      eq2 = -
1/h*dhdr+pm*Fr*f/sqrt(g*R*c*h)+Fr^2/r; % Cossu
& Wells Eq 1; Stevenson Eq 2 %for channel bends
else

```

```
    eq2 = -1/h*dhdr+pm*Fr*f/sqrt(g*R*c*h); %  
    Cossu & Wells Eq 1; Stevenson Eq 2 %for  
    straight sections
```

```
end
```

```
F = [eq1,eq2];
```